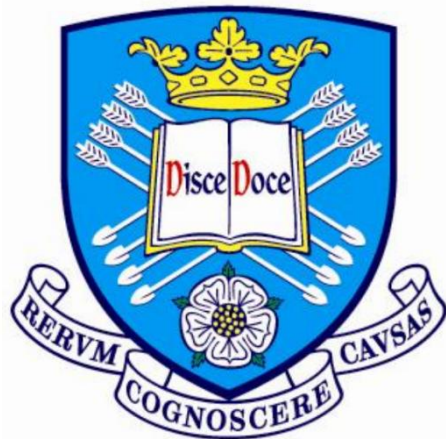


**Effects of Variable Load and Rotational Speed Conditions on  
Gear Micropitting in Wind Turbine Gearboxes**



**Issa Saif Mohammed Al Tubi**

**A thesis submitted for the degree of Doctor of Philosophy**

**Department of Mechanical Engineering**

**Faculty of Engineering**

**The University of Sheffield**

**Supervised by:**

**Dr. Hui Long**

**Dr. Brian Shaw**

**Dr. Jishan Zhang**

**October 2014**



## ABSTRACT

Micropitting damage is one of the failure modes commonly observed on gears and bearings in wind turbine (WT) gearboxes. It can lead to destructive failures which, in turn, lead to unplanned WT shutdown and expensive replacement. This research provides an insight into effects of variable load and rotational speed condition on micropitting in WT gearboxes. It also investigates in detail the occurrence of micropitting in WT gearboxes under various operational conditions using an experimental study and an analytical study, employing two methods: an analytical method based on selected SCADA (Supervisory Control and Data Acquisition) data and a probabilistic modelling of SCADA data method.

This study focuses predominantly on the micropitting of the high speed shaft (HSS) gear of a WT gearbox operating under nominal and varying load and speed conditions. The SCADA datasets recorded from WT gearboxes in operation are used. Based on the SCADA data, the recorded WT generator power output and generator rotational speed are used to obtain the shaft torque of the HSS driven gear. Based on ISO Technical Report ISO/TR 15144-1 (2010) and various ISO gear standards, an analytical study is carried out to assess the risk of gear micropitting by determining the contact stress, sliding parameter, local contact temperature, lubricant film thickness and specific lubricant film thickness along the line of action of the gear tooth contact by considering the WT operating load and speed conditions.

The experimental study investigates the initiation and progression of gear micropitting when gear tooth flanks are subjected to varying torque levels at a constant rotational speed. The study is conducted by carrying out gear micropitting testing and surface inspection, as well as validating implementing analytical evaluations by comparing the obtained results with that obtained by using various commercial software packages based on ISO Technical Report ISO/TR 15144-1 and AGMA 925-A03 standard. The surface inspection of tested gears is carried out using procedures of surface roughness measurement, replica of surface micropits and profile deviation measurement. The analytical results are compared to the experimental results to predict the occurrence of gear micropitting through evaluating tooth contact stress, sliding parameter, local contact temperature and specific lubricant film thickness at different points along the gear tooth flank.

The surface roughness measurements, obtained from the tested gears after each cycle run under specific torque levels, are considered in the analytical investigation. The gear testing results show that micropitting initiates at the pinion dedendum, but escalates at the addendum because of the greater severity of progressive micropitting at the mating wheel dedendum. The micropitting initiates at the beginning of the tip relief area of the pinion and at the root of the pinion with which the wheel tip relief area first starts to mesh. The analytical results confirm that maximum contact stresses and minimum lubricant film thickness occur at these areas. The lubricant film thickness varies considerably because of changes in surface roughness after the gears undergo various

running cycles under varying torque levels. The validation process reveals that the ISO/TR 15144-1 results provide a better correlation with experimental results, as compared to AGMA 925-A03 results.

The analysis of WT operational condition using selected one month SCADA data identifies three regions of relationships between the generator power and wind speed, the generator speed and wind speed variations. Non-uniform distributions of contact stress, contact temperature and lubricant film thickness over the tooth flank are observed. This is due to the conditions of torque and rotational speed variations and sliding contact along the gear tooth flanks. The lubricant film thickness varies along the tooth flank and is at its lowest when the tip of the HSS wheel gear engages with the root of the HSS driven gear. The lubricant film thickness increases with the increase of the rotational speed and decreases as the torque and sliding increase. It can be concluded that micropitting is most likely to initiate at the dedendum of pinion gear. The lowest film thickness occurs when the torque is high and the rotational speed is at its lowest, which may cause direct tooth surface contact. In low torque condition, the varying rotational speed condition may cause a considerable variation in lubricant film thickness, thus interrupting the lubrication, which may result in micropitting.

Finally, a probabilistic analysis is carried out to investigate the probabilistic risk of tooth flank micropitting failure using the entire SCADA datasets. A random number of datasets of smaller sizes of gear shaft torque and rotational speed are generated to substitute for the large amounts of data in the original SCADA datasets. Based on the selected random number datasets, the effect of variations in gear shaft torque and rotational speed on the probabilistic characteristics of gear tooth flank micropitting is investigated. The study shows that the HSS driven pinion gear is subject to overloading conditions, resulting in maximum contact stresses higher than the allowable contact stress of the material. Thus, the high torque value, which occurs at low rotational speed according to the data analysis, is the main cause of micropitting in WTs as it leads to high contact stress. In addition, the results of the analysis of specific lubricant film thickness show that there is a considerable risk of micropitting at the dedendum region of gear teeth under variable operational condition.

## **ACKNOWLEDGMENTS**

First of all, I thank Almighty Allah for instilling in me the ability and determination to complete this piece of work.

In writing this thesis, I sought the assistance of other people who kindly offered their support and cooperation. I would like to hereby acknowledge their help because “Those who do not thank people, do not thank Allah” (Prophet Mohammed). For their valuable assistance, I am indebted to the following individuals: I would like to express my appreciative thanks and gratitude to my supervisor Dr. Hui Long, who enlightened me with her precious thoughts and opinion during all time of this work. I deeply appreciate her generous efforts in reviewing this dissertation, patient, guidance and consistent support.

I am also deeply indebted to my second supervisors, Dr. Brian Shaw and Dr. Jishan Zhang, from Newcastle University-Design Unit for their helpful comments and guidance while performing the experiments in their laboratories. Dr. Zhang’s generous technical support has positively impacted the effectiveness of the practical work. Thanks also go to the members within the department of materials and metrology Laboratories from the Design Unit, Chris Aylott and Steve Charlton for their cooperation throughout the experimental stage.

A word of appreciation and gratitude is due to the Ministry of Manpower (Sultanate of Oman) for giving me the chance to pursue studies to obtain my PhD degree.

My heartfelt gratitude is due to my mother for her sincere prayers and unconditional love. My sincere appreciations go to my wife (Raya) and Children (Al Ozd, Faris, Munia, Yumn, Alia and Sana) for their unwavering support and encouragement. Special thanks also go to all my brothers, sister, friends and all members of my family, who always encouraged and supported me throughout my postgraduate journey.

---

**TABLE OF CONTENTS**

ABSTRACT .....	i
ACKNOWLEDGMENTS .....	iii
LIST OF FIGURES .....	viii
LIST OF TABLES .....	xiii
NOMENCLATURE.....	xiv
<b>Chapter 1: Introduction .....</b>	<b>1</b>
1.1 RESEARCH BACKGROUND.....	2
1.1.1 Recent Development of Wind Energy Industry .....	3
1.1.2 Failures of Wind Turbine Subsystems and Components .....	4
1.2 GEAR MICROPITTING .....	5
1.3 PROBLEM STATEMENT .....	7
1.4 RESEARCH OBJECTIVES .....	9
1.5 DISSERTATION OUTLINE.....	9
<b>Chapter 2: Literature Review.....</b>	<b>12</b>
2.1 GEAR INTRODUCTION.....	13
2.1.1 Gear Materials .....	13
2.1.2 Gear Manufacturing Methods .....	14
2.1.3 Gear Surface Treatment Methods .....	15
2.1.3.1 Carburising .....	16
2.1.3.2 Nitriding .....	17
2.1.3.3 Induction Hardening .....	17
2.1.3.4 Flame Hardening.....	18
2.1.3.5 Shot Peening .....	18
2.1.3.6 Combined Heat Treatments Method .....	18
2.2 GEAR DESIGN STANDARDS .....	19
2.3 WIND TURBINE GEARBOX CONFIGURATIONS .....	20
2.4 GEAR FAILURE MODES .....	23
2.4.1 Pitting .....	24
2.4.2 Sliding Wear.....	26
2.4.3 Scuffing .....	26
2.5 ROOT CAUSES OF MICROPITTING.....	27
2.6 SCADA DATA AND APPLICATIONS .....	33
2.7 FACTORS AFFECTING MICROPITTING .....	33

2.7.1 Contact Stress.....	34
2.7.2 Rotational Speed .....	38
2.7.3 Sliding Parameter .....	39
2.7.4 Local Contact Temperature.....	40
2.7.5 Lubricant Film Thickness .....	41
2.8 EXPERIMENTAL STUDIES OF MICROPITTING .....	42
2.8.1 Effects of Lubrication and Varying Loading Conditions.....	43
2.8.2 Effects of Surface Treatment and Surface Finish .....	45
2.8.3 Effects of Material Microstructures and Other Related Factors .....	48
2.8.4 Effects of Sliding and Crack Characteristics .....	49
2.9 SUMMARY .....	51
<b>Chapter 3: Experimental Study of Micropitting .....</b>	<b>53</b>
3.1 BACK TO BACK GEAR TEST RIG .....	54
3.2 EXPERIMENTAL EQUIPMENT AND DEVICES .....	56
3.2.1 Gear Surface Finishing Machine.....	56
3.2.2 Taylor Hobson Form Talysurf 50e Instrument .....	57
3.2.3 Nikon LV150 and SMZ1500 Microscopes .....	59
3.3 EXPERIMENTAL TEST PROCEDURE.....	59
3.3.1 Test Procedure.....	59
3.3.2 Gear Specimens and Heat Treatment.....	60
3.3.3 Test-run Matrix .....	62
3.3.4 Lubrication System .....	62
3.4 SURFACE INSPECTION METHODS .....	63
3.4.1 Surface Roughness Measurement .....	64
3.4.2 Replica Optical Image Analysis.....	65
3.4.3 Gear Profile Measurement .....	66
3.5 SUMMARY .....	67
<b>Chapter 4: Analytical Models in Predicting Contact Stress, Sliding Parameter, Local Contact Temperature and Lubricant Film Thickness.....</b>	<b>69</b>
4.1 GEAR TOOTH CONTACT STRESS ANALYSIS .....	70
4.1.1 Hertz's Formula for Gear Contact Stress .....	70
4.1.2 Application Factor.....	73
4.1.3 Dynamic Factor .....	73
4.1.4 Face Load and Transverse Load Factor .....	74

4.1.5 Load Sharing Factor and Loading Variations Caused by Gear Meshing .....	75
4.1.6 Tip Relief and Effective Tip Relief.....	79
4.2 ANALYSIS AND MODELLING PROCEDURE.....	81
4.2.1 Radii of Relative Curvature of Mated Profiles .....	81
4.2.2 Material Parameter .....	82
4.2.3 Load parameter.....	82
4.2.4 Sliding parameter .....	83
4.2.5 Velocity parameter .....	85
4.2.6 Gear Tooth Lubricant Film Thickness Analysis .....	85
4.3 DIFFERENCE BETWEEN ISO AND AGMA STANDARDS .....	88
4.4 LIMITATIONS OF THE STUDY.....	89
4.5 SUMMARY .....	90
<b>Chapter 5: SCADA Data Analysis .....</b>	<b>91</b>
5.1 WT GEARBOX AND PARAMETERS .....	92
5.2 SCADA DATA ANALYSIS .....	93
5.2.1 Analysis of Rated Conditions .....	95
5.2.2 Probabilistic Analysis of Torque and Rotational Speed Variation .....	96
5.2.3 Random Numbers Generation.....	100
5.2.4 Probabilistic Analysis of Gear Micropitting .....	102
5.3 SUMMARY .....	104
<b>Chapter 6: Experimental Results and Analysis Validation .....</b>	<b>105</b>
6.1 REPLICA OPTICAL IMAGE ANALYSIS OF MICROPITTING .....	106
6.2 SURFACE ROUGHNESS ANALYSIS .....	112
6.3 PROFILE DEVIATION ANALYSIS.....	114
6.4 VALIDATION OF ANALYTICAL METHOD AND CALCULATION.....	116
6.4.1 Comparison at 0.5 Torque Ratio .....	117
6.4.2 Comparisons at 1.0 Torque Ratio.....	123
6.5 ANALYTICAL RESULTS OF TESTED GEARS .....	128
6.6 MICROPITTING RISK ASSESSMENT .....	131
6.7 DISCUSSION .....	133
6.8 SUMMARY .....	136
<b>Chapter 7: Analytical Results Using Selected SCADA Data.....</b>	<b>138</b>
7.1 TORQUE AND SPEED DERIVED FROM SCADA .....	139
7.2 LOCAL CONTACT STRESS .....	140

---

7.3 LOCAL SLIDING PARAMETER .....	141
7.4 LOCAL CONTACT TEMPERATURE .....	143
7.5 LUBRICANT FILM THICKNESS .....	146
7.6 ASSESSMENT OF GEAR MICROPITTING RISK .....	150
7.7 DISCUSSION .....	152
7.8 SUMMARY .....	153
<b>Chapter 8 Analytical Results Using Probabilistic Modelling of SCADA Data.....</b>	<b>155</b>
8.1 HISTOGRAMS OF SCADA DATA .....	156
8.2 HISTOGRAMS OF RANDOM NUMBERS .....	157
8.3 PROBABILITY DISTRIBUTION OF CONTACT STRESS VARIATIONS.....	159
8.4 PROBABILITY DISTRIBUTION OF LOCAL TEMPERATURE VARIATIONS .....	161
8.5 PROBABILITY DISTRIBUTION OF SLIDING PARAMETER VARIATIONS	162
8.6 PROBABILITY DISTRIBUTION OF LUBRICANT FILM THICKNESS VARIATIONS .....	163
8.7 SUMMARY .....	168
<b>Chapter 9: Conclusions and Future Work.....</b>	<b>170</b>
9.1 CONCLUSIONS.....	171
9.1.1 Conclusions Drawn From Experimental Results .....	171
9.1.2 Conclusions Drawn From Analytical Results of Selected SCADA Data.....	172
9.1.3 Conclusions Drawn From Analytical Results of Probabilistic Modelling of SCADA Data.....	173
9.2 RECOMMENDATIONS FOR FUTURE WORK .....	175
<b>REFERENCES.....</b>	<b>177</b>
<b>APPENDICES .....</b>	<b>188</b>
PUBLICATIONS .....	236

---

**LIST OF FIGURES**

<b>Figure 1.1:</b>	Typical WT gearbox configuration (Feng et al, 2012).....	2
<b>Figure 1.2:</b>	The global annual installed wind power capacity 1996-2012 (GWEC, 2013).....	3
<b>Figure 1.3:</b>	The global cumulative offshore wind power capacity installed in 2012 (EWEA, 2013).....	4
<b>Figure 1.4:</b>	Failure rate and downtime in WT subassemblies (Goch et al, 2012).....	5
<b>Figure 1.5:</b>	Distribution of WT failure cost (cited in Goch et al, 2012).....	5
<b>Figure 1.6:</b>	Micropitting characteristics, (a) depth and length of micropit (Zhang et al, 2009) and (b) microscopic view of micropitting..	7
<b>Figure 2.1:</b>	Outline of gear manufacturing methods (Dudley, 1994).....	15
<b>Figure 2.2:</b>	Manufacturing cost of typical gears (Otto and Herring, 2002)..	15
<b>Figure 2.3:</b>	Gear surface treatment methods (Swift and Booker, 2003).....	16
<b>Figure 2.4:</b>	A typical horizontal wind turbine.....	20
<b>Figure 2.5:</b>	Wind turbine nacelle main components (AWEA, 2013) .....	21
<b>Figure 2.6:</b>	WT gearbox with one planetary and two parallel stages (IEC 61400-4, 2012).....	22
<b>Figure 2.7:</b>	Spur gear nomenclature (Shigley,1989).....	23
<b>Figure 2.8:</b>	Different gear failure modes (Adopted from ISO 10825: 1995 (E/F) and BS 7848 (1996)).....	24
<b>Figure 2.9:</b>	Tooth flank micropitting.....	27
<b>Figure 2.10:</b>	Different lubrication regimes between the gear contact surface roughness, (Spikes and Olver, 2002 cited in Olver, 2002).....	28
<b>Figure 2.11:</b>	Surface origin pit (Shiple, 1974).....	29
<b>Figure 2.12:</b>	Subsurface origin pit (Shiple, 1974).....	30
<b>Figure 2.13:</b>	Pitting and spalling (Ding and Rieger, 2003).....	30
<b>Figure 2.14:</b>	Gear tooth surface rolling and sliding.....	31
<b>Figure 2.15:</b>	Relative sliding during tooth meshing (Childs, 2004).....	32
<b>Figure 2.16:</b>	Spur gear load distribution.....	32
<b>Figure 2.17:</b>	Shapes of predicted pit combinations of contact stresses and equivalent curvature radius (Glodez and Ren, 1998).....	36
<b>Figure 2.18:</b>	Example of the results obtained for different equivalent radius (Abersek and Flaker, 2004).....	36
<b>Figure 2.19:</b>	Experimental result of surface pit shape and size (Flaker et al, 2001).....	37
<b>Figure 2.20:</b>	Driven gear micropitting crack direction (cited in Errichello, 2012).....	38
<b>Figure 2.21:</b>	Schematic of crack of (a) micropitting initiation and (b) propagation mechanism according to Oila and Bull (2005).....	48
<b>Figure 2.22:</b>	Two different distributions of load cases along the width of tooth (Glodež et al, 1998).....	50

<b>Figure 3.1:</b>	Schematic of back-to-back gear test rig layout.....	54
<b>Figure 3.2:</b>	Control screen of the test rig computer.....	55
<b>Figure 3.3:</b>	Back-to-back test rig facility at Design Unit, the Newcastle University.....	56
<b>Figure 3.4:</b>	Photograph of surface finish machine.....	57
<b>Figure 3.5:</b>	Taylor Hobson instrument.....	57
<b>Figure 3.6:</b>	Numbers of cut-off of the surface roughness measurement.....	58
<b>Figure 3.7:</b>	Hofler machine and tested gear (inset).....	58
<b>Figure 3.8:</b>	Photograph of microscopic analysis and tooth flank replica optical image (inset.).....	59
<b>Figure 3.9:</b>	Dimension of pinion gear.....	61
<b>Figure 3.10:</b>	Helical gear set (pinion and wheel) used in the test.....	61
<b>Figure 3.11:</b>	Surface-roughness measurement on the Talysurf instrument....	64
<b>Figure 3.12:</b>	Roughness measurement direction.....	65
<b>Figure 3.13:</b>	Five samples peak to valley height.....	65
<b>Figure 3.14:</b>	Photographs of replica injecting.....	66
<b>Figure 3.15:</b>	Microscope to inspect micropitting development.....	66
<b>Figure 3.16:</b>	Hofler machine setting for profile deviation measurement.....	67
<b>Figure 3.17:</b>	Measurement position of gear tooth profile deviation.....	67
<b>Figure 4.1:</b>	Fundamentals of Hertz's contact stress theory.....	71
<b>Figure 4.2:</b>	Contact points along the line of action.....	76
<b>Figure 4.3:</b>	Contact points of spur pinion gear (driven) used in the calculation for rated condition.....	77
<b>Figure 4.4:</b>	Contact points of spur pinion gear (driven) used in the calculation for probabilistic analysis.....	77
<b>Figure 4.5:</b>	Load distribution of the helical pinion gear (driver) within a meshing cycle, (a) unmodified profile, (b) modified profile and (c) points on tooth flank.....	78
<b>Figure 4.6:</b>	Flowchart for calculating the load sharing factor (ISO/TR 15144-1, 2010).....	79
<b>Figure 4.7:</b>	Flowchart diagram for calculating tip relief factor.....	80
<b>Figure 4.8:</b>	Diagram representing the lubricant film thickness parameters..	81
<b>Figure 4.9:</b>	Determination of sliding parameter.....	83
<b>Figure 4-10:</b>	Elastohydrodynamic theory of pressure distribution and lubricant film thickness (cited in Jelaska, 2012).....	86
<b>Figure 4.11:</b>	Inputs and outputs of gear micropitting analysis procedure.....	87
<b>Figure 5.1:</b>	High speed stage within a three stage WT gearbox.....	92
<b>Figure 5.2:</b>	Comparisons between the calculated average and recorded average power ratios.....	94
<b>Figure 5.3:</b>	Generator power and generator speed curves vs. wind speed (one month data).....	96
<b>Figure 5.4:</b>	Histogram of WT1 HSS pinion shaft torque ratio.....	97
<b>Figure 5.5:</b>	Histogram of WT2 HSS pinion shaft torque ratio.....	97
<b>Figure 5.6:</b>	Simulated load case distribution based on IEC (Greaves et al, 2011).....	98

<b>Figure 5.7:</b>	Histogram of WT1 HSS pinion shaft rotational speed ratio.....	98
<b>Figure 5.8:</b>	Histogram of WT2 HSS pinion shaft rotational speed ratio.....	99
<b>Figure 5.9:</b>	Random number dataset generator.....	101
<b>Figure 5.10:</b>	Probability distribution of $x$ .....	103
<b>Figure 6.1:</b>	Replica of pinion flank surface at torque ratio 0.3, no micropitting observed.....	106
<b>Figure 6.2:</b>	Replica and microscopic view of pinion flank surface at torque ratio 0.5: micropitting observed at dedendum.....	107
<b>Figure 6.3:</b>	Replica and microscopic view of pinion flank surface at torque ratio 0.6: micropitting observed at addendum.....	107
<b>Figure 6.4:</b>	Replica and microscopic view of pinion flank surface at torque ratio 0.7: micropitting observed at addendum (very little progress observed between torque ratio 0.6 and 0.7).....	107
<b>Figure 6.5:</b>	Replica and microscopic views of pinion flank surface at torque ratio 0.8: micropitting at dedendum appeared as spots and at addendum developed progressively by comparing with Figures 6.2, 6.3 and 6.4.....	108
<b>Figure 6.6:</b>	: Replica and microscopic views of pinion flank surface at torque ratio 0.9: micropitting at dedendum with little progress but at addendum developed progressively and densely.....	108
<b>Figure 6.7:</b>	Replica and microscopic views of pinion tooth flank surface at torque ratio 1.0: micropitting at dedendum with more progress but at the addendum developed progressively and densely with bigger micropitting area compared with torque ratio 0.9...	108
<b>Figure 6.8:</b>	Progression of micropitting of mating gear teeth.....	111
<b>Figure 6.9:</b>	Tooth surface roughness of pinion before being tested (0 cycle) .....	112
<b>Figure 6.10:</b>	Tooth surface roughness of pinion after being tested at torque ratio of 0.3.....	113
<b>Figure 6.11:</b>	Tooth surface roughness of pinion after being tested at torque ratio of 0.7.....	113
<b>Figure 6.12:</b>	Tooth surface roughness of pinion after being tested at torque ratio of 1.0.....	113
<b>Figure 6.13:</b>	Tooth surface roughness values $R_a$ after being tested at different torque ratios .....	114
<b>Figure 6.14:</b>	Tooth surface roughness values $R_z$ after being tested at different torque ratios.....	114
<b>Figure 6.15:</b>	Tooth profile deviation of pinion.....	115
<b>Figure 6.16:</b>	Tooth profile deviation of wheel.....	116
<b>Figure 6.17:</b>	Contact stress comparison at pitch point using different software.....	117
<b>Figure 6.18:</b>	Comparisons of contact stresses at 0.5 torque ratio.....	118
<b>Figure 6.19:</b>	3D contact stress distribution by KISSsoft at 0.5 torque ratio...	119
<b>Figure 6.20:</b>	Comparisons of contact temperatures at 0.5 torque ratio.....	120
<b>Figure 6.21:</b>	KISSsoft result of 3D local contact temperature by KISSsoft	120

	at 0.5 torque ratio, considering fine mesh points along the line of action.....	
<b>Figure 6.22:</b>	Comparisons of lubricant film thicknesses at 0.5 torque ratio...	121
<b>Figure 6.23:</b>	3D distribution of lubricant film thickness of ISO/TR by KISSsoft.....	121
<b>Figure 6.24:</b>	Comparisons of specific lubricant film thicknesses at 0.5 torque ratio.....	122
<b>Figure 6.25:</b>	Specific lubricant film thickness of AGMA by KISSsoft at 0.5 torque ratio.....	123
<b>Figure 6.26:</b>	Comparisons of contact stresses at 1.0 torque ratio.....	123
<b>Figure 6.27:</b>	3D contact stress distribution by KISSsoft at 1.0 torque ratio...	124
<b>Figure 6.28:</b>	Comparisons of contact temperatures at 1.0 torque ratio.....	124
<b>Figure 6.29:</b>	KISSsoft result of 3D local contact temperature by KISSsoft at 1.0 torque ratio, considering fine mesh points along the line of action.....	125
<b>Figure 6.30:</b>	Comparisons of lubricant film thicknesses at 1.0 torque ratio...	125
<b>Figure 6.31:</b>	KISSsoft result of 3D lubricant film thickness.....	126
<b>Figure 6.32:</b>	Comparisons of specific lubricant film thicknesses at 1.0 torque ratio.....	126
<b>Figure 6.33:</b>	Specific lubricant film thickness of AGMA by KISSsoft at 1.0 torque ratio.....	127
<b>Figure 6.34:</b>	3D distribution of specific lubricant film thickness of ISO/TR by KISSsoft.....	127
<b>Figure 6.35:</b>	Contact stress at varying torque ratios.....	128
<b>Figure 6.36:</b>	Variation of sliding parameter at different torque ratios.....	129
<b>Figure 6.37:</b>	Local contact temperatures at different torque ratios and surface roughness values.....	130
<b>Figure 6.38:</b>	Specific lubricant film thickness at different torque ratios and surface roughness values.....	131
<b>Figure 6.39:</b>	Specific film thickness vs. hardness according to Linke (cited in Jelaska 2012).....	132
<b>Figure 7.1:</b>	Contact stress variation at the highest speed and varying torque ratios.....	140
<b>Figure 7.2:</b>	Contact stresses of pinion gear vs. torque at highest and lowest speed ratios.....	141
<b>Figure 7.3:</b>	Contact stress variation at the lowest speed and varying torque ratios.....	141
<b>Figure 7.4:</b>	Variation of sliding parameter along the line of action.....	142
<b>Figure 7.5:</b>	Variation of sliding parameter at the minimum torque and varying speed ratios.....	142
<b>Figure 7.6:</b>	Variation of sliding parameter at the maximum torque ratio and varying speed ratios.....	143
<b>Figure 7.7:</b>	Variation of flash and bulk temperature on the tooth surface...	143
<b>Figure 7.8:</b>	Variation of local contact temperature at the lowest speed and varying torque ratios.....	144

<b>Figure 7.9:</b>	Variation of local temperature at the highest speed and varying torque ratios.....	145
<b>Figure 7.10:</b>	Variation of local temperature at the lowest torque and varying speed ratios.....	146
<b>Figure 7.11:</b>	Variation of local temperature at torque of 0.59 and varying speed ratios.....	146
<b>Figure 7.12:</b>	Variation of film thickness at the nominal torque and speed....	147
<b>Figure 7.13:</b>	Variation of film thickness at the lowest speed and varying torque ratios.....	148
<b>Figure 7.14:</b>	Variation of film thickness at the highest speed ratio and varying torque ratios.....	148
<b>Figure 7.15:</b>	Variation of film thickness at torque ratio of 0.59 and varying speed ratios.....	149
<b>Figure 7.16:</b>	Variation of film thickness at the lowest torque and varying speed ratios.....	150
<b>Figure 8.1:</b>	WT1 Contour plot of HSS pinion torque ratio vs. power ratio and rotational speed ratio.....	156
<b>Figure 8.2:</b>	WT 2 Contour plots of HSS pinion torque ratio vs. power ratio and rotational speed ratio.....	157
<b>Figure 8.3:</b>	Histogram of 3000 random numbers of HSS pinion shaft torque ratio (WT1).....	158
<b>Figure 8.4:</b>	Histogram of 3000 random numbers of HSS pinion shaft rotational speed ratio (WT1).....	158
<b>Figure 8.5:</b>	Histogram of contact stresses at 5 points on gear tooth flank...	160
<b>Figure 8.6:</b>	Histogram of contact stresses at point D on the path of contact	161
<b>Figure 8.7:</b>	Allowable contact stress for case hardened wrought steels material (ISO 6336- 5).....	161
<b>Figure 8.8:</b>	Histogram of local contact temperature at 5 points on gear tooth flank.....	162
<b>Figure 8.9:</b>	Histogram of sliding parameter at 5 points on gear tooth flank.....	163
<b>Figure 8.10:</b>	Histogram of lubricant film thickness at 5 points on gear tooth flank.....	164
<b>Figure 8.11:</b>	Histogram of specific lubricant film thickness of gear tooth flank (0.7 $\mu\text{m}$ surface roughness).....	165
<b>Figure 8.12:</b>	Histogram of specific lubricant film thickness at points E and D (0.7 $\mu\text{m}$ surface roughness).....	166
<b>Figure 8.13:</b>	Histogram of specific lubricant film thickness of gear tooth flank (0.3 $\mu\text{m}$ surface roughness).....	166
<b>Figure 8.14:</b>	Histogram of specific lubricant film thickness at point E (0.3 $\mu\text{m}$ surface roughness).....	167
<b>Figure 8.15:</b>	Histogram of specific lubricant film thickness of gear tooth flank (0.1 $\mu\text{m}$ surface roughness).....	168

---

**LIST OF TABLES**

<b>Table 2-1:</b>	Influence of composite surface roughness calculations on specific lubricant film thickness (Bell et al, 2012).....	29
<b>Table 3-1:</b>	Chemical composition (wt. %) of 18CrNiMo7 .....	60
<b>Table 3-2:</b>	Pinion and wheel gears parameters.....	61
<b>Table 3-3:</b>	Torque ratios of the test programme.....	62
<b>Table 3-4:</b>	Lubricant data.....	63
<b>Table 4-1:</b>	The application factor guidance values (ISO 6336-6, 2006).....	73
<b>Table 5-1:</b>	Wheel and pinion parameters.....	93
<b>Table 5-2:</b>	Material data.....	93
<b>Table 5-3:</b>	Lubricant data.....	93
<b>Table 6-1:</b>	Micropitting occurrence at various teeth of pinion at torque ratio 1.0.....	110
<b>Table 6-2:</b>	Summary of the micropitting progression under different torque levels.....	111
<b>Table 7-1:</b>	Variations of torque and rotational speed ratios of pinion gear shaft.....	139
<b>Table 7.2:</b>	Lubricant film thickness under the considered variable conditions..	150
<b>Table 8-1:</b>	Comparisons of different datasets.....	159
<b>Table 8-2:</b>	Micropitting Safety Factor (Kissling, 2012).....	167

## NOMENCLATURE

Symbol	Description	Units
$a$	Centre distance	mm
$B_{M1,2}$	Thermal contact coefficient of pinion and wheel	$N/(m \cdot s^{0.5} \cdot K)$
$B_p, B_f, B_k$	Non- dimensional parameters	-
$b$	Cylinder face width	mm
$C_a$	Tip relief	$\mu m$
$C_{eff}$	Effective tip relief	$\mu m$
$C_{\gamma\alpha} \& C_{\gamma\beta}$	Mean value of mesh stiffness per unit face width	$(N/(mm \cdot \mu m))$
$d_{1,2}$	Diameters of body 1,2	mm
$d_{a1,2}$	Tip diameter of pinion and wheel	mm
$d_{b1,2}$	Base diameter of pinion and wheel	mm
$d_{w1,2}$	Pitch diameter of pinion and wheel	mm
$d_{Y1,2}$	Circle diameter of pinion and wheel	mm
$E_r$	Reduced modulus of elasticity	$N/mm^2$
$E$	Young Modulus	$N/mm^2$
$F_{tH}$	Tangential load in a transverse plane	N
$F_{bt}$	Nominal transverse load in plane of action (base tangent plane)	N
$F_m$	Mean transverse tangential load	N
$F_t$	Tangential load	N
$F$	Force	N
$F_{\beta\gamma}$	Effective equivalent misalignment	$\mu m$
$f_{pb}$	Transverse base pitch deviation	$\mu m$
$f$	Frequency	Hz
$G_M$	Material parameter	-
$g_Y$	Parameter on the path of contact	mm
$g_\alpha$	Length of path of contact	mm
$H_V$	Local losses factor	-
$h_Y$	Local lubricant film thickness	$\mu m$
$K_A$	Load application factor	-
$K_{BY}$	Helical load factor	-
$K_{H\alpha}$	Transverse load factor	-

$K_{H\beta}$	Face load factor	-
$K_V$	Load dynamic factor	-
$m_n$	Normal module	mm
$n$	Safety factor against micropitting	-
$n_{1,2}$	Rotation speed of pinion and wheel	rpm
$P_s$	Magnetic poles	No.
$P$	Power transmission	kw
$P_{max}$	Maximum contact stress	N/mm <sup>2</sup>
$P_{Gen}$	Generator power	MW
$p_{dyn,Y}$	Local Hertzian contact stress	N/mm <sup>2</sup>
$R_a$	Effective arithmetic mean roughness value	μm
$Rz(DIN)$	mean of the height of the five peaks to valley	μm
$r$	Semi-width of contact	mm
$S_{GF,Y}$	Local sliding parameter	-
$T$	Torque	Nm
$U_Y$	Local velocity parameter	-
$U$	Gear ratio	-
$V_{g,Y}$	Local sliding velocity	m/s
$W_Y$	Local load parameter	-
$X_{ca}$	Tip relief factor	-
$X_L$	Lubricant factor	-
$X_S$	Lubrication factor	-
$X_Y$	Local load sharing factor	-
$\gamma_\alpha$	Running-in allowance for a gear pair	μm
$Z_E$	Elasticity factor	(N/mm <sup>2</sup> ) <sup>0.5</sup>
$Z_{1,2}$	Number of teeth of pinion and wheel	-
$\alpha_t$	Transverse pressure angle	degree
$\alpha_{wt}$	Pressure angle at the pitch cylinder	degree
$\alpha_{\theta B,Y}$	Pressure-viscosity coefficient at local contact temperature	m <sup>2</sup> /N
$\alpha_{\theta M}$	Pressure-viscosity coefficient at bulk temperature	m <sup>2</sup> /N
$\alpha_{38}$	Pressure-viscosity coefficient at 38 °C	m <sup>2</sup> /N
$\beta_b$	Base helix angle	degree
$\epsilon_{max}$	Maximum addendum contact ratio	-
$\epsilon_\alpha$	Transverse contact ratio	-

$\varepsilon_{\beta}$	Overlap ratio	-
$\varepsilon_{\gamma}$	Total contact ratio	-
$\varepsilon_{1,2}$	Addendum contact ratio of the pinion and wheel	-
$\eta_{\theta B,Y}$	Dynamic viscosity at local contact temperature	N·s/m
$\eta_{\theta M}$	Dynamic viscosity at bulk temperature	N·s/m <sup>2</sup>
$\eta_{\theta oil}$	Dynamic viscosity at oil inlet/sump temperature	N·s/m <sup>2</sup>
$\eta$	Efficiency	-
$\theta_{B,Y}$	Local contact temperature	°C
$\theta_{fl,Y}$	Local flash temperature	°C
$\theta_M$	Bulk temperature	°C
$\theta_{oil}$	Oil inlet/sump temperature	°C
$\lambda_{GF,min}$	Minimum Specific lubricant film thickness	-
$\lambda_{GF,Y}$	Local specific lubricant film thickness	-
$\lambda_{GFP}$	Permissible lubricant film thickness	-
$\mu_m$	Mean coefficient of friction	-
$\nu_{\theta B,Y}$	Kinematic viscosity at local contact temperature	mm <sup>2</sup> /s
$\nu_{\theta M}$	Kinematic viscosity at bulk temperature	mm <sup>2</sup> /s
$\nu_{1,2}$	Poisson's ratio of pinion and wheel	-
$\nu_{100}$	Kinematic viscosity at 100 °C	mm <sup>2</sup> /s
$\nu_{40}$	Kinematic viscosity at 40 °C	mm <sup>2</sup> /s
$\omega_{Gen}$	Generator rotational speed	rpm
$\rho_{n,Y}$	Normal radius of relative curvature at point Y	mm
$\rho_{t,Y}$	Transverse radius of relative curvature	mm
$\rho_{\theta B,Y}$	Density of lubricant at local contact temperature	kg/m <sup>3</sup>
$\rho_{\theta M}$	Density of lubricant at bulk temperature	kg/m <sup>3</sup>

## *Chapter 1: Introduction*

---

*This chapter presents the project background, aims and methods developed in this research. It gives an overview of the problems faced by wind industry. It has been observed that the gear micropitting is one of the common failure modes of wind turbine gearboxes although the best practice of wind turbine gearbox design and manufacturing has been maintained. Therefore, further investigation of the wind turbine gear micropitting and development of a general prediction method are required. This chapter outlines the research problem and formulates it into the research objectives of this project. An outline of the dissertation structure is also presented.*

## 1.1 RESEARCH BACKGROUND

Gear is one of the most important mechanical components to play a vital role in the power transmission for various industrial applications. A variety of different types of gears, with various geometrical shapes, sizes and transmission ratios can be produced using different gear manufacturing processes such as milling, hobbing, shaping, casting, roll forming, etc. Gears are widely used in gearboxes for wind turbine (WT), automobiles, electronic devices, robotics, marine equipment, aircrafts, medical devices, and many others. However, gear systems are susceptible to failure which eventually leads to total system failure. At present, numerous research projects are being conducted at different institutions around the world to address inherent gear failure problems such as micropitting, scuffing, breakage, sliding wear, etc. Described as the least reliable WT subassembly (Spinato, 2008), gearboxes are the most susceptible to various failures due to stochastic wind variation and operational conditions. Figure 1.1 illustrates a WT gearbox and a more detailed description is provided in Chapter 2, Section 2.3.

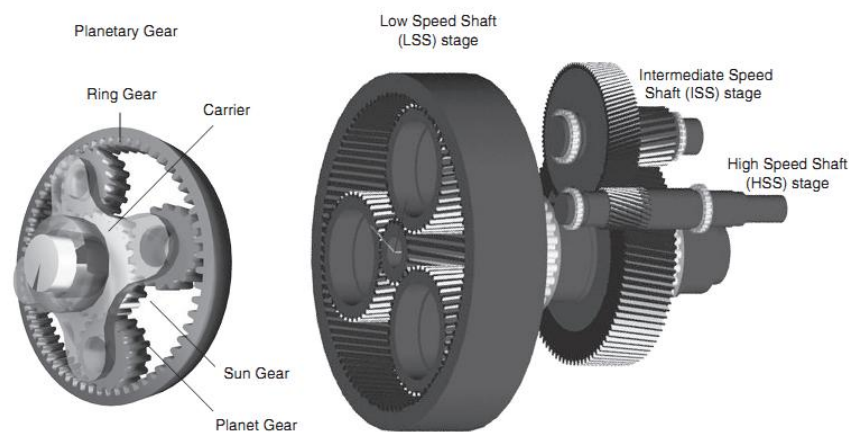


*Figure 1.1: Typical WT gearbox configuration (Feng et al, 2012)*

Gears are made of different materials such as cast iron, steel, bronze, or different types of plastics. The selection of gear materials depends on the operational speed and loading conditions they are subjected to. It also depends on the material properties, surface heat treatment and the requirement of reliability level for a specific application. Moreover, the selection of gear manufacturing methods depends on the factors such as the material type, gear size, design specification, service conditions, etc. Various methods are used to harden the surface of gear teeth, the most commonly used methods for steel gear tooth surfaces include carburising, induction, shot peening and nitriding. The methods of gear surface-hardening are briefly discussed in Chapter 2, Section 2.1.

### 1.1.1 Recent Development of Wind Energy Industry

Wind power plays an important role in clean electricity generation by using renewable energy sources. Wind energy is environmentally clean because of WTs' zero CO<sub>2</sub> emission and no waste production during operation (EWEA, 2004; IEA, 2010). Furthermore, wind power is cost effective and has a growing importance as a well-known method to generate electricity. Wind power has become a competitive energy source to meet energy demand in modern times due to its inherent characteristics of sustainability, pollution-free and free-of-cost availability, which are favourable over conventional energy sources (EWEA, 2004). According to Global Wind Energy Council (GWEC), nearly 40,500 megawatts (MW) of wind power capacity was installed in 2011 and nearly 45,000 MW in 2012, (GWEC, 2013). Around the world, wind power has a growing importance in generating electricity using both onshore and offshore WTs, as shown in Figure 1.2.

**Wind power capacity (MW)**

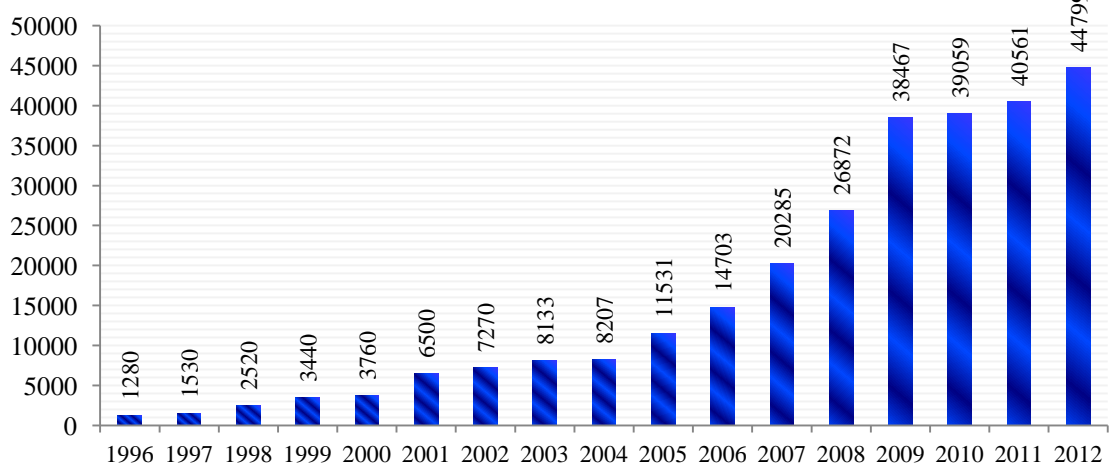


*Figure 1.2: The global annual installed wind power capacity 1996-2012 (GWEC, 2013)*

According to the European Wind Energy Association's (EWEA) annual report (2013), the wind power production in megawatts using offshore wind in Europe has increased rapidly and reached about 1050 MW in the first half of 2013. This means that the offshore WT installations during the first six months of 2013 have doubled compared to 2012 for the same period.

In addition to the above installation data, the statistical review of the EWEA in January 2013 shows that the global cumulative offshore capacity of wind power in 2012 was 5415 MW as shown in Figure 1.3. Compared to other countries in the world, the United

Kingdom (UK) has the best wind resources with a production of around 2948 MW in 2012 featuring an increase of about one third in its wind energy output compared to 2011. According to the EWEA, an expectation of 230 GW will be produced in the EU by 2020 using both onshore and offshore wind power to meet 15-17% of the EU's electricity demand and expected to supply 50% of its demand in 2050 (EWEA, 2013). The UK government produced an updated plan in December 2012 aiming to produce 18 GW of power using offshore wind energy by 2020. As shown in Figure 1.3, the total cumulative offshore wind energy production has increased about 1298 MW in 2012 compared to 2011.

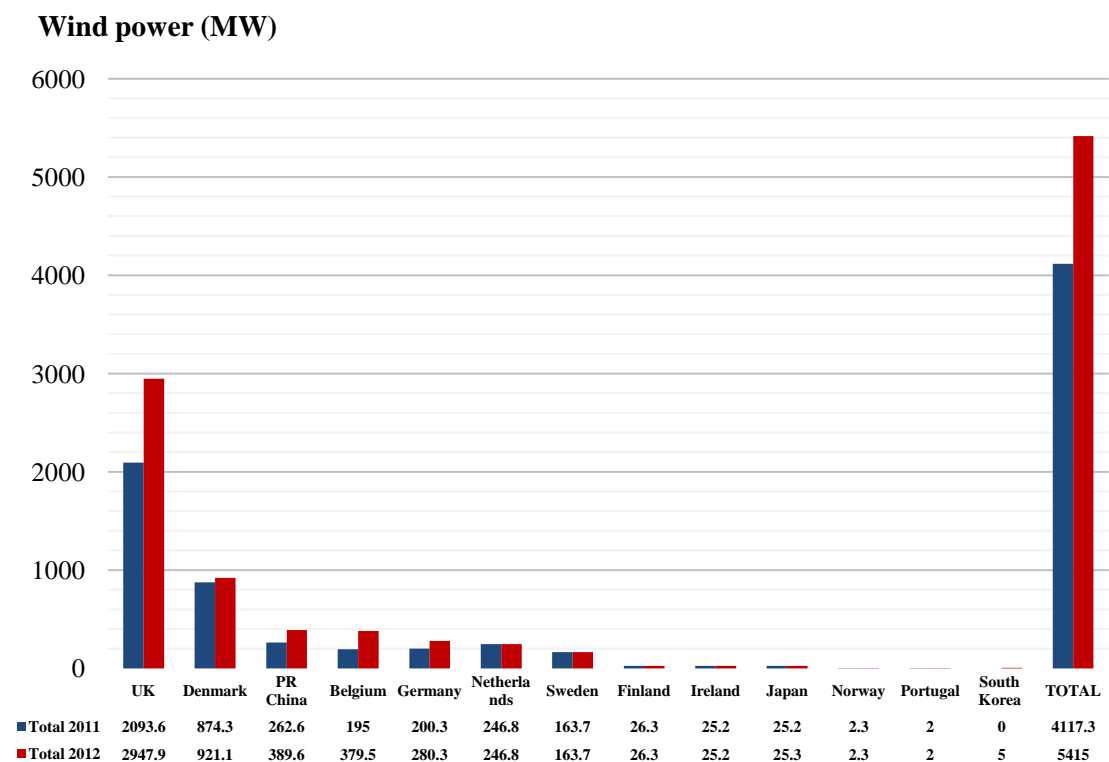


*Figure 1.3: The global cumulative offshore wind power capacity installed in 2012 (EWEA, 2013)*

### 1.1.2 Failures of Wind Turbine Subsystems and Components

A WT system consists of both electrical and mechanical subassemblies. Limited publications provide failure information data on WTs and their subassemblies in operation. WT gearbox failures can be caused by various reasons such as design of gear geometry, lubrication and material selection and environmental conditions (Errichello and Muller, 1994). A survey conducted by Spinato (2008), interviewing nine high level WT academic and industrial professionals, revealed that the gearbox is the least reliable subassembly. A survey of data collected from different regions in the EU conducted by

Tavner et al (2006) showed that the WT gearboxes had a failure rate of about 0.1 failures per turbine per year. The findings of a similar study conducted by Kim et al (2011); Sheng, (2011) showed that the overall downtime per WT per year is caused mainly by gearboxes. While Figures 1.4 illustrates the possible failure frequencies and downtime of key WT subassemblies, Figure 1.5 shows the cost distribution of some subassemblies including gearbox of WT. The repair and replacement costs of WT gearbox was the highest among other subassemblies, as shown in Figure 1.5.

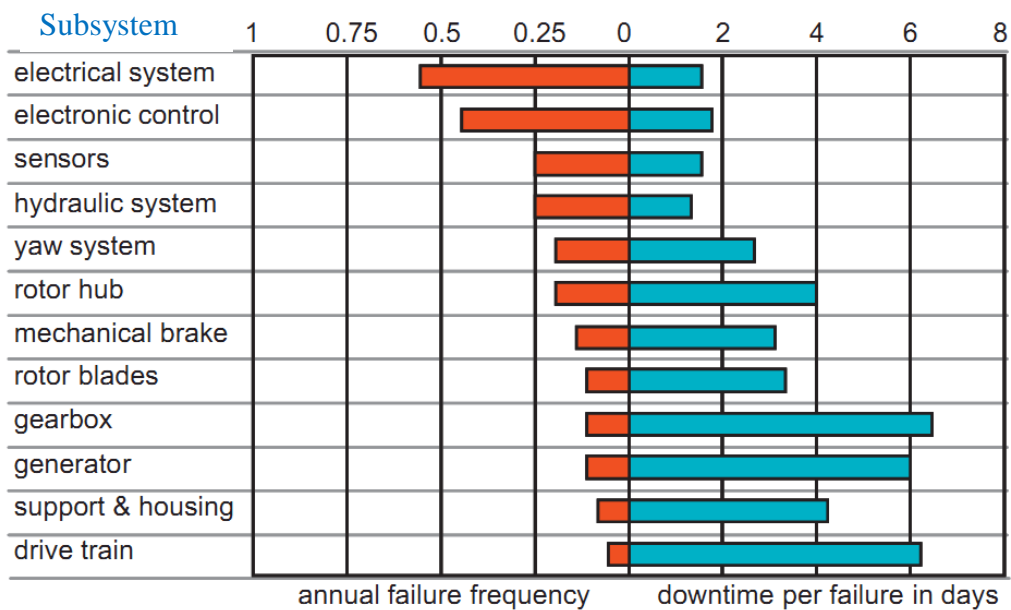


Figure 1.4: Failure rate and downtime of WT subassemblies (Goch et al, 2012)

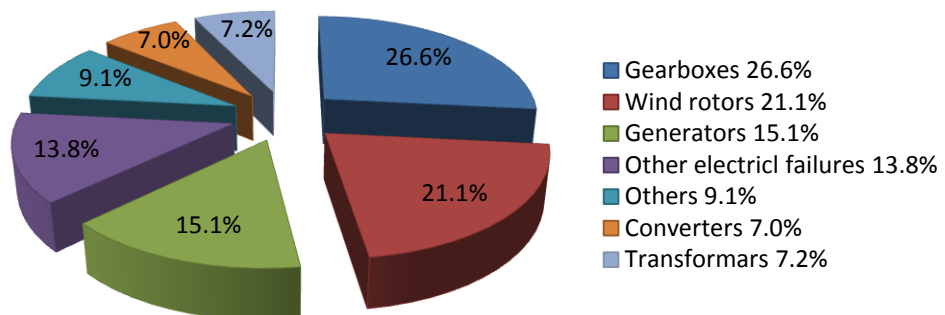


Figure 1.5: Distribution of WT failure cost (Cited in Goch et al, 2012)

## 1.2 GEAR MICROPITTING

WT gearbox operates under a wide array of highly fluctuating and dynamic loading conditions caused by the stochastic nature of wind and operational WT controls. The WT gears can be affected by various types of failure modes which occur due to different

root causes. Micropitting damage is one of failure modes commonly observed in multi-megawatt WT gearboxes (McNiff, 1991; Errichello and Muller, 1994; Sheng, 2010; Skriver, 2010; Errichello, 2012). Micropitting is a Hertzian fatigue phenomenon and it is a form of localised surface fatigue damage that occurs under rolling and sliding contact conditions when operating under elastohydrodynamic or boundary lubrication regimes (ISO/TR 15144-1, 2010). Micropitting leads to destructive gear damage which consequently incurs high cost in replacement and loss of time in operation. Hence, there is an industrial need to develop in-depth understanding of gear failures and find solutions to improve gear operational performance.

The gear tooth flanks are subjected to different operational conditions such as variable loading and sliding velocity when getting into contact along the tooth flank. The exposure of the tooth surface to different loading and sliding conditions could cause lubricant film breaking down resulting in direct metal to metal contact. This leads to high temperatures due to poor lubrication and high tooth surface sliding between the mating surfaces. These collective conditions result in a change in the gear material properties causing the damage in gears which can be attributed to different failure modes such as micropitting and scuffing. Micropitting as a form of surface fatigue damage is also found in WT bearings. The occurrence of gear micropitting is influenced by many factors. Apart from gear surface treatment, surface roughness, tooth profile modification, and gear misalignment, factors resulting from variable loading and speed conditions in operation, such as high contact stress, high and negative tooth surface sliding, high surface temperature, insufficient lubrication or disrupted lubricant film thickness, can contribute significantly to the occurrence of micropitting damage. Figure 1.6 shows a microscopic view of micropitting and the depth and length of a typical pit according to the experimental data of Zhang et al (2009). The micropits are small and shallow and they are about 5-10  $\mu\text{m}$  long and 5-20  $\mu\text{m}$  deep.

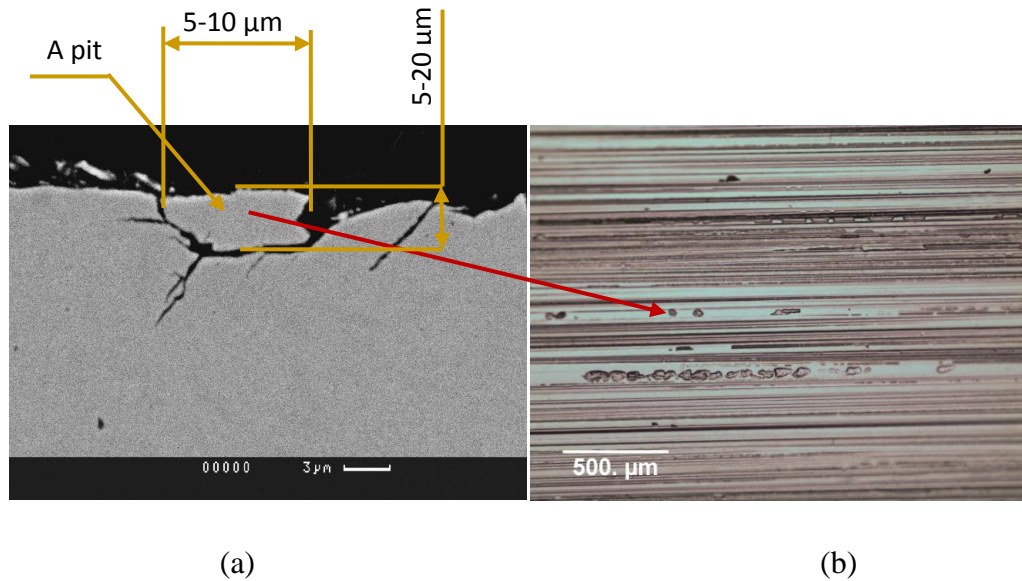


**Figure 1.6: Micropitting characteristics: (a) depth and length of a micropit (Zhang et al, 2009) and (b) microscopic view of micropitting**

The gradual loss of gear involute profile due to micropitting, wear and degrading gear tooth accuracy may all lead to other failure modes such as macropitting and scuffing. Gear life and spread of micropitting are influenced by many factors such as surface hardness and grinding process as well as operational conditions. The variation of contact stress, temperature and lubricant film thickness may play an important role in the occurrence of micropitting under fluctuating load and variable speed conditions.

### 1.3 PROBLEM STATEMENT

The early WT operation has seen high costs associated with premature failures, particularly in gearboxes, resulting from fundamental design errors and underestimation of operating loads (Musial et al, 2007). Operational controls are implemented to control WT loading and serving purposes such as reducing the rotor speed variation, maximising energy extraction and preventing turbine damages. However, these are found to complicate drive train loading conditions and worsen stochastic wind effects which may lead to critical damages and shortening service life (Long et al, 2012). Reliability of WTs has improved considerably in the past decades; however, high gear and bearing micropitting failures in WT gearboxes still frequently occur. These failures occur in all WT models and sizes suggesting systemic problems rather than manufacturing-related issues (Long et al, 2012).

Regardless of the rigorous investigation, gear failures in WT gearboxes still frequently occur which hampers the optimal operation of multi-megawatt WTs, increasing the cost of wind energy as the replacement of each WT gearbox costs between £0.1–0.3 million depending on the wind farm location and the size of WT (Evans, 2013). Premature failures, not only significantly reduce WT service life, but also cause unplanned shutdowns and early component replacements. Consequently, these failures culminate into reducing WT availability and increasing cost of wind energy, problems which are exacerbated in offshore operation due to constrained accessibility and increased maintenance costs.

Previous research has concluded that the gearbox has a greater failure rate than all other WT subassemblies (Goch et al, 2012; Spinato, 2008; Tavner et al, 2006), causing the highest proportion of WT overall downtime (Goch et al, 2012; Kim et al, 2011; Sheng, 2011). Goch et al (2012) concluded that the gearbox failure is one of the areas in which major persisting problems still exist in WTs and which requires intensified experimental and analytical research. The WT gearboxes are designed for up to 20~25 years of life but it is common that premature failures occur within approximately five to seven years owing to stochastic nature of wind and variable loading and speed operating conditions (Rensselar, 2013; Evans, 2013; Goch et al, 2012). Despite the provision of high maintenance efforts, only a few number of WTs reach the design lifetime (Goch et al, 2012).

Micropitting, a surface failure, is considered one of the most common types of gear failures which can lead to significant gear replacements. Given its criticality and widespread commonness, the prediction and prevention mechanisms of this failure need improvement. Even though the introduction of internationally recognised standards over the past decade has substantially assisted the design improvement to reduce these failures, a more general design method which considers the influence of gear micropitting on WT failure is needed. Thus, this research seeks to address the micropitting failure through investigating the effect of a combination of various parameters on gear micropitting as well as employing some analytical and experimental methods for this purpose, as outlined in the following section.

## 1.4 RESEARCH OBJECTIVES

The overall aim of this research project is to investigate how variable load and rotational speed conditions in operation affect gear micropitting of wind turbine gearboxes. The objectives of this research are to:

- ❖ Use ISO Technical Report ISO/TR 15144-1 (2010) to assess gear micropitting risk under variable torque and rotational speed conditions by developing a micropitting analysis tool.
- ❖ Conduct experimental tests of gear micropitting to investigate the effect of gear load level and load cycle on the initiation and progression of micropitting.
- ❖ Validate the analytical results of gear micropitting using ISO Technical Report ISO/TR 15144-1 (2010) with the experimental results.
- ❖ Develop an analytical method of SCADA (Supervisory Control and Data Acquisition) data to derive the probability distribution of gear shaft torque and rotational speed variations.
- ❖ Develop an analytical method, considering the WT controls, to investigate the effect of varying rotational speed and torque conditions on gear micropitting.
- ❖ Develop probabilistic modelling, considering SCADA data over 2.2 years, to investigate the HSS gear tooth flank micropitting risk based on the selected random number datasets derived from the SCADA datasets.
- ❖ Investigate the effect of key parameters, including contact stress, sliding parameter, local contact temperatures and lubricant film thicknesses, on gear micropitting.

## 1.5 DISSERTATION OUTLINE

This thesis consists of chapters of an introduction, a literature review, experimental investigation, analytical investigation, probabilistic modelling of gear micropitting, followed by chapters presenting the analytical and experimental results, conclusions and

recommendations for further research. More detailed results and technical information are listed in appendices.

**Chapter 1** presents the general introduction of WT's gearbox and other subsystem failures. It also outlines the background of this research study. Furthermore, it defines the research problem and the objectives of this research.

**Chapter 2** provides the literature review of the areas relevant to this study. A review on various gear failure modes and pitting characteristics is presented. The chapter also provides the details of WT gearbox design configuration, gear material and manufacturing, and tooth surface treatment methods. In addition, it includes an analysis and discussion of previous studies related to experimental and analytical work of gear micropitting.

**Chapter 3** presents the details of experimental test rig, test procedure and micropitting inspection methods. This chapter provides experimental evidence to understand the micropitting initiation and propagation. Details of the test samples and devices used in the experiment to investigate micropitting are described. This chapter also includes the test-run matrix and microscopic results for observing micropitting characteristics.

**Chapter 4** reviews and describes the Hertz theory and presents explanations of modified load factors used for gear contact analysis. Furthermore, the ISO standards relevant to this study are outlined. The load sharing factor with tip relief modification and loading variations at different contact points along the line of action is presented. A brief outline of Elastohydrodynamic theory and key parameters that affect the lubricant film thickness are also described in this chapter.

**Chapter 5** provides the design parameters of the WT gearbox high speed shaft (HSS) used in this study. The HSS rotational speed and calculated torque derived from the recorded SCADA datasets of 2.2 years are presented. Furthermore, the modelling procedure and the random number generator which are used to generate the smaller sizes of datasets from the original SCADA datasets are explained. In addition, an analytical procedure based on SCADA datasets to assess micropitting risk at the rated and selected operational conditions are outlined. Also, probabilistic distributions of the HSS pinion gear torque and rotational speed shaft using SCADA data recorded from two WTs in operation are presented.

**Chapter 6** presents the experimental results derived from the testing method and procedure presented in Chapter 3. After being subjected to varying torque levels, the tooth flank is inspected to investigate the initiation and progression of micropitting failure. Results of inspections, namely, surface roughness, replica and digital images and profile scanning, are discussed. A comparison of analytical results obtained from ISO Technical Report and AGMA standard using commercial software is conducted. In addition, a validation of developed toolkit calculation sheet (TCS) against commercial software is undertaken. Moreover, the micropitting prediction using the analytical method is compared with the experimental observations.

**Chapter 7** focuses on the analytical results investigating effects of variable load and rotational speed conditions by considering the rated and variable conditions of the WT gearbox in operation through the use of one month SCADA data. Contact stress, sliding parameter, local contact temperature and lubricant film thickness results are determined based on the rated and variable conditions of SCADA data.

**Chapter 8** presents the results of probabilistic modelling of micropitting risk of HSS gear tooth flank using random number datasets derived from the SCADA datasets. Recorded SCADA data from two WTs gearboxes are investigated to derive histograms of variations of HSS pinion gear rotational speed and calculated torque. The statistical comparisons between the original SCADA datasets and reduced datasets are compared. Probability distribution of contact stress, sliding parameter, local contact temperature and lubricant film thickness and their effects on the risk of gear micropitting are discussed.

**Chapter 9** concludes the key findings of this study and provides recommendations of future work.

## *Chapter 2: Literature Review*

---

*This chapter presents a review relating to the gear material, manufacturing processes and the most practical gear surface treatment methods. It also discusses the WT types and their gearbox design configurations. Gear geometrical parameters and common gear tooth failure modes, including micropitting, are outlined in this chapter. The operational conditions that influence the micropitting are discussed by referring to previous research work. Furthermore, an extensive review of published literature in analytical and experimental work related to various contact surface failures of gears is presented.*

## 2.1 GEAR INTRODUCTION

### 2.1.1 Gear Materials

Gears are toothed wheels, which mesh with another toothed part in order to transmit power or motion. Geared devices can change the speed, torque and direction of a power source. The use of gears in power transmission dated back to over 3000 years. Initially, used gears were manufactured with wood and the animal fat grease was used for lubrication (Tharmakulasingam, 2009). The use of steel gears started in the eighteenth century and the development and the use of gears had increased in the nineteenth century. Gear design, manufacture, maintenance and control are highly demanding processes owing to the gear's complex working conditions (Jelaska, 2012). Nowadays gear designers and manufacturers are able to produce different types of gears from different materials with good mechanical properties, long cycle runs, high power efficiency and low prices depending on their applications. The most commonly used gears types are included in Appendix A.

Gears are made from different types of materials, the selection of which depends on the operational speed and the loading conditions. Moreover, it also depends on application, reliability level and service life required. Steel is commonly preferred over other different types of materials because it is cheaper and has better surface fatigue strength (Oila, 2003; Jelaska, 2012). The types of steel that are used to manufacture gears range from plain carbon steels to high alloy steels with low to high carbon contents. Cast iron is also widely used in gear manufacturing due to their good wearing characteristics and machinability (Dudley, 1994). Some common gear materials used in different applications are listed below (Jindal, 2010).

- ❖ Steel gears are used for medium to high duty cycle conditions.
- ❖ Cast iron gears are used in light stress conditions.
- ❖ Various alloy steels, including stainless steels, are used in conditions involving considerable corrosion, heat and wear.
- ❖ Hardened and tempered steels should be used when the gear stress is high.
- ❖ Bronzes, aluminium and zinc alloys are used if high strength is required.

The selection of gear material depends on factors such as mechanical strength and properties, gear size and design and service requirements, etc. For example, alloy steels are used in automotive for durability and high impact strength. Combination of different materials used in meshing gears such as a steel pinion mated against cast iron gear is recommended in certain applications (Carvill, 1993).

### **2.1.2 Gear Manufacturing Methods**

The various methods used to manufacture gear teeth can be divided into three categories: casting, forming and metal removal, as shown in Figure 2.1. Firstly, gears can be formed by using different casting processes such as sand casting and shell molding, and these processes in general need minor finishing operation, depending on the quality of the die, to obtain the required accuracy of gears (Swift and Booker, 2003). Secondly, the forming methods can be divided into two types: cold drawing and thread rolling processes. In forming processes, the blank gear is passed against series of forming rolls to form the shape of teeth gradually until the required tooth profile is obtained. The rolling process method is used to improve metal mechanical properties whereby tooth profiles of a high quality can be obtained. The gears manufactured by forming processes are more accurate than those by casting processes (Dudley, 1994). Finally, gear teeth can also be produced using shaping, milling and hopping machines. As outlined in Figure 2.1, additional cutters are needed in the machining processes such as shaving and grinding to obtain good finishing and high accuracy of gears. Figure 2.2 shows the typical gears manufacturing costs, 60% of which is consumed by the machining and finishing processes, and 30% for heat treatment processes, leaving only 10% for material cost.

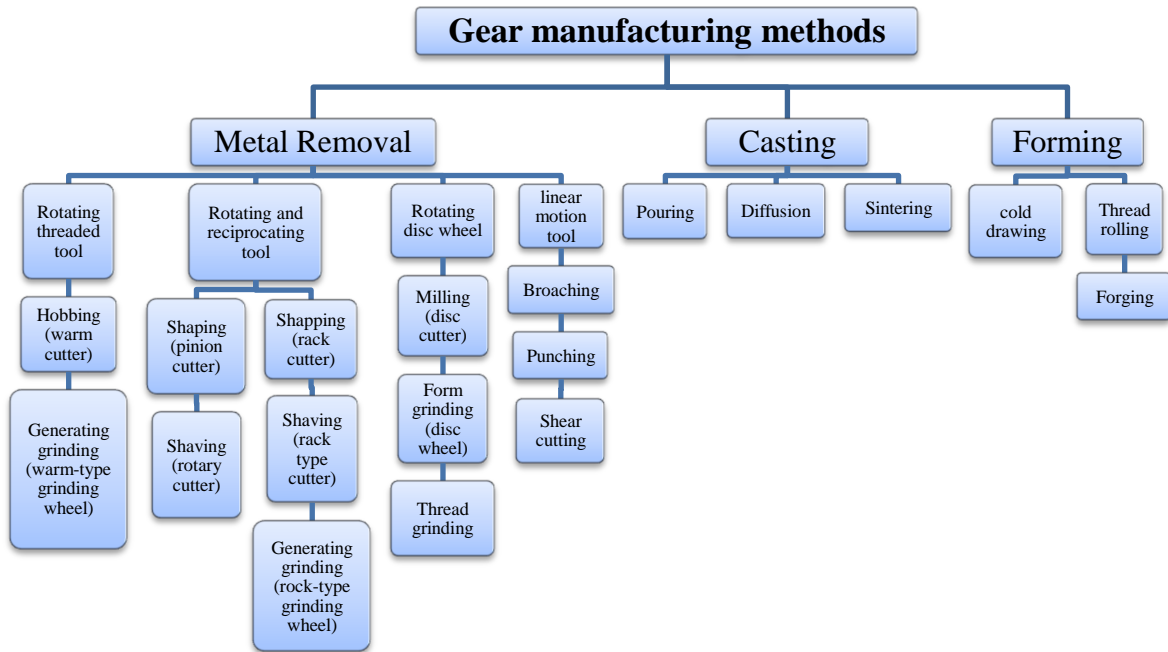


Figure 2:1: Outline of gear manufacturing methods (Dudley, 1994)

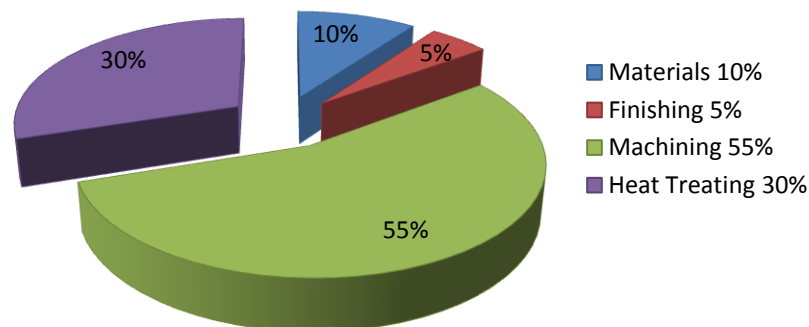
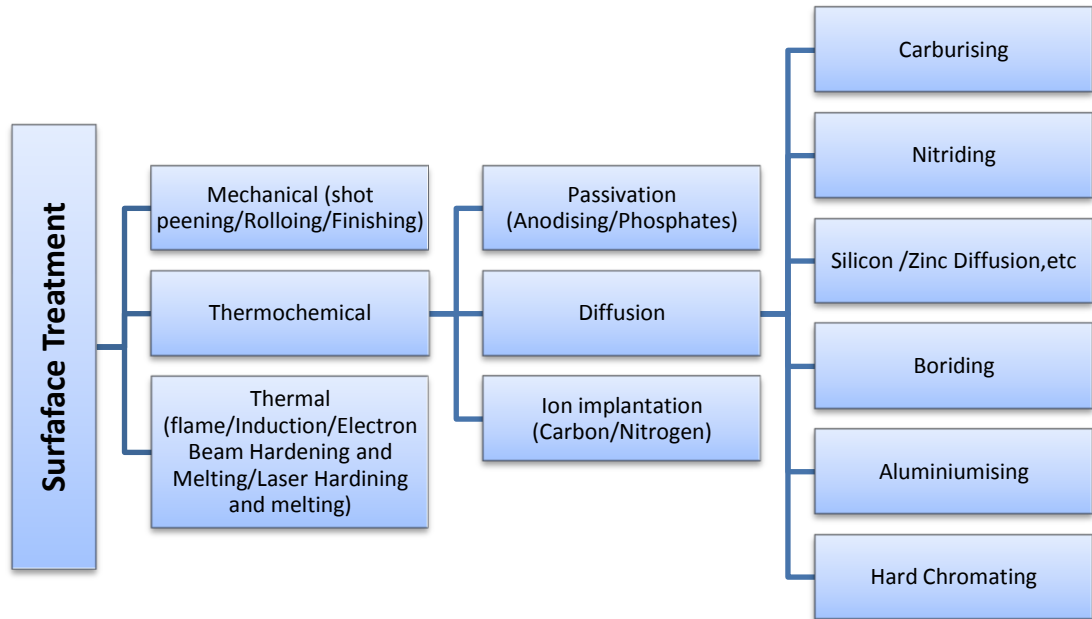


Figure2:2: Manufacturing cost of typical gears (Otto and Herring, 2002)

### 2.1.3 Gear Surface Treatment Methods

Gear tooth surface hardness is the most important factor for designing the gear set because it is subjected to surface contact stress, thus the surface durability to resist failure caused by contact stress is extremely important. The ability of gear material to resist plastic deformation or scratching by a pointed tool is defined as the hardness and can be measured using different scales such as Brinell (HB), Rockwell (HR) and Vickers (HV). These tests are widely used to measure the material hardness.

Three methods are commonly used to treat surface of steel materials using mechanical, thermochemical and thermal processes (Swift and Booker, 2003). Some of the most commonly used surface treatment methods for gear teeth are shown in Figure 2.3. These are shot peening, induction and flame hardening, carburising, nitriding and other methods which are used to produce harder steel gear teeth. The following discussion summarises the most important types of gear surface treatment.



*Figure 2.3: Gear surface treatment methods (Swift and Booker, 2003)*

### 2.1.3.1 Carburising

Carburising is a diffusion process and it is widely used for case hardening gear teeth. After heating the material to the required temperature, the surface layer of gear teeth changes to a high degree of hardness. The carburising temperature ranges between 871 and 954°C depending on the case depth required. For ideal toughness and core strength, carbon concentration in the gear surface layer should be less than one percent. Carburised gears are reheated to give better metallurgical structures to ensure that the gear can serve up to  $10^9$  cycles (Dudley, 1994). When it is red-hot, gear is quenched by using water or oil depending on gear application, the outer surface cools fastest because of contact with the quenching medium. In this case the outer surface size of carburised gears changes very slightly in volume and leads to change of gear pressure and helix angle. However, the core material retains the same volume. The dimensional change can be remedied by grinding process after carburising.

Carburised gears need to have sufficient surface hardness to resist crushing, spalling and surface initiated pitting due to contact loads. The permissible contact stress depends on the surface hardness and size of gears. The hardened gear teeth using carburising have a greater load-carrying capacity (Terry, 2013).

### **2.1.3.2 Nitriding**

Nitriding is a process of adding nitrogen to solid-base alloys by heating the steel in contact with ammonia gas. Nitriding and carburising are similar diffusion processes, but the penetration rate in nitriding process is slower and takes a longer period of time. The nitriding process depends on the factors of gear surface condition, temperature and time period of nitriding. Because surface oxidation impacts on nitrogen absorption it is essential to remove surface oxidation by mechanical or chemical means. The rate of nitrogen absorption and the thickness of surface layer are determined by the nitriding process.

For the best results of nitriding treatment, gears need to be rough-machined, case hardened and then quenched and tempered. Cracking can be decreased by using tempering processes (Errichello and Muller, 1994). The temperature of tempering is from 538 to 621 °C (Maitra, 1994 and Dudley, 1994). After heat treatment by tempering, the gear is machine-finished and then nitrided after being stress-relieved at about 593 °C. The nitriding and carburising are typical case hardening processes that can resist many types of gear failure modes such as pitting and scoring. It is important to choose the suitable treatment process for the different materials of gears to best serve the required gear application.

### **2.1.3.3 Induction Hardening**

Induction hardening of steel is a fast heating process by using a special power machine producing high power or high-frequency alternating currents. The amount of power required to harden a gear is difficult to estimate and depends on the coil efficiency, the amount of preheat used and heating time without distortion. Induction hardening is used for gears made of both alloy steels and plain carbon steels. Gears using induction hardening and carburising processes may have the same load-carrying capacity. During induction hardening the gear materials experience two different temperatures: low in the gear body and high in the surface layer. Thus, this process yields two conflicting tendencies of thermal expansion and contraction. One is a tendency for one part of

material to expand and the other is a tendency of other parts of the material to shrink. If the appropriate material and technique are used on the right teeth then residual compression can be obtained (Dudley, 1994). Otherwise, damaging residual tension stresses may be induced.

Problems with induction hardening include fast heating gear surface and the difficulty in controlling cooling time which can cause variation in metallurgical structure and residual stress pattern. In general, case carburised gears have better survival than induction hardened gears under serious pitting.

#### **2.1.3.4 Flame Hardening**

Induction and flame hardening are similar surface heat treatment methods. The only difference is that in flame hardening the heat is applied to surface by oxyacetylene flames instead of being generated electrically to the surface as that in induction hardening. It is difficult in some cases to get the same hardness layer below the gear surface by flame hardening; however this can be obtained by induction process (Dudley, 1994). Some types of flame hardening equipment are used to control the flame when the gear reaches the required temperature. Compared to previous hardening processes, flame hardening can be a handier process either to harden the working part of the tooth or to harden the whole tooth. However, carburised gears have more resistance to micropitting than the flame and induction hardening owing to the low carbon contents on the gears surface layer as experiments revealed (Winter and Weiss, 1980 cited in Errichello and Muller, 1994).

#### **2.1.3.5 Shot Peening**

Shot peening is a mechanical process where residual compressive stresses are induced in the surface by repeated large numbers of shots acting as a peen hammer. It significantly increases the surface life of the components. Gears surface materials treated by shot peening can improve the bending fatigue strength and reduce the shear stress which occur on sub-surface of gears (Townsend and Zaretsky, 1986). It helps to prevent the crack propagation that initiates on sub-surface of gears causing the pits.

#### **2.1.3.6 Combined Heat Treatments Method**

Nowadays, different combinations of heat treatment methods have been developed. Gear materials can be made stronger and long-wearing through using a double-cycle

carburised heat treatment. However, this treatment is more time consuming than single operation cycle and also results in gear distortions. Carburising and nitriding methods can be combined by using gases or molten salts to release the available carbon and nitrogen (Dudley, 1994). Austempering is a type of hot quenching treatment and it is used for highly alloyed steels to minimise the material structural distortion. The quench temperature is below the critical temperature of the case and above the Martensite starting temperature. In the austempering process the range of hardness variation depends on temperature that is used; it can range between 400-650 HV (Dudley, 1994). In order to determine the appropriate hardening process for the particular gear application type, experimental investigations are widely used. Heat treatment methods depend on several factors, such as type of the steel used, application requirements, etc.

## **2.2 GEAR DESIGN STANDARDS**

Many international standards have been published to guide gear design and manufacturing procedures to prevent gear failures and to ensure sufficient load capacity calculation. Gear design and analysis methods are standardised by many international manufacturers and committees such as AGMA (American Gear Manufacturers Association), ISO (International Standard Organization), JIS (Japanese Industrial Standard) and DIN (Deutsches Institut für Normung) to guide the various aspects of gear design. These standards are based on the comparison of the maximum static contact stress at the pitch point of tooth with the permissible contact stress for the gear material (Abersek and Flasker 2004). Different safety factors, depending on the application field, are considered in these standards for the gear wheel and pinion based on Hertzian contact stress induced by the load applied (ISO 6336-2, 2006).

The values of the minimum safety factor should be agreed between the manufacturer and customer and there is no standard for minimum safety factor that can be relied on for individual applications. The contact stress must not exceed the permissible contact stress which depends on the type of gear material and surface hardness values. Reference contact stress of the gear material is the most important factor when determining the permissible contact stress. It is defined as the maximum stress applied to gear tooth which is safe for no pitting occurrence within a definite number of stress cycles. It is a material parameter determined by experimental testing of reference gear (Abersek and Flasker, 2004). Due to inconsistency between various standards, over 40

gears experts attempted to establish “gear industry vision” by 2025 (Anderson et al, 2004). Their report emphasises the collaboration between all members such as the gear manufactures, academia, researchers and material suppliers to come up with global design and testing standards by 2015. Nevertheless, this target seems illusive as by 2014 nothing was accomplished in this regard.

### 2.3 WIND TURBINE GEARBOX CONFIGURATIONS

Two types of WTs are used to produce electricity: vertical axis and horizontal axis WTs. The generators and gearboxes of horizontal WTs are located at the top of the tower, whereas the generators and gearboxes of vertical WTs can be located near the ground. Figure 2.4 shows a typical three blades horizontal axis WT and a nacelle is mounted on top of the tower. The nacelle, the housing of the generating components, consists of low speed shaft, gearbox, generator, brake assembly and electric control subsystems. The horizontal axis WTs are mostly used because they are more effective (Errichello and Muller, 1994). The turbine’s nacelle is always in the direction of wind to obtain the maximum energy extraction by the blades, positioned on a rotating hub. WTs are subject to stochastic wind variation and their gearbox is designed to increase the speed from the rotor shaft to the generator rotating shaft.



*Figure 2.4: A typical horizontal wind turbine*

The WT main components inside the nacelle are labelled in Figure 2.5. The rotor is connected to the low speed shaft which drives the generator through the gearbox which

in turn increases the rotational speed at the generator. Wind speed which rotates the blades can be used to determine the generator speed and power output. Generally, WTs operate in a range of wind speed between 4 m/s and 25 m/s (56 mile/h) and the mean wind speed can be determined using the mean rotor speed recorded at the site (IEC 61400-1, 2005; Greaves et al, 2011; Dong et al, 2013).

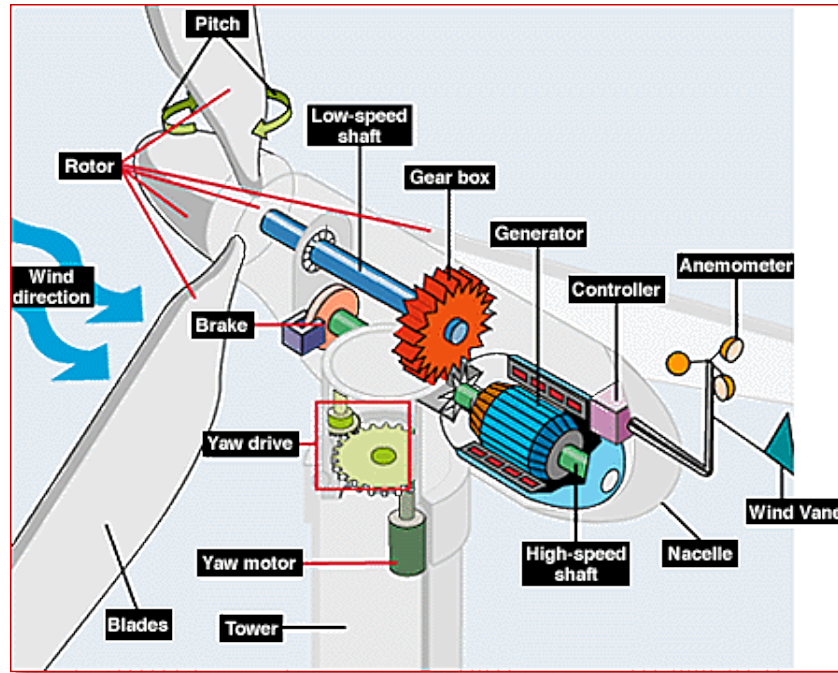


*Figure 2.5: Wind turbine nacelle main components (AWEA, 2013)*

WT manufacturers have used a variety of generator designs and most modern large scale WTs use synchronous or asynchronous generators with different magnetic poles depending on the designed nominal speed of generator. Different options have been developed to control the varying speed, such as variable-resistance asynchronous generators which are used in the low variable speed and doubly fed induction generators (DFIGs) which are used to control variable speed in strong wind conditions (Spinato et al, 2009; Sourkounis and Tourou, 2013). The DFIGs are the most commonly used type of WT generators with megawatt capacity because they are cost effective and power efficient systems (Müller et al, 2002). The generator electrical output must be maintained at a fixed frequency of the electrical grid and the generator synchronous speed,  $n_s$ , can be calculated using Equation 2.1.

$$n_s = \frac{120 * f}{p_s} \quad (2.1)$$

where,  $p_s$ , is the number of magnetic poles and,  $f$ , is the grid frequency in Hz which is typically 60 and 50 hertz as used in the United States and Europe respectively (El-Sharkawi, 2013).

The WT gearboxes typically consist of three stages with one or two planetary stages depending on the torque to be transmitted and the capacity of wind power to be produced (IEC 61400-4, 2012). Normally each gearbox has one planetary and two parallel stages or two planetary stages and one parallel stage. Based on the required output speed of the gearbox, the first planetary stage may be followed by another planetary stage or a parallel stage. Figure 2.6 illustrates a one stage planetary gear set followed by two parallel stages.

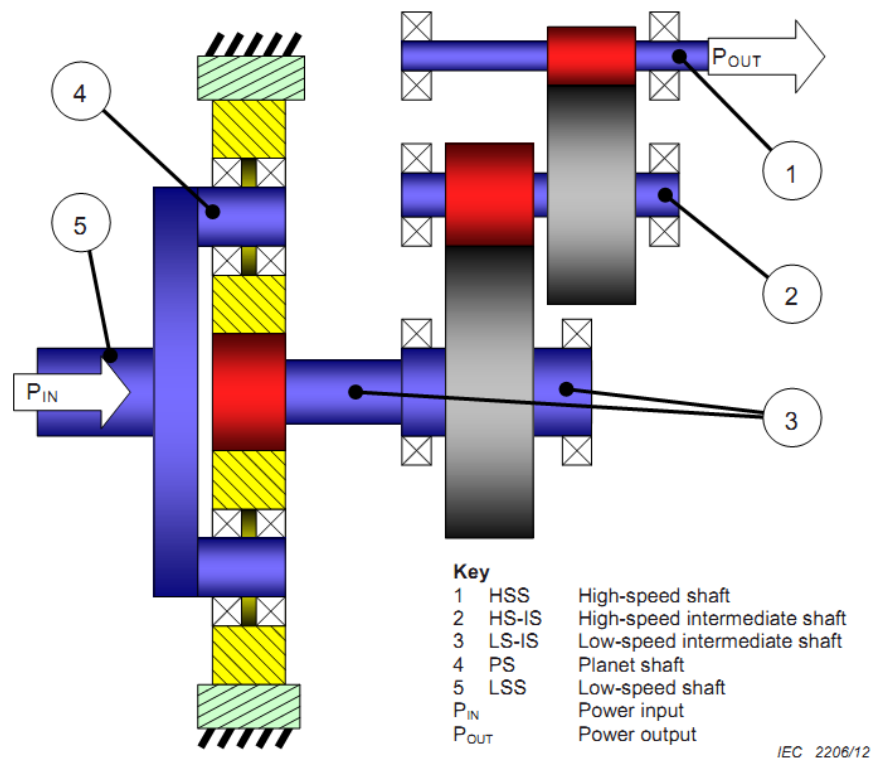


**Figure 2.6: WT gearbox with one planetary and two parallel stages (IEC 61400-4, 2012)**

The planetary stage consists of a sun gear, a ring gear and planet carrier with several planet gears. Figure 2.6 illustrates the layout of the gear stages and gives details of planetary and parallel stages such as the low-speed shaft (LSS), high-speed intermediate shaft (HS-IS), high-speed shaft (HSS), power input and power output. Two common types of gears are used in the WT gearbox: spur and helical gears. The variation between the low speed and high torque at the LSS (input) and a high speed and low torque (output) at the HSS create a complex working condition in the WT gearbox

(Smolders et al, 2010). The present study focuses mainly on investigation of gear micropitting failure of the HSS gear pinion of WT gearbox.

## 2.4 GEAR FAILURE MODES

Before discussing the common gear failure modes, it is useful to highlight the gear's key parts and features. The definition of nomenclatures of a spur gear is shown in Figure 2.7, showing the location of addendum and dedendum of the gear tooth. The dedendum covers an area between the dedendum circle and the pitch circle, while the addendum covers the area between the addendum circle and the pitch circle. The pitch circle diameter or reference diameter is one of the most important parameters because many other gear parameters are determined based on it. Gear modulus is defined by dividing the pitch diameter by the teeth number. When two gears are meshed, the diameters at the pitch circle are tangential and the distance between both gears is represented by the sum of their radii. The larger of any two meshing gears is called the wheel, and the smaller one is called the pinion.

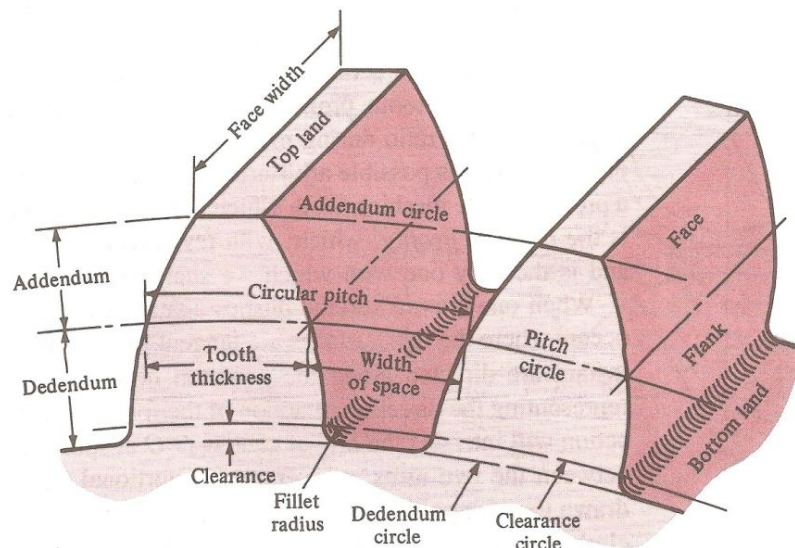


*Figure 2.7: Spur gear nomenclature (Shigley, 1989)*

The two major types of gear failure are tooth breakage and surface failure as shown in Figure 2.8. Tooth breakage denotes the gear tooth fracture which is commonly caused by overload stresses that exceed the endurance limit of material. The surface failure is dependent on a number of factors, such as surface treatment, relative motion (sliding and rolling), lubrication and type of material. Pitting is one, among many, surface

failure modes, which commonly occur in the WT gearbox, as discussed in Chapter 1, Section 1.2.

The most common types of tooth surface failure are micropitting, scuffing, sliding wear and spalling, as illustrated in Figure 2.8. Each type of gear failure has its unique features and causes, a description of the common gear failure modes and their causes and consequences is presented in the following sub-sections.

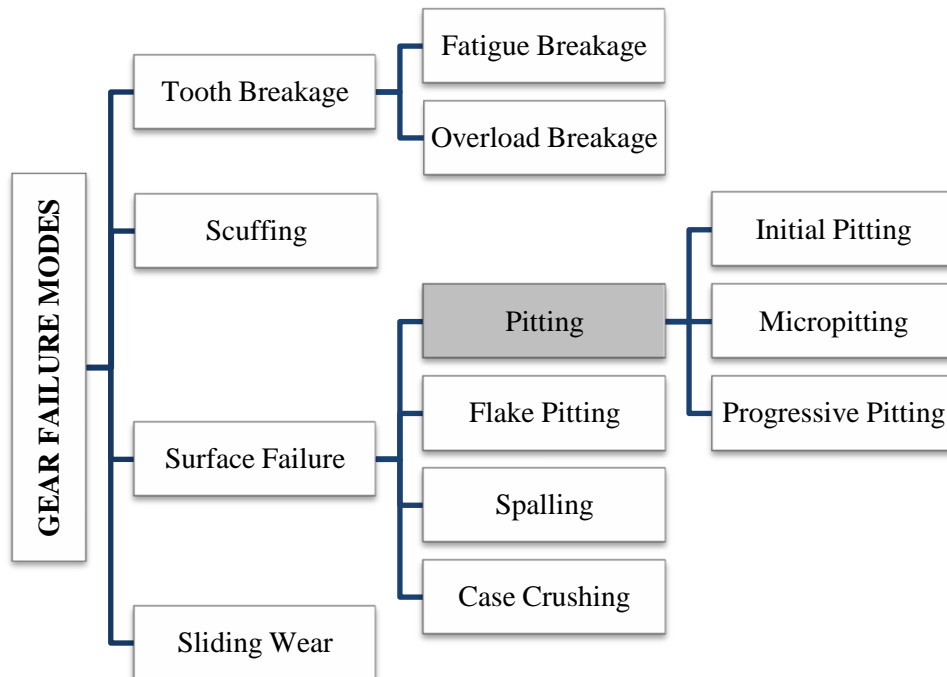


*Figure 2.8: Different gear failure modes (Adopted from ISO 10825, 1995 (E/F) and BS 7848 (1996))*

### 2.4.1 Pitting

According to ISO 10825 (1995) and BS 7848 (1996), which defines the terminology of gear failure modes, pitting can be divided into three different types of failure: initial pitting, micropitting and progressive pitting, as shown in Figure 2.8. It can be initiated on the surface or on subsurface of gear tooth flank and can lead to destructive pitting. According to ISO 10825 (1995) and BS 7848 (1996) surface failure is defined as “material damage due to surface and subsurface stresses produced by the repeated application of forces. It is characterised by the removal of metal and the formation of cavities” (P.31). A case crushing, one of the other subsurface failure modes, occurs due to excessive compressive loads, insufficient core hardness and insufficient case depth. It

occurs when the subsurface stresses exceed the core strength. It appears perpendicular to the surface and occurs suddenly, without any warning signs (Industries, 1978).

The surface failure mode occurs slightly below or above the pitch line at the addendum or dedendum or both of them on the gear tooth flank. This failure can be reduced by using different surface treatments of the gear tooth flank. The first stage of micropitting is initial pitting and it is characterised by the formation of small pits on the tooth surface. The initial pitting can be described as small shallow pits caused by contact with irregularities. It normally occurs at the first stage of running at reduced load (ISO 10825, 1995 and BS 7848, 1996). The other stage is progressive pitting or macropitting where pits are larger than 1 mm and have irregular shapes (Errichello and Muller, 1994; Oyague, 2009). Progressive pitting usually starts below the pitch line of the gear flank and it sharply increases in both the pit size and number after a certain number of cycles. Overload conditions is one of the main causes of progressive pitting. The surface progressive pitting occurs on the flank surface of gears and it normally occurs because of the thin oil film and some sharpness of contact (Shiple, 1974). It mostly takes place first in the dedendum and then on the addendum area of the pinion.

Spalling is a type of surface failure and it is a progressive macropitting characterised by more irregular pit shapes and quite shallow depths of pits. It occurs more frequently in materials of medium hardness, but it can also occur in highly loaded gears of fully hardened materials (Dudley, 1994). According to Zhang (2005), macropitting types like spalling can be classified into two categories: middle and large-size pitting. The diameter of middle-size pits ranges from 0.1 to 1 mm. In large-size pitting the pits' diameter is usually bigger than 1 mm. Sizes of pits diameter are related to pits depth, pits of bigger sizes are deeper in depth and range between 0.08 and 0.45 mm. Spalling flakes are thicker and more progressive than flank pitting.

Micropitting is type of surface failure which generally appears in lubricated gears and occurs due to exceeding the surface load capacity of the gear material. If gear material is subject to high contact stress that exceeds the yield strength, a plastic deformation at the surface or subsurface of the contact gear teeth occurs. The micropitting in lubricated gears occurs after a certain number of cycles and micropitted gears need to be replaced owing to the vibration and noise caused by tooth profile deviation (Oila, 2003; Wink, 2012; IEC 61400-4, 2012). Micropitting happens when two surfaces slide and roll

against each other in opposing directions or when any sufficient stress is present. It mainly occurs when the lubricant film between contact surfaces is insufficient, after a certain number of operation cycles. Contact surfaces start to get affected after a certain number of cycles depending on many factors such as the surface hardness, material types and surface treatments of the materials. When these surfaces are in contact and pressed together, a maximum shear stress is developed close to, but not exactly on, the pitch line of contacting surfaces. The pitch line has zero sliding velocity but the sliding velocity becomes maximum at the end of tooth tip and root. If the gears are kept in operation after pitting, the surface of the tooth starts to be worn away leading to other types of surface failures, such as sliding wear, including abrasion (ISO 10825, 1995 and BS 7848, 1996).

### **2.4.2 Sliding Wear**

ISO 10825, (1995) and BS 7848, (1996) describe many types of gear wear such as normal wear, abrasive wear and excessive wear. In general, wear occurs due to sliding between metal contact of gear pair indicating the removal of material from the tooth contact area. This material removal may be the result of the abrasive action due to the presence of individual particles. These particles can engage between the gear tooth pair in the lubricant. Although the AGMA 6006-A03 (2003) and IEC 61400-4 (2012) standards recommend considering the abrasive wear in any assessment of a lubricant fluid in WT gears, they do not offer a standardised test to assess it. The three common causes of gear tooth wear are the entrance of individual particles in oil, metal to metal contact due to lack of oil film and chemical wear due to the composition of liquids inside gears. By using a good filtering system, large particles and other contaminants can be eliminated (Dowling, 2007).

### **2.4.3 Scuffing**

Scuffing occurs at high speed (hot scuffing) or low speed (cold scuffing). It occurs due to the combination of two distinct activities, which are lubrication failure and metal contact due to foreign material wear. Moreover, the surface finish is an important factor affecting scuffing. If the load and oil temperature increase after initial scuffing, the scuffing extends over to a large area and this is called severe scuffing. However, a light

scuffing, which normally occurs at tooth tips, may stop progression on its own if gears operate under good condition (ISO 10825, 1995 and BS 7848, 1996).

Since micropitting is the major focus of this thesis, it will be discussed in more detail. The following section discusses the root causes and characteristics of micropitting and research work published.

## 2.5 ROOT CAUSES OF MICROPITTING

Way (cited in Ku, 1974) was the pioneer who pointed out pitting failure in gears in 1953. Micropitting failure is commonly observed in materials with high surface hardness (ISO/TR 15144-1, 2010). Low surface roughness (smooth surface) of high surface hardness can resist the micropitting (Errichello, 2012). Gear teeth flank micropitting is characterised by a continuous deterioration of the rolling and sliding contacting surfaces. These surfaces are influenced gradually by repeated contact loading and sliding and the micropitting can spread out to cover most contact surfaces of tooth flanks. An example of tooth flank micropitting is shown in Figure 2.9.

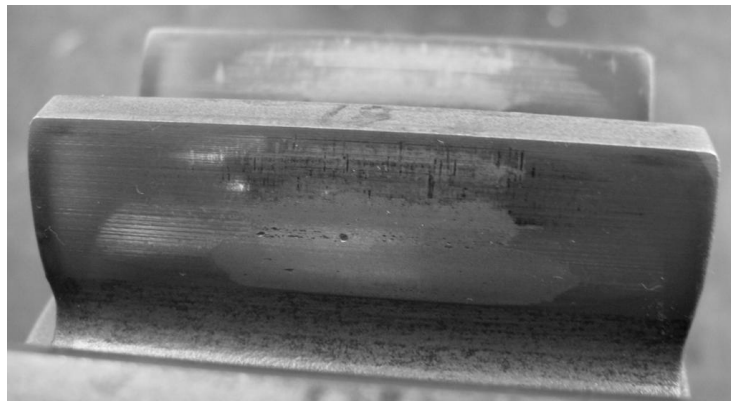


*Figure 2.9: Tooth flank micropitting*

The Elastohydrodynamic (EHD) film does not prevent surfaces from cyclic stressing. Micropitting may occur when peaks of surface roughness contact under mixed or boundary lubrications. The main effect of EHD film is to modulate the stress distribution in the mating gear surface asperity points by preventing the direct contact between surfaces. As a result, the pitting life is based on the EHD film thickness (greater film thickness leads to longer life) (Ku, 1974). Pitting can take place when the EHD system is in a boundary lubrication condition, making different wears such as scuffing become unavoidable (Errichello and Muller, 1994). The lubrication conditions

between two contact surfaces in relative motion can be divided into four lubrication regimes:

- ❖ Full film lubrication: the oil film thickness between tooth surfaces is separated sufficiently and the load is fully supported by fluid film. This case mainly occurs when gears operate under certain conditions such as high rotational speed, high-quality surface roughness, good lubricant oil with additives and good lubricant cooling.
- ❖ Micro-EHL lubrication: it is similar to the full film lubrication but the oil film thickness fluctuates owing to the surface roughness where the load is mostly supported by the EHD film.
- ❖ Mixed lubrication: The oil film is not thick enough to separate the contact surfaces. There is a possibility of metal to metal contact due to the existence of a few asperities or high peaks of tooth surface roughness causing micropitting.
- ❖ Boundary lubrication: The lubricant film is present at valleys only and the surfaces roughness peaks are in direct contact which causes the plastic deformation due to the very thin film (Oliver, 2002).

These regimes are illustrated in Figure 2.10 below.

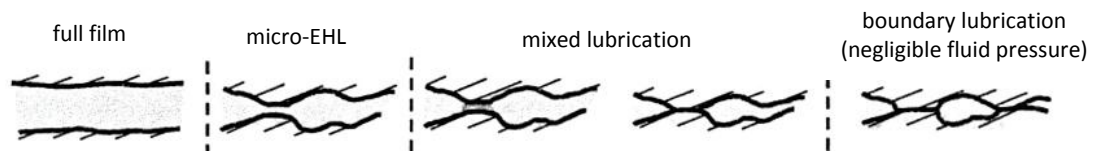


**Figure 2.10: Different lubrication regimes between the gear contact surface roughness, (Spikes and Olver, 2002 cited in Olver, 2002)**

Different parameters are used to characterise the surface roughness such as mean surface roughness ( $R_a$ ), mean peak-to-valley height ( $R_q$ ) and root mean square roughness (RMS). The specific lubricant film thickness is dimensionless and it can be defined as the ratio between the lubricant film thickness and the effective mean surface roughness, as shown in Equation 4-26. The specific lubricant film thickness ratio depends on the composite surface roughness calculation and the type of roughness parameter used to obtain the specific lubricant film thickness. Drawing on previous research, Bell et al (2012) compared the three most common lubrication regimes at different ranges of specific lubricant film thickness results, as shown in Table 2-1.

**Table 2-1 Influence of composite surface roughness calculations on specific lubricant film thickness (Bell et al, 2012)**

Lubrication regime	Specific lubricant film thickness		
	Authors/source	Dudley (1994)	Frequently used (Maru, 2007 and Hutchings, 1992)
Full film lubrication	> 1.0	> 3	> 5
Mixed lubrication	0.4 - 1.0	1 - 3	1 - 5
Boundary lubrication	0.1 – 0.3	< 1	< 1

The Dowson and Higginson formula (Dowson and Higginson, 1966), can be used in conjunction with the mean surface roughness value of gears in order to determine the specific lubricant film thickness to assess the actual gear flank surface EHL behaviour. This method is adopted by ISO/TR 15144-1 (2010). The gear tooth lubricant film thickness analysis is briefly discussed in Chapter 4, Section 4.2.6.

After a certain number of stress cycles, gears may start to pit either at the surface or subsurface. Figure 2.11 and Figure 2.12 show surface and subsurface originated pits in gears respectively. Generally, the diameter of initial pit is very small and it falls in the range of 0.4 to 0.79 mm (Shipley, 1974). Zhang (2005) documented the following gear micropits characteristics: they usually show a grey or glittery surface, they are small and shallow with only a few microns in size and that a micropitted area is made of many micropits and cracks. Jelaska (2012) described micropitting as various surface cracks growing at shallow angles to the contact surface, the typical depth of which is 10-20  $\mu\text{m}$ . Macropitting pits are larger in size and after a certain number of cycles they can take over the whole tooth flank (Shipley, 1974). Figure 2.13 shows the depth of pitting and spalling. It illustrates that the pitting appears on surfaces with a depth of the work hardened layer of approximately 10 $\mu\text{m}$  and spalling with a depth of 20-100  $\mu\text{m}$  (Ding and Rieger, 2003).

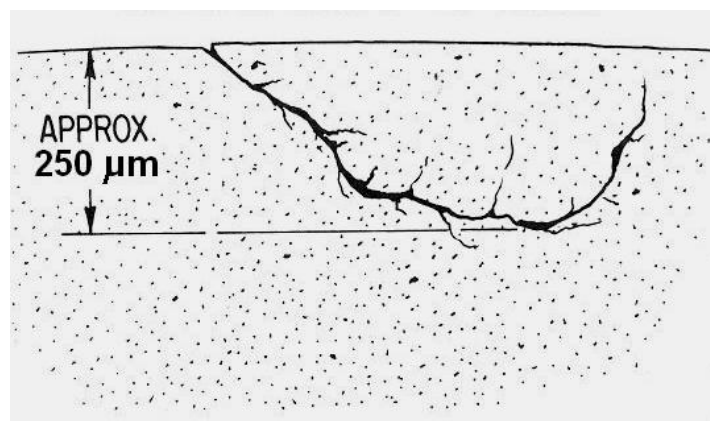


**Figure 2.11: Surface origin pit (Shipley, 1974)**

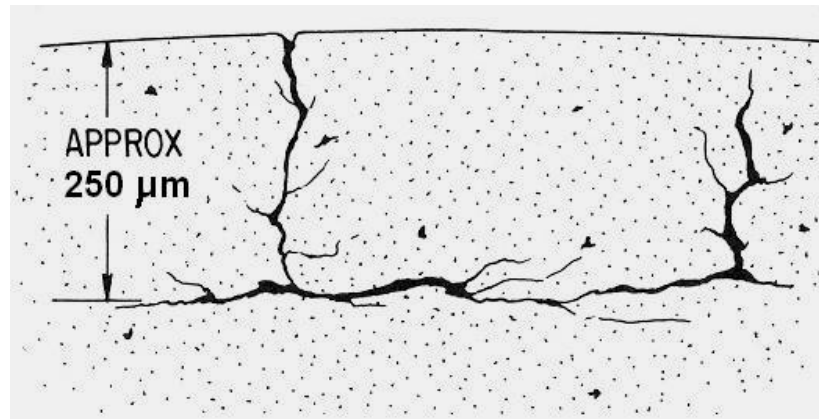


Figure 2.12: Subsurface origin pit (Shipley, 1974)

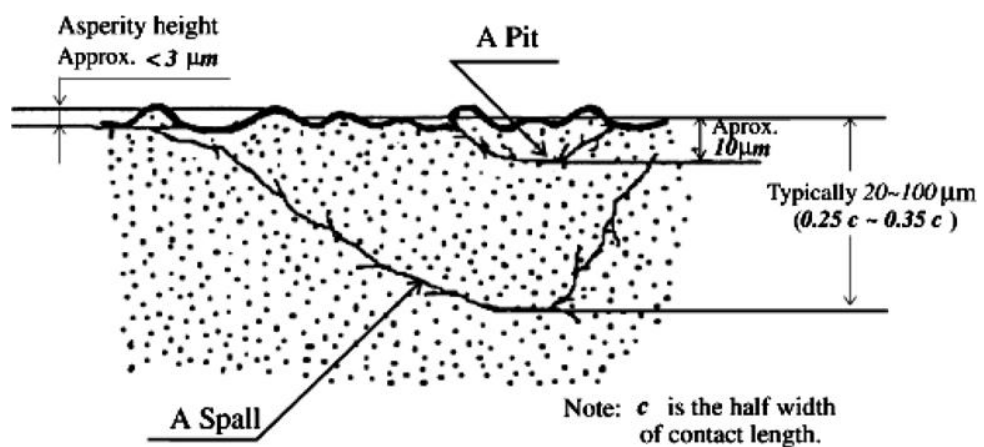
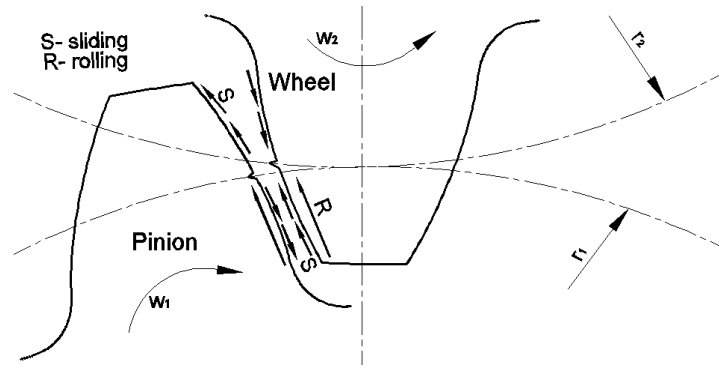


Figure 2.13: Pitting and spalling (Ding and Rieger, 2003)

During gear engagement, gear teeth experience a complex combination of surface sliding and rolling contact which varies along the tooth flank as shown in Figure 2.14. When the pinion is used as a driving gear, contact starts at the root of the pinion tooth and ends at the tooth tip and vice versa for the wheel tooth. The contact points along the gear profile and pinion undergo a pure rolling at pitch point and a mixture of rolling and sliding for other contact points (Fernandes and McDuling, 1997). In the scenario of mixed rolling and sliding plus pure rolling, initiation of pitting might occur after a certain limit of operation cycles. When used as a driving gear, the pinion sliding direction is away from the pitch line, whereas the driven wheel gear slides towards the pitch line. For the pinion gear, this makes the sliding motion apt to tension the material away from the pitch line (Dudley, 1994; Fernandes and McDuling, 1997; Errichello, 2012).



**Figure 2.14: Gear tooth surface rolling and sliding**

The extremely high shear stresses contribute to the formation of tooth surface sliding which occurs primarily due to plastic deformation when constrained by the surrounding material. If the two tangential velocities are the same for contacting curved bodies, the pure rolling conditions occur. If these velocities are not the same, sliding occurs which significantly changes the stress distribution in the surface and sub-surface. Rolling and sliding may occur in the same or opposite directions, as shown in Figure 2.14, depending on the contacting bodies' relative velocities. Opposite direction rolling results in higher stresses because rolling is in one direction and sliding is in the other. Under combined rolling and sliding motion, modified gear tooth profiles are commonly used to change the surface shear stress distribution. As a result, the maximum shear stress position is moved to the contacting interface where the crack initiation occurs (Glodež et al, 1998).

Under pure rolling condition the maximum shear stress exists at about 0.18-0.3 mm below the contact surface and the crack propagates parallel to the surface (Fernandes and McDuling, 1997; Seireg, 2001). At the pitch line of the wheel gear, however, the tooth material is compressed by the sliding motion and the tooth material is pulled away from the pitch line in pinion. The dedendum of both gears has a relatively short contact length and negative sliding as the direction of the sliding velocity is in the opposite direction of the rolling velocity as shown in Figures 2.14 and 2.15. Furthermore, the contact stress changes continuously throughout the meshing process and high contact stresses can occur at the single tooth contact region where the load is supported by single pair of gear teeth as shown in Figure 2.16. The failure may initiate in this region if the contact stress exceeds the allowable contact stress of the gear material.

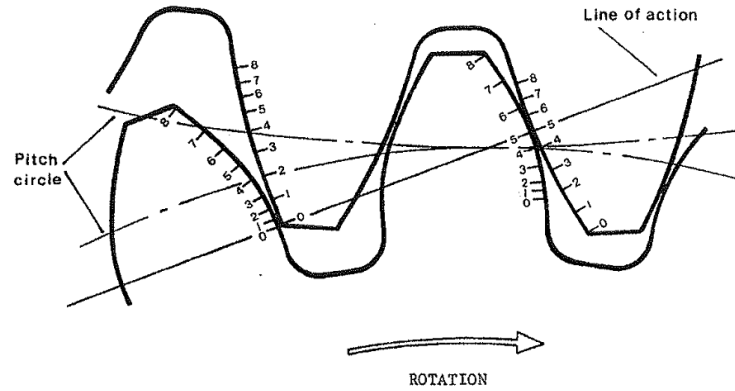


**Figure 2.15: Relative sliding during tooth meshing (Childs, 2004)**

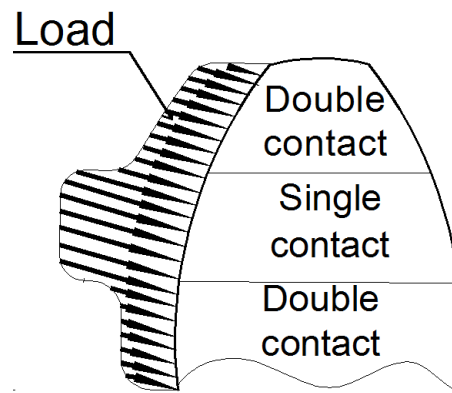


**Figure 2.16: Spur gear load distribution**

In addition to the above, the variation of contact stresses and sliding directions can cause high temperatures and mixed lubrication conditions at contact surfaces, or even break down the lubrication film along the tooth flank. Moreover, the surface roughness of meshing gear teeth will change instantaneously after contact points undergoing certain running cycles under loading. This leads to a variation of specific lubricant film thickness resulting in direct metal to metal contact and initiation of micropitting (Seireg, 2001).

Fernandes and McDuling perceived that material plastic deformation occurs under rolling/sliding conditions can result in change of material microstructures. In addition, gear teeth surface micropitting is influenced by the geometry of the contact bodies of gears and the chemical properties of lubricant. These variables together with the aspects stated above are the main factors that lead to initiation of micropitting. Furthermore, these factors have a great impact on lubricant film thickness which plays a major role in

initiation of micropitting. Section 2.7 reviews the previous studies related to micropitting using different investigation methods.

## **2.6 SCADA DATA AND APPLICATIONS**

A wide range of research explores the application of SCADA data as a Condition Monitoring (CM) tool for WTs using various approaches. Kim et al, (2011) used SCADA data for WT fault detection by developing algorithms and diagnostic techniques. The measurement of the relationship between the ratio of high speed shaft torque to high speed shaft speed versus power shows that there was an observed fault at lower power level. Feng et al (2012) analysed SCADA data using simple physics models combined with CM system signals to predict WT gearbox failures. Similar studies had been carried out by Wilkinson et al (2013) using SCADA data for condition monitoring by employing a number of methods to detect the WT components failures.

The comparison between Artificial Neural Network, Signal Trending and Physical model reveals that the physical model was a useful method in predicting imminent failure in WTs. The direct SCADA data signals were used by Gray and Watson (2009) to predict WT bearing failure using physics of failure approach. Zaher et al (2009) also explored the SCADA data to detect the WT gearbox faults using anomaly detection. To detect faults of pitch and converter systems, Qiu et al (2011) introduced two methods of SCADA alarm analysis, namely time-sequence and probability-based. However, the previous studies related to the CM of the SCADA signals have limited ability to detect the exact gearbox faulty part or component and associated failure root causes. The SCADA signals cannot be used to directly assess the performance of gears for its intended function. Furthermore, SCADA signals in time series do not directly present probabilistic characteristics of gearbox loading conditions for the design life of 20 years.

## **2.7 FACTORS AFFECTING MICROPITTING**

In addition to the key factors discussed in Chapter 1, Section 1.2 and Chapter 2, Section 2.5, gears used in WT gearbox are subjected to severe operational conditions: variable loading and variable rotational speed resulting in variation in sliding velocity, which all affect lubrication condition leading to the occurrence of micropitting. A factor

associated with micropitting occurrence is the deterioration of the surface roughness and change in material microstructure properties. The following sections review the research on the key factors affecting micropitting by using analytical methods.

### **2.7.1 Contact Stress**

A considerable research has investigated the influence of contact stress on lubrication conditions and the prediction of pit shapes under different contact loading and radii of curvatures. Thus, the investigation of different contact surface radii, sliding contact, material microstructure and crack angles and growth is indispensable from the study of contact stress. Abersek and Flaker (2004) compared contact stress results by two different analyses methods, Hertzian theory and finite element numerical method. The contact algorithm was used to calculate the distribution of contact stress at five characteristic points along the profiles of the mating gear teeth. These five characteristic point locations along the engagement line were:

- ❖ Initial mating point;
- ❖ Inner single point;
- ❖ Pitch point;
- ❖ Outer single pair mesh point;
- ❖ Final mating point.

Contact stress values calculated using the two different approaches were in good agreement. Ognjanovic (2004) found that the probability of pitting was higher if the flank contact stress level was close to the material endurance limit of gear surface. In addition, carburised hardened tooth surfaces had greater resistance to pitting and sliding wear along the tooth flank. The Hertz stress entails that the maximum stress is below the surface layer and that the oil layer modulates the stress distribution and causes stress reduction between moving tooth surfaces. In the case of good lubrication, the cracks may start at peaks of surface roughness between contacting tooth flanks. Subsurface cracks can develop and cause pitting due to poor lubrication (Ognjanovic, 2004). Evans et al (2013) modelled and tested gear tooth contacts, with the consideration of surface roughness in the contact analysis. The authors found that the direction of cracks on the driven gear flank characterised from tip to root and gear tooth flank micropitting failure mainly initiated at the roughness asperity level.

Due to different operational conditions, materials types and microstructure, surface treatments and surface hardness, it is difficult to know the exact service life of gears. Cheng et al (1994) (cited in Abersek and Flasker, 2004) investigated fatigue crack initiation and considered that the average length of the initial crack was equal to the grain size. The authors assumed that crack size was initiated at the point of the maximum von Mises stress at some distance below the surface. The fatigue crack propagation can be divided into different stages. The first stage is short growth propagation in material microstructure which occurs in initial stages of the crack growth. Zhou et al (1989) (cited in Glodez and Ren, 1998) summarised the material failure process stages that lead to cracks then pitting as:

- ❖ Travelling and build-up of dislocations,
- ❖ Micro-crack initiation,
- ❖ Fatigue crack growth,
- ❖ Final surface failure.

The transition from one stage to another is determined by the influence of the microstructure of material on crack growth. Material microstructure has a significant influence on the crack initiation (Glodez and Ren, 1998). In their study, Glodez and Ren modelled a virtual crack extension based on results of numerous previous research conducted by others. The finite element simulation used with two cylinders and the initial cracks length assumed in all simulation was 0.05 mm. In their computational model, they considered different maximum contact stress ( $P_o$ ), maximum von Mises stress and the depth under the contact surface. When the contact stress and the equivalent curvature radius ( $R^*$ ) increase, the maximum von Mises appears deeper under the contact surface. The authors reported that the critical length of crack ( $a$ ) is the shortest for smaller curvature radii and contact loading and vice versa. The relationship between the crack length and stress intensity factor ( $K$ ) under different contact stress conditions is shown in Figure 2.18. This study did not consider the variation of rotational speed, sliding velocity and lubrication effect. However, it is a good method and can be used to predict pit shapes and subsurface fatigue crack, as shown in Figures 2.17 and 2.18.

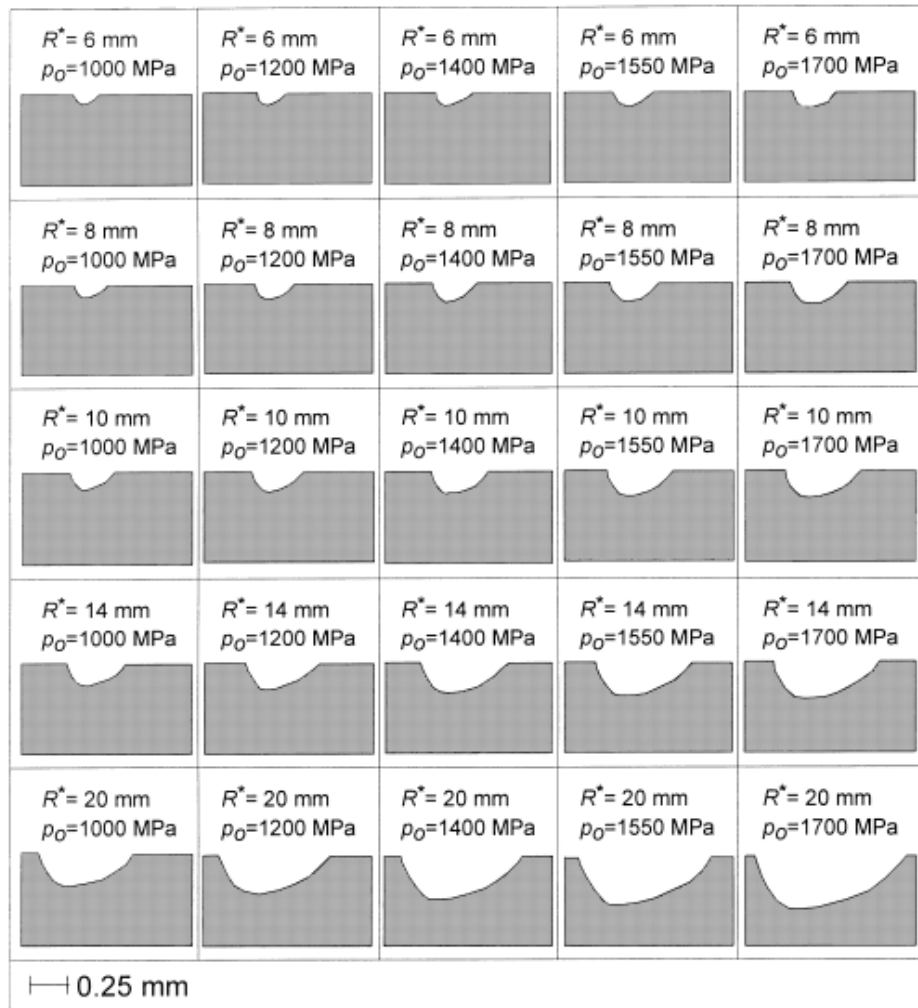


Figure 2.17: Shapes of predicted pit combinations of contact stresses and equivalent curvature radius (Glodez and Ren, 1998)

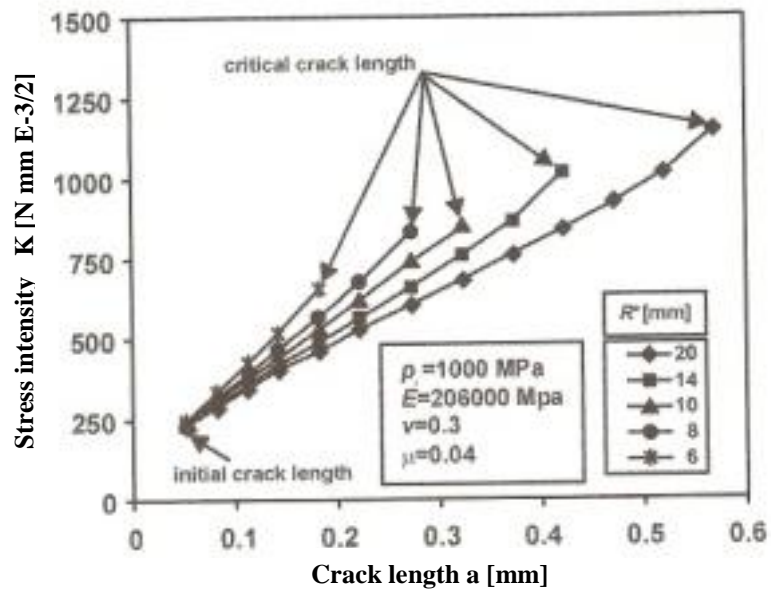
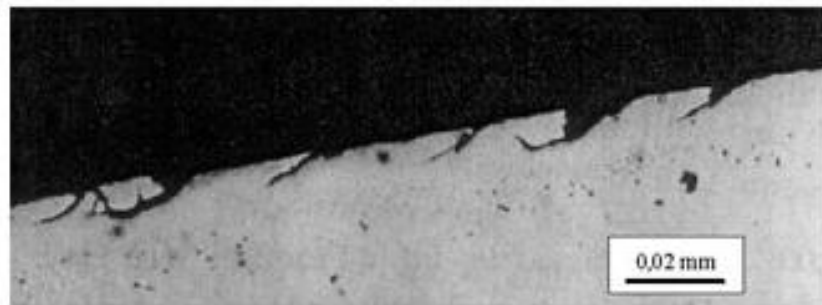


Figure 2.18: Example of the results obtained for different equivalent radius (Abersek and Flaker, 2004)

Glodez and Ren's study was extended by Flasker et al (2001) who assumed the initial length of crack to be 0.015 mm instead of 0.05 mm in their investigation of crack propagation under different contact loading. Furthermore, the authors considered the lubrication effects on sliding and the hydraulic pressure inside the crack. Coulomb friction law was used due to the sliding contact between the gear teeth. Figure 2.19 shows the shape and pits size of a spur gear obtained from experimental data by using FZG testing. However, this study concentrated only on the surface crack propagation and did not consider the material behaviours under different contact temperatures. A similar study conducted by Fajdiga and Sraml (2009), explored virtual crack extension using finite element analysis. They described the initiation and propagation of fatigue crack in the area of gear tooth flanks contact. In their computational model they considered Hertzain contact stress, friction and motion and approximated lubricant pressure inside the crack but dislocation motion at the contact surfaces, residual stress and contact temperatures were not considered.



*Figure 2.19: Experimental result of surface pit shape and size (Flasker et al, 2001)*

Various studies focused on the angles of cracks between the contacting surfaces. The angle between the initial crack and the direction of frictional force under rolling contact does not exceed  $21^\circ$  due to large shear stress, as suggested by experimental evidence (Abersek and Flasker, 2004). These cracks of irregular shapes are usually inclined at an oblique angle. Results achieved by Errichello (2012) indicated that the cracks mostly occur near the pitch line and propagate at a shallow angle between 10 and 30 degrees. Similar results were reached by Bull et al (1999), Oila (2003) and Zhang (2005) who found that the cracks propagate against the sliding direction on the driven gear tooth flank, as shown in Figure 2.20. Tooth profile of the dedendum region can be seriously damaged by continuous micropitting. Thus, it can result in increased dynamic forces and lead to further types of gear surface failure, such as scuffing.

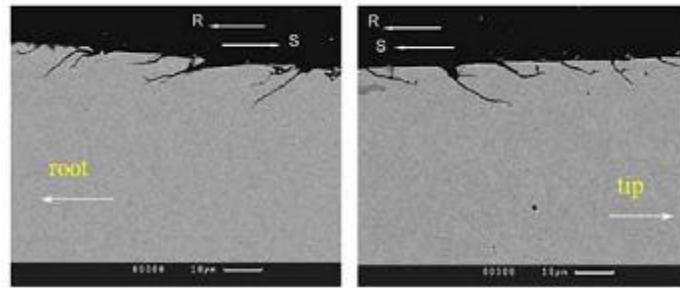


*Figure 2.20: Driven gear micropitting crack direction (cited in Errichello, 2012)*

Djeddou and Zegadi (2007) used the procedure of ISO 6336 standards for statistical analysis to predict the life and reliability of fine pitch gear pairs. The Monte Carlo method showed good agreement in predicting the stresses and the reliability of gear pairs. Zhang et al (2003) developed a numerical method for calculating the reliability of gear pair by considering all contact stresses and bending strength parameters as random variables except the gear ratio. Gear dynamic load, bulk and flash temperature and lubricant film thickness were analysed by Wang and Cheng (1981). They found that when the pitch diameter increased or the face width decreased for the same specific loading, better lubrication performance was observed. The favourable condition for preventing pitting development but still maintaining a maximum operational life is to ensure the contact stress to be slightly lower than the endurance limit because higher contact stresses lead to fast pitting.

### **2.7.2 Rotational Speed**

Due to stochastic nature of wind conditions, it leads to the variation of rotational speed in the WT gearboxes. The international standards IEC 61400-1 (2005), parts 1 and 4 and IEC 61400-4 (2012(E)) provide the guideline of design requirements for WT gearboxes. These standards consider the statistic characteristics of wind speed variations and WT controls by determining various design load cases based on computational simulations. Veldkamp (2008) presented a probabilistic method for WT design, which considered important stochastic parameters, such as turbulence intensity, wind speed and material fatigue strength, with their estimated distributions (normal, lognormal and deterministic) that influenced fatigue loads. The author concluded that the “*uncertainties in material fatigue properties and life prediction methods dominate total uncertainty, and hence determine the required partial factors*” (P.655).

According to Seireg (2001) the size and depth of the pits are related to the rotational speed. At the higher rotational speed the characteristics of pits are smaller and shallower and vice versa at the lower rotational speed. On one hand the higher rotational speed can help to increase the lubricant film thickness. However, it increases the local contact temperature as it is directly proportional to the local sliding velocity (more details in Chapter 4, Section 4.2.4). It was shown that the variation of rotational speed may contribute in causing micropitting. Gears can be used for longer cycles without micropitting initiation if the sliding speed is reduced. Wang and Cheng (1981) found that the film thickness increased slightly when increasing the rotational speed.

### **2.7.3 Sliding Parameter**

Being a significant factor leading to micropitting, sliding velocity received considerable attention in gear research. In his review of gear lubrication research, Olver (2002) referred to one of his previous studies conducted in 1995 which investigated the correlation between the sliding velocity and gear micropitting life. He concluded that, when sliding motion was present, the micropitting life was reduced and gears failed where the sliding velocity was the greatest. He confirmed his findings experimentally where he found that micropitting did not occur at the highest contact stress location, but where the sliding velocity was greater. Winkelmann (2011) showed that the most common type of micropitting was wear and it mostly occurred in dedendum owing to the negative sliding which speeded up crack propagation. Oila (2003) proved that the sliding strongly influenced the initiation of micropitting among the other operational conditions. The micropitting can be eliminated by reducing the slide-to-roll ratio and the probability of pitting increases if high slide-to-roll ratio existed (Graham et al, 1981; Webster and Norbart, 1995 cited in Oila, 2003). Yi and Quinonez (2005) confirmed that the maximum spur gear sliding velocity occurred at the tip of the tooth. Tangential stresses in gears, which occur due to the sliding and rolling scenarios during meshing, are explained in Section 2.5.

The relative sliding under high load can be reduced by using different methods such as low surface roughness, surface coating and microgeometry modification. It significantly accelerates the micropitting initiation because high sliding leads to high operating temperature which in turn leads to lower lubrication condition.

### 2.7.4 Local Contact Temperature

One of the pioneering research work that investigated flash temperature caused by gear tooth contact was published in 1937 by Blok. Nevertheless, the equation used in this work did not consider the coefficient of friction in relation to gear tooth surface roughness, which was addressed later by Kelly (1953, cited in AGMA 925-A03, 2003). This led to further research by Terauchi and Mori (1974) who studied the surface temperature by considering the effects of dynamic loading on flash temperature. They found that the flash temperature varied along the gear flank of contact. This is due to the mixture of rolling and sliding motions and the Hertzian contact stresses which vary along the gear tooth surface. Long et al (2003) used finite element analysis to predict the gear tooth temperature variation by varying the shaft rotational speeds and gear loads. The authors found that the load had a greater effect on tooth surface temperature than the rotational speed. The finite element method was used by Townsend and Akin (1981) to analyse the gear tooth temperature and the influence of the oil jet impact depth. In addition, they measured the average temperature of gear tooth surface with different oil jet pressures as well as instantaneous gear surface temperature using an infrared radiometric microscope. Experimental and calculation results for gear tooth temperature were close for high oil jet penetration depths while they were significantly different for low oil jet penetration depths.

Anifantis and Dimarogonas (1993) investigated gear tooth temperature rise by developing a numerical method for the computation of the flank temperatures of mating gear teeth. They studied the correlation between the gear teeth overheating and lubricant film breakdown. The study found that the mean and maximum flank temperatures depended mainly on the “Biot” number (the relation between heat conduction and transfer resistance) and the number of teeth. Yi and Quinonez (2005) used thermocouple to measure gear surface temperatures at different locations along the gear tooth flank. The highest temperature occurred at the dedendum due to the “*windage*” effect produced by rotating speed of the gear. In addition, the surface area was larger at the tip circle for heat dissipation than that at the root circle.

The local contact temperature mainly affects the gear material microstructures, lubricant viscosity and additives conditions. Consequently, high temperature leads to reduce the lubricant viscosity and the lubricant film thickness which leads to possible contact of

roughness asperities. Thus, the probability of micropitting increases due to high contact temperature as the lubricant film thickness is correlated with the sliding parameter and contact temperature as explained in Section 2.7.5. Low lubricant viscosity can lead to micropitting, scuffing and other failure modes especially in low pitch line velocity and high load conditions (Errichello and Muller, 1994). As explained in Section 2.7.2 and found by Seireg (2001) the pits are shallower at high operational speed. This may be owing to the short transit time during gear pair meshing at high rotational speed. Therefore, shallow and small pits occur at higher speed due to low heat depth penetration below the contact zone.

### **2.7.5 Lubricant Film Thickness**

Several studies investigated how the lubricant film thickness influences micropitting on different contact surfaces and under different working conditions. Crook (1957), Dowson and Higginson (1959), Dowson and Toyoda (1978) and Johnson (1985) had some pioneering work in the simulation and development of the numerical solution to the Elastohydrodynamic lubrication (EHL) problem. Crook (1957) investigated the influence of film thickness on roller contact with the consideration of thermal effect, contact stress, rolling and sliding contact. This early work on the EHL laid the foundations for subsequently rigorous research development, which have taken place in the last 20 years in the field of EHL in relevance to gear working conditions. Later, Dawson (1962) carried out one of the early work on pitting and found that its behaviour was influenced by the ratio of the oil film thickness and the surface roughness. In addition to studies focusing on the role of lubricant film thickness in preventing micropitting, considerable research revealed that the factors influencing micropitting include gear tooth flank contact temperature (more details are provided in Chapter 4, Section 4.2.6).

The lubrication film thickness largely depends on load and speed conditions. If the lubricating film is too thin the gear tooth flanks rub against each other leading to micropitting on the gear contact surfaces. These are documented in the International Standards and Technical Reports, ISO/TR15144-1 (2010), ISO 10825 (1995) and BS 7848 (1996). Holmes et al (2005) used a transient analysis method to analyse lubricant film thickness in elliptical point contact, in a transverse direction. One of their key results was that the lowest film thickness occurred because of surface valleys, which

helped the lubricant oil to escape between the contact surfaces in the transverse direction. Zhu and Wang (2013) used different types of contact geometry and three types of contact surfaces which were transverse, longitudinal and isotropic, for the purpose of exploring the impact of roughness on EHL film thickness. One of their results obtained by numerical simulation was that the film thickness was greater in the longitudinal roughness, when the elliptical ratio was smaller than one, than in transverse and isotropic. When this ratio was greater than one, the film thickness was smaller compared with transverse and isotropic roughness.

Gear tooth flank pitting is characterised by a continuous deterioration of the contacting surfaces under rolling and sliding conditions and it can occur regardless if lubrication is used or not as the function of EHL film does not prevent surfaces from cyclic stressing, as explained earlier in Section 2.5. As a result, pitting life is affected by the EHL film thickness (Ku, 1974). Zhu et al (2008) developed stress-based pitting life prediction approach using 3-D line contact mixed Elastohydrodynamic lubrication (EHL). Fifteen sets of gears were analysed and the prediction results were compared with previous experimental data. The authors found that the predicted pitting life results match the test data.

Antoine and Besson (2002) proposed a micropitting calculation model in order to compare the results of calculations with the experimental observation on discs and gears of a planetary train of a helicopter. The model considered the contact stress, roughness, plastic effect of roughness and oil film thickness. The model results and experimental observation were in good agreement. Different materials, case hardening and surface finishing were studied and one of their important results was that the carburised ring gear was more prone to micropitting compared with other parts of planetary gears. The authors' model results were limited to one contact point which was the pitch point where the pure rolling and zero sliding velocity occur. In addition, the temperature was not considered in their model.

## **2.8 EXPERIMENTAL STUDIES OF MICROPITTING**

Gear tooth flank micropitting is characterised by continuous deterioration due to various operational and contact conditions. Owing to these conditions, gear material surface and subsurface microstructure may change with the occurrence of micropitting due to high

localised contact stress, high sliding, high local temperature and metal to metal contact. Many experimental procedures were used to investigate the micropitting capacity under variable torque levels, different surface treatments, different types of surface finishing and different lubricant conditions. Other research studied the influence of other parameters such as gear profile modification and material microstructure. The following sections shed light on prior research addressing the most investigated parameters.

### **2.8.1 Effects of Lubrication and Varying Loading Conditions**

Different research addressed how the lubrication and loading conditions influence micropitting. In relation to lubrication, research has investigated aspects such as lubricants temperatures, lubricant film thickness and different pitch line velocities. Other research studied the combined influence of lubrication condition and load levels on micropitting. Hohn and Michaelis (2004) tested different lubricants at different oil temperatures, and found that higher levels of micropitting was related to high contact stress and oil temperature as thin lubricant film thickness and low viscosity took place at high oil temperature. The authors suggested that pitting life decreased at high oil temperature. However, their study was restricted to low pitch line velocities (0.05 m/s) and a high oil inlet temperature of 120°C. A higher pitch line velocity (46.5 m/s) was investigated by Townsend and Shimski (1995). They used different lubricant additives but at a lower temperature of 49°C to investigate the effects of specific lubricant film thickness and lubricant viscosity on gear failure life. The different lubricants with different viscosities resulted in specific lubricant film thickness less than one at pitch line. Furthermore, the authors found that when using the lubricant with additives package the gears lives were 4 to 8.6 times longer than when using only the lubricant with viscosity without additives. In this case, the specific film thickness at pitch line is greater than one and the gears surface fatigue lives improved when the lubricant viscosity was increased. The influence of different lubricants on wear of gears under slow speed conditions (0.05 and 0.57 m/s pitch line velocity) was investigated by Hoehn et al (2012). The authors used FZG back-to-back test rig at two different lubricant temperatures of 90°C and 120°C. Some of the tested lubricants show that the wear rates were reduced at higher lubricant temperature while others had no influence. This is owing to the lubricant viscosity, type of oil and additives which reacted to the high temperature and resulted in wear reduction at certain conditions. Lainé et al (2008) experimentally tested carburised steel rollers. One of the main findings was that the

micropitting was influenced by the lubricant film thickness and surface roughness. The micropitting may be exacerbated by the use of different types of anti-additives.

Brechot et al (2000) tested case hardened gears by using gear rig tests at different load levels. The main goal of these tests was to detect the occurrence of micropitting with different industrial lubricant oil samples. One of their conclusions was that an improved performance of new mineral oil against micropitting and wear was observed. A FZG test rig was used by Zhang et al (2014) to investigate the contact fatigue characteristics of spur gear made from 20MnCr5 alloy steel under different load levels. The authors' found that the pitting and spalling occurred at the dedendum area in the pinion gear due to the severe load and lubricants that accelerated the pitting crack. The influences of gear tooth surface roughness, contact temperature and sliding parameter were not considered in this study.

Li and Kahraman (2011) developed a high-cycle fatigue methodology for point contacts under mixed EHL condition to predict the pitting crack nucleation and quantify its position. To validate the model they used a set of rolling contact fatigue experiments to prove the cycles to pitting failure and to test their agreement with the predictions of the model. The results of the experiments revealed a good agreement between the model prediction and the actual results. When the oil inlet temperature was reduced from 90 to 60°C at four different loading levels, the crack nucleation fatigue lives of the roller specimens were more than double. This result is primarily and directly attributed to the increase of the lubricant kinematic viscosity from 6.61 to 15.39 mm<sup>2</sup>/s. This increase had a positive impact on the lubrication conditions. Through experiments, McDuling, (1996, cited in Fernandes and McDuling, 1997) showed how a lever hoist driving gear of 1.5 ton produced severe pitting in the dedendum, where the direction of rolling and sliding was opposite at the point of single tooth contact, after only 500 cycles under test conditions. The contact fatigue damage became smaller by maintaining the correct lubrication condition.

Using a different approach, a FZG test rig was used for spur gear pitting experimental test (Glodež, 1995 cited in Abersek and Flasker, 2004). Four tests were conducted using a back-to-back gear test rig with a new dip lubrication of the same type for each test. Gears were inspected during tests for any pitting occurrence. When pits in gear tooth were observed, the test was stopped when the pits reached the size of 0.5 mm and the numbers of loading cycles were recorded. In the four tests the average number of

loading cycles which were required for the occurrence of pitting on gear tooth were  $3.447 \times 10^6$  cycles. The author compared the numerical estimated cycles for pitting occurrences using lognormal distribution and experiment results of load cycles with 90% probability. The numeric results of load cycles were in good agreement with their estimations. However, the surface roughness, where the initial pitting normally occurs and the effect of lubricant film thickness are not addressed in this study.

The progression of micropitting on gears increases under higher contact stresses. Surface high contact stress, dynamic load and profile deviation are operational conditions related to micropitting which may lead to macropitting and scuffing gear failures (Glodez et al, 1998). Generally the dedendum area is the prime target of material loss due to many stress cycles at the microscopic level and because the curvature radius is smaller at the dedendum surface (more details are explained in Section 2.5). Düzcükoglu and Imrek (2008) reduced the high load at the single tooth contact area which resulted in an increase in service life through making tooth width modification  $f/b$  (force to gear width); wider in pitch area at the single tooth meshing region, thereby decreasing the Hertzian surface contact stress. Their experiment aimed to delay the pitting failure and increase service life by keeping  $f/b$  constant through increasing the width proportionally according to the load applied. The results showed that the initial pitting was delayed in the modified gears but later occurred in most tooth flanks, while in the unmodified gears pitting occurred earlier than modified gears and pitting only appeared on the dedendum area.

### **2.8.2 Effects of Surface Treatment and Surface Finish**

Because micropitting is commonly a surface failure, the surface features including treatment and finishing were targeted with considerable research. Moorthy and Shaw (2012) experimentally tested helical gears with different coating compared with as-ground (uncoated) gears, using a back-to-back test rig. The authors studied the micropitting progression and profile deviation at different load levels and cycle numbers. It was found that two types of coated gears (Nb-S and Balinit C), out of five studied, were more resistant to micropitting and profile deviation. The micropitting and greater profile deviation of the gear tooth occurred at the dedendum area. Zhang and Shaw (2011) used a back-to-back gear test rig to investigate two pairs of spur gears made from the same material, but with a different surface finish. One pair was grounded

and the other pair was superfinished, and the authors concluded that the superfinished gear performed better against micropitting and tooth profile deviation. The superfinishing process, achieved by chemically accelerated vibratory finishing, produces a surface roughness value to or less than  $0.1 \mu\text{m}$  (Arvin et al, 2002). After the gears are put into a vibratory machine, millions of cycles are applied with the active chemistry until the desired surface finish is achieved using non-abrasive finishing media.

Zhang (2005) used standard gears for gear experiments. The gear materials used for the experiment were through hardened 16MnCr5, case carburised 16MnCr5 and 17CrNiM06. Many surface finish treatment types for gear materials were used. Some examples are: grinding and superfinishing, shot peening and re-grinding. The author found that superfinished gears were most resistance to micropitting under certain operating cycle numbers and loading conditions. However, the wear in superfinished gears was more visible because of the very smooth surface finish. Gear tests showed that after about  $5 \times 10^6$  running cycles the micropitting occurred on every tooth of ground and shot peened gears. Micropitting occurred in the dedendum more than the addendum. After increasing the number of cycles at around  $3 \times 10^7$  cycles under  $1860 \text{ N/mm}^2$  of stress, micropits started to spread out in both the addendum and dedendum until the pits met at the pitch line of superfinished surface gears. However, macropitting rarely occurred at the pitch line position. Brandão et al (2010) presented a numerical model compared with a FZG testing of the meshing gear surface-initiated damage to predict the micropitting and gear tooth wear loss. The predictions and measurement of wear losses were correlated, but the surface roughness results did not compare well.

Evans et al (2013) analysed micro-Elastohydrodynamic lubrication of two helical gears sets (A and B) to investigate the gear micropitting, using a gear test rig and subsurface predicted damage accumulation analysis. The two sets of gears were only different in the tooth surface finishing processes; one set (A) was finished by generation-grinding process, and the other by form-grinding. Some of the significant key results were that set A was more prone to micropitting in the addendum, but progressively in the dedendum of the tooth flanks. According to the gear test result, the micropitting in set A had more profile deviation than that of set B. However, set B was more likely to be damaged, according to contours of the subsurface damage prediction analysis. Muraro et al (2012) experimented with spur gears of two different surface finishes, shaving and milling, to observe the wear mechanism. Two torque levels were implemented in their

tests and the main findings obtained showed gear flank wear, based on the calculated lubricant film thickness. The wear was lower for the shaved gears due to the impact of the lubricant film thickness. Wear and pitting occurred in the dedendum area of the milled gear, and abrasive wear occurred in the addendum. Predki et al (2011) investigated micropitting on big spur gears with profile modification. Some of their key findings were that higher surface roughness was related to wider micropitting zone, and the micropitting was influenced greatly by the amount of tip relief. The micropitting in the dedendum of pinion gear prevailed and the lower surface roughness resulted in a narrower micropitting area. The affected gear surface was the main cause for the micropitting spreading on the gear flank, since the original involute profile was gradually lost. Case hardening techniques such as case carburised gears with superfinished treatment can prevent, to some extent, both micropitting and macropitting. These techniques have been successfully used for UK marine gearing since 1960 (Gowans and Porter, 1970). The ISO 6336 (2003), part 5 provides various gear materials properties with different types, qualities and hardness that can be relied on.

Khan et al (2009) compared ISO 6336-2 (2006) standard with test experiments for wear mechanism to predict the lifetime of helical gear. Two pairs of case hardened low-carbon steel gears were tested at two different loading conditions. Back-to-back testing rig and PODS (Portable Oil Diagnostic System) for oil sampling machines were used. Oil samples were taken after a certain operation time for both tests. Wear intensity and wear rate during gear operation reached maximum values at  $5.4 \times 10^5$  and  $1.08 \times 10^6$  cycles for tests 1 and 2 respectively. The authors found that the mathematical formula of ISO 6336-2 standard can be used to predict the lifetime of helical gear.

Residual stress was compared in gear tooth depth profiles for shot peened gears, reground gears and superfinished gears by Zhang (2005). The results showed that all profiles had shown similar patterns of the residual stress. The author reported that the value of compressive residual stress reached a maximum value at the position of 200 microns under the tooth surface by using the peening treatment. This depth could be related to the depth of the maximum shear stress. It was found that shot peened gears had a greater tendency to macropitting failure. These had endurance of less than  $2.5 \times 10^6$  cycles, whereas the surface fatigue lives were more than  $4.2 \times 10^6$  cycles for normally ground gears. The shot peening process might have reduced the micropitting propagation and surface fatigue of small sized gears. Reground and shot peened gears

shared the same pattern of macropitting development as normal ground gears. The regrinding process indicated that the surface fatigue strength of gears is influenced by surface roughness. The superfinished gear tests showed that no gear failure occurred until  $5 \times 10^6$  cycles. The superfinished gears can reduce friction, pitting fatigue and wear. This surface treatment method allows gears to endure more numbers of cycles compared with gears with other surface treatments. Surface durability of Sursulf-treated (*sulphur-accelerated salt bath treatment*) and untreated gears loaded at different torque levels was tested using a back-to-back gear test rig by Krishnamurthy and Rao (1987). The treated gear surface endured higher contact stresses and had a longer service life than that of untreated gears.

### 2.8.3 Effects of Material Microstructures and Other Related Factors

Several studies investigated the microstructure of the gear material and how the plastic deformation occurs. An interesting experimental work done by Oila and Bull (2005) related to micropitting initiation and propagation considered material microstructural behaviour on discs. Some features observed in tested discs were: the plastic deformation region (PDR), the dark etching region (DER) and the white etching band (WEB). The boundaries of PDR positioned under roughness peaks are the site where the cracks are more likely to occur or initiate due to high plastic deformation and the DER and WEB occurred due to martensite decay. Figure 2.21 shows an illustration of how the crack of micropitting initiated opposite of the sliding direction between the DER and PDR; similar results were obtained by Errichello (2012). Oila (2003) found that the martensite decay can occur in gears and discs that are subjected to rolling and sliding contact.

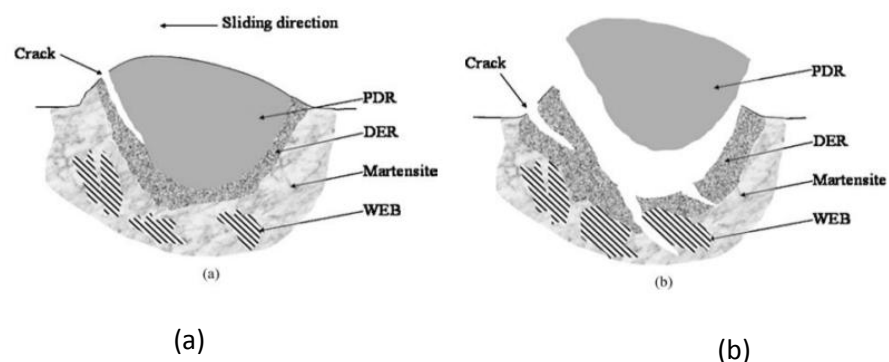


**Figure 2.21: Schematic of crack of (a) micropitting initiation and (b) propagation mechanism according to Oila and Bull (2005)**

Fernandes and McDuling (1997) found that the contact fatigue damage caused plastic deformation to the surface material, either by rolling only or by combined sliding and

rolling action. Contact fatigue damage became smaller through maintaining three conditions: using the correct lubrication condition, surface hardness should be greater than HRC 60 and austenite should be fixed at level of 10-20%. If austenite is greater than 30% it can reduce micropitting resistance due to reducing material strength, compressive residual stress and hardness in carburised gears (Errichello, 2012). An Austenite or gamma phase iron layer up to 20% in the tooth can reduce the contact fatigue.

Pitting in helical gear may start at one point, and continues upwards and outwards along the tooth profile to form a feature known as the “cyclone” effect. In gears with a case hardened layer consisting of hardened steel with little or no maintained austenite, micropitting forms a microstructural feature called butterfly wings. *“These are formed when plastic deformation is constrained by the surrounding material and is more common when shear stresses are extremely high”* (Alban, 1985 cited in Fernandes and McDuling, 1997, p. 101). The butterfly wings and DER have the same microstructures and similar hardness. These were assessed by Oila and Bull (2005) using nanoindentation to measure microstructures properties and microindentation technique to monitor the test surface hardness. A similar study was conducted by Evans (2103) to test WT gearbox bearings using roller machines under different loading conditions. The author investigated the propagation of the butterfly crack in a form of white etching cracks. The butterfly crack propagation was analysed to understand how material microstructure changes. Oila and Bull (2005) investigated micropitting experimentally, using a two-disc machine and two different lubricant oils. One of their important conclusions was that the plastic deformation boundaries were preferred regions for micropitting initiation. It can be concluded that more research is needed on the microstructure behaviour and response of gear material during rolling/sliding contact.

#### **2.8.4 Effects of Sliding and Crack Characteristics**

The influence of sliding action and the development of cracks received considerable research. Different studies focused on slide-to-roll ratio and crack growth on gear tooth flank using different approaches such as tooth profile modification and tooth surface inspection. Errichello (2012) showed that cracks of micropitting initiated opposite to the sliding direction (negative sliding) at the gear tooth flank. This accelerated the cracks to develop because of the hydraulic pressure mechanism which forced the lubricant oil to

move into surface crack. When meshing at the pitch line tooth flanks experience pure rolling thus zero sliding velocity; however, the amount of relative sliding increases on gear tooth as the meshing point moves away from the pitch line contact. Therefore, micropitting is most likely to occur at tooth flank located away from the pitch line where sliding exists and it is more prone to micropitting when no tooth profile modifications are used. Glodez et al (1998) investigated the load effect on the tooth along the gear tooth width. The authors used a testing device to measure the growth of fatigue crack in the tooth root of gears. Two types of load distribution were applied, uniform load distribution along the whole tooth width (case 1) and half-side load distribution along half width of the tooth (case 2), as shown in Figure 2.22. The experimental results revealed that case 2 had a faster crack growth and shorter service life than case 1 and the fracture planes in the tooth for both cases were different, symmetrical for case 1 and non-symmetrical for case 2. This test showed the relationship between one of the operational conditions (load) and crack propagation.

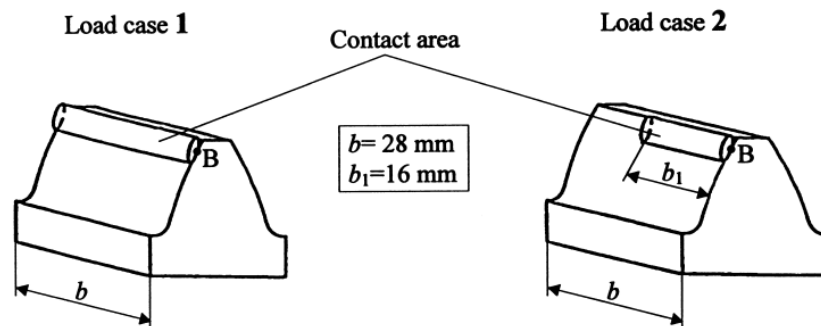


*Figure 2.22: Two different distributions of load cases along the width of tooth (Glodež et al, 1998)*

Zhang (2005) described the initiation and growth of shell-shaped pits in through hardened gears. He found that they normally initiate from a small crack beneath the tooth contact surface and later they grow along the rolling direction. They start to propagate towards the tooth surface from shallow angle of 5-10 degrees and grow to a sharp angle of 30-60 degrees to the contact surface. Then the cracks grow outwards at a sharp angle until they reach the contact surface. At the final phase, a shell-shaped pit is formed after a small piece of material breaks off. Although in his experiments the author indicated that the diameters of these shells vary from 0.1mm to 2mm, he did not address the depth of these shells.

Way and others (cited in Dudley, 1994), pointed out how these surface cracks propagated due to the trapping of lubricant oil inside the surface cracks. Based on his

work of using pinion as driver, Way found that the oil trapping occurred on the driver dedendum but not on the addendum due to the highest Hertz contact stress occurring on the pinion dedendum. Back to back test rig was used by Bull et al (1999) to study microcracks using carburised gears. These microcracks were found to incline at an angle between 35 and 55 degrees with a depth varying between 3 and 8  $\mu\text{m}$  below the tooth contact surface.

Experiments conducted by Webster and Norbart (1995) used different test rigs with roller specimens to investigate micropitting. The authors found that the minimum lubricant film thickness occurred when both load and sliding were high and resulted in the increasing rate of micropitting. The high slide-to-roll ratio play a significant role in the increase of the micropitting wear rate. The micropitting is almost eliminated at low slide-to-roll ratio. Over many years of observations, Seireg (2001) concluded that the micropitting occurs in the dedendum area where the negative sliding exists. Errichello (2012) showed a typical profile deviation of a gear tooth flank of WT high speed shaft (HSS) pinion and a number of examples of WT gears due to micropitting. In his study, the author compared active and inactive gear flank profiles of the same gear and found that the inactive flank showed a high accuracy of the flank profile. However, the active gear flank profile deviates from root to tip as a result of severe micropitting.

Winkelmann (2011) showed that the most common type of micropitting was wear and it occurred mostly in the dedendum. Tests conducted by Dudley (1994) used helical gear and pinion of medium hardness with a ratio ranging from 4 to 1. It was found that sliding action is worst on the driving gear due to its bigger size and the fact that this gear pits first. Kleemola and Lehtovaara (2009) developed a twin-disc test device to investigate three different parameters of gear tooth contact along the line of action. These were friction coefficient, temperature and lubrication conditions. Their results showed that higher sliding led to a higher temperature increase and lower film thickness. The highest temperature occurred at the tip and root of the tooth flank, with risks of failures, such as scuffing and pitting. The lowest temperature was observed at the pitch point.

## **2.9 SUMMARY**

Presented in this literature review are many noteworthy contributions that have been made as a result of the WT gearbox research which has been published by leading

researchers in national and international sources over the past few decades. The above literature review showed that the surface pitting occurs in all types of surface treatments, lubrications, materials and different operational conditions which all make an important contribution to gear micropitting failure. Frequently the occurrence and spreading out of micropitting failure vary according to the transmitted loads and speed conditions. The size of micropits is affected by different factors such as different gear materials and microstructures, operational conditions, surface treatment, gear surface roughness and lubrication type and tooth contact temperature. The above review revealed that even though different types of gear materials, surface treatment techniques, surface finishing were used, micropitting and other failure modes were still observed after a certain numbers of cycles when subjected to different levels of load. Micropitting is associated with different characteristics such as microcracks, micropits and martensite decay and occurs with all surface heat treatments types.

Due to the inconclusive results of previous research, the micropitting failure and its causes need further investigation and analysis. Until now, there is no international standard available in the area of preventing micropitting that includes all the parameters that influence micropitting. Different experimental methods such as FZG gear rig test had been used by different researchers to test failure of gears. These experiments are costly, time consuming and fall short of covering all parameters that can cause micropitting. Accordingly, analytical procedure may offer more practical, cost-effective and alternative methods to investigate the different parameters and aspects of micropitting. Thus, experimental methods can be used to validate the results of analytical procedure to build a database of verified results.

Despite the large number of previous studies on micropitting, covering the different aspects such as lubricant types and material microstructures, the micropitting initiation during gear contact scenarios requires further research. Limited research was reported in the area of investigating micropitting through varying load and rotational speed conditions. Hence, there remains a gap in the literature in covering different loads and speed conditions by using real data that represents real life operating conditions. Accordingly, the primary goal of this study is to develop a multi-approach methodology (experimental, probabilistic and analytical) to analyse and investigate a number of parameters that significantly influence the gear flank micropitting. These experimental analytical and probabilistic modelling procedures are described in Chapters 3, 4 and 5.

## ***Chapter 3: Experimental Study of Micropitting***

---

*As detailed in the literature review in Chapter 2, the micropitting failure occurs under various operational conditions for gears with different surface treatments. This research investigates micropitting under varying rotational speed and torque conditions by employing analytical and experimental approaches. While the analytical work focuses on varying both shaft rotational speed and torque, the experimental test considers varying torque levels only due to the limitation of the gear test rig available. Specifically, the test procedure is designed to investigate the initiation and progression of micropitting under varying torque conditions after operating a certain number of cycles. In this chapter, the experimental test rig set-up, test rig specifications and test-run matrix used to investigate micropitting on the tooth flank of helical pinion gear are presented. Three different surface inspection methods of gear tooth flanks are explained and the inspection devices used in the experiment are outlined.*

### 3.1 BACK TO BACK GEAR TEST RIG

The micropitting experiment is carried out using a back-to-back gear test rig in the Design Unit of the University of Newcastle. Using the 160 mm back-to-back gear test rig, different levels of loading are applied to observe micropitting initiation and progression in gear teeth. The test rig is capable of testing two sets of identical gear sets with equal gear ratios.

Two pairs of gears are manufactured, case carburised and surface-finished in the Design Unit to perform this experiment. The schematic layout of the gear test rig is shown in Figure 3.1. Two gearboxes (A and B sets) are connected back-to-back by a flexible elastic shaft to isolate gears from any vibration and prevent them from affecting each other. Torque is applied through a van-type hydraulic torque actuator and transmitted through the shafts to the meshing gear sets A and B. The torque actuator is used in the test rig to enable the torque to be applied gradually while the rig is running and to be maintained using a close electric/hydraulic loop control mechanism. The micropitting experiment is conducted using this test rig designed based on a recirculating power loop principle, which provides a desired amount of fixed torque level through the tested gears, only consuming a small amount of power to drive them. Due to rig friction during operation, about 2% of the total power in circulation is considered to compensate against the friction loss. The maximum power that the test rig can circulate between two gearboxes of the test rig can reach up to 2800 kW, and the rotational speed and torque of rig can be controlled from zero to 4500 rpm and from zero to 6000 Nm, respectively.

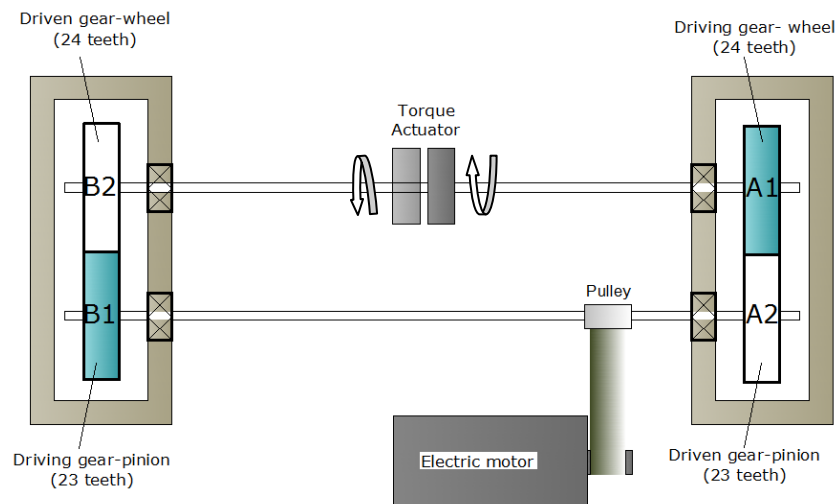


*Figure 3.1: Schematic of back-to-back gear test rig layout*

The back-to-back test rig can test the spur and helical gears with a centre distance of tested gearboxes of 160 mm. The same gear ratio for both gear sets is used with a varying gear module between 4 and 10 mm. The test rig has been equipped with many electrical motors for different purposes. One motor is used to recycle and maintain the lubricant temperature, and another is used to lubricate the test gears with a double-oil jet (50% of lubrication upwards and 50% downwards), directed at the mesh location of gear teeth. Figure 3.3 shows the back-to-back gear test rig used in this study, with helical tested gear sets A and B installed.

In the experiment, the test rig is controlled by software installed on the control computer, as shown in Figure 3.2, to control the lubricant inlet temperature, torque levels, rotational speed and to monitor vibration levels. If any of these test conditions exceeds above or falls below the user-defined limits the system will shut down for the safety and to preserve the planned conditions of test run.

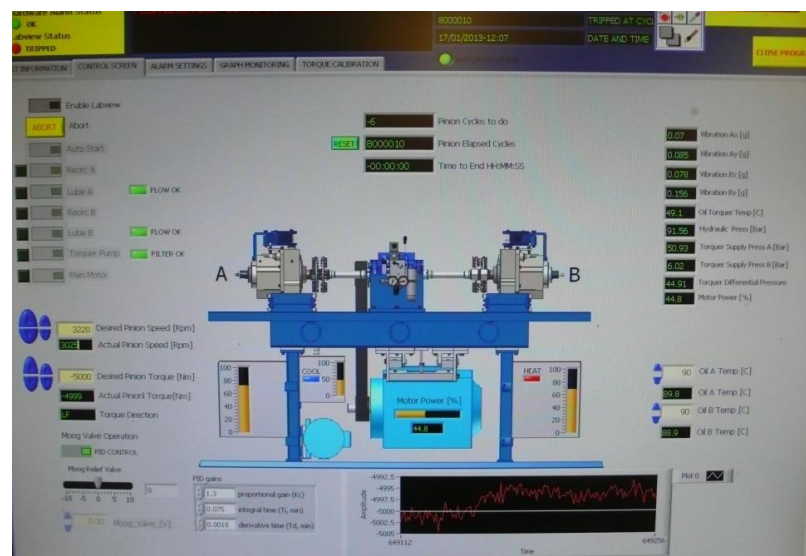


*Figure 3.2: Control screen of the test rig computer*

The tested gear sets that are used for this study are designed and manufactured in Design Unit (Newcastle University). The inspection of tested gears using different machines such as surface roughness measurements and gear profile measurements are carried out by the candidate with the help of technicians from the materials and metrology laboratories of the Design Unit. In addition, the candidate performed the tooth surface replica injection, analysis of the replica optical images and digital images as well as carrying out the analytical procedures.

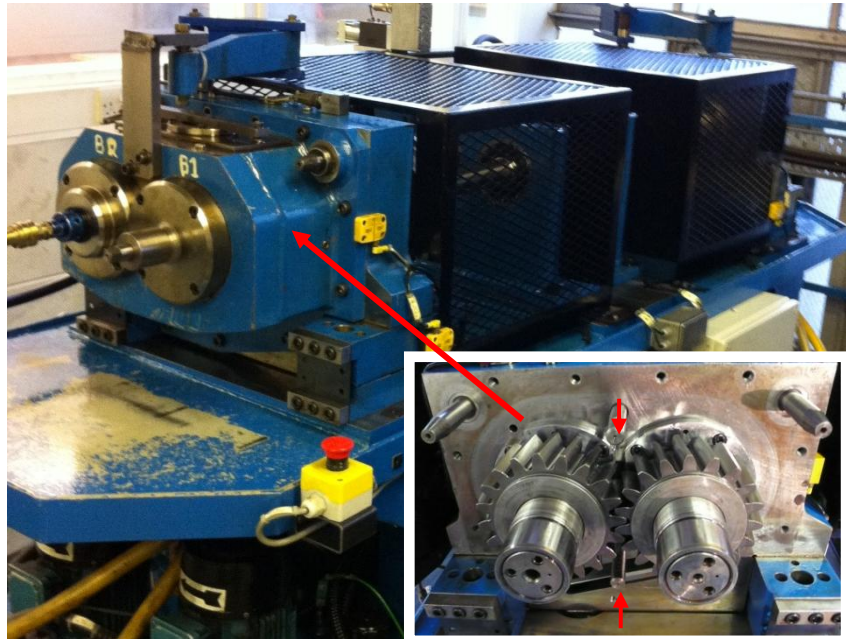


*Figure 3.3: Back-to-back test rig facility at Design Unit, the Newcastle University*

## 3.2 EXPERIMENTAL EQUIPMENT AND DEVICES

The most direct method to investigate the gear micropitting is to use gear test rigs with gear test samples. Although the use of a test rig is very expensive and time-consuming, it is the most appropriate method to investigate the initiation and progression of micropitting. Various equipment and devices are used to prepare gear test samples to perform the test and to inspect the tested samples. The manufacturing equipment and testing devices used for preparing and analysing gear samples are outlined below.

### 3.2.1 Gear Surface Finishing Machine

The helical gears samples were manufactured using the hobbing process followed by the heat treatment process, involving case carburising, hardening and tempering. The grinder machine used for the grinding process of the two gear pairs is the HOLROYD GTG2 (Gear and Tread Grinding machine), as shown in Figure 3.4. The grinding machining process is used to finish the gear tooth flanks of the two gear pairs, with a specific tooth geometrical profile of linear tip relief and symmetrical lead crowning. The machine automatic control is used to programme the entire grinding, loading and unloading process according to the parameters of the tested gears.



*Figure 3.4: Photograph of surface finish machine*

### **3.2.2 Taylor Hobson Form Talysurf 50e Instrument**

Measurement of surface roughness is conducted using a Taylor Hobson Form Talysurf 50e Instrument as shown in Figure 3.5. The surface features of the gear tooth flanks can be measured using a stylus with a  $2\ \mu\text{m}$  radius. The cut off length is 0.8 mm. Half of the cut off length is neglected from each side of measurement as shown in Figure 3.6. This is to ensure the consistency and accuracy of net measurement results. The net measurement of surface texture data is 3.2 mm long in the radial direction on the gear flank. More details of measurement results are provided in Section 3.4.1 of this chapter.

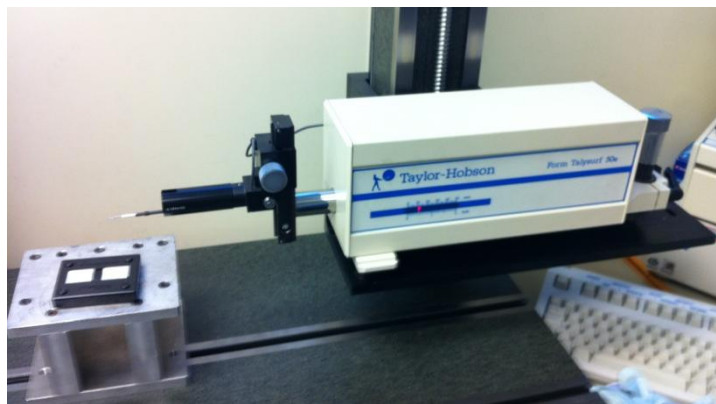


*Figure 3.5: Taylor Hobson instrument*

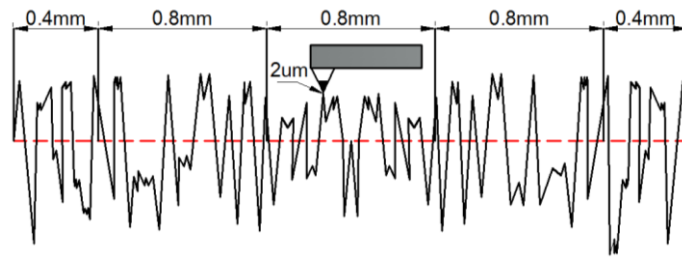


*Figure 3.6: Numbers of cut-off of the surface roughness measurement*

### 3.2.3 Hofler EMZ632 CNC Gear Measuring Instrument

A profile deviation inspection is performed to check the profile deviation of both the pinion and wheel gear after the progression of the micropitting at the end of running cycles of the final load. The Hofler EMZ632 CNC Gear-Measuring Instrument is used to check the relation between the original tooth profile and the amount of the profile deviation due to micropitting. This profile-measuring machine can measure a gear module between 0.5 and 20 mm. The machine can be used for gears with the maximum wheel diameter of 630 mm and width of 500 mm. Figure 3.7 shows the Hofler EMZ632 CNC profile-measuring machine with the inset photo showing the tested driver gear fixed on the rotary table.



*Figure 3.7: Hofler machine and tested gear (inset)*

### 3.2.3 Nikon LV150 and SMZ1500 Microscopes

Two microscopes, — namely Nikon LV150 and Nikon SMZ1500 — in the Metallurgy Laboratory at the University of Newcastle, are used to carry out gear surface inspection and micro-geometry measurements by using different focusing lens. These microscopes are used to obtain details of the micropit development by inspecting the full image of tooth flank, a detailed view of micropitting zone by injecting a replication medium onto the tooth flank. Nikon LV150 is used to observe micropits with a detail-focused view, while Nikon SMZ1500 is used to produce the full image of the driving gear tooth flank. Figure 3.8 shows the Nikon SMZ1500 microscope, with the inset photo showing the replica samples of driver gear tooth number 1, produced after completing the required running cycles under different load levels.

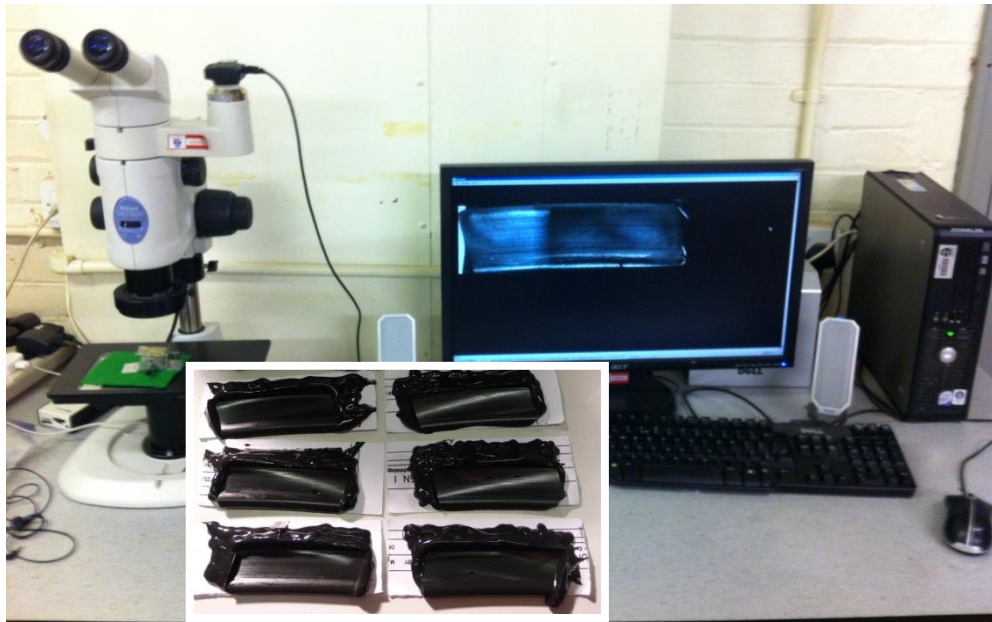


*Figure 3.8: Photograph of microscopic analysis and tooth flank replica optical image (inset)*

## 3.3 EXPERIMENTAL TEST PROCEDURE

The experimental test methods and details of testing gear parameters are outlined in the following sections.

### 3.3.1 Test Procedure

One pair of gears is used to investigate the development of micropitting. The experiment is conducted under a varying torque condition, from low load to high load levels, to determine at which torque level the micropitting occurs and propagates. The

same gears are used to inspect the micropitting initiation and progression after being tested at different torque levels. At each torque level the test runs nonstop for 8 million cycles. The surface inspection procedures, such as surface roughness measurement, replica sample analysis and profile scanning are used on the tested pinion gear to observe the micropitting after each cycle run at a certain torque level. These replicas are used to observe the change of the gear tooth flank after each loading stage. After replicas are extracted, the two microscopes are used to inspect the initiation and progression of the micropitting after completing each cycle run under each loading level.

To compare with the experimental results of micropitting the analytical method based on Technical Report ISO/TR 15144-1 (2010) is used to predict the micropitting failure mimicking the same condition of the experimental test under varying torque levels. The details of analytical method of micropitting are provided in Chapter 4.

### 3.3.2 Gear Specimens and Heat Treatment

Chrome Nickel-Moly steel (18CrNiMo7) is used as the gear material in this experiment. This material, after being carburised and heat-treated, can achieve a high wear-resistance with surface hardness ranging from about 697 to 770 HV. The test specimens of helical gears are heat-treated with a surface hardness of 764 HV. The chemical compositions of the material of the tested gears are shown in Table 3-1.

*Table 3-1: Chemical composition (wt. %) of 18CrNiMo7*

C	Si	Mn	Ni
0.15 - 0.21	max 0.4	0.5 - 0.9	1.4 - 1.7
P	S	Cr	Mo
max 0.025	max 0.035	1.5 - 1.8	0.25 - 0.35

The geometrical parameters of helical pinion and wheel gears of set B are shown in Table 3-2. The key dimensions of the helical pinion gear are shown in Figure 3.9. A photograph of one set of the helical gears used in the test is shown in Figure 3.10.

*Table 3-2: Pinion and wheel gears parameters*

Parameters	Pinion/Driver	Wheel/Driven
Number of gear teeth	23	24
Face width	44 mm	
Pressure angle	20 degree	
Helix angle	28.1 degree	
Module	6 mm	
Centre distance	160 mm	
Pitch diameter	156.44 mm	163.24 mm
Outer diameter	168.76 mm	175.24 mm
Base diameter	144.61 mm	150.90 mm

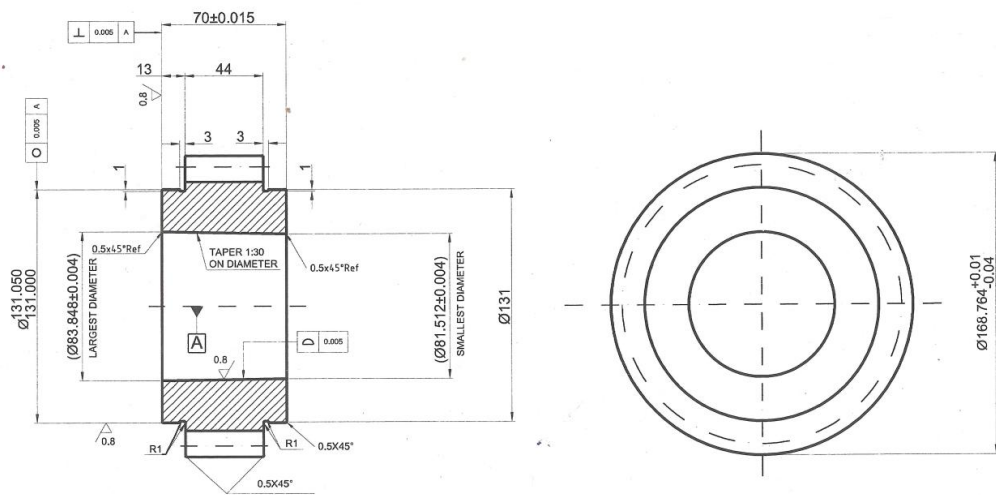


*Figure 3.9: Dimension of pinion gear*



*Figure 3.10: Helical gear set (pinion and wheel) used in the test*

### 3.3.3 Test-run Matrix

The micropitting test is started at low torque level and is increased incrementally, and at each torque level a cycle run of 8 million cycles is conducted at a constant rotational speed. For confidentiality considerations of the test programme, the varying torque values are normalised as torque ratios. Table 3-3 shows the micropitting test programme and the increment of torque ratios which is used to investigate how the gear micropitting progresses.

*Table 3-3: Torque ratios of the test programme*

Seq. No.	Cycles No. (millions)	Torque ratio
1	8	0.3
2	8	0.5
3	8	0.6
4	8	0.7
5	8	0.8
6	8	0.9
7	8	1

### 3.3.4 Lubrication System

The lubricant used in this study is mineral oil from Shell with a kinematic viscosity of 320 mm<sup>2</sup>/s at 40°C. The inlet lubricant temperature was maintained at 90°C. This type of lubricant can withstand severe operating conditions, leading to long service life, and has a high resistance to gear surface wear and scuffing (Shell, 2013). It is used in most enclosed industrial steel spur and helical gearboxes. The physical parameters of the lubricant are summarised in Table 3-4.

*Table 3-4: Lubricant data*

<b>Parameters</b>	<b>Wheel and Pinion</b>
Lubricant type	Mineral oil with additives
Oil inlet temperature	90°C
Kinematic viscosity at 100°C	26 mm <sup>2</sup> /s
Density of the lubricant at 15°C	903 kg/m <sup>3</sup>

The two gearboxes used in the experiment have two separate lubricant oil tanks. Each gearbox has a separate lubrication system. The same type of lubricant oil is used for both tanks and a filtration system is provided in the test rig to remove any debris from the system. A spray lubrication is used, which is directed to the gear tooth meshing position, at both mesh-in and mesh-out locations, across the face width of the tested gears. The double oil-jet nozzles, as indicated by arrows in the detailed gear view in Figure 3.3, have a diameter of about 3 mm to deliver high-pressure oil into the tested gear mesh. The lubricant temperature is controlled by a heat exchanger to cool the lubricant and by using recycled water to maintain the temperature range. Moreover, an electric heater is provided to heat up the lubricant to the required temperature.

### **3.4 SURFACE INSPECTION METHODS**

All teeth, for both pinion and wheel gears, are given engraved numbers, on the land area of teeth for clear identification of locations of micropitting. The driver gear is subjected to a number of inspections before the micropitting tests are performed and after each cycle run of the tested torque levels. The tooth flank surface inspection of tested gears is carried out using procedures of surface roughness measurement, a replica of surface micropits, profile deviation measurement and digital imaging of the contact surfaces, as detailed in Sections 3.4.1, 3.4.2 and 3.4.3. After each test stage, the tested gears are dismantled from the test rig, and the inspection and measurements are carried out. For the surface roughness measurement, one tooth surface of the driving gear (tooth number one) is measured before and after each load stage. The same tooth is inspected using the replica for all test stages and using profile deviation measurement at the final stage of the torque levels. The measurement of profile deviation is taken in order to specify the tooth flank deviation caused by the micropitting damage. The measurement and inspection procedures are described in details below.

### 3.4.1 Surface Roughness Measurement

Measurement of surface roughness is conducted using the Taylor Hobson instrument. The profile surface features can be seen with details such as the peaks and valleys by using the stylus instrument. These valleys and details created by the grinding process can be seen clearly along the axial direction of gears. This instrument is calibrated before surface roughness of the tested tooth flank is taken; the calibration output is shown in Appendix B. The calibration is performed to ensure that high precision of surface roughness measurement is maintained. Figure 3.11 shows the tested tooth flank of pinion gear being measured.



*Figure 3.11: Surface-roughness measurement on the Talysurf instrument*

Two parameters, the average surface roughness ( $R_a$ ); and the mean of the height of the five peaks to valley ( $R_z$ , DIN), are used to observe changes in the tooth surface roughness. Figures 3.12 and 3.13 illustrate the method in determining  $R_a$  and  $R_z$  values. Surface roughness variation of gear flanks is one of the main problems in maintaining adequate gear lubrication condition. Therefore, surface roughness of a specific pair of gear teeth is measured before and after all testing stages of the torque levels, each of which consists of 8 million cycles. This procedure is to quantify and analyse how the variation of gear surface roughness affects micropitting after each cycle run. Surface features of the gear tooth flanks after each cycle run, such as valleys and peaks, can be measured using the stylus of  $2\ \mu\text{m}$  radius as detailed in Chapter 3, Section 3.2.

The values of the tooth surface roughness, before and after each test run, are obtained and used to calculate the specific lubricant film thickness in the analytical study. The low waviness of the surface roughness measurement are not considered in the mean surface roughness ( $R_a$ ) analysis. The 0.8 mm cut off is implemented to eliminate error and distortions, and to ensure that the actual details are included in the analysis of the surface roughness measurement. The measurement is taken in the radial direction on the gear flank, close to the pitch line, as shown in Figure 3.12, over a 3.2 mm in length from the tooth dedendum to the tooth addendum direction, as explained in Section 3.2.2. The mean of 5 samples'  $R_z$  values,  $R_{zi}$ , of the peak to valley height can be calculated by:

$$R_z \text{ DIN} = \frac{1}{n_x} \sum_{i=1}^{n_x} R_{zi} \quad (3-1)$$

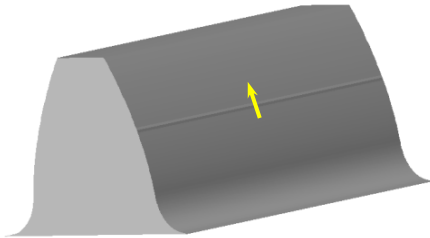


**Figure 3.12: Roughness measurement direction**

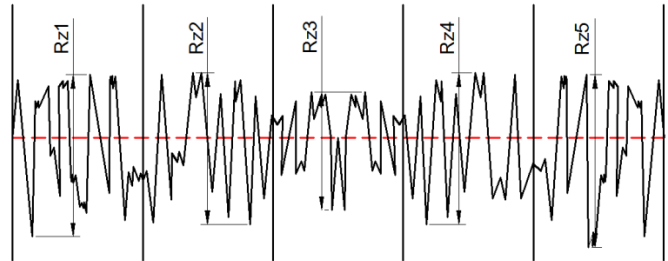


**Figure 3.13: Five samples of peak to valley height**

### 3.4.2 Replica Optical Image Analysis

In addition to the surface roughness measurements, the replicas of the pinion tooth surfaces are obtained and investigated after each test run of 8 million cycles. The replica samples for a tooth are produced by injecting a replication medium onto the tooth flank, according to the size of tooth surface, as shown in Figure 3.14. These replicas are used to observe the change of the gear tooth flank after each loading stage. Before injecting the replica, the tooth is cleaned with solvent cleaner/degreaser, and wiped with a clean piece of cloth, to remove the remaining oil and contaminants. This procedure is performed after each load level, to ensure that none of the impurities sticks to the tooth flank, in order to produce a good quality replica. After the replica is extracted, a microscope is used to inspect the initiation and progression of the micropitting after each loading stage and cycle run, as shown in Figure 3.15. The Nikon SMZ1500 stereo microscope is used to obtain details of the micropitting development of the pinion tooth

surface. Different magnifications are used to trace the progression of micropitting by amplifying the full size of the replica.



*Figure 3.14: Photographs of replica injecting*



*Figure 3.15: Microscope to inspect micropitting development*

### **3.4.3 Gear Profile Measurement**

A profile deviation inspection is performed to check the profile of both pinion and gear after the progression of the micropitting under the final torque level. The Holfler EMZ632 CNC machine is used to check the relation between original tooth profile and the amount of the profile deviation due to micropitting. Figure 3.16 shows a typical setting of Holfler machine after the helical gear parameters (number of teeth, normal pressure angle, helix angle, normal module and face width) are fed into the machine's computer. Figure 3.17 shows the measurement of profile deviation taken in the middle of the face width on the tooth flank. Profile deviations of four teeth (tooth numbers 1, 7,

13 and 19), circumferentially spaced at 90° intervals of the tested gears, are measured, and the location of deviation and the extent of difference from the original profile are obtained. The details of measurement results are presented in Chapter 6.

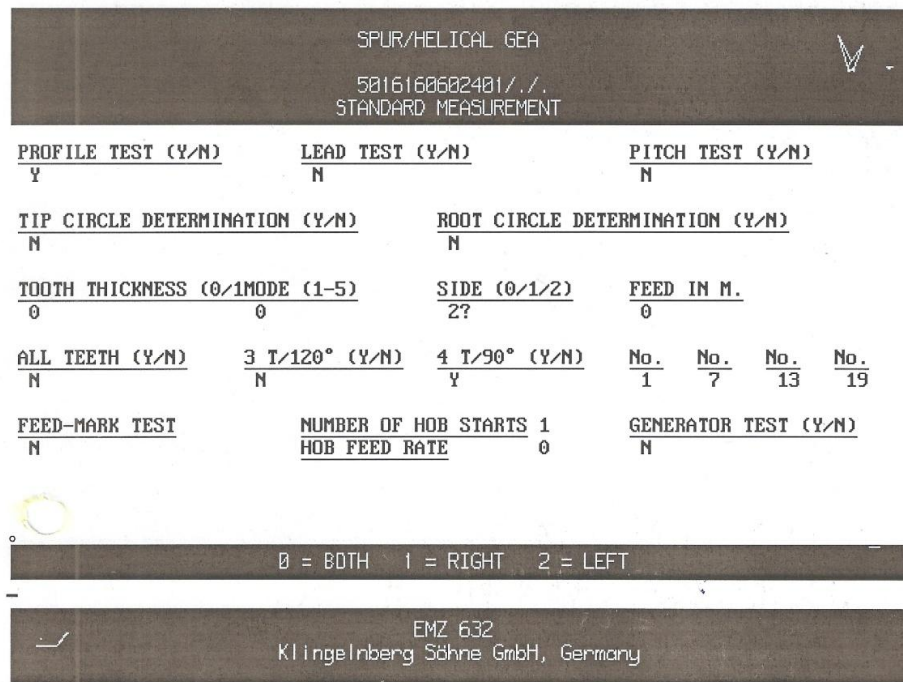


Figure 3.16: Holfler machine setting for profile deviation measurement

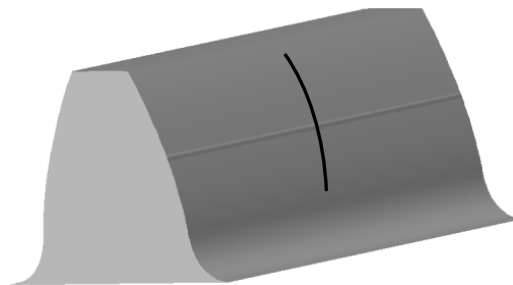


Figure 3.17: Measurement position of gear tooth profile deviation

### 3.5 SUMMARY

This chapter presents the experimental procedures employed in this research to investigate micropitting initiation and progression under different load levels. It describes the back-to-back gear test rig and its specifications as well as tested gear parameters. Three gear surface inspection methods and the equipment and devices used to analyse the micropitting are outlined. In particular, the gear surface replicas, surface

roughness measurement and microscopes at all test stages to investigate the development of the micropitting when subjected to various load levels are described. Moreover, the employment of gear tooth profile measurement instrument is discussed.

## ***Chapter 4: Analytical Models in Predicting Contact Stress, Sliding Parameter, Local Contact Temperature and Lubricant Film Thickness***

---

*In this chapter, analytical methods using various ISO standards are introduced in conjunction with the Hertz contact theory. Various methods to determine load factors, that are used to modify the Hertz contact stress, are explained. Chapter 3 presents the procedure for the investigation of micropitting through experimental testing under varying torque levels. This chapter details the analytical method and modelling procedure to determine a number of key parameters that affect micropitting of spur and helical gears. The analysis methods relating to the gear tooth profile modification, such as effective tip relief and helical gear tip relief, are described. Furthermore, the load sharing factors at different contact points along the line of action for spur and helical gears are presented.*

*Methods used to analyse the contact stress, sliding parameter, local contact temperature and lubricant film thickness at different contact points along the tooth flank are described. Drawing from the elastohydrodynamic lubrication theory the method for analysis of lubricant film thickness and the influencing parameters are outlined. The chapter concludes by presenting the development of a toolkit calculation sheet (TCS) and required key parameters based on the ISO Technical Report ISO/TR 15144-1 for gear micropitting analysis.*

## 4.1 GEAR TOOTH CONTACT STRESS ANALYSIS

In this chapter the parameters and formulas used for analysis of spur and helical gears, as defined in the ISO 6336 standards and newly published micropitting ISO Technical Report ISO/TR 15144-1 (2010), are discussed. The formulas of the contact stress and related load factors are used to analyse the cases in Chapters 6, 7 and 8 of this thesis. The micropitting analysis is applied to two gear types: spur gears that are used in the high speed shaft of a WT gearbox and helical gears that are used in experimental tests. ISO 6336 standards were first published in 1996 and then have been revised on several occasions and republished in 2006 with considerable improvements. ISO 6336 consists of the following parts:

- ❖ 6336-1:2006 Basic principles, introduction and general influence factors
- ❖ 6336-2:2006 Calculation of surface durability (pitting)
- ❖ 6336-3:2006 Calculation of tooth bending strength
- ❖ 6336-5:2003 Strength and quality of materials
- ❖ 6336-6:2006 Calculation of service life under variable load

The ISO standard denotes gear manufacturing accuracy grades ranging from 0 to 12, where 12 denotes the lowest quality gear tooth level and zero being the highest quality level, as stated in ISO 1328-1 (1995) which is also referred to as BS 436-4 (1996). The spur and helical gears of this study are a high quality grade of five. The main aspects of calculating gear contact stress with load factors with the consideration of the gear geometry are discussed in the following sections.

### 4.1.1 Hertz's Formula for Gear Contact Stress

As early as 1880, Heinrich Hertz developed analytical methods to determine cylindrical and spherical contact stresses, now known as Hertzian theory. The theory considers the contact force, the cylindrical radius of curvature and the modulus of elasticity of material. For more than 133 years Hertz's theory has contributed immensely to the area of contact stress (Hertzian stress) analysis. The theory can be used for semi or curved cylindrical surfaces which are in contact against each other; with the initial line or point of contact to be changed to an area of contact under loading, as shown in Figure 4.1. Under loading by a force,  $F$ , uniformly distributed along the cylinder's width,  $b$ , the contact area,  $2r$ , can be obtained. The half width,  $r$ , of the elliptical force distribution

can be determined by the force,  $F$ , diameter of cylinders,  $d_1$ , and,  $d_2$ , the modulus of elasticity,  $E_1$ , and,  $E_2$ , and Poisson's ratio,  $\nu_1$ , and,  $\nu_2$ , as shown in Equation 4-1.

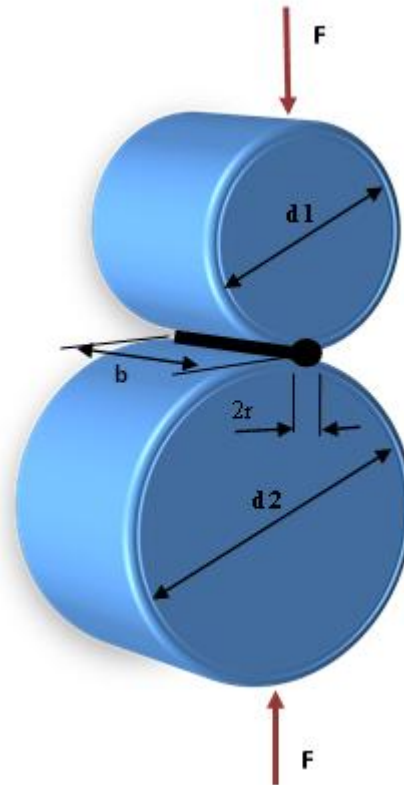


*Figure 4.1: Fundamentals of Hertz's contact stress theory*

$$r = \sqrt{\frac{2F}{\pi b} \frac{\frac{1-\nu_1^2}{E_1} + \frac{1-\nu_2^2}{E_2}}{\frac{1}{d_1} + \frac{1}{d_2}}} \quad (4-1)$$

The maximum contact stress,  $P_{max}$ , occurs at the centre of the contact area, it can be determined according to Equation 4-2.

$$P_{max} = \frac{2F}{\pi r b} \quad (4-2)$$

The gear contact stress calculation is based on the Hertzian theory. Hertzian theory has been revised by adding some load modification factors to broaden design coverage and to suit the working conditions of gears. Hertzian theory was also adopted by the newly published micropitting ISO Technical Report, ISO/TR 15144-1 (2010) to calculate the gear contact stresses along the path of contact,  $P_{dyn,Y}$ , as shown in Equation 4-3. The

modified load factors,  $K_A$ ,  $K_V$ ,  $K_{H\alpha}$ ,  $K_{H\beta}$ , and the elasticity factor,  $Z_E$ , are calculated and selected from tables according to ISO 6336-2 (2006). The total profile deviation according to the gear accuracy grades is also selected according to ISO 1328-1 (1995) standard and BS 436-4 (1996). This standard specifies appropriate definitions for the gear tooth accuracy, the allowable values of pitch deviations, total profile deviations and total helix deviations.

$$P_{dyn,Y=Z_E} = \sqrt{\frac{F_t * X_Y}{b * \rho_{t,Y} * \cos_{\alpha t} * \cos_{\beta b}}} * \sqrt{K_A * K_V * K_{H\alpha} * K_{H\beta}} \quad (4-3)$$

The load factors  $K_A$ ,  $K_V$ ,  $K_{H\beta}$  and  $K_{H\alpha}$  are largely selected based on specific physical dimensions of gears to suit the particular application. These K factors can be calculated using three methods, A, B or C, which are illustrated in ISO 6336 standards. Depending on the accuracy and reliability requirement of the application, these methods have their own advantages, in general, method A is superior to method B and method B is superior to method C. The factors in method A are derived from the results of full scale load tests and presuppose precise measurements or comprehensive mathematical analysis of the transmission system. Due to some practical issues such as incomplete details about the operating condition, unavailability of suitable measuring equipment and cost effectiveness, usage of method A is limited. In method B, the factors are derived with sufficient accuracy for most gear applications. Method C is similar to method B except that simplified approximations are specified for some factors. These K factors play a substantial role in considering the increased contact stresses of gear teeth under the realistic operational condition. These include the external dynamic loads caused by the driving and driven gears' load conditions, the internal loads caused by elastic deformation and inaccuracy of the tooth profile in manufacturing. They also consider the non-uniform load distribution over the tooth face width (ISO 6336-1, 2006).

It is worth mentioning that there are two different methods, method A and B in the ISO Technical Report of micropitting ISO/TR 15144-1 (2010) for determining the local specific lubricant film thickness,  $\lambda_{GF,Y}$ . Method A can be used by applying a load distribution programme that calculates the contact stresses on the whole tooth contact area in order to determine the specific lubricant film thickness. Method B considers the negative sliding on the tooth flank in order to determine the local specific lubricant film

thickness. This method is used in this research to calculate the local specific lubricant film thickness by developing analytical solution at different locations of the tooth flank along the line of action. These locations (A, AB, B, C, D, DE, E) correspond to the start and end of the path of contact. The start and end points depend on the start and end of the active profile of gear teeth, which is based on the pinion that is used as the driver or driven gear. Point C is the pitch point and two more points are located between the pitch point and the start and end of the path of contact, as shown in Figures 4.2 and 4.3.

### 4.1.2 Application Factor

The application factor,  $K_A$ , is determined using method B, which uses the guideline values from experience with similar machines for high speed gears and industry gears. This study uses the guidance values for the application factor in Table 4-1, as given in ISO 6336-6 (2006). The application factor,  $K_A$ , is considered to be unity (uniform loads) for the test gear experiments, based on the micropitting experiments conducted by Newcastle University Design Unit. The  $K_A$  is considered as 1.25 (light shocks) for the WT pinion gear as advised by the standard 6336-6 in consideration of wind turbine working characteristics. This factor takes into account loads additional to nominal loads,  $F_t$ , due to the variation of the input torque.

*Table 4-1: The application factor guidance values (ISO 6336-6, 2006)*

Working characteristic of driving machine	Working characteristic of driven machine			
	Uniform	Light shocks	Moderate shocks	Heavy shocks
Uniform	1,00	1,25	1,50	1,75
Light shocks	1,10	1,35	1,60	1,85
Moderate shocks	1,25	1,50	1,75	2,00
Heavy shocks	1,50	1,75	2,00	≥ 2,25

### 4.1.3 Dynamic Factor

The dynamic factor,  $K_V$ , considers the load increments due to internal dynamic effects. Method B is used to determine the dynamic factor for both the WT pinion gear and the tested gear. However, there are some constraints that should be considered when calculating the dynamic factor, such as the application and operation condition of the gears. For example, the total contact ratio has to be greater than 1 and less than or equal to 2.5. This factor is determined using different speed ranges based on the resonance ratio (N), which is defined as the ratio of the running speed to the resonance speed. The

WT dynamic factor can be determined using Equation 4-4 as advised by ISO 6336-1 for the high speed and high precision gears used in the turbine.

$$K_V = (C_{V5}B_p) + (C_{V6}B_f) + C_{V7} \quad (4-4)$$

The tested gear dynamic factor is calculated according to Equation 4-5 based on the resonance ratio provided by the Newcastle University Design Unit.

$$K_V = 1 + [N^*(C_{V1}B_p) + (C_{V2}B_f) + (C_{V3}B_k)] \quad (4-5)$$

The factors  $C_{V1}$ ,  $C_{V2}$ ,  $C_{V3}$ ,  $C_{V5}$ ,  $C_{V6}$  and  $C_{V7}$  can be calculated or obtained from the data provided in ISO 6336-1.  $C_{V1}$  and  $C_{V5}$  consider pitch deviation and  $C_{V6}$  and  $C_{V2}$  consider the effect of tooth profile deviation. The effect of tangential load, on the dynamic load which is generated by tooth bending deflections during constant speed as a result of mesh stiffness variation, is considered in  $C_{V3}$  and  $C_{V7}$ .  $B_p$ ,  $B_f$  and  $B_k$  are non-dimensional parameters which consider the effect of profile modification and tooth deviations on the dynamic load.

#### 4.1.4 Face Load and Transverse Load Factor

The face load factor,  $K_{H\beta}$ , and transverse load factor,  $K_{H\alpha}$ , consider the uneven load distribution over the gear face width and in the transverse direction respectively. This is due to shaft deflection errors, gear manufacturing errors and shaft alignment errors. The face load factor is obtained according to method C, as method B requires computer-aided calculations which depend on the stiffness of the whole elastic system, elastic deflections of gear and gear shaft under load and static displacements (ISO 6336-1, 2006). Normally these components are sufficiently stiff and their deflection can be ignored (Bergseth, 2009). Method C considers the manufacturing deviations and equivalent misalignment that assumes a similar separation of the working flank. The  $K_{H\beta}$  in method C is calculated by considering the mesh stiffness,  $C_{\gamma\beta}$ , mean load intensity across the tooth face,  $F_m/b$ , and an effective total mesh misalignment,  $F_{\beta\gamma}$ . The face load factor using method C can be calculated using Equation 4-6.

$$K_{H\beta} = 1 + \frac{C_{\gamma\beta} * F_{\beta\gamma}}{2 * F_m / b} \quad (4-6)$$

The transverse load factor is determined according to method B, there are two methods depending on the total contact ratio for WT spur gears and tested helical gears, however

they produce identical results. Method B is appropriate for all types of spur and helical gears with any gear accuracy. This method assumes that the average load distribution differs between the base pitches of the pinion and wheel gears in the meshing zone. The transverse load factor for the pair of tested helical gears has a total contact ratio of less than two and the transverse load factor is calculated using Equation 4-7.

$$K_{H\alpha} = \frac{\varepsilon_{\gamma}}{2} * \left[ 0.9 + 0.4 * \frac{C_{\gamma\alpha} * (f_{pb} - \gamma_{\alpha})}{F_{tH}/b} \right] \quad (4-7)$$

Where,  $C_{\gamma\alpha}$ , is the mean value of mesh stiffness per unit face width,  $f_{pb}$ , is the transverse base pitch deviation and,  $\gamma_{\alpha}$ , is the running-in allowance which reduces the initial base pitch deviation through running-in from the start of operation.  $F_{tH}$  can be calculated using Equation 4-8, which considers the tangential load in a transverse plane.

$$F_{tH} = F_t K_A K_V K_{H\beta} \quad (4-8)$$

ISO 6336-1 advises that the transverse base pitch deviation,  $f_{pb}$ , can be considered as 40  $\mu\text{m}$  for case hardened wrought steel material for all velocities, and the maximum limit of running-in allowance,  $\gamma_{\alpha}$ , can be determined using Equation 4-9.

$$\gamma_{\alpha} = 0.075 f_{pb} \quad (4-9)$$

The HSS pinion spur gear has a total contact ratio of more than two thus some adjustments are made to Equation 4-7 to determine the transverse load ratio using equation 4-10.

$$K_{H\alpha} = 0.9 + 0.4 * \sqrt{\frac{2(\varepsilon_{\gamma} - 1)}{\varepsilon_{\gamma}}} * \frac{C_{\gamma\alpha} * (f_{pb} - \gamma_{\alpha})}{F_{tH}/b} \quad (4-10)$$

#### 4.1.5 Load Sharing Factor and Loading Variations Caused by Gear Meshing

The load sharing factor depends mainly on the value of the contact ratio and the profile modification. Distribution of load can be presented across the line of contact points as a linear function. Two types of gears are used in this study: the WT HSS has unmodified spur gears; however in the experiment helical gears with modified profiles are used. The contact points along the line of action between the meshing gear pair are shown in Figure 4.2. As illustrated the gear meshing starts when point A (the approach point) at

the tip of the pinion (driven) gear engages with point A at the root of the wheel (driver) gear; this is considered for the calculation points on the line of action for the WT spur gears. For the helical gears tested in the experiment, as the pinion is the driver, the meshing starts when point A (the approach point) at the root of the pinion gear engages with the tip of the wheel gear. Y indicates a specific point along the tooth flank (total 7 points in the calculation), in determining Hertzian contact stress, sliding parameter, local flash temperature and specific lubricant film thickness.

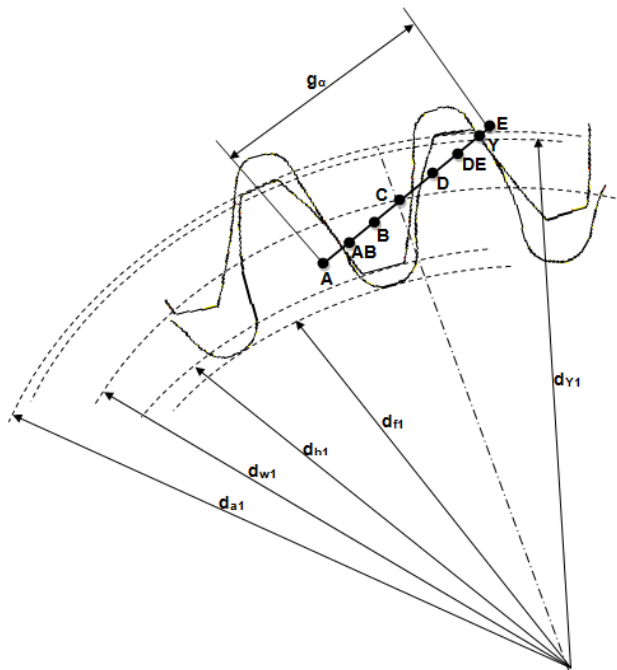


**Figure 4.2: Contact points along the line of action**

The load sharing factor for the cylindrical gears does not exceed unity at a single tooth contact, as shown in Figure 4.3. The load sharing on seven points along the line of action for the spur gears is determined according to the load sharing ratio as illustrated in Figure 4.3. For the analysis of WT pinion gear under the rated operation condition, the seven points along the line of the action are used in the calculation of the key parameters to evaluate the micropitting risk. However, for the probabilistic analysis of the WT gear, only five points along the line of action are considered due to the huge SCADA-analysed dataset of 3000 samples, as explained in Chapter 5. In addition, these locations are selected based on the ISO Technical Report of gear micropitting (ISO/TR 15144-1, 2010), where the single and double tooth contact occurs. As a result, the load along the line of action is calculated at points A, B, C, D and E, where the maximum load occurs at the region of single tooth pair contact, as shown in Figure 4.4. The

maximum sliding occurs in mesh-in, point A and mesh-out, point E. These points help to determine the Hertzian contact stress, local flash temperature, sliding parameter and lubricant film thickness on the gear profile while the gear is meshing along the path of contact under different operational conditions.

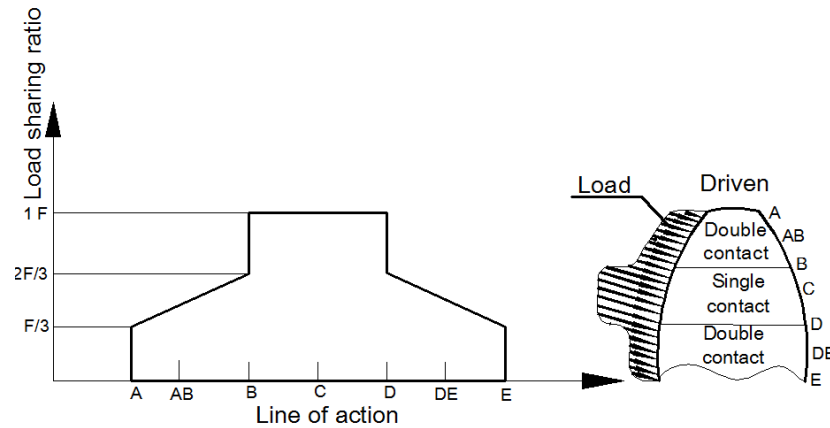


**Figure 4.3: Contact points of spur pinion gear (driven) used in the calculation for rated condition**

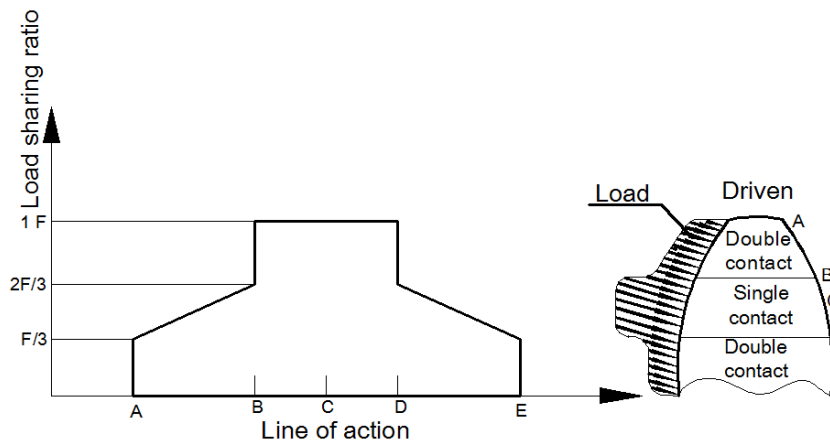


**Figure 4.4: Contact points of spur pinion gear (driven) used in the calculation for probabilistic analysis**

For the tested helical gears with tooth tip relief, the load sharing factor,  $X_y$ , considers the relations between the tooth tip relief and effective tip relief, as shown in Figure 4.5. The tip relief is a tooth modification in which a small amount of material is removed near the tip and/or root of the tooth to reduce the impact of meshing in/out in order to make the gears operate smoothly and with less vibration. Owing to the elastic deformation of loaded teeth and overload which builds up at the tooth tips, caused by oblique contact lines where high sliding occurs, the tip relief extensions are considered to be equal at points A and E. As indicated in ISO TR/15144-1, (2010), when the overlap ratio is equal to or greater than unity, the optimum profile modification should

be considered. The helical overlap contact ratio,  $\varepsilon_\beta$ , can be defined by the helical gear face width divided by the gear axial pitch. It can be determined by using the equation in the flowchart in Figure 4.6.

For the experiment case, the calculated overlap contact ratio in the helical tested gears is 1.099, considering the helix angle. Thus, the load sharing factor can be determined using the equations in Figure 4.6. The total contact ratio can be defined as the sum of the transverse contact ratio and overlap ratio. The tooth tip relief is considered in the calculation procedures of the load sharing factor. The tip relief can reduce the load sharing factor and provides smooth meshing at the mesh in/out regions of both gears during meshing cycles. It reduces the load sharing factor in the ranges A–AB and DE–E, but increases the load sharing factor in the range of AB–DE, as shown in Figure 4.5. The tip and root relief of three-dimensional drawing is provided in Appendix C. The load sharing at the mesh in/out between the modified and unmodified gears differs mainly if the tooth tip relief modification is used.

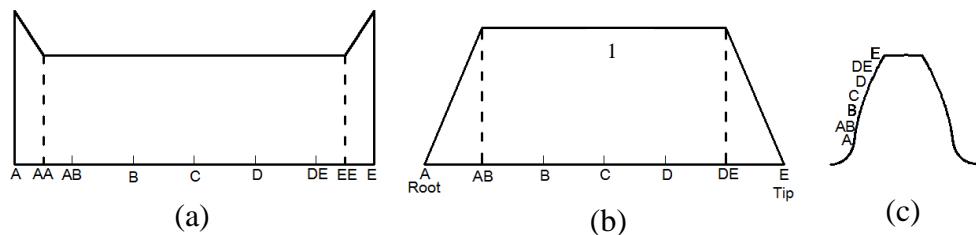


**Figure 4.5: Load distribution of the helical pinion gear (driver) within a meshing cycle, (a) unmodified profile, (b) modified profile and (c) points on tooth flank**

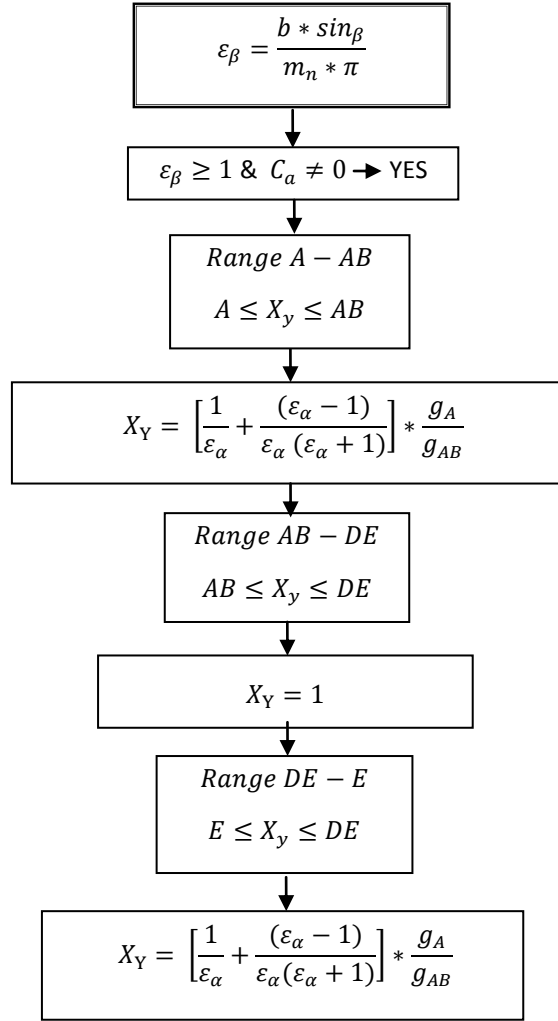


Figure 4.6: Flowchart for calculating the load sharing factor (ISO/TR 15144-1, 2010)

#### 4.1.6 Tip Relief and Effective Tip Relief

As explained above, the calculation of the load sharing factor,  $X_Y$ , is determined along the path of contact in accordance with ISO/TR 15144-1 (2010), with consideration of the tip relief and the gear contact ratio, as shown in the flowchart in Figure 4.6. In this research, the tested helical gears are subjected to variable loads. Due to the elastic deformation of loaded teeth and the overload that builds up at tooth tips in the area where high sliding occurs, the tip relief factor considers the impact of the profile modification on this overload (BS ISO/TR 13989-2 (2000(E))). The actual values of tip relief,  $C_a$ , the maximum addendum contact ratios,  $\varepsilon_{max}$ , and the effective tip relief,  $C_{eff}$  are considered to determine the tip relief factor,  $X_{ca}$ , as illustrated in the flowchart shown in Figure 4.7.

When the gears are subjected to higher loads, the effective tip relief has bigger values compared with the value of actual tip relief used on the tested gears. In this case, the tip relief factor is considered to be equal to unity, as advised by ISO TR15144-1 (2010). The flowchart in Figure 4.7 illustrates the procedure of how the tip relief factor is determined and Appendix D shows the relation between the maximum addendum contact ratio and the tip relief factor. When the gears are subjected to lower loads, the tip relief has values that are equal to or smaller than the effective tip relief, thus the tip relief factor is calculated as illustrated in Figure 4.7. The pinion gear (driver) used in the experiment has a symmetrical lead crowning; however, its effect is ignored in the analysis because the calculation is only carried out at the middle of the face width and the crowning has no effect in this area.

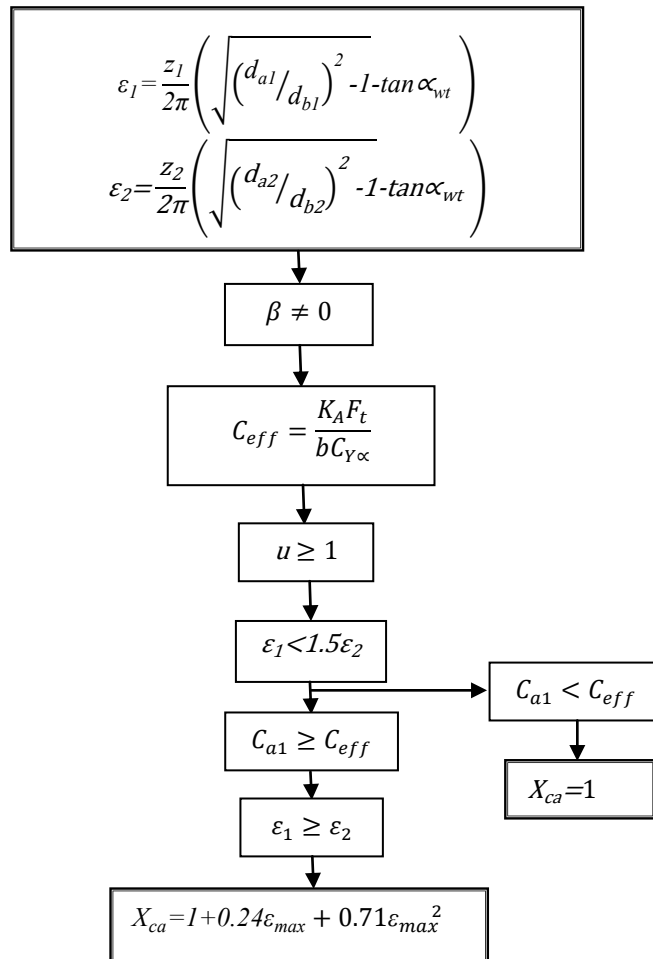
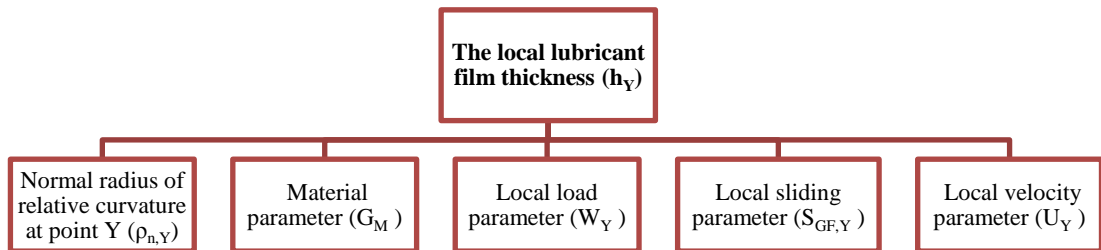


Figure 4.7: Flowchart diagram for calculating tip relief factor

## 4.2 ANALYSIS AND MODELLING PROCEDURE

The gear contact stress, sliding parameter, local contact temperature, and lubricant film thickness are calculated by developing an analytical solution to predict the micropitting failure. The lubricant film thickness,  $h_Y$ , is determined analytically under conditions of a mixture of rolling and sliding and pure rolling contact. The calculation of the local lubricant film thickness considers each contact point along the line of action based on the new Technical Report of micropitting, ISO/TR 15144-1 (2010). As mentioned above, the prefix Y refers to a specific point on the tooth flank and it takes into account the relative radii of curvature of the tooth flanks,  $\rho_{n,Y}$ , material parameters,  $G_M$ , local velocity parameter,  $U_Y$ , local load parameter,  $W_Y$ , and sliding parameter,  $S_{GF,Y}$ . Ideally, the most desirable method for calculating gear lubrication conditions should include variations of all these parameters, as shown in Figure 4.8. This section briefly outlines the analysis procedures with the equations used to calculate the lubricant film thickness. The expressions of the Dowson and Higginson film thickness equation is explained in detail and compared with the equations used in the Technical Report ISO/TR 15144-1 (2010).



*Figure 4.8: Diagram representing the lubricant film thickness parameters*

### 4.2.1 Radii of Relative Curvature of Mated Profiles

The radii of curvature of the mated profiles depend on each other as they are in contact at instantaneous point Y, as shown in Figure 4.2. When the gears mesh the radius of curvature of gear profile at the points of contact varies continuously along the line of the action. However, the pitch point C keeps a constant position on the centreline of the gear pair, whereas the other contact points (A, AB, B, D, DE and E) change their position along the contact flank. Equations 4-11 and 4-12 can be used to calculate the location of the contact from the base to tip diameters,  $d_{Y1\&2}$ , of the pinion and wheel on

the path of contact ( $g_Y$ ), where,  $d_a$ , is the tip diameter,  $d_b$ , is the base diameter and ,  $g_\alpha$ , is the length of the contact path.

$$d_{Y1} = 2 * \left( \sqrt{\frac{d_{b1}^2}{4} + \left( \sqrt{\frac{d_{a1}^2}{4} - \frac{d_{b1}^2}{4}} \right) - g_\alpha + g_Y} \right)^2 \quad (4-11)$$

$$d_{Y2} = 2 * \left( \sqrt{\frac{d_{b2}^2}{4} + \left( \sqrt{\frac{d_{a2}^2}{4} - \frac{d_{b2}^2}{4}} \right) - g_\alpha} \right)^2 \quad (4-12)$$

The equivalent radius of relative curvature,  $\rho_{t,Y}$ , of the mating tooth profiles can be determined by Equation 4-13 while the normal radius of relative curvature considering the helix angle can be calculated using Equation 4-14 :

$$\rho_{t,Y} = \frac{\sqrt{\frac{d_{Y1}^2 - d_{b1}^2}{4}} * \sqrt{\frac{d_{Y2}^2 - d_{b2}^2}{4}}}{\sqrt{\frac{d_{Y1}^2 - d_{b1}^2}{4}} + \sqrt{\frac{d_{Y2}^2 - d_{b2}^2}{4}}} \quad (4-13)$$

$$\rho_{n,Y} = \frac{\rho_{t,Y}}{\cos \beta_b} \quad (4-14)$$

### 4.2.2 Material Parameter

The dimensionless material parameter,  $G_M$ , takes into consideration the lubricant pressure-viscosity coefficient at bulk temperature,  $\alpha_{\theta M}$ , and the influence of the reduced elastic modulus,  $E_r$ . The material parameter is defined by Equation 4-15.

$$G_M = 10^6 * \alpha_{\theta M} * E_r \quad (4-15)$$

The reduced elastic modulus,  $E_r$ , which considers the modulus of elasticity and material Poisson's ratio,  $\nu$ , of the mated gears, can be calculated by Equation 4-16.

$$\frac{1}{E_r} = \frac{1}{2} * \left( \frac{1-\nu_1^2}{E_1} + \frac{1-\nu_2^2}{E_2} \right) \quad (4-16)$$

### 4.2.3 Load parameter

The dimensionless load parameter,  $W_Y$ , can be calculated using the reduced modulus of elasticity and gear contact stress as shown in Equation 4-3 and can be determined according to Equation 4-17.

$$W_Y = \frac{2 * \pi * P_{dyn,Y}^2}{E_r^2} \quad (4-17)$$

#### 4.2.4 Sliding parameter

The sliding velocity of the gear tooth is defined as the relative velocity of two tooth flanks sliding over each other. The inequality of the relative curvature radius results in differences in the rolling and sliding velocities of each contact point between the pinion and wheel gears. In this case, the relative sliding occurs even under a constant rotational speed of gears. The sliding parameter,  $S_{GF,Y}$ , takes into consideration the effect of local sliding on the local contact temperature and it is determined according to Equation 4-18. The local contact temperature,  $\theta_{B,Y}$ , is defined as the sum of the local flash temperature and the bulk temperature. The local pressure-viscosity coefficient,  $\alpha_{\theta_{B,Y}}$ , and the local dynamic viscosity,  $\eta_{\theta_{B,Y}}$ , are influenced by the local contact temperature,  $\theta_{B,Y}$ . This in turn has an effect on the local lubricant film thickness. Figure 4.9 shows how the sliding parameter is calculated and it summarises the relation between the local contact and bulk temperatures. The kinematic viscosity at bulk temperature,  $v_{\theta_M}$ , and at local contact temperatures,  $v_{\theta_{B,Y}}$ , can be determined from the kinematic viscosity at 40°C and 100°C based on the equations as shown in Figure 4.9.

$$S_{GF,Y} = \frac{\alpha_{\theta_{B,Y}} * \eta_{\theta_{B,Y}}}{\alpha_{\theta_M} * \eta_{\theta_M}} \quad (4-18)$$

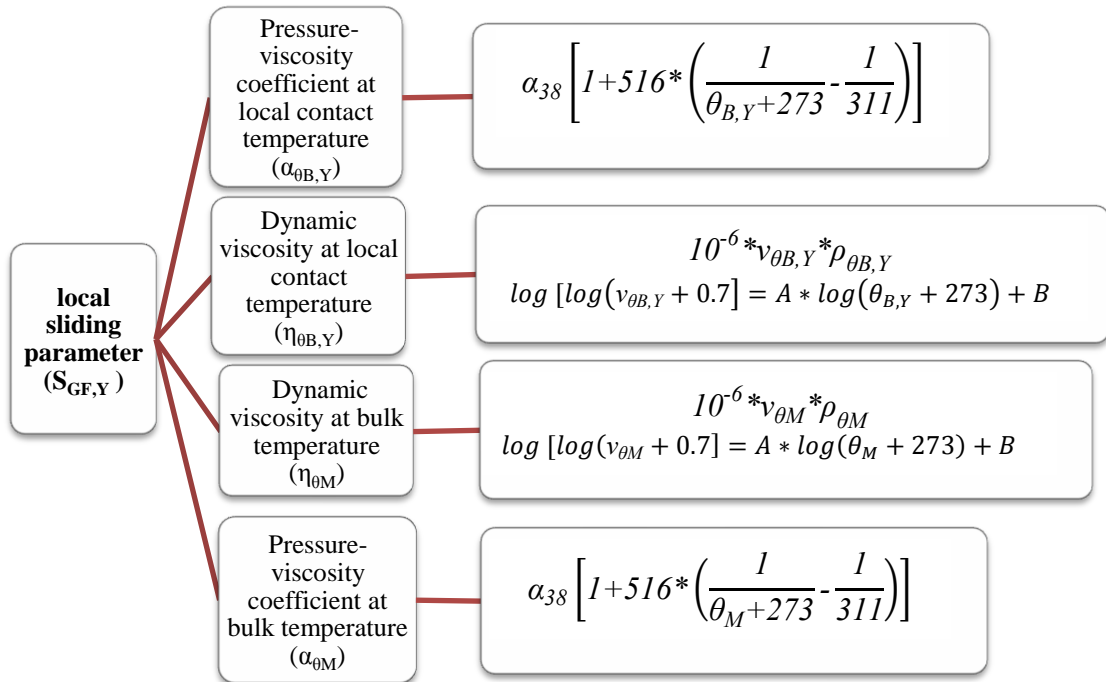


Figure 4.9: Determination of sliding parameter

The dynamic viscosity and pressure-viscosity coefficient at both flash temperature,  $\theta_{fI,Y}$ , and bulk temperature,  $\theta_M$ , are considered for the purpose of determining the local sliding parameter, as shown in Figure 4.9. The bulk temperature,  $\theta_M$ , is the equilibrium temperature before the gear enters meshing and it is directly proportional to the mean coefficient of friction and the power transmitted, which is directly proportional to the rotational speed and torque, as expressed in Equation 4-19. The flash temperature is the instantaneous temperature at the local contact point, which fluctuates due to the varying meshing points on the tooth flank. It is directly proportional to the local sliding velocity,  $V_{g,Y}$ , which differs between the tangential velocities of the pinion and wheel gears, and the flash temperature can be determined according to Equation 4-20. It defines the flash temperature at each contact point along the line of action by considering the local tangential velocities,  $V_{r,Y}$ , on the pinion and wheel gears, local radii on the tooth flanks,  $\rho_{n,Y}$ , coefficient of friction,  $\mu_m$ , and gear contact stresses,  $\rho_{dyn,Y}$ . The highest temperature point can be determined along the line of action of the gear pair and the tooth profile modification can be used to reduce the critical temperature at that point.

$$\theta_M = \theta_{oil} + 7400 * \left( \frac{P * \mu_m * H_v}{\partial * b} \right)^{0.72} * \frac{X_s}{1,2 * X_{ca}} \quad (4-19)$$

$$\theta_{fl, Y} = \frac{\sqrt{\pi}}{2} * \frac{\mu_m * P_{dyn, Y} * 10^6 * |V_{g, Y}|}{B_{M1} * \sqrt{V_{r1, Y}} + B_{M2} * \sqrt{V_{r2, Y}}} * \sqrt{8 * \rho_{n, Y} * \frac{\rho_{dyn, Y}}{1000 * E_r}} \quad (4-20)$$

The unavailability of a measurement method for the instantaneous coefficient of friction,  $\mu_m$ , makes its assessment difficult (BS ISO/TR 13989-2, 2000). However, the mean coefficient of friction between the tooth flanks can be approximated by Equation 4-21. The mean coefficient of friction depends on many parameters, such as the surface roughness, tangential velocity, oil dynamic viscosity at inlet temperature,  $\eta_{\theta oil}$ , lubricant factor,  $X_L$ , and gear geometry. The lubricant factor depends on the oil type and can be obtained through the table provided in ISO/TR 15144-1 (2010). In experimental tests, the mineral oil is used for testing the helical gears and the lubricant factor is equal to unity. Polyalphaolefin oil is used for the analytical calculation of the WT spur gears, and the lubricant factor is equal to 0.8, as indicated in the above mentioned table. The load factor of helical gears,  $K_{BY}$ , is directly proportional to the mean coefficient of friction and depends on the total contact ratio. The load factor is considered to be equal to unity for the WT spur gears. For the tested helical gears

Equation 4-22 is used to determine the helical load factor, where the calculated total contact ratio,  $\varepsilon_y$ , is equal to 2.45.

$$\mu_m = 0.045 * \left( \frac{K_A * K_V * K_{H\alpha} * K_{H\beta} * K_{BY} * F_{bt}}{b * V_{\Sigma,C} * \rho_{n,c}} \right)^{0.2} * (10^3 * \eta_{\theta oil})^{-0.05} * 2.2 * \left( \frac{R_a}{\rho_{n,c}} \right)^{0.25} * X_L \quad (4-21)$$

$$K_{BY} = 1 + 0.2 * \sqrt{(\varepsilon_y - 2) * (5 - \varepsilon_y)} \quad \text{if } 2 < \varepsilon_y < 3.5 \quad (4-22)$$

#### 4.2.5 Velocity parameter

The velocity parameter,  $U_y$ , is directly proportional to the dynamic viscosity,  $\eta_{\theta M}$ , of the lubricant at bulk temperature and the sum of the tangential velocities, and inversely proportional to the normal radius of relative curvature,  $\rho_{n,Y}$ , as shown in Equation 4-23. It is used to determine the variation of the lubricant film thickness related to the sum of the tangential velocities.

$$U_y = \eta_{\theta M} * \frac{\left( 2\pi * \frac{n_2}{U * 60} * \frac{d_{w1}}{2000} * \sin \alpha_{wt} * \sqrt{\frac{d_{y1}^2 - d_{b1}^2}{d_{w1}^2 - d_{b1}^2}} \right) + \left( 2\pi * \frac{n_2}{60} * \frac{d_{w2}}{2000} * \sin \alpha_{wt} * \sqrt{\frac{d_{y2}^2 - d_{b2}^2}{d_{w2}^2 - d_{b2}^2}} \right)}{2000 * E_r * \rho_{n,Y}} \quad (4-23)$$

The dynamic viscosity,  $\eta_{\theta M}$ , at bulk temperature is considered as a measure of the lubricant resistance to the relative sliding, as shown in Equation 4-18. Dynamic viscosity can be determined using the equation in Figure 4.9, where,  $\nu_{\theta M}$ , and  $\rho_{\theta M}$ , are the lubricant kinematic viscosity and lubricant density at bulk temperature respectively. The kinematic viscosity at bulk temperature can be determined from the lubricant kinematic viscosity at 40°C and kinematic viscosity at 100°C.

#### 4.2.6 Gear Tooth Lubricant Film Thickness Analysis

The elastohydrodynamic lubrication (EHL) is a form of oil film that occurs under different contact pressures between two contact surfaces. The problem of hydrodynamic lubrication was studied and published by Reynolds in 1886. The theory was based on cylindrical and spherical contact stresses theory, as shown in Figure 4.10, as Reynold developed his theory a few years after the publication of Hertz's contact theory. By

neglecting the lubricant loss and by considering a constant lubricant density with a pure cylindrical rotational rolling, the Reynolds equation can be written as in the following Equation 4-24.

$$\frac{\partial}{\partial x} \left( \frac{h^3}{12\eta'} \frac{\partial p}{\partial x} \right) = v' \frac{\partial h}{\partial x} \quad (4-24)$$

Where,  $\eta'$ , is the effective viscosity determined by the lubricant model, temperature and pressure, and,  $v'$ , is the equivalent speed. The Reynolds equation has unknown values of pressure,  $P$ , and lubricant film thickness,  $h$ , and they can be solved by regression analysis. These values can be analysed through the minimum value of oil film thickness at the point of maximum contact pressure, as represented in Figure 4-10.

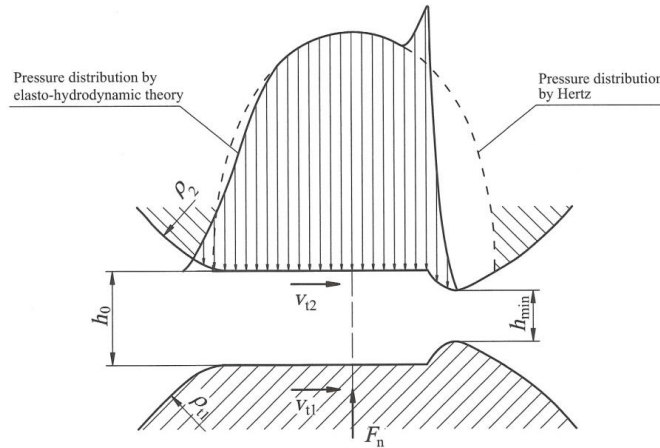


**Figure 4-10: Elasto-hydrodynamic theory of pressure distribution and lubricant film thickness (cited in Jelaska, 2012)**

Since the publication of the Reynolds theory, many papers were published, such as those by Martin (1916) and Ertel (1939, cited in Lu H, 2006), that considered the geometry of the spur gear teeth as having an identical radius of curvature (equivalent discs), the same face width, contact loading and steady state of rotational speed. Under these assumptions, Dowson and Higginson (1966) introduced their work based on numerical calculation methods, using different parameters to determine the lubricant film thickness. The equation by Dowson and Higginson for the purpose of film thickness calculation has been widely used in engineering applications. The newly published micropitting Technical Report ISO/TR 15144-1 (2010) is based on the Dowson and Higginson method and can be written as Equation 4-25. It shows that the lubricant film thickness considers all the parameters explained above and depends mostly on load, sliding parameter and lubricant temperature conditions.

$$h_Y = 1600 \cdot \rho_{n,Y} * G_M^{0.6} * U_Y^{0.7} * W_Y^{-0.13} * S_{GF,Y}^{0.22} \quad (4-25)$$

The lubricant film thickness derived from the Dowson and Higginson equation is used together with the gears' surface roughness in order to obtain the specific lubricant film thickness,  $\lambda_{GF,Y}$ . It is a dimensionless parameter and can be defined as the ratio between the lubricant film thickness,  $h_Y$ , and the measurements of mean surface roughness,  $R_a$ , of the driving and driven gears, as shown in Equation 4-26. The mean value of surface roughness of the meshed flanks can be defined as shown in Equation 4-27. The location where the thinnest lubrication film thickness exists bears a high risk of micropitting. The calculation of the micropitting safety factor can be defined by Equation 4-28.

$$\lambda_{GF,Y} = \frac{h_Y}{R_a} \quad (4-26)$$

$$R_a = \frac{R_{a1} + R_{a2}}{2} \quad (4-27)$$

$$n = \frac{\lambda_{GF,min}}{\lambda_{GFP}} \geq n_{min} \quad (4-28)$$

Based on the above analysis procedure of gear micropitting, Figure 4.11 summarises this procedure, giving the input parameters required to determine the key parameters which affect micropitting. The inputs are geometric parameters (such as the number of teeth, face width, pressure angle, radius of curvature...etc.), material parameters (for example, modulus of elasticity and Poisson's ratio), gear operating parameters (torque, speed, and dynamic factors), lubricant parameters (kinematic viscosity, density of lubricant and lubricant type). The outputs are Hertzian contact stresses along the path of contact, surface temperature, sliding parameter and specific lubricant film thickness of the gear flanks in every mesh position, as summarised in Figure 4.11.

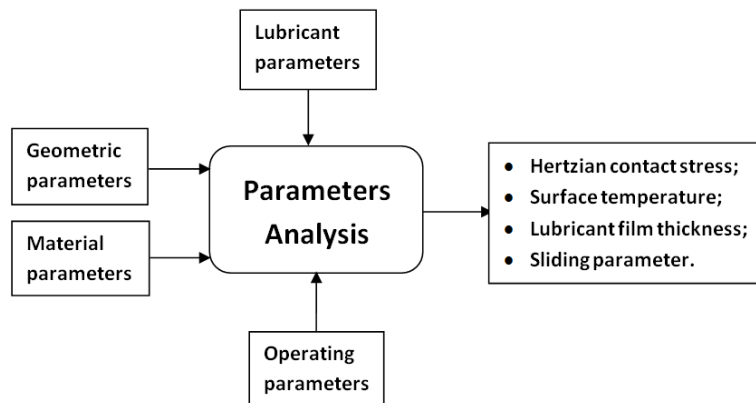


**Figure 4.11: Inputs and outputs of gear micropitting analysis procedure**

### 4.3 DIFFERENCE BETWEEN ISO AND AGMA STANDARDS

The AGMA 925-A03 standard was published in 2003. It includes different calculation methods of various gear surface failures including micropitting. The more recently published ISO/TR 15144-1 (2010) *Calculation of Micro-pitting Load Capacity of Cylindrical Spur and Helical Gears - Part 1: Introduction and Basic Principles*, is based on different methods and considers most parameters that affect gears micropitting failure. There are some differences in the calculation methods used in ISO/TR and AGMA standard. The main differences can be summarised as follows:

- ❖ AGMA standard provides three different methods to calculate and approximate the mean coefficient of friction on the tooth flank in order to calculate the flash temperatures. Two methods consider surface roughness using constant values that are derived from previous experimental work. The third method is based on empirical equation which cannot be used at or near the pitch area where the pure rolling occurs. However, this equation can be used in other areas along the line of action while considering some factors such as surface roughness, lubricant dynamic viscosity, sliding velocity and load sharing factor.
- ❖ The Dowson theory is used in both AGMA and ISO/TR. However, it is used for calculating the central film thickness of the Hertz contact zone in the former and the minimum film thickness along the line of the contact path in the latter. However, there is a slight variation in the factors used in calculating the lubricant film thickness (Kissling, 2012). In addition, they both use Blok equation to calculate the flash temperature.
- ❖ The key difference between these two standards lies in the calculation of various load factors that are used in ISO 6336 when determining the mean coefficient of friction. Another main difference is that the ISO/TR considers the local contact temperature when calculating the sliding parameter while AGMA does not and instead it takes an account of the dynamic viscosity at the mean tooth temperature. The AGMA standard estimates the tooth temperature as the sum of the lubricant temperature and the maximum flash temperature along the line of action.

## 4.4 LIMITATIONS OF THE STUDY

Although the present study provides an in-depth investigation of micropitting in WT gearboxes, it has some discernible limitations.

The study focuses on micropitting only and does not address other gear surface failure modes. It concentrates on spur and helical gears and does not investigate other types of gears because these are the most commonly used in WTs.

The limitations are linked to the use of ISO Technical Report ISO/TR 15144-1 (2010). This report provides two different methods, A and B, for the calculation of spur and helical gears micropitting. Method A requires advance analytical tools as it considers the tooth flank and shaft deflection to determine the Hertzian contact stress in every meshing position along the tooth flank (Kissling, 2012). Method B, which is used in this research, calculates the contact stress, sliding parameter, local contact temperature and lubricant film thickness at seven specific locations of the tooth flank from start to end of the path of contact (as discussed earlier in Section 4.2). The limitations associated with this ISO/TR are:

- ❖ To determine the specific lubricant film thickness, the ISO/TR uses mean surface roughness ( $R_a$ ) which is the most important and a key parameter that influences micropitting. However, the roughness profile of contact surfaces has peaks and valleys which are not considered despite their significant effects on the specific lubricant film thickness. Some surfaces can have identical mean surface roughness but completely different characteristics (Bell et al, 2012). Thus, different surface roughness parameters should be considered when calculating the specific lubricant film thickness.
- ❖ Method B provides two methods to calculate the load sharing distribution between the meshing gear pair. One method is for the unmodified profile and the other is for the optimum modified profile. The calculation of load sharing factor depends on tip relief of gear tooth profile which contributes to reduce the load at the beginning and the end of the contact path and provides smooth meshing at the mesh in/out regions. The ISO/TR does not provide/recommend the values of the optimum short/long tip relief compared to the effective tip relief. Thus, this

method provides limited accuracy of load distribution results for gears with profile modification.

- ❖ The ISO-TR provides a method to estimate the mean coefficient of friction, which is used to determine others factors, to calculate the flash and bulk temperatures. It would be more accurate if the coefficient of friction considers a variety of points along the line of action instead of a single value.

Despite of its limitations, ISO/TR 15144-1 (2010) is the only official and first technical report published by the ISO to determine the micropitting risk and micropitting safety factor. It provides the analytical principles in order to assess gear micropitting risk by determining the minimum specific lubricant film thickness in the local contact area along the path of gear contact.

## **4.5 SUMMARY**

This chapter summarises the analysis methods used to determine the key parameters affecting gear micropitting. These methods are based on various international standards for gears and the newly published ISO Technical Report ISO/TR 15144-1 (2010) for gear micropitting. The chapter briefly outlines how these standards are used to determine the contact stress, sliding parameter, local contact temperature and lubricant film thickness along the line of action of gear tooth contact. The determination of minimum specific lubricant film thickness at any contact point along the tooth flank is discussed. The chapter briefly describes the method that the safety factor against micropitting may be determined if the permissible specific lubricant film thickness is known. The limitations of the ISO Technical Report ISO/TR are highlighted and the differences between ISO/TR 15144-1 and the AGMA 925-A03 standard are outlined. The chapter concludes with pointing out the limitations of this study.

## *Chapter 5: SCADA Data Analysis*

---

*In this chapter, an analytical method and a modelling procedure are developed to investigate the high speed shaft (HSS) gear of WT gearboxes under different operational conditions. The recorded WT gearbox SCADA data including wind speed, generator power and rotational speed is used to select the representative operational conditions considering the WT controls. Furthermore, the recorded SCADA data over 2.2 years period from two WTs in operation is used to derive the probabilistic distributions of HSS driven gear shaft torque and rotational speed. Furthermore, the process of generating smaller datasets representing original SCADA datasets using Mersenne Twister (MT) random number generator is explained. Detailed SCADA data analysis and results are provided in Chapter 8.*

## 5.1 WT GEARBOX AND PARAMETERS

This study investigates the risk of micropitting of the HSS of a three-stage wind turbine gearbox. The SCADA data used for this study was recorded for a period over 2.2 years from WTs of MW scale in operation onshore. The WT has a three-stage gearbox design, a synchronized DFIG (doubly fed induction generator) with a partially-rated converter, and an electric pitch-regulation. The gearbox has one planetary gear stage and two parallel gear stages. The HSS gears, including pinion (driven) and wheel (driving) as marked in Figure 5.1, are analysed in this work. The illustration of the gearbox design is shown in Figure 5.1 and the main characteristics of the planetary and intermediate stages are shown in Appendix E. The main objective of this work is to obtain the contact stress, sliding parameter, local contact temperature and lubricant film thickness to assess the risk of micropitting under rated conditions and varying operational conditions of a WT gearbox.

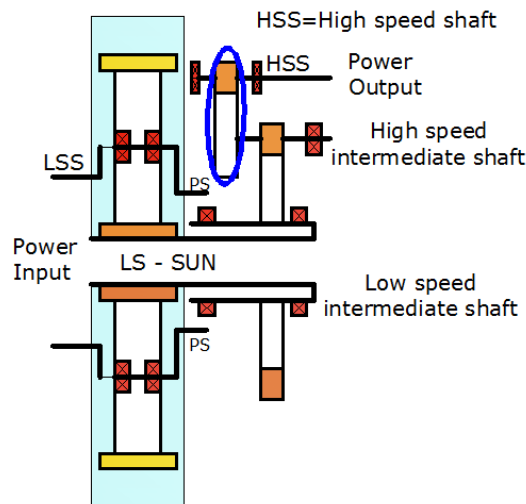


*Figure 5.1: High speed stage within a three stage WT gearbox*

The wheel and pinion are spur gears and their parameters are shown in Table 5-1. The gear material and lubricant parameters are shown in Tables 5-2 and 5-3 respectively. These are used to analyse the HSS gear of the wind turbine gearbox as shown in Figure 5.1. The contact stresses, local contact temperatures, sliding parameter and lubricant film thicknesses can be determined based on Method B (explained in Chapter 4) as recommended in ISO Technical Report ISO/TR 15144-1 (2010).

*Table 5-1: Wheel and pinion parameters*

Parameters	Wheel/Driver	Pinion/Driven
Number of gear teeth	86	23
Effective face width	165 mm	165 mm
Pressure angle	20 degree	
Module	7 mm	
Centre distance	381.5 mm	
pitch diameter	602 mm	161 mm
Nominal pitch line velocity	15.2 m/s	
Nominal rotational speed	482 rpm	1800 rpm

*Table 5-2: Material data*

Parameters	Wheel and Pinion
Material	Case Hardened Wrought Steels
Modulus of Elasticity	$206 \times 10^9 \text{ N/m}^2$
Poisson's ratio	0.3
Specific heat conductivity	45 W/(mK)
Specific heat	440 W/(kgK)
Density	$7800 \text{ kg/m}^3$

*Table 5-3: Lubricant data*

Parameters	Wheel and Pinion
Oil type	Mobilegear SHC XMP 230
Oil inlet temperature (splash lubrication)	$65^\circ\text{C}$
Kinematic viscosity at $40^\circ\text{C}$	$335 \text{ mm}^2/\text{s}$
Kinematic viscosity at $100^\circ\text{C}$	$38.3 \text{ mm}^2/\text{s}$
Density of the lubricant at $15^\circ\text{C}$	$860 \text{ kg/m}^3$

## 5.2 SCADA DATA ANALYSIS

The SCADA data consists of three values of power output; they are minimum, average and maximum values. Numerous signals are recorded by WT SCADA system in each interval, for the generator rotational speed only the average value is recorded during the ten minutes intervals. In this case further analysis of power outputs is required to ensure that the average recorded power is valid for the purposes of this study. The recorded minimum, average and maximum values of power outputs are analysed and a

comparison between the recorded average and calculated average power is made by using the maximum and minimum values of power. The recorded power is converted to power ratio to aid the consistency in analysis of results throughout the different results chapters. The comparison shows that the recorded average power value is more accurate than the calculated power as it is less dispersed compared to the calculated average power as shown in Figure 5.2. In addition, the recorded average value of SCADA data during 10 minutes intervals is more representative of the data centre because it is not influenced by the outliers.

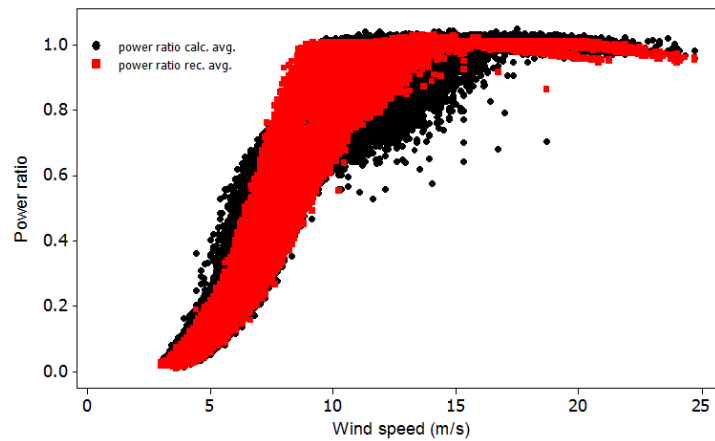


**Figure 5.2: Comparisons between the calculated average and recorded average power ratios**

The recorded signals of generator power output and generator rotational speed by SCADA are used to calculate the shaft torque of HSS pinion by considering the average efficiency of the generator and HSS gear stage,  $\eta_{Gen}$  and  $\eta_{Gear}$ . The original SCADA dataset is in time series and the average generator power output and average generator rotational speed of ten minutes are recorded in ten minute intervals. The shaft torque of HSS pinion is calculated by using the average generator power output,  $P_{Gen, i}$  and the average generator rotational speed,  $\omega_{Gen, i}$ , both recorded by SCADA at ten minute interval  $i$ . The torque ratio of HSS pinion shaft,  $TR_{HSS\ pinion, i}$ , is defined as the calculated torque divided by the rated torque of the shaft, Equation 5-1. Similarly, the speed ratio of HSS pinion shaft,  $SR_{HSS\ pinion, i}$ , is determined by using the average generator rotational speed, recorded by SCADA, divided by the rated rotational speed of generator shaft, Equation 5-2. To derive probabilistic characteristics of the pinion shaft torque variations, the calculated torque ratio is represented as torque ratio percentage histograms. Similarly, the rotational speed histograms of HSS pinion shaft are generated to analyse its probabilistic characteristics. Forty (40) bin size of torque ratio and speed

ratio are selected according to the data set size in order to produce meaningful representation of the distribution of histograms.

$$TR_{HSS\ pinion,i} = \left( \frac{P_{Gen,i}}{\eta_{Gen}\eta_{Gear}\omega_{Gen,i}} \right) / \left( \frac{P_{Gen,rated}}{\omega_{Gen,rated}} \right) \quad (5-1)$$

$$SR_{HSS\ pinion,i} = \frac{\omega_{Gen,i}}{\omega_{Gen,rated}} \quad (5-2)$$

### 5.2.1 Analysis of Rated Conditions

WT recorded SCADA data is used to generate the power ratio and generator speed ratio curves against the wind speed, as shown in Figure 5.3. It shows the variation of power and generator rotational speed based on one month recorded SCADA data. The generation of electrical power begins after the turbine blades rotate at above the cut-in speed (4 m/s). The power reaches the rated value when the wind speed increases above 12 m/s, as shown in Figure 5.3. The rated power stays constant while the wind speed increases until it reaches up to 25 m/s. After that, the certain control or breaking system automatically disconnects the rotor from the generator when the wind speed reaches its maximum limit (cut-out speed) to protect the turbine machine from the risk of damage, IEC61400-1, 2005.

Due to the stochastic effect of wind speed variation and complex WT controls, the WT gearbox is subjected to a variable speed and torque conditions. The ranges of speed and torque variations are determined based on a statistical analysis of SCADA data measured in field operation of a WT (Long et al, 2012). Three regions can be identified in Figure 5.3 which depict the relationship between the generator speed and wind speed. In Region 1 and 3 the generator speed is constant at 1000 rpm (0.56 speed ratio), and at rated 1800 rpm (1.00 speed ratio) respectively, while in Region 2 the generator speed varies from above 0.56 to below the rated condition of the speed ratio. These three regions can aid in locating the generator speed using the generator speed versus wind speed curve. The generator power and generator rotational speed curve are then used to calculate the generator torque of the HSS pinion with an overall efficiency of 0.961. In chapter 7, the range of HSS pinion rotational speed and torque variations is analysed according to the operational conditions of one month SCADA data. Table 7-1 in

Chapter 7 summarises the variations in ranges that are used to calculate the contact stress, local contact temperature and lubricant film thickness.

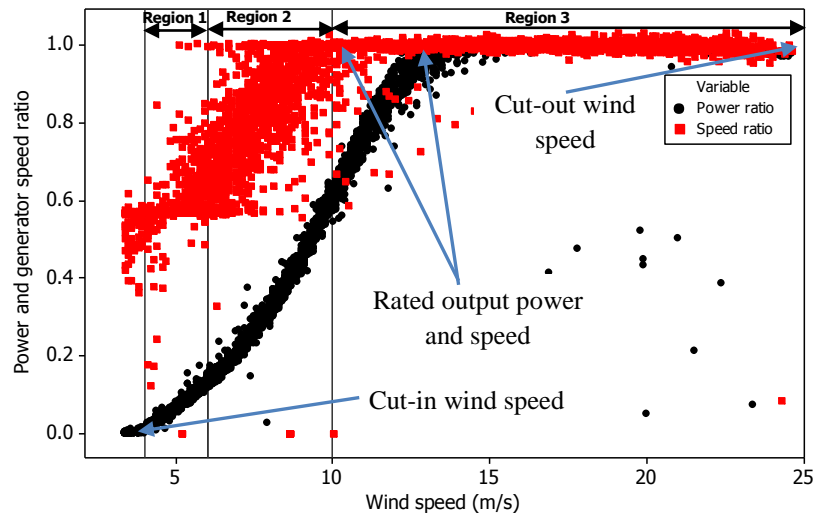


*Figure 5.3: Generator power and generator speed curves vs. wind speed ( one month data)*

### 5.2.2 Probabilistic Analysis of Torque and Rotational Speed Variation

Two different WTs, WT1 and WT2, located at different onshore wind farms, are selected to investigate their probabilistic variations of shaft torque and rotational speed. The data collected by SCADA is analysed for the purpose of comparing operational conditions of the gearbox at different locations. The original SCADA datasets are filtered to derive the analysed datasets which only include records of generator power output and generator rotational speed when the generator shaft is synchronised with the rotor shaft. The filtering process excludes zero and below values for power and values below 940 rpm for the rotational speed. Based on these analysed datasets, histograms of HSS pinion shaft torque ratio and rotational speed ratio are derived to show the probability density distribution. Figures 5.4 and 5.5 show the histograms of HSS pinion shaft torque ratio of the two WT gearboxes.

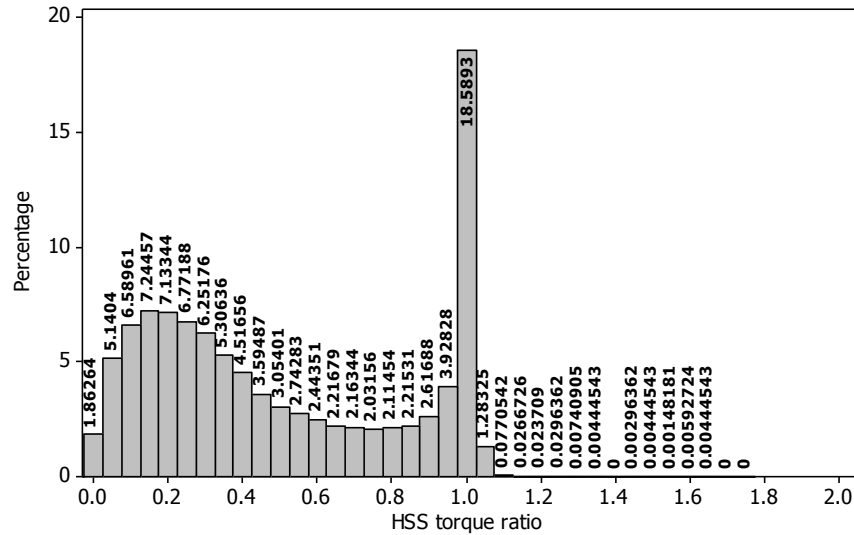


Figure 5.4: Histogram of WT1 HSS pinion shaft torque ratio

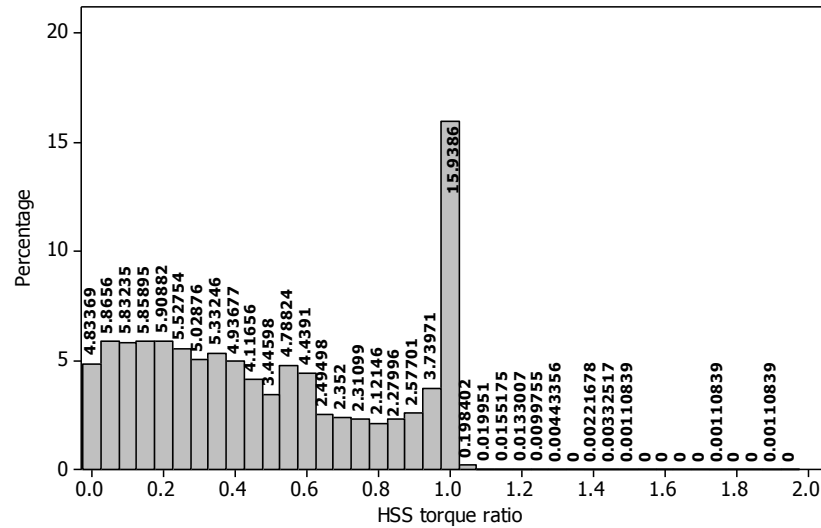
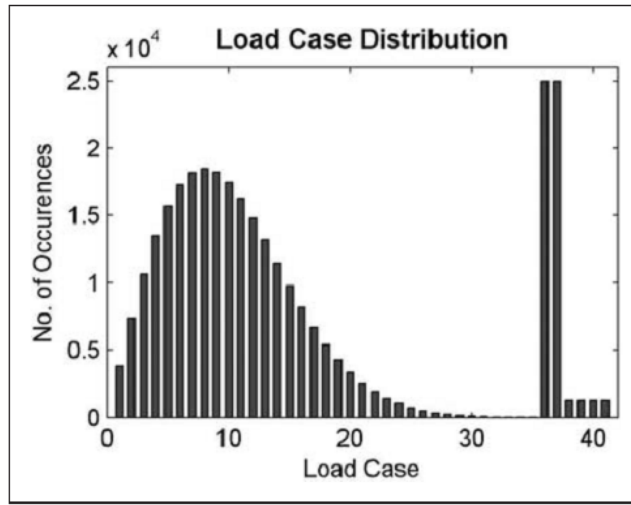


Figure 5.5: Histogram of WT2 HSS pinion shaft torque ratio

Torque ratio histograms obtained from the SCADA analysis dataset are compared with that obtained by computational simulations as shown in Figure 5.6, reported by Greaves et al (2011). In their work, the simulations considered all the fatigue load cases defined in the international standard IEC 61400-1 (2005), with wind simulations of strong gusts and 3D turbulent wind conditions chosen according to the appropriate wind turbine design standards IEC 61400-1 and Lloyd G (2003). The load cases considered included: power production at wind speed between 4 and 25 m/s; Parked; Start-ups and Shut-downs at cut-in, cut-out and rated wind speed. The Rayleigh wind speed distribution defined in the standards was used to determine how many times each load cases would

occur over a 25-years design life (Greaves et al, 2011). The load case histogram based on computational simulation provides a benchmark when compared with the torque ratio histograms derived from SCADA data in this study.



*Figure 5.6: Simulated load case distribution based on IEC (Greaves et al, 2011)*

As explained above in this section, HSS pinion gear of WT1 and WT2 gearboxes are used in the analysis. The histograms of rotational speed ratio of the HSS pinion shaft are shown in Figures 5.7 and 5.8.

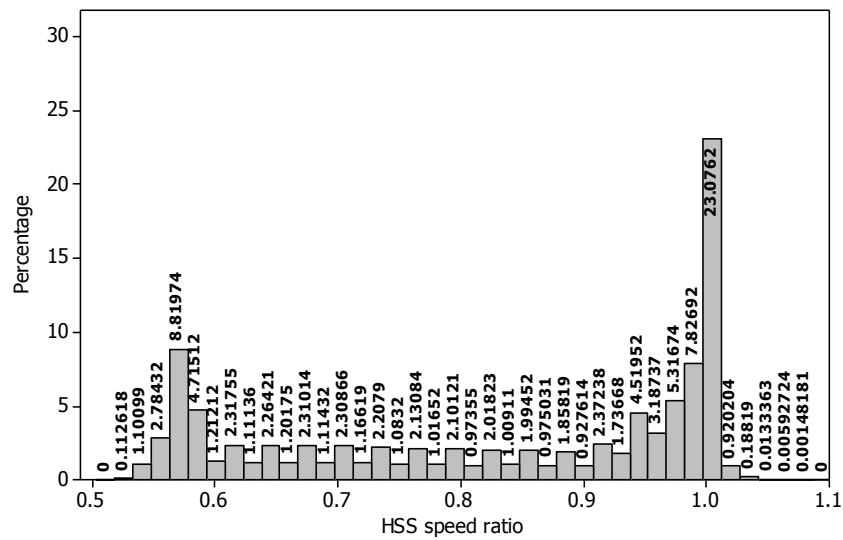


*Figure 5.7: Histogram of WT1 HSS pinion shaft rotational speed ratio*

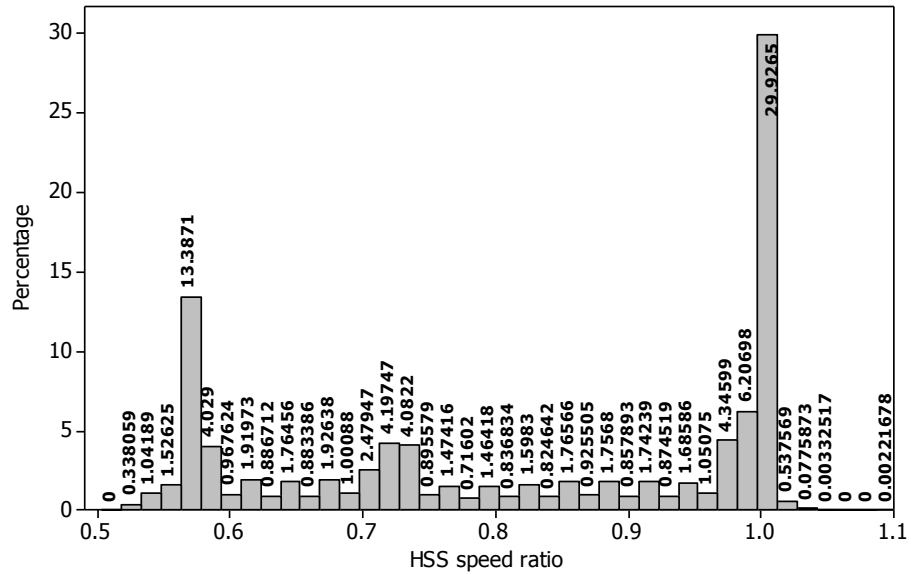


*Figure 5.8: Histogram of WT2 HSS pinion shaft rotational speed ratio*

Figures 5.4, 5.5, 5.7 and 5.8 show that WT1 and WT2 have similar probability distributions of shaft torque and rotational speed and the gearboxes operate at the rated torque and rated rotational speed for most of the time, as expected. The torque ratio histogram of WT1 based on the analysed SCADA datasets of the 2.2 years period is similar to the simulated load case distribution of 25 years' design life based on the IEC standard using GH Blade software (Greaves et al, 2011). However, the torque ratio histogram of the analysed SCADA data shows more occurrences above the rated torque ratio than that of the computational model, indicating a higher probability of overloading which can be attributed to the turbulence intensity depending on location of WT. Furthermore, the torque ratio histogram of WT2 has a slightly different distribution, confirming that the wind farm and turbine locations contribute to the loading variations.

The WT1 has a higher number of occurrences at the rated torque ratio which reaches 18.6% while WT2 only reaches 15.9%, as shown in Figures 5.4 and 5.5. It is noteworthy that the WT2 has the highest torque ratio of 1.9 (1.9 times higher than the rated torque), while WT1 has only the highest torque ratio of over 1.6, as shown in Figures 5.4 and 5.5.

Figures 5.7 and 5.8 show that, for both WT1 and WT2, high numbers of occurrences of speed ratios are concentrated between 0.55 and 0.6 and at rated speed ratios. WT2 has

more occurrences in the range between 0.7 and 0.75 of speed ratio compared to WT1. Nevertheless, the comparison between the speed ratios of WT1 and WT2 shows that they have similar probability distributions and their gearboxes operate for most of the time at the rated rotational speed ratio, as shown in Figures 5.7 and 5.8.

### **5.2.3 Random Numbers Generation**

The analysed datasets of HSS pinion shaft torque and rotational speed, derived from SCADA data recorded over two years, consist of over 63000 data points after biased data are filtered. It is computationally expensive to use all data points in determining gear flank contact stresses, local contact temperatures, sliding parameter and lubricant film thicknesses in order to assess the probability of micropitting risk. Random number generators are useful tools for producing random numbers to guarantee that the generated small datasets are unique and representative of the analysed SCADA datasets. A random number generator with strong randomness guarantee is essential in producing simulation results as the generated random number set is a key determinant that approximates the probabilistic properties of the analysed SCADA datasets. The Mersenne Twister (MT) random number generator was proposed by Matsumoto and Nishimura in 1998 as stronger uniform pseudorandom number generators. It is a reliable and fast generator for use in stochastic modelling (Davis, 2006). Thus it is employed in this study to generate a random number to be used by the MT generator to produce a unique smaller dataset representing the analysed SCADA datasets of HSS pinion shaft torque and rotational speed respectively.

To generate smaller datasets of random numbers, the analysed datasets of HSS pinion shaft torque and rotational speed are imported to statistical analysis software, Statistical Package for the Social Sciences (SPSS). This package can handle and analyse a large amount of data and perform a wide variety of statistical analyses. The generation of random numbers involves duplicates of original datasets to ensure they are independent and identically distributed over the close interval (0, 1), representing the same probability distribution of the original datasets. The MT generator operates different functions some of which are employed to read the analysed SCADA datasets as input and produce smaller datasets as output for a specified dataset size. It also uses deterministic algorithms and is considered to be an uniform pseudorandom number

generator that can convert all data points into specific random numbers of original HSS pinion shaft torque and rotational speed respectively.

The MT generator functioning follows a certain procedure for the generation of random datasets. The procedure includes functions which are specifically designed for the datasets generation, such as `smaller_dataset_generator(dataset_size)`. This function can read the SCADA dataset and produce a smaller dataset by using the specified `dataset_size` as random number. For example, `smaller_dataset_generator(3000, random_number)` will produce a dataset of size 3000 data points from the original SCADA dataset. This function takes the SCADA dataset as input and produces a unique smaller dataset as an output, as shown in Figure 5.9. To produce a different random number each time, this function can be used to generate a new smaller dataset with a new dataset size.

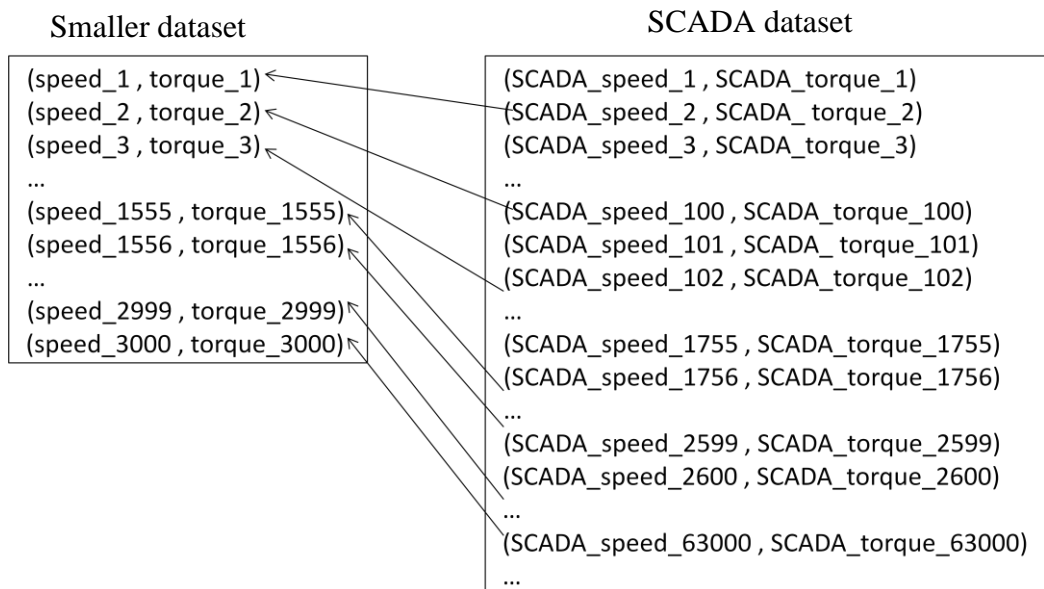


**Figure 5.9: Random number dataset generator**

After selecting the required size of random samples from the original analysed datasets, comparisons between the random samples and the original SCADA analysed datasets are carried out to validate that the generated datasets have similar probabilistic properties of the original analysed datasets. The original analysed and random generated datasets are compared by dividing the data into three portions selected according to the similarity (clustered and dispersed) of histogram data distribution. The comparison results of probabilistic characteristics are discussed in Chapter 8.

### 5.2.4 Probabilistic Analysis of Gear Micropitting

The micropitting analysis is based on the gear micropitting ISO Technical Report ISO/TR 15144-1 (2010) considering important factors and associated parameters that contribute to micropitting occurrence. The gear tooth flanks are subjected to varying loading and rotational speed conditions that cause variation of contact stresses, sliding parameter, local contact temperatures and lubricant film thicknesses. The variations of these parameters are used to assess the micropitting risk as they significantly influence the occurrence of micropitting damage. The specific lubricant film thickness, defined as the ratio between the lubricant film thickness and the mean surface roughness, is used in this study to assess the probability of micropitting failure.

Let  $x$  represents the random variable of the specific lubricant film thickness. A lower limit state function,  $g(x)$ , can be defined as

$$g(x) = x - n \quad (5 - 1)$$

where  $n$ , is a known lower boundary (LB) limit value of  $x$ ,  $g(x) > 0$  denotes the safe region without the probability of failure. The probability of failure,  $P_f$ , occurs when the random variable,  $x$ , is equal to or less than the limit value  $n$ , as shown in Equation 5-2 and illustrated in Figure 5.10. For illustration, the probability density function of random variable  $x$  is represented as the Gaussian distribution. The risk of micropitting failure may be reduced by ensuring that the specific lubricant film thickness,  $x$ , is greater than the lower boundary value of  $n$ , by reducing the effective mean surface roughness.

$$P_f = P(g(x) \leq 0) \quad (5 - 2)$$

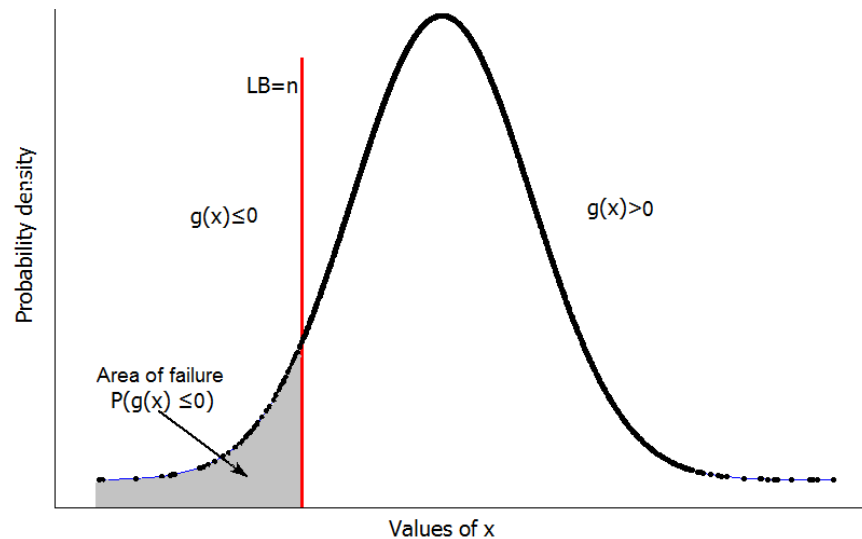


*Figure 5.10: Probability distribution of  $x$*

The micropitting probabilistic failure analysis procedure is outlined in the following steps:

- ❖ Using original SCADA datasets to drive the SCADA analysed datasets of HSS pinion shaft torque and rotational speed, by filtering out the biased data.
- ❖ Using a suitable random number generator to generate smaller datasets representing the SCADA analysed datasets.
- ❖ Checking the validity of the generated smaller datasets by comparing their statistical properties with that of the SCADA analysed datasets.
- ❖ Deriving the probability distributions of the HSS pinion shaft torque and rotational speed.
- ❖ Calculating the contact stresses, sliding parameters, local contact temperatures and lubricant film thicknesses using the values of the smaller datasets.
- ❖ Determining the probability distributions of the contact stresses, sliding parameters, local contact temperatures and lubricant film thicknesses in the form of frequency diagrams.
- ❖ Using the frequency diagram of a specific parameter to identify the failure region resulting micropitting using the lower boundary value recommended by the international standards.

The above probability failure analysis procedure is used to find the probability of micropitting failure using key parameters under the effects of random variations of shaft torque and rotational speed. This procedure can be used for each parameter, such as contact stress or lubricant film thickness, to determine the probabilistic characteristics of the parameter and to identify their contribution to micropitting. Using the generated random samples of HSS pinion shaft torque and rotational speed values a TCS with macros is written (details in Appendix F) to facilitate automatic calculations of 3000 values of gear contact stresses, local contact temperatures, sliding parameters and lubricant film thicknesses at each location of five contact points on gear tooth flank. The TCS results have been validated through comparing its results with those of different commercial software.

### **5.3 SUMMARY**

This chapter presents the analytical and probabilistic assessment procedures to investigate micropitting under rated and varying operational conditions. The WT gearbox SCADA data recorded from operating WTs is used to generate the variation of generator power and rotational speed against the wind speed based on one month recorded data. The histograms of HSS pinion shaft torque ratio and rotational speed ratio of the two WT gearboxes are derived to show the probability density distribution. The Mersenne Twister (MT) is selected to generate smaller datasets of random numbers that represent the SCADA dataset of HSS pinion shaft torque and rotational speed. The analysis procedure and steps of the probabilistic modelling of WT gear micropitting risk are outlined.

## ***Chapter 6: Experimental Results and Analysis Validation***

---

*In this chapter the initiation and progression of micropitting failure under varying torque levels is investigated by carrying out gear testing and surface inspection. Surface inspection procedures, such as surface roughness measurement, replica samples and digital images analysis, and profile scanning are used to observe the micropitting of the tested pinion gear. Initiation and progression of micropitting are assessed by quantifying the development of micropits and their progressive rate after specific numbers of running cycles at step-up torque levels.*

*In addition, the ISO Technical Report of micropitting, ISO/TR 15144-1 (2010), is used to analyse the gear tooth contact stress, sliding parameter, local contact temperature and lubricant film thickness at different contact points along the tooth flank of the tested gear. The analytical study is conducted to validate the analytical solution by comparing the prediction of micropitting with the occurrence of micropits in the testing gears. To check the validity of the analytical calculation, comparisons of the results obtained based on ISO/TR 15144-1 and AGMA925-A03 by using commercial software KISSsoft and their correlation with the experimental results are presented and discussed.*

## 6.1 REPLICA OPTICAL IMAGE ANALYSIS OF MICROPITTING

The experimental tests are performed under varying torque levels with a constant rotational speed to investigate micropitting initiation and progression in gear teeth. Figures 6.1 - 6.7 show the gear surface replicas of pinion gear (driver) tooth number 1 and microscopic inspection at different load levels to observe the micropitting occurrence and development at all test stages, as explained in Chapter 3, Section 3.4.2. At the minimum torque ratio of 0.3, no micropitting is observed as shown in Figure 6.1, but at the torque ratio of 0.4 micropitting occurs at the dedendum as shown in Figure 6.2. Seireg (2001) observed that the micropitting generally occurs early in the operating life of the gears. This micropitting is non-progressive and occurs infrequently along the dedendum area throughout the test, as shown in the microscopic views in Figures 6.2, 6.5, 6.6 and 6.7. However, the micropitting occurs densely and progressively at the dedendum of wheel gear (driven) at high torque ratios of 0.8 to 1.0, as shown in Figures 6.5, 6.6 and 6.7. As the dedendum of wheel meshes with the addendum of pinion, it causes progressive micropitting in the addendum of pinion, as discussed later in Chapter 6, Section 6.5. The micropitting is initiated where the grinding cutting edges are parallel to the tooth face width. These microscopic edges are parallel to the gear axial direction showing the high peaks on the tooth flank as a result of the grinding process, as shown in the microscopic views in Figures 6.2, 6.3 and 6.4. At the end of the test when the tested gears are subjected to higher loads, the micropitting spreads out on most of the tooth surface at various locations, and could easily be seen with the naked eye in both addendum and dedendum areas, as shown in Figure 6.7. It is found that the tooth surface has a series of hills and valleys, and micropitting appears as lines where the peak height of the hills exists in the addendum and dedendum of the tooth flank, as shown in Figures 6.5, 6.6 and 6.7. This result was also observed by Brechot et al (2000), Snidle et al (2004) and Morales-Espejel and Brizmer (2011).

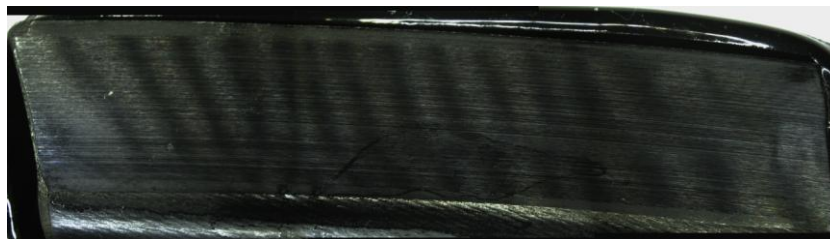


*Figure 6.1: Replica of pinion flank surface at torque ratio 0.3, no micropitting observed*



*Figure 6.2: Replica and microscopic view of pinion flank surface at torque ratio 0.5: micropitting observed at dedendum*

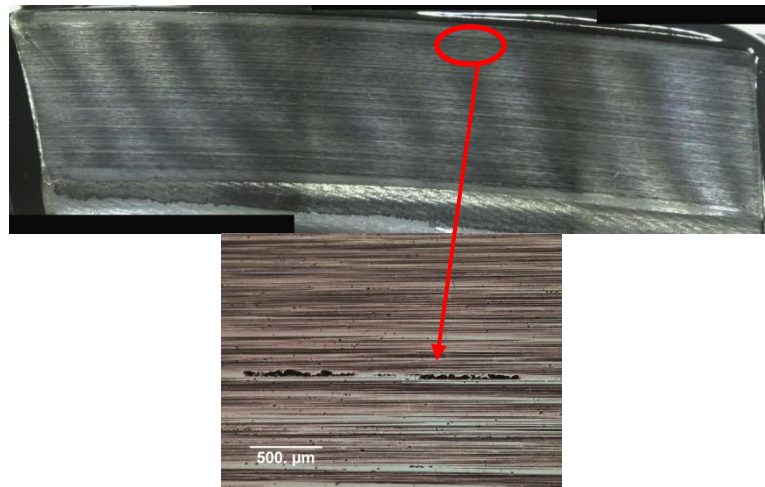


*Figure 6.3: Replica and microscopic view of pinion flank surface at torque ratio 0.6: micropitting observed at addendum*

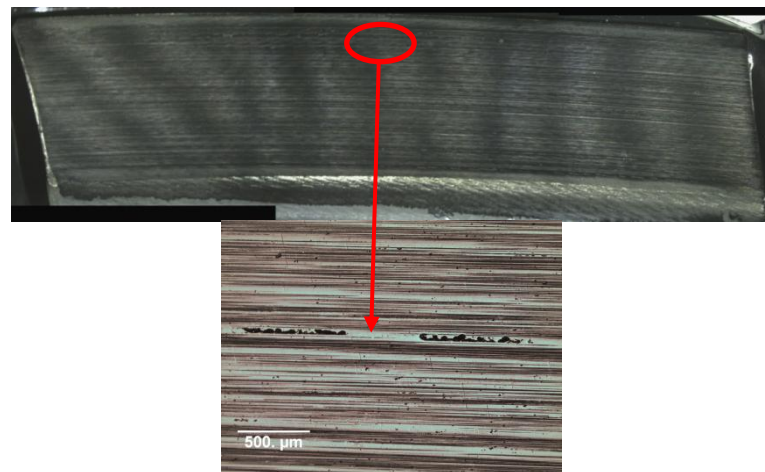


*Figure 6.4: Replica and microscopic view of pinion flank surface at torque ratio 0.7: micropitting observed at addendum (very little progress observed between torque ratio 0.6 and 0.7)*

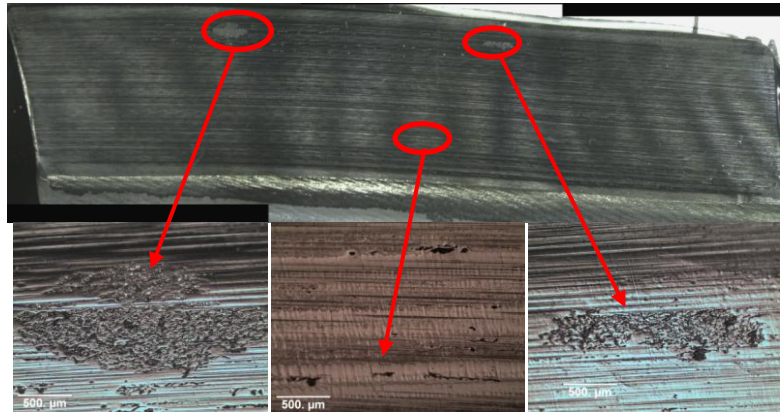


**Figure 6.5:** *Replica and microscopic views of pinion flank surface at torque ratio 0.8: micropitting at dedendum appeared as spots and at addendum developed progressively by comparing with Figures 6.2, 6.3 and 6.4*

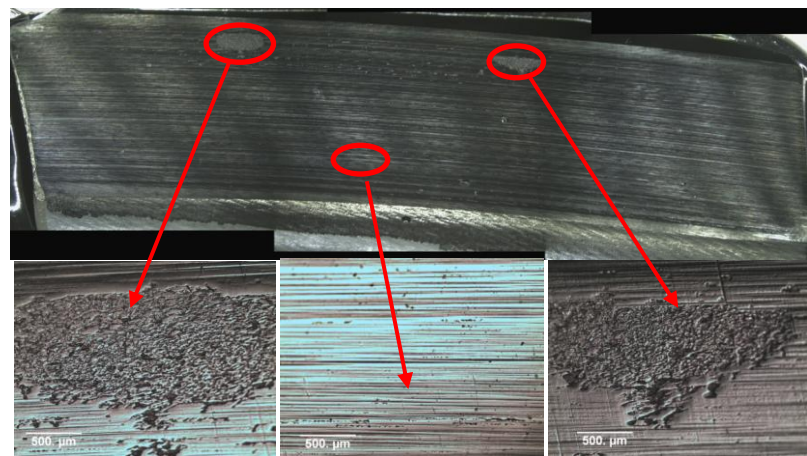


**Figure 6.6:** *Replica and microscopic views of pinion flank surface at torque ratio 0.9: micropitting at dedendum with little progress but at addendum developed progressively and densely*

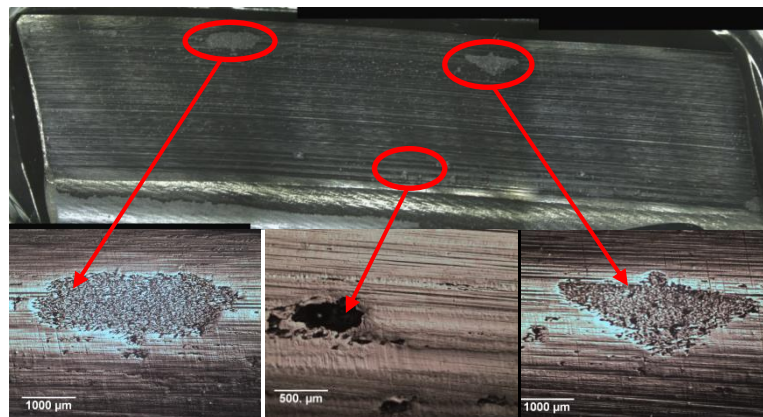


**Figure 6.7:** *Replica and microscopic views of pinion tooth flank surface at torque ratio 1.0: micropitting at dedendum with more progress but at the addendum developed progressively and densely with bigger micropitting area compared with torque ratio 0.9*

In addition to the above surface replicas and microscopic observations, some illustrations representing the areas of micropitting occurrence, their shapes and sizes on the teeth of pinion gear are produced, as shown in Table 6-1. The micropitting spreads

out in both dedendum and addendum of the pinion tooth flank, but it prevails at the pinion addendum as the result of progressive micropitting at the dedendum of the wheel. The micropitting area at the pinion dedendum is smaller than that at the addendum area, however deeper pits occur at the dedendum. This is further explained in the profile deviation results in Section 6.3. Dudley (1994) tested helical gears of same hardness with gear ratio of 4 to 1 but a transmission of using wheel to drive pinion. The author found that the micropitting occurred in wheel first but he did not specify if the micropitting first occurred at addendum or dedendum. In the present research, the pinion is used as driver and the micropitting initiates at dedendum first but non-progressively while progressive micropitting occurs at addendum. Due to the fast micropitting progression at wheel dedendum it escalates the micropitting in the mating pinion addendum. Moreover, the sliding direction at the addendum area of pinion is the same as rolling direction which apt to pull the material away from the pitch line towards the tip, as shown in Figure 2.14 and explained in Section 2.5 of Chapter 2. Dudley (1994) confirmed that the pitting can occur at addendum area of a driven wheel due to the severe load. Similar to Dudley's results, in the experimental tested gears in this study micropitting occurs as a result of severe load. The difference in teeth number of the tested gears is only one tooth as shown in Table 3-2, Chapter 3. This might indicate that addendum and dedendum of both gears have a chance of pitting occurrence as shown in Figure 6.8 and Table 6-1. However, the difference in micropitting initiation and progression over the surfaces areas of gear teeth may be attributed to the different values of surface roughness as explained in Section 6.2. More experimental investigations are needed to investigate if using wheel as driver affects the position of micropitting initiation.

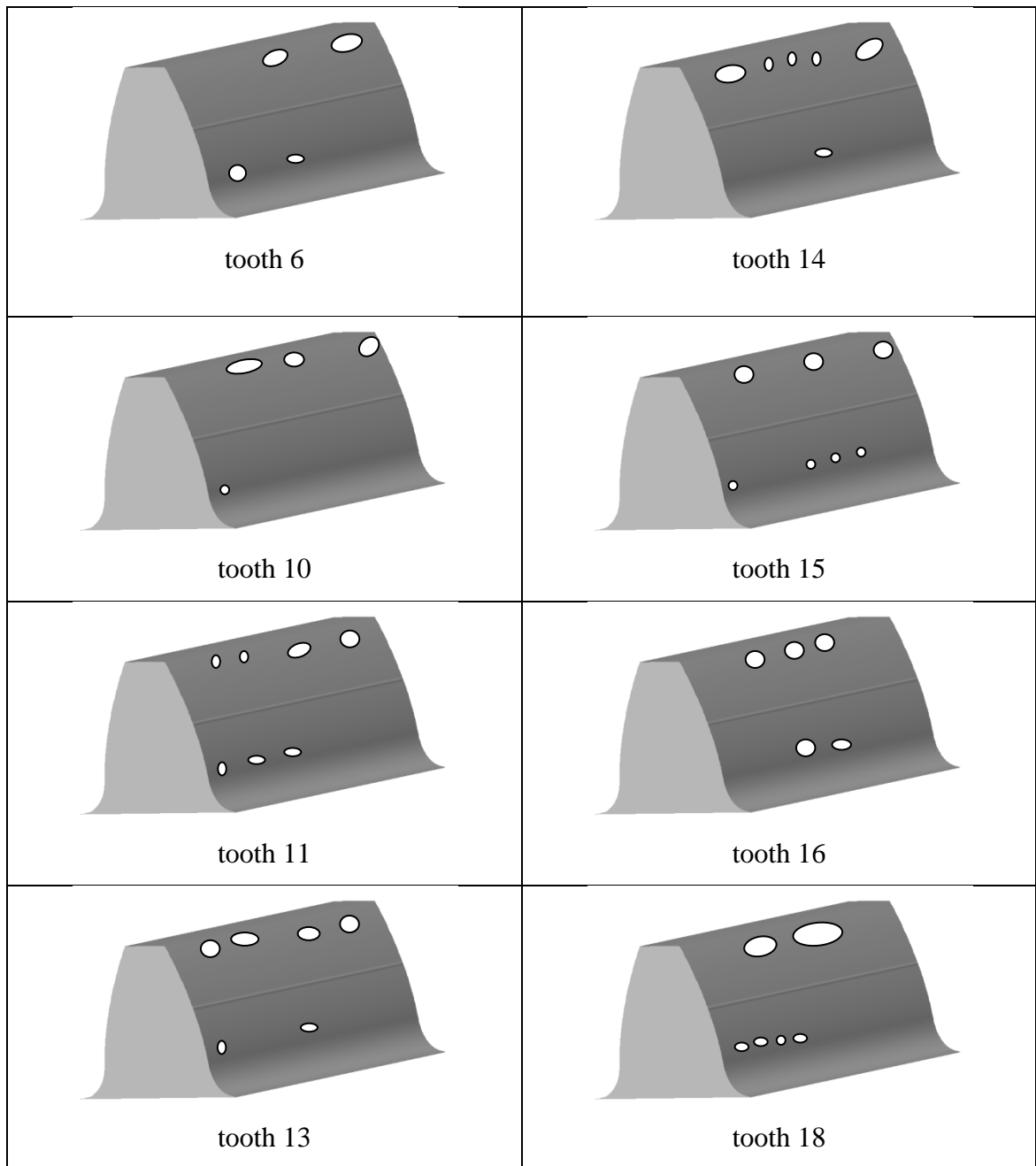
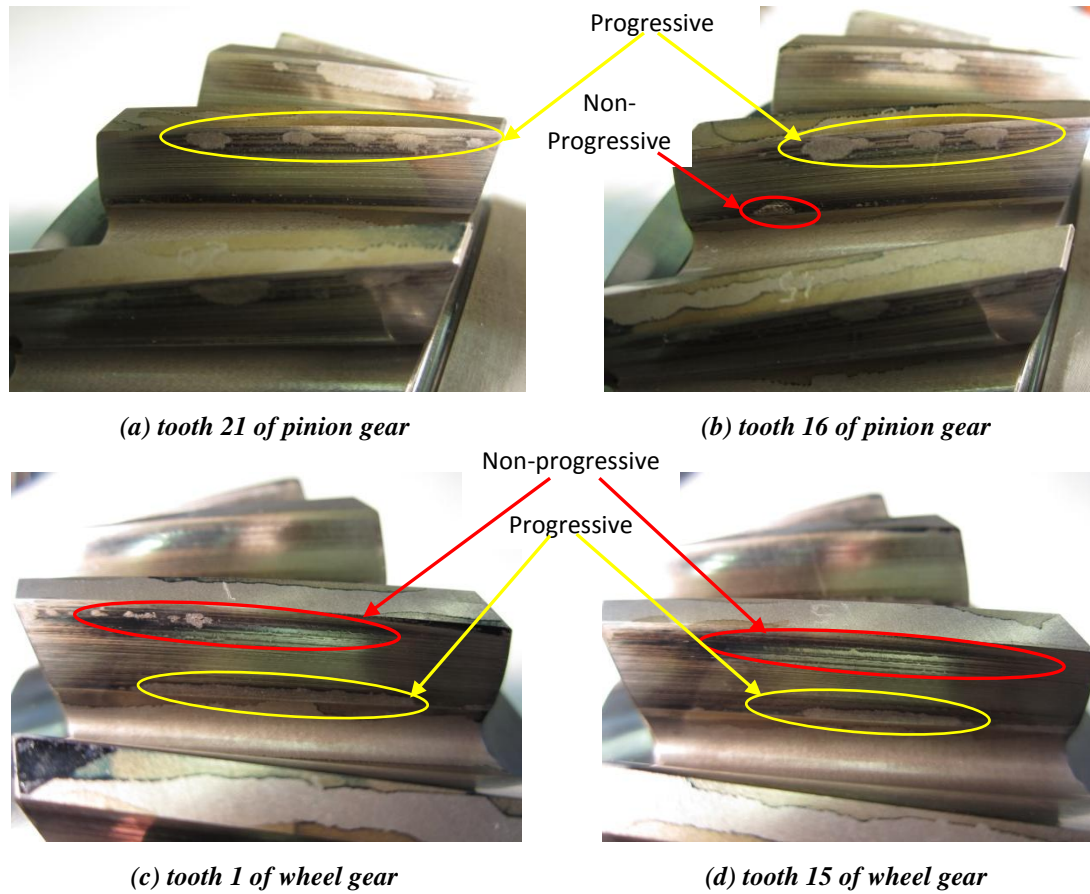
*Table 6-1: Micropitting occurrence at various teeth of pinion at torque ratio 1.0*

Figure 6.8 shows the surface damages in mating gear teeth of pinion and wheel. These images illustrate how the micropitting spreads out on tooth flanks of the pinion and wheel after being subjected to different levels of load. The wheel has non-progressive micropitting at the addendum area as shown in Figure 6.8 (C) and (d). It is clear that the wheel gear has more progressive micropitting at the dedendum which almost covers about 60–70% of the wheel dedendum area along the face width. Thus, the addendum of pinion gear is prone to more progressive micropitting as shown in Figure 6.8 (a) and (b).

The observation reveals that the micropitting can initiate at the dedendum and/or at the addendum, but the area of fast progression can trigger the initiation of micropitting in the mating tooth surface. Table 6-2 summarises the initiation and progression of micropitting under different torque levels.



**Figure 6.8: Progression of micropitting of mating gear teeth**

**Table 6-2: Summary of the micropitting progression under different torque levels**

Seq. No.	Cycles No. (millions)	Torque ratio	Contact stress at pitch point (MPa)	Test results
1	8	0.3	1076	no micropitting
2	8	0.5	1332	initial micropitting
3	8	0.6	1452	slight progression of micropitting
4	8	0.7	1563	very little progression of micropitting
5	8	0.8	1666	increased progression of micropitting
6	8	0.9	1763	micropitting appeared in some areas
7	8	1	1855	micropitting appeared in most areas

## 6.2 SURFACE ROUGHNESS ANALYSIS

The surface roughness measurements, which are obtained through stylus instrument of pinion gear in the radial direction facilitate detailed observations of features of contact surfaces such as the peaks and valleys. The surface roughness measurements show that the tooth surface roughness is changed after every cycle run under different torque levels, as shown in Figures 6.9 - 6.12 (complete results are included in Appendix G). The comparisons between the values of surface roughness illustrate that the peak values of surface roughness deteriorate after each cycle run. The peaks decrease from 1.42 to 0.76  $\mu\text{m}$ , but the valleys increase from 2.2 to 2.6  $\mu\text{m}$ , at unloaded and after loaded to torque ratio of 1.0, as the comparison of Figures 6.9 and 6.12 reveals. The surface roughness of pinion gear ( $R_a$ ) has a steady trend of decrease, as Figure 6.13 shows; however, it increases slightly by about 0.01  $\mu\text{m}$  at torque ratio 0.7. This may be because of sliding motion apt to pull the material away from the pitch line as the micropitting starts to spread out. The deeper valleys of the tooth surface indicate that some material is removed from the tooth surface as the micropitting spreads on the tooth flank. The  $R_z$  value shows that the peak to valley height is decreased in some areas after each cycle run, as shown in Figure 6.14. The slight increase of  $R_z$  at torque ratio 1.0 may indicate that the deep valleys are present, and the difference between the peaks and valleys is increased owing to micropits occurrence on the tooth flank.

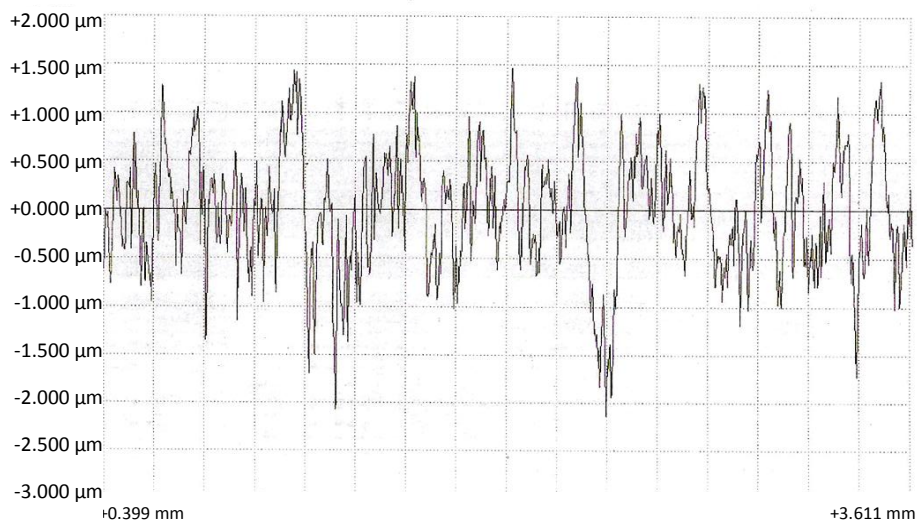


**Figure 6.9:** *Tooth surface roughness of pinion before being tested (0 cycle)*

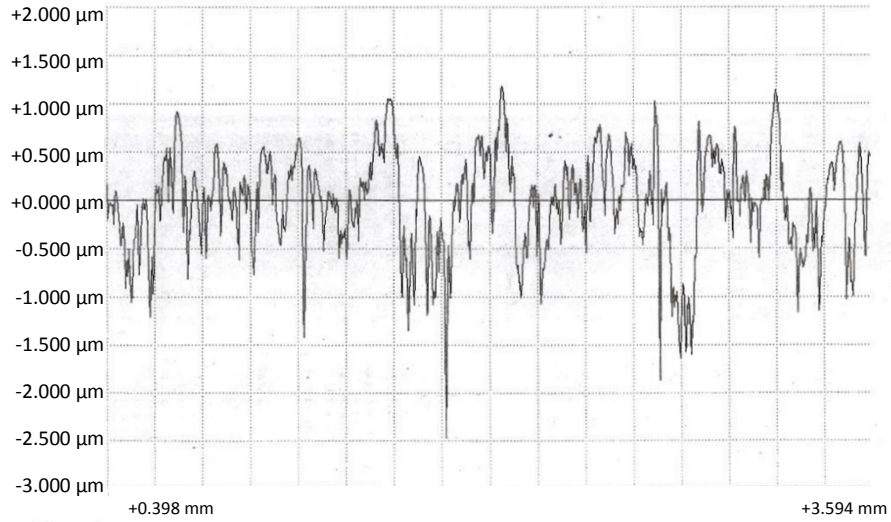


**Figure 6.10:** *Tooth surface roughness of pinion after being tested at torque ratio of 0.3*

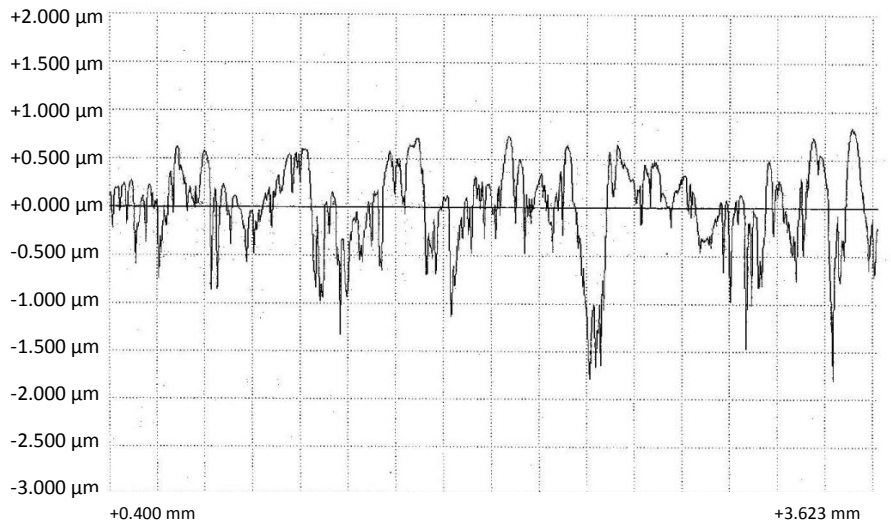


**Figure 6.11:** *Tooth surface roughness of pinion after being tested at torque ratio of 0.7*

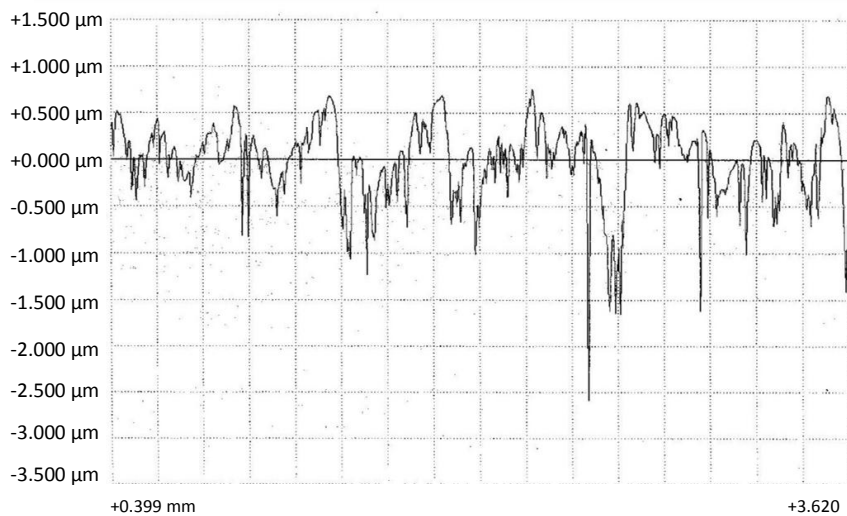


**Figure 6.12:** *Tooth surface roughness of pinion after being tested at torque ratio of 1.0*

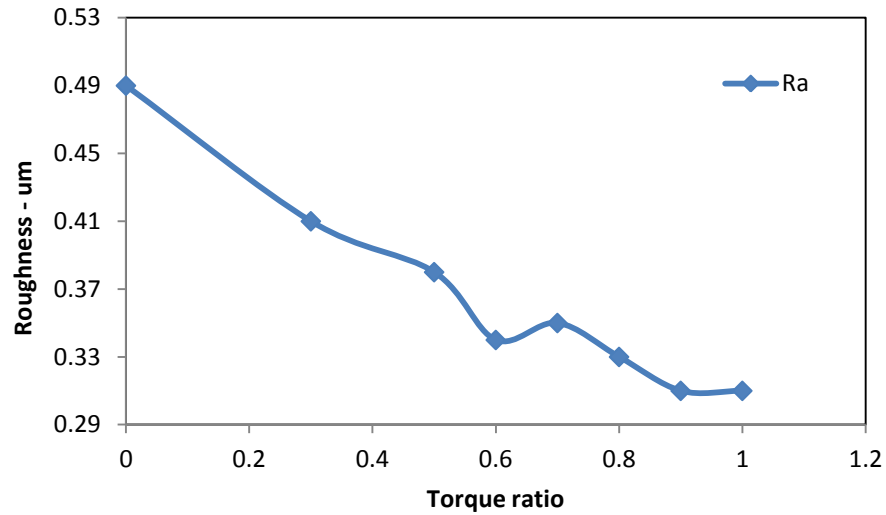


*Figure 6.13: Tooth surface roughness values Ra after being tested at different torque ratios*

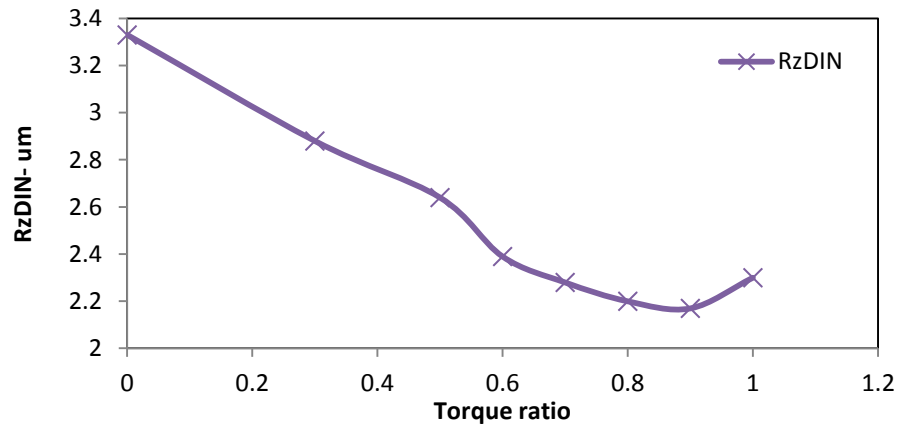


*Figure 6.14: Tooth surface roughness values Rz after being tested at different torque ratios*

### 6.3 PROFILE DEVIATION ANALYSIS

The tooth profile deviation is measured after the cycle run at the torque ratio of 1.0, which induces the maximum contact stress on the gear teeth. At this stage the micropitting spreads over most surfaces areas of gear teeth. The damaged areas of tooth number 1 for the pinion and wheel, as well as the tooth profile deviation measurements for teeth number 1, 7, 13 and 19 are shown in Figures 6.15 and 6.16. The maximum value of profile deviation of pinion gear occurs at the dedendum, located about 151.5 mm from the base circle of the pinion. Moreover, the profile deviation occurs at the addendum located at about 164.3 mm (near the beginning of the tip relief) from the base circle of the pinion. The area near the beginning of tip relief of tooth number 7 starts to erode compared with that of tooth number 1, 13 and 19, as shown in Figure 6.15.

The tooth profile deviation caused by micropitting at the dedendum area of the wheel locates about 158 mm from the base circle (155.08 mm), as shown in Figure 6.16. The deviation of wheel gear teeth is greater and the micropit is deeper than that on the pinion gear. It is clear that the profile deviation of wheel teeth extends from base circle (diameter of 155.08 mm) to the pitch line position (diameter of 163.2 mm), and from the pitch line to the tip circle (diameter of 175.24 mm) of the wheel. This indicates that the micropitting on the surface of driven gear can lead to the loss of the tooth profile from root to tip. This can result in loss of transmission efficiency and increase the level of vibration, which further affects the gear tooth meshing accuracy and causes additional stress concentration on the micropitting area. It is noted that for both gears the micropitting at the dedendum is deeper than that of addendum, as illustrated by the results of the profile measurement. As shown in Figure 6.7, the pits at the middle of the dedendum shapes like a shell, which indicates that profile loss or deep pitting have occurred in this area. The tooth number 1 of tested pinion gear has a greater profile deviation at dedendum compared with that of tooth number 7, 13 and 19, as shown in profile measurement in Figure 6.15. This maximum profile deviation, of 5  $\mu\text{m}$  in depth and about 4 mm in length, occurred at the dedendum area of tooth number 1.

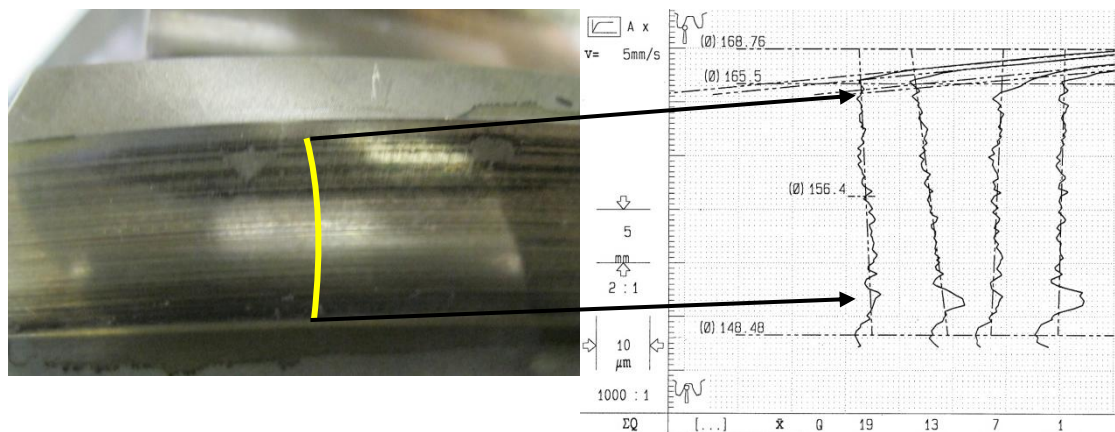


**Figure 6.15: Tooth profile deviation of pinion**

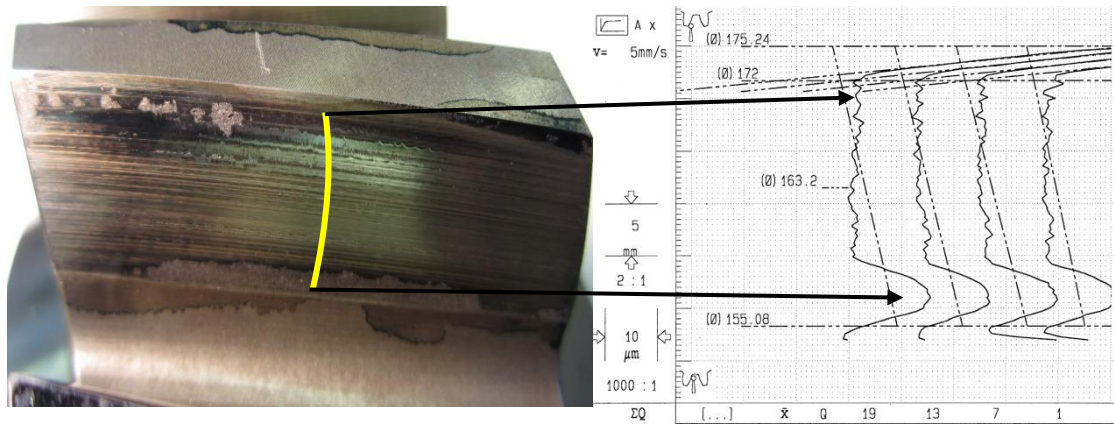


*Figure 6.16: Tooth profile deviation of wheel*

## 6.4 VALIDATION OF ANALYTICAL METHOD AND CALCULATION

To validate the analytical calculations conducted using ISO Technical Report ISO/TR 15144-1, a comparison between the results obtained from the developed toolkit calculation sheet (TCS) and commercial software KISSsoft, is carried out. The KISSsoft software is used for the comparison as it provides different analysis methods integrated into this software. Two different approaches (ISO/TR 15144 and AGMA 925-A03) are used to compare the results. To correlate analytical results with the initiation of micropitting, two cases of experimental tests at two different torque ratios are considered. One is at torque ratio of 0.5 when micropitting starts to occur and the other is at the maximum torque ratio of 1.0.

The comparison involves contrasting the results obtained by ISO/TR and AGMA standard through applying the KISSsoft gear design software. In addition, the results from the TCS are compared with the results obtained from the Technical Report ISO/TR 15144-1 by using the KISSsoft software. The comparison focuses on contact stress, local contact temperature, lubricant film thickness and specific lubricant film thickness.

### Comparison of contact stress at pitch point

A preliminary comparison of contact stress results at the pitch point is carried out to ascertain the validity of the TCS. The contact stress results at the pitch point from three different software, KISSsoft, Dontyne and eAssistant are compared with that obtained from the TCS. The detailed comparison of geometry, material, operating conditions and other different parameters using different software is provided in the tables and sheets in

Appendix H. The pitch point serves as an ideal comparison area because it can be easily located along the tooth flank of the tested gear compared to other contact points. As shown in Figure 6.17, there are negligible differences between the results obtained from the TCS and other software. The differences in contact stresses range between 2% and 10% which can be attributed to the difference in values of load factors, such as the dynamic factor and transverse load factor, used in different software. However, due to the differences in determining these factors (because of the different methods provided in ISO 6336-1 (2006) standard, as explained in Chapter 4, Section 4.1) the differences in contact stress results lead to subsequent differences in local contact temperature and lubricant film thickness results.

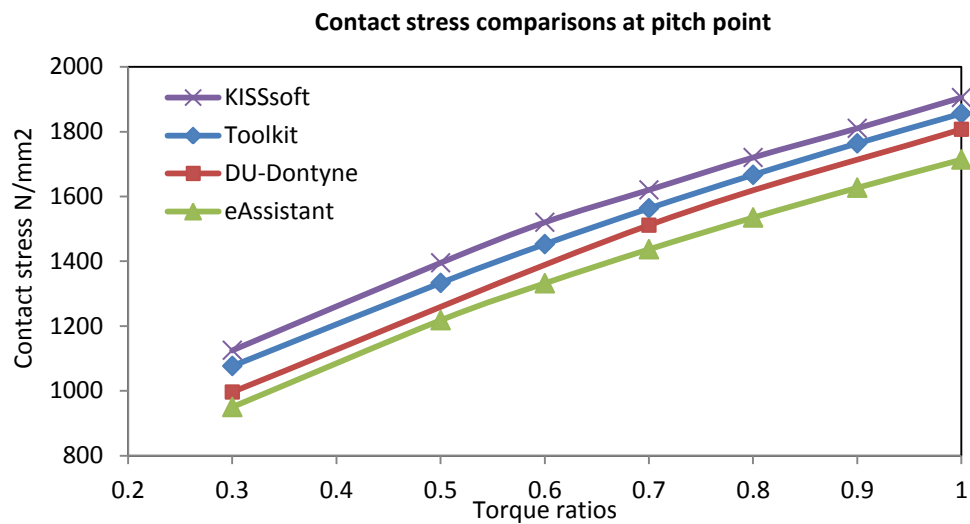
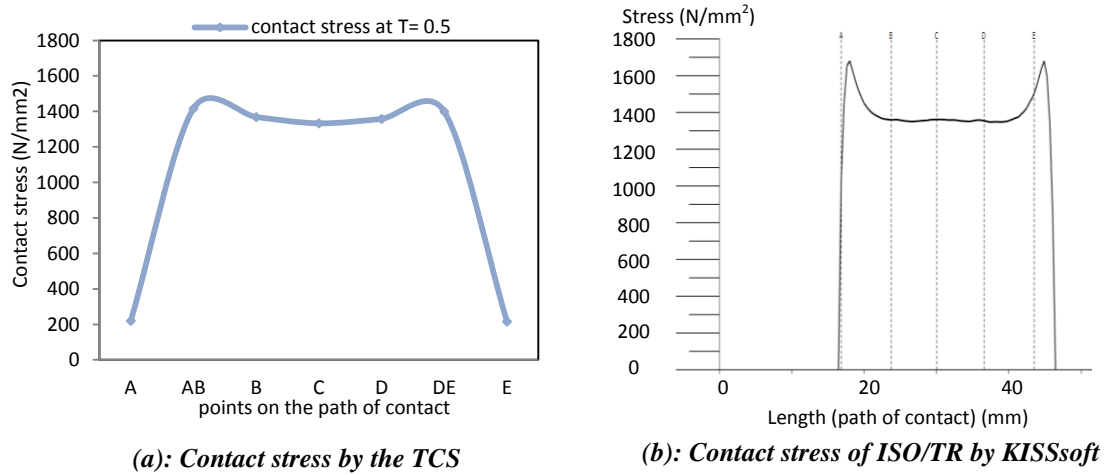


*Figure 6.17: Contact stress comparison at pitch point using different software*

### 6.4.1 Comparison at 0.5 Torque Ratio

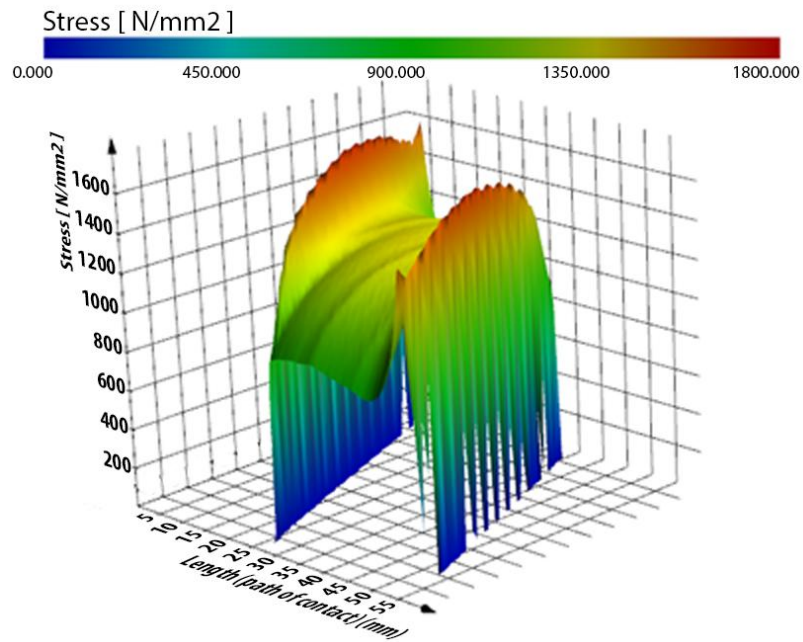
#### Contact stress

Figure 6.18 (a) and (b) reveals that the trend shapes in both the TCS (a) and the KISSsoft (b) have similar distributions of contact stress along the path of action and it shows close results with a trivial difference that does not exceed 13%.



**Figure 6.18: Comparisons of contact stresses at 0.5 torque ratio**

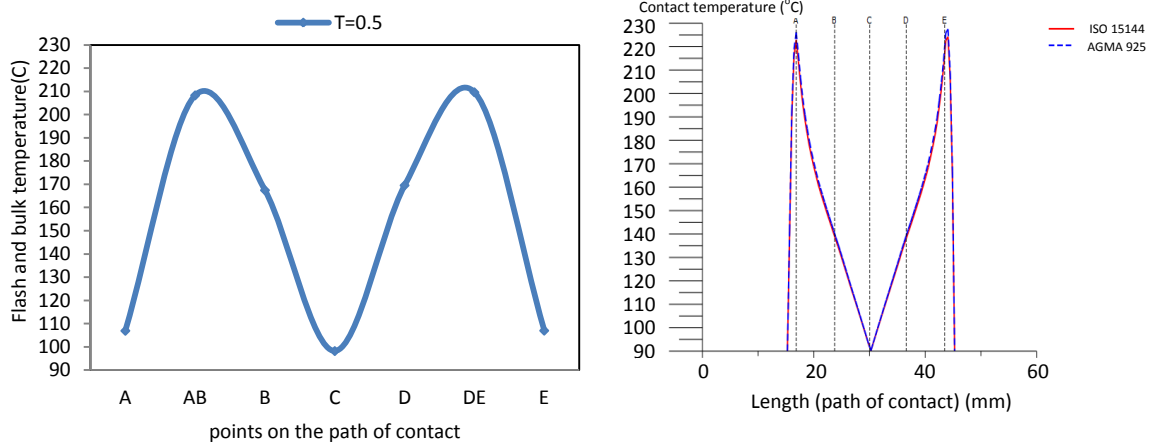
The differences in results are attributable to that the TCS considers only seven points along the path of contact, while the commercial software uses a very fine mesh considering more than 50 contact points along the path of contact. This is illustrated in 3D distribution of contact stresses, contact temperatures and lubricant film thicknesses as shown in figures 6.19 and 6.27, 6.21 and 6.29, 6.23 and 6.31 respectively. These various factors may affect the results as they may be located at different locations along the tooth flank different from those used in the toolkit. A possible further cause of this difference is that some software does not offer parameter modification such as lubricant and material parameters. In addition, some commercial software (KISSsoft) considers the variation of gear mesh stiffness at different rotational positions on the tooth flank. In contrast, a single gear mesh stiffness is used in the TCS. The variation of mesh stiffness requires a consideration of the micro-geometry and a very fine mesh along the line of action and along the face width. The mesh stiffness variation affects the load factors such as the face load and dynamic factors. The following figures illustrate the comparisons between the results obtained from the TCS based on ISO/TR and the KISSsoft results using ISO/TR and AGMA standard.



*Figure 6.19: 3D contact stress distribution by KISSsoft at 0.5 torque ratio*

### Contact temperature

Both ISO Technical report ISO/TR 15144 and AGMA 925-A03 standard are based on the Blok equation to determine the flash temperature. However, there are small differences between the analysis procedures of the ISO/TR and AGMA when obtaining the flash temperature. This leads to differences in gear surface temperature results which are mainly attributed to the numerous factors considered in calculating the mean coefficient of friction in ISO/TR 15144-1 Technical Report, as discussed in Chapter 4, Section 4.3. As indicated by Figure 6.20 (b), there are very minor differences in contact temperature values between the ISO/TR and AGMA standard due to using the same Blok equation. As shown in Figure 6.20 (a) and (b), the toolkit and the KISSSoft have similar local contact temperature results based on the ISO/TR and AGMA methods. The differences do not exceed 8%, which can be caused by the differences in contact stress and lubricant and material parameters used, as explained earlier.



(a): Local contact temperature by the TCS

(b): Comparisons of contact temperature of ISO/TR and AGMA methods by KISSsoft

Figure 6.20: Comparisons of contact temperatures at 0.5 torque ratio

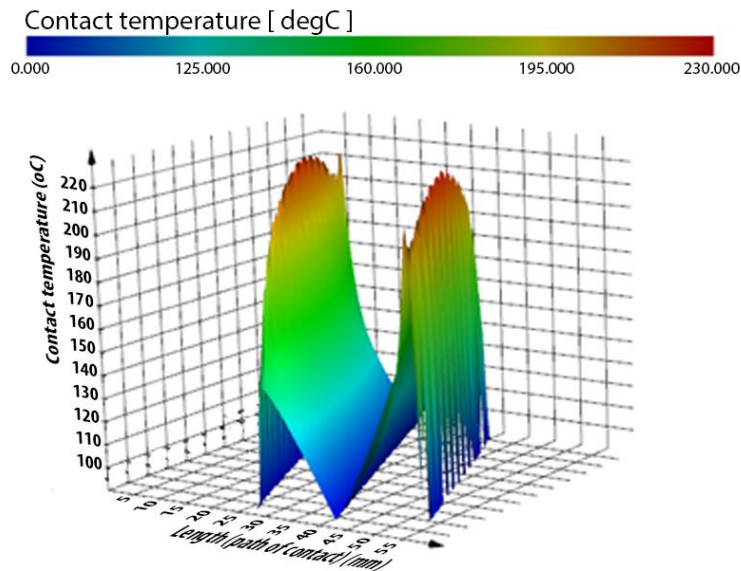


Figure 6.21: KISSsoft result of 3D local contact temperature by KISSsoft at 0.5 torque ratio, considering fine mesh points along the line of action

### Lubricant film thickness

The comparisons of lubricant film thickness between the toolkit result, Figure 6.22 (a), and KISSsoft result using ISO/TR methods, Figures 6.22 (b) and 6.23, show that the distributions of variation are very similar. However, the actual values are slightly different due to the differences in the contact stress and contact temperature results. Figure 6.22 (b) shows that the AGMA standard predicts higher values of lubricant film thickness than those of ISO/TR. By considering the minimum values of lubricant film thickness where the high risk of micropitting occurs along the path of contact, the

AGMA minimum value is about 1.1  $\mu\text{m}$  while the ISO/TR is about 0.35  $\mu\text{m}$ , as shown in Figure 6.22 (b). This big difference can be attributed to the fact that the AGMA calculates the line contact central film thickness while the ISO/TR uses the local lubricant film thickness, as discussed in Chapter 4, Section 4.3. The lubricant film thickness result obtained by the TCS is about 1.0  $\mu\text{m}$  at the mesh in/out regions while in the KISSsoft it is about double that value. This difference can be attributed to the difference in the considered position of load sharing factor contact points along the path of contact. The contact stresses results in KISSsoft are equal to zero (before and after mesh in/out regions) whereas these are about 200  $\text{N}/\text{mm}^2$  (mesh in/out regions) using the toolkit at these areas, as the comparison Figures 6.18 (a) and 6.18 (b) reveal.

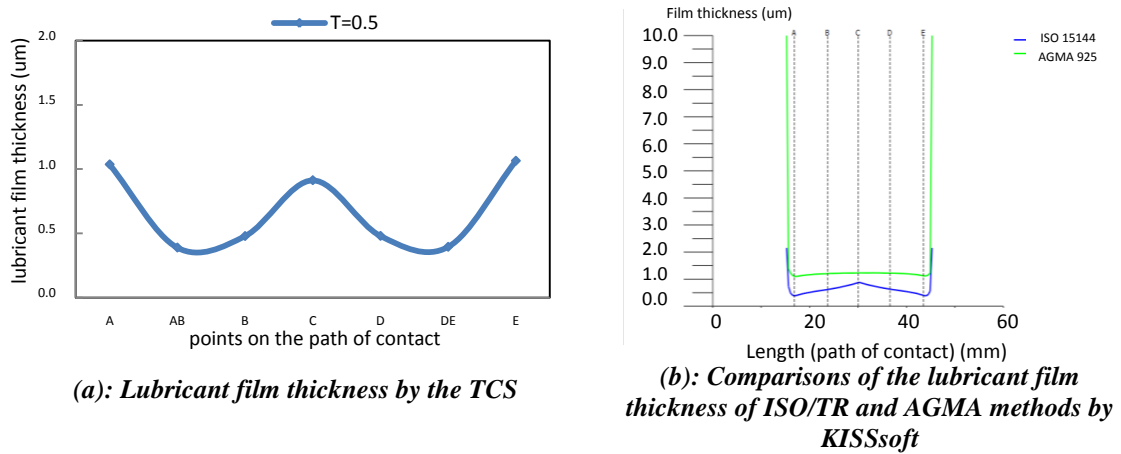


Figure 6.22: Comparisons of lubricant film thicknesses at 0.5 torque ratio

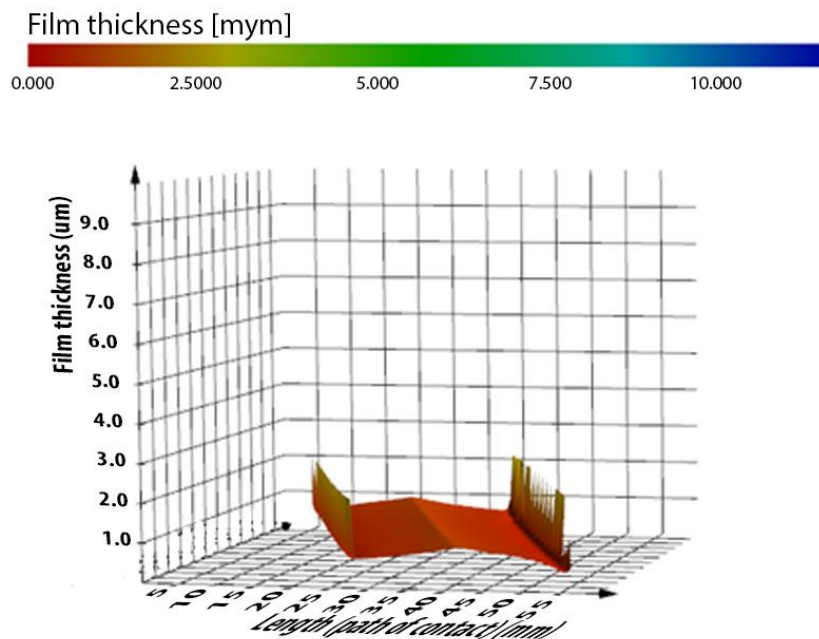
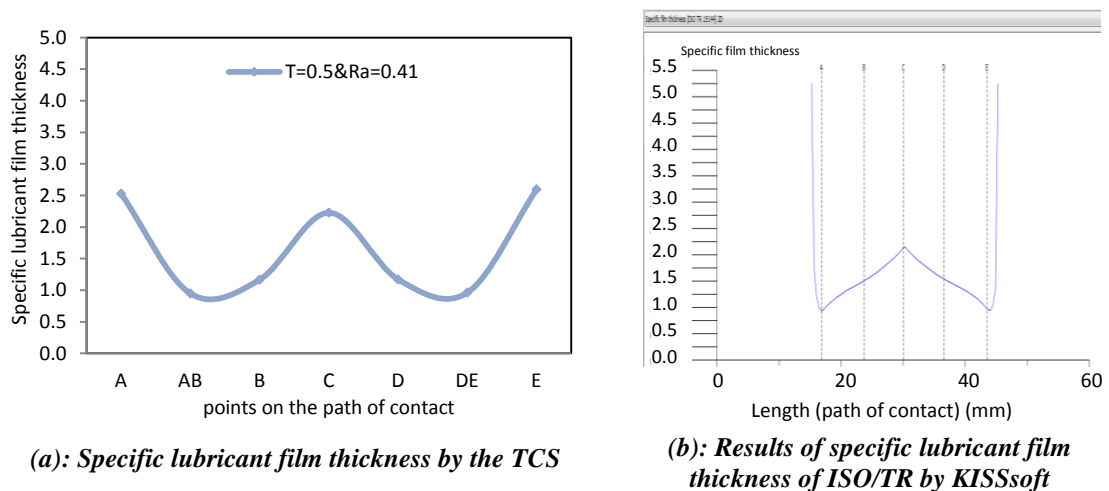


Figure 6.23: 3D distribution of lubricant film thickness of ISO/TR by KISSsoft

### Specific lubricant film thickness

The comparison of the specific lubricant film thickness results show that there is a good agreement between the TCS and KISSsoft, Figure 6.24 (a) and (b). The differences at points AB and DE do not exceed 11% at the minimum values of lubricant film thickness where the high risk of micropitting is predicted. This small difference can be explained by the differences in local flash temperature and contact stress. However, the KISSsoft reveals a big difference between the ISO/TR and AGMA results of the minimum specific lubricant film thickness; it is about 0.9 in ISO/TR but about 2.45 in the AGMA standard. This is owing to the different calculation methods used in calculating the lubricant film thickness. Moreover, The ISO/TR and AGMA use different methods to determine the effective surface roughness in order to obtain the specific lubricant film thickness. The ISO/TR uses the mean surface roughness, while the AGMA uses the root mean square surface roughness of meshing gear teeth. For instance, the ISO/TR uses the minimum lubricant film thickness and considers the sliding parameter along the path of contact while AGMA uses the dynamic viscosity at the mean tooth temperature in order to determine the central film thickness. Thus, the ISO/TR and AGMA results of specific lubricant film thickness have a big difference, as the comparison between Figures 6.24 (b) and 6.25 shows. In addition, other factors, such as that the ISO/TR considers more load factors when determining the mean coefficient of friction as explained earlier, influence these results. Thus, the calculation of the lubricant conditions along the path of contact using AGMA method produces higher results than those using the ISO/TR method.



**Figure 6.24: Comparisons of specific lubricant film thicknesses at 0.5 torque ratio**

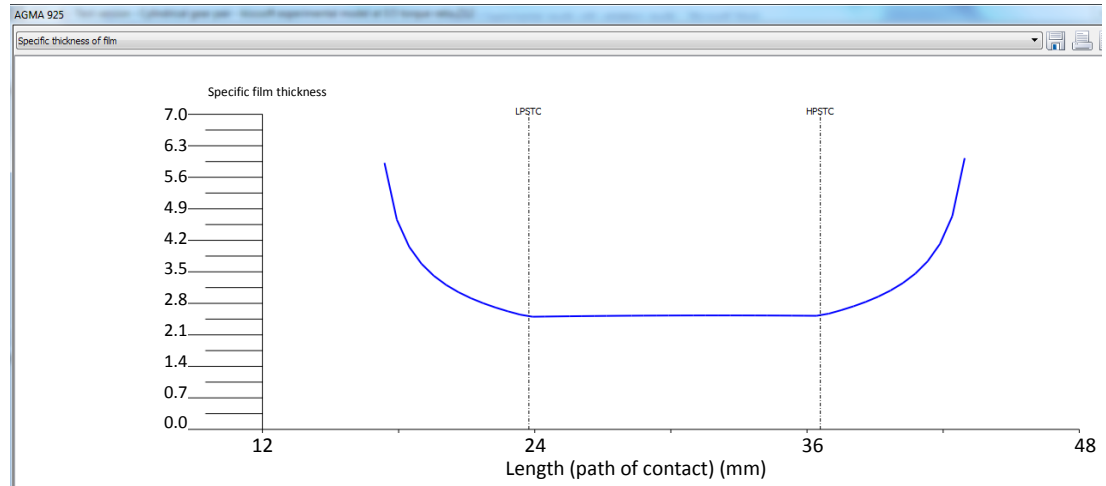
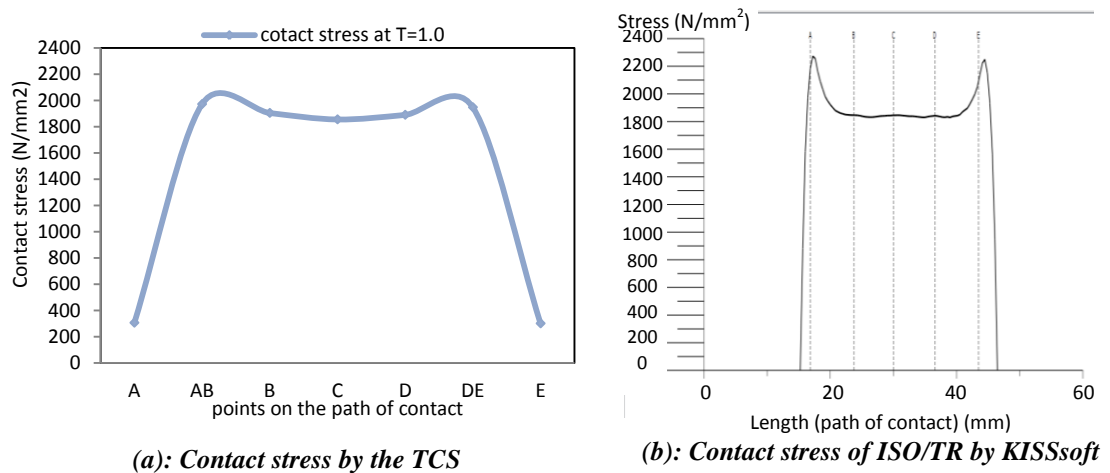


Figure 6.25: Specific lubricant film thickness of AGMA by KISSsoft at 0.5 torque ratio

### 6.4.2 Comparisons at 1.0 Torque Ratio

#### Contact stress

The contact stress distribution results at torque ratio 1.0, shown in Figures 6.26 (a) and 6.26 (b), are similar; where the difference between the toolkit and the KISSsoft results is about 9% when comparing the highest contact points (AB and DE). The differences can be attributed to the variation of loading factors; as the torque increases, the differences in load factors increase leading to an increase in contact stress results. Furthermore, the differences may be due to the toolkit calculation points' different locations along the tooth profile, as explained earlier. Additional results of contact stress, local contact temperature and specific lubricant film thickness at 1.0 torque ratio, using Dontyne commercial software, are provided in Appendix I. In addition, a report of detailed results obtained at 1.0 torque ratio using KISSsoft is included in Appendix J.



(a): Contact stress by the TCS

(b): Contact stress of ISO/TR by KISSsoft

Figure 6.26: Comparisons of contact stresses at 1.0 torque ratio

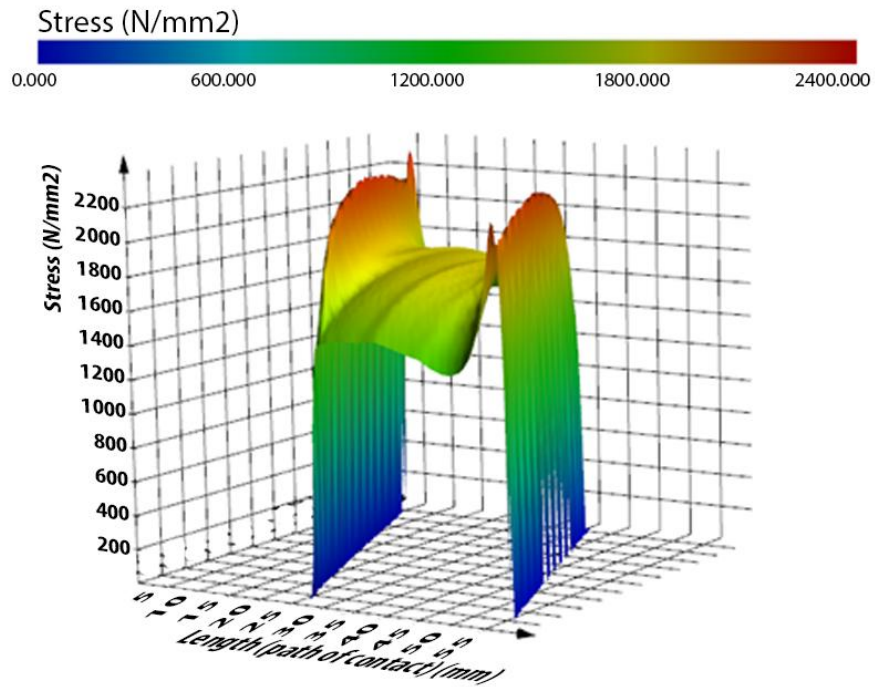
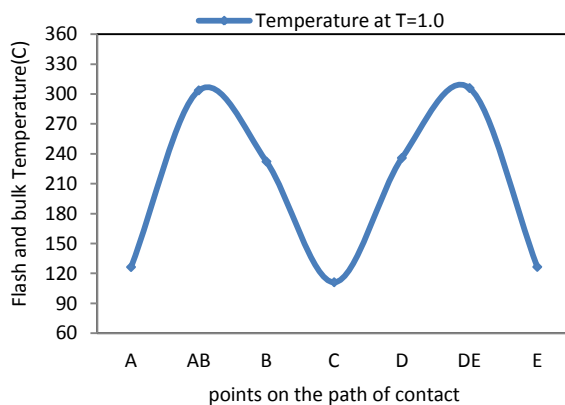


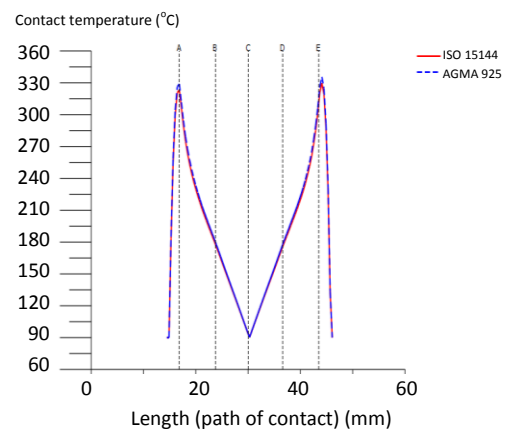
Figure 6.27: 3D contact stress distribution by KISSsoft at 1.0 torque ratio

### Contact temperature

The toolkit and the KISSSoft, using both AGMA and ISO/TR methods, have roughly approximate results pertaining to local contact temperature at 1.0 torque ratio. The comparison reveals differences of about 9% owing to the differences in contact stress, different contact location along the tooth profile as well as other lubricant and material parameters, as explained earlier.



(a): Local contact temperature by the TCS



(b): Comparisons of contact temperature of ISO/TR and AGMA methods by KISSsoft

Figure 6.28: Comparisons of contact temperatures at 1.0 torque ratio

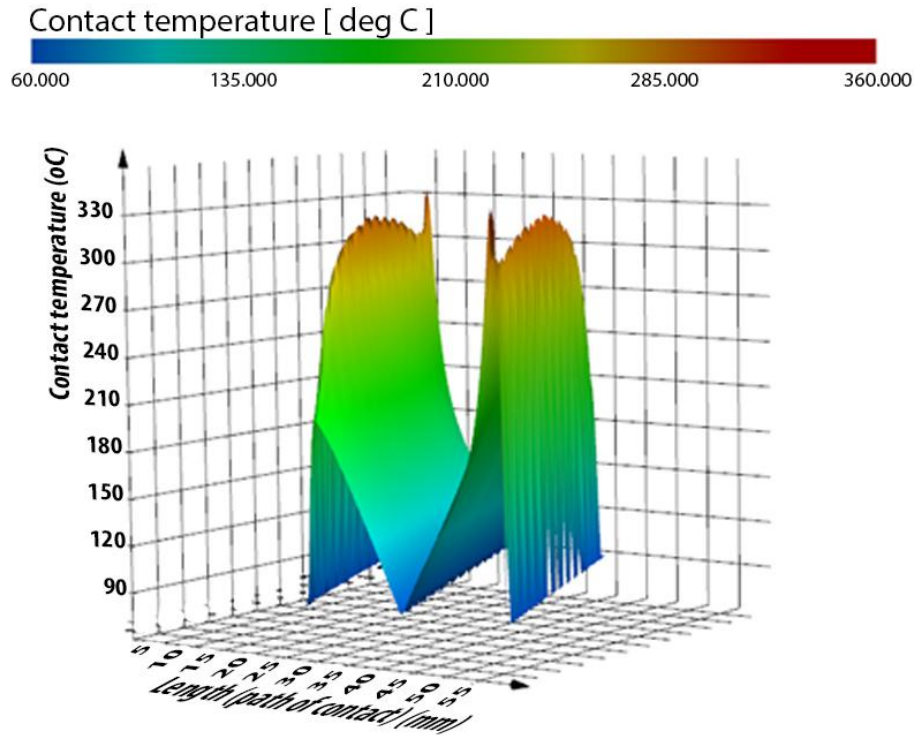
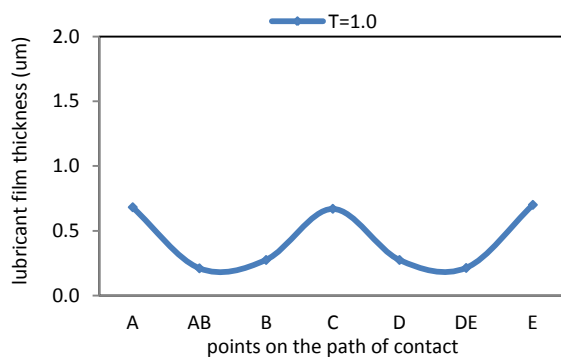


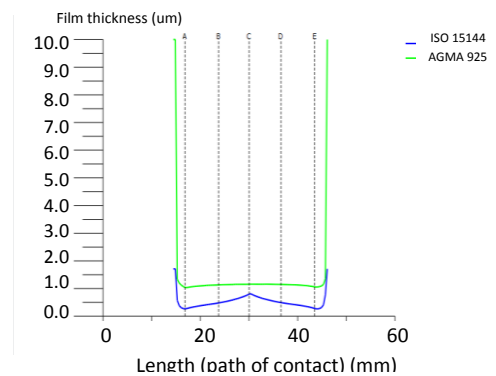
*Figure 6.29: KISSsoft result of 3D local contact temperature by KISSsoft at 1.0 torque ratio, considering fine mesh points along the line of action*

**Lubricant film thickness**

Similar to the results at 0.5 torque ratio, the comparison between the results of lubricant film thickness obtained from the toolkit and KISSsoft using ISO/TR, Figure 6.30 (a) and (b), shows close results. However, the AGMA standard produces higher values of lubricant film thickness, as shown in Figure 6.30 (b).



*(a): Lubricant film thickness by the TCS*



*(b): Comparisons of the lubricant film thickness of ISO/TR and AGMA methods by KISSsoft*

*Figure 6.30: Comparisons of lubricant film thicknesses at 1.0 torque ratio*

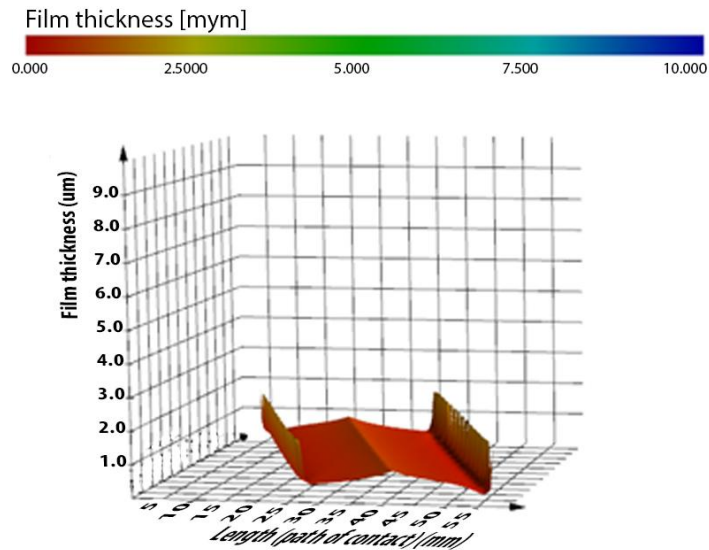
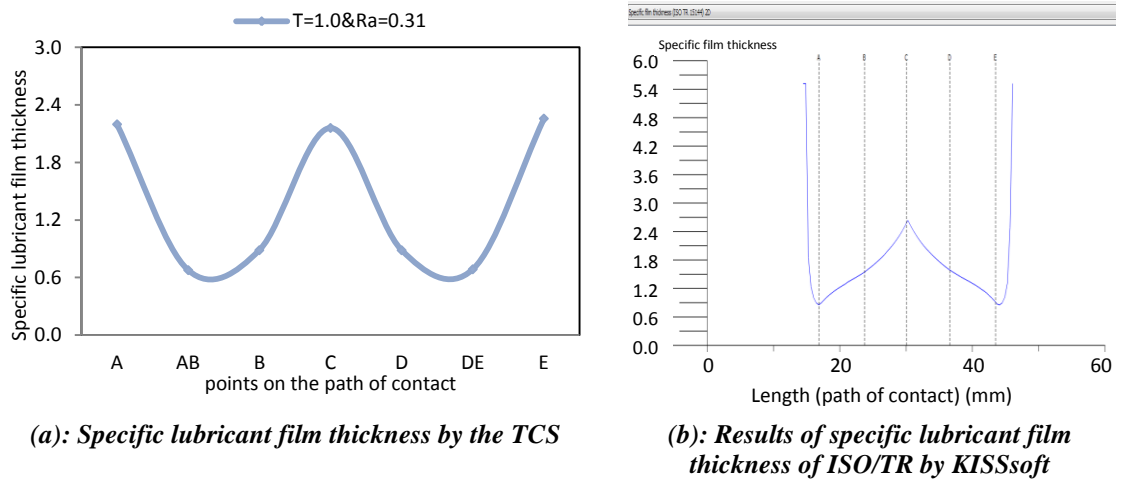


Figure 6.31: KISSsoft result of 3D lubricant film thickness

**Specific film thickness**

For the specific film thickness results, there is a good agreement between the TCS and KISSsoft ISO/TR results, as shown in Figures 6.32 (a) and 6.32 (b). However, a big difference is found between the ISO/TR and AGMA results, which is also found and explained in 0.5 torque ratio results. The minimum specific lubricant film thickness is about 0.7 at contact points AB and DE using ISO/TR method but about 2.45 using the AGMA standard as shown in Figures 6.32 and 6.33 respectively. Comparing ISO/TR and AGMA results of the specific lubricant film thickness, it is found that the differences between 0.5 and 1.0 torque ratios are minimal owing to the change in surface roughness from 0.41 to 0.31 respectively. Figure 6.34 shows the 3D distribution of specific lubricant film thickness at 1.0 torque ratio using ISO/TR method.



(a): Specific lubricant film thickness by the TCS

(b): Results of specific lubricant film thickness of ISO/TR by KISSsoft

Figure 6.32: Comparisons of specific lubricant film thicknesses at 1.0 torque ratio

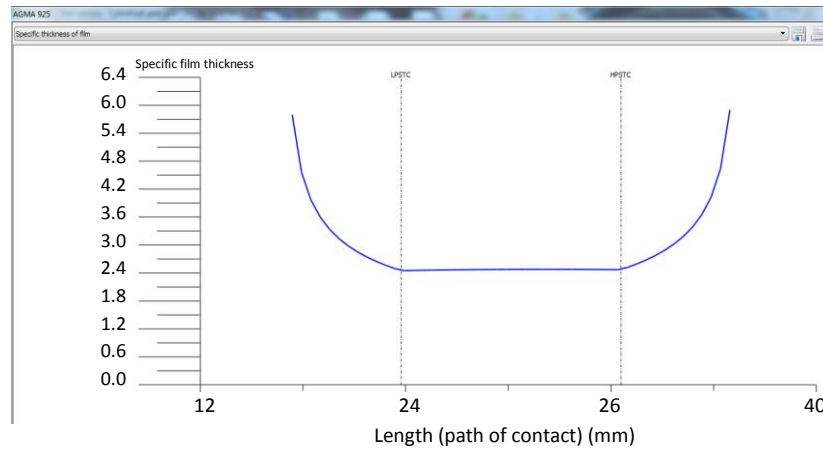


**Figure 6.33: Specific lubricant film thickness of AGMA by KISSsoft at 1.0 torque ratio**

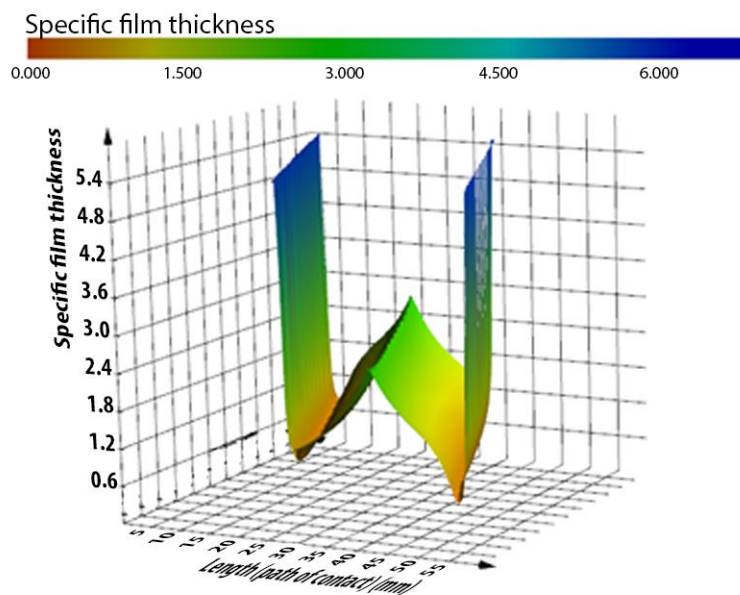


**Figure 6.34: 3D distribution of specific lubricant film thickness of ISO/TR by KISSsoft**

The validation of contact stress, local contact temperature, lubricant film thickness and specific lubricant film thickness for results obtained using the toolkit calculation sheet and KISSsoft commercial software at different torque ratio is discussed. The validation comparison reveals small differences in contact temperature values between the AGMA and ISO/TR methods. However, a big difference in lubricant film thickness and specific lubricant film thickness results is found. The lubricant film thickness results using AGMA are higher than ISO/TR. Such a difference can be explained by the fact that the AGMA uses a particular method to calculate the central film thickness, as explained earlier in this chapter and in Chapter 4, Section 4.3. The toolkit calculation shows a good agreement with the KISSsoft software within an acceptable level of differences by using ISO/TR. As a result, the TCS can be considered as accurate to carry out

micropitting assessment for the tested helical pinion gear and the HSS pinion gear of a WT gearbox.

## 6.5 ANALYTICAL RESULTS OF TESTED GEARS

Based on the above validation of the TCS, it is used to carry out the prediction of micropitting in the tested gear tooth through investigating the effect of key variables. Using the method provided in ISO Technical Report ISO/TR 15144-1, the tooth contact stress, sliding parameter, local contact temperature and specific lubricant film thickness are determined at different torque levels at a constant rotational speed, the same conditions of the experiment. Variations of surface roughness are considered in the analysis, based on the surface roughness values obtained from the measurement of tested gears after each cycle run under specific torque levels.

### Contact stress

As shown in Figure 6.35, the contact stress increases proportionally as the torque ratio is increased from 0.3 to 1.0. The maximum contact stresses occur at the beginning of the tip relief (point DE) of tooth surface of the pinion gear which meshes with the root of the wheel gear, and at root point AB, with which the beginning of the wheel tip relief meshes (as detailed in Chapter 4, Figure 4.5). The contact stress results reveal that the micropitting can initiate at the beginning of the tip relief because these areas are subjected to high contact stresses.

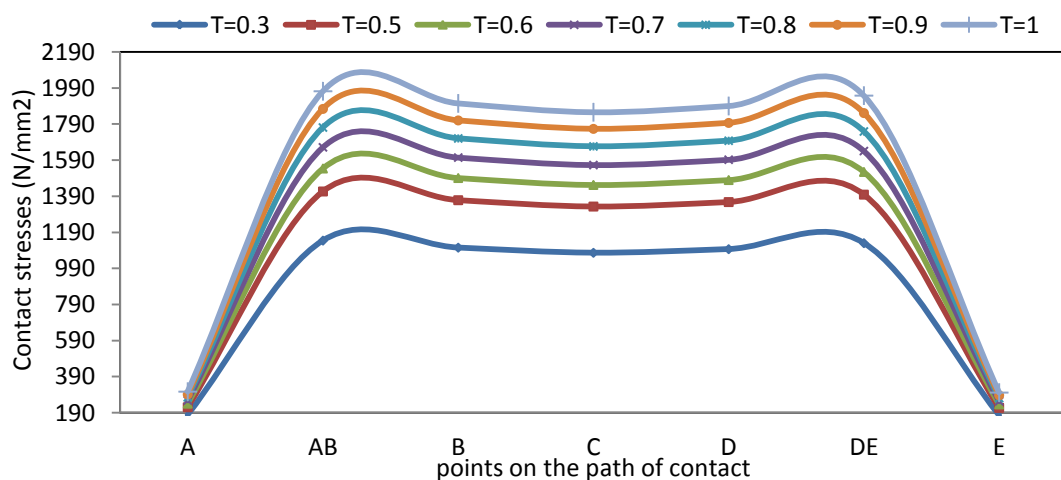
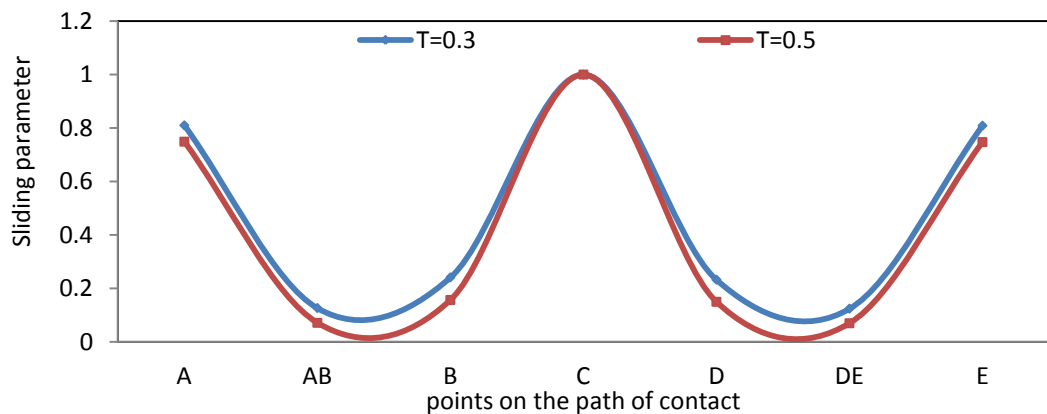


Figure 6.35: Contact stress at varying torque ratios

### Sliding parameter

Figure 6.36 shows the local sliding parameter along the path of contact points at different torque levels at a constant rotational speed. The sliding parameter changes continuously throughout the meshing process with the maximum sliding occurs at the beginning of the tip relief (point DE) of pinion and at root point AB with which the beginning of the tip relief of the wheel meshes. A pure rolling occurs at pitch point (C), which means zero sliding (100% rolling). As can be seen, the tip relief modification has a great impact on reducing relative sliding between the contact surfaces of teeth at the mesh in/out regions (points A and E). The sliding parameter at the end of tip relief of wheel and pinion is similar at point A (mesh in) and point E (mesh out). Less sliding occurs (more rolling) at points E and A due to lower contact stresses and bigger radii of relative curvature at the end of tip relief and root relief, as explained in Chapter 7, Section 7.5. Figure 6.36 includes only two torque levels as other sliding parameters are very close to the 0.5 torque level which may produce a dense and cramped figure if all torque ratios are included.



*Figure 6.36: Variation of sliding parameter at different torque ratios*

### Local contact temperature

The contact temperature on the tooth flank changes periodically, owing to the variation of the sliding parameter between contact surfaces during each meshing cycle. Figure 6.37 shows that the local contact temperature (sum of flash and bulk temperatures) increases as the torque is increased. The maximum temperatures occur at the locations where both contact stress and sliding are greater. The minimum temperature occurs at the pitch line, owing to zero sliding and pure rolling.

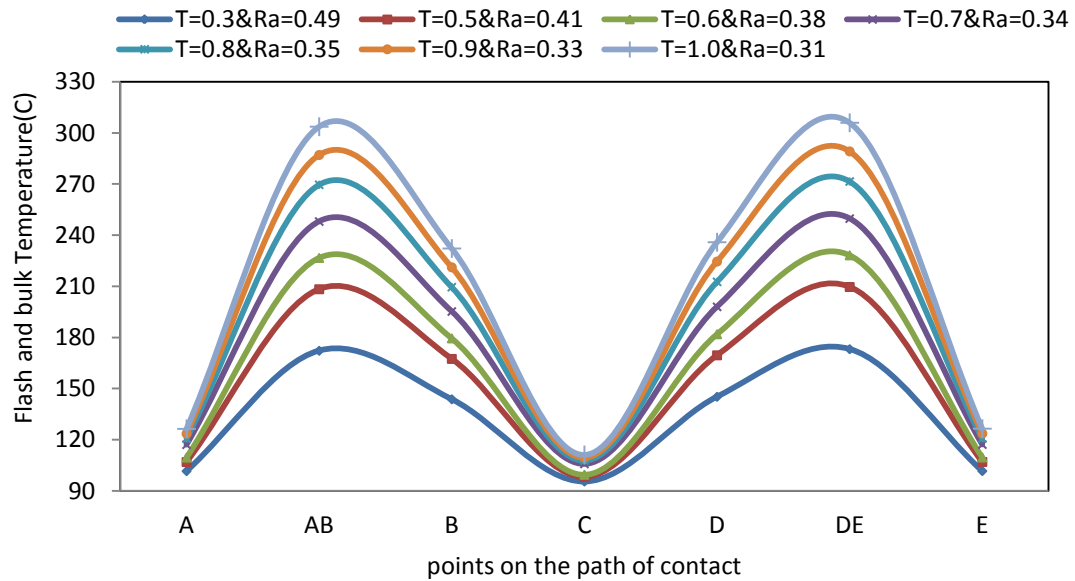


*Figure 6.37: Local contact temperatures at different torque ratios and surface roughness values*

### Specific lubricant film thickness

The specific lubricant film thickness varies greatly along the tooth flank during each meshing cycle, and the maximum film thickness occurs at pitch point. The analysis shows different values of specific lubricant film thickness at the end and at the beginning of the tip relief of pinion, points E and DE respectively, as shown in Figure 6.38. The beginning of tip relief, point DE for pinion and point AB for wheel, have a greater risk of the initiation of micropitting due to lowest lubricant film thicknesses at these regions compared with other contact points. In the analytical calculations, effects of both torque variations and surface roughness values as measured from the tested pinion gear are considered. As the surface roughness is inversely proportional to the specific lubricant film thickness (Equation 4-26), its reduction after each test cycle run contributes the variation of specific film thickness. The maximum value of specific lubricant film thickness is at mesh in/out regions and at the pitch point where the pure rolling occurs as the bulk temperature, which is directly related to the oil inlet temperature. The temperature at pitch point depends largely on the bulk temperature, as the flash temperature has little impact because of the zero sliding occurring at this point. The variation of specific lubricant film thickness along the tooth flank between the different torque ratios is trivial and it can be attributed to two factors. The first of these is the variation of the tip relief factor,  $X_{ca}$ , -as recommended in the ISO/TR15144-1 (2010) Technical Report- which is inversely proportional to the bulk temperature

(Equation 4.19) under different load levels. The second factor is the variation of the surface roughness after gears have been tested under increased load cycles and which is inversely proportional to the specific lubricant film thickness (Equation 4.26), as explained in Chapter 4, Section 4.2 and illustrated in Figure 6.13. The varying surface roughness throughout the experimental testing has a greater effect on the specific lubricant film thickness than the varying torque. The considerable variation of lubricant film thickness along the tooth flank during each meshing cycle may also cause the interruption of lubrication resulting in micropitting. The surface treatments comprising high quality coating and superfinishing processes are immensely beneficial to solve this problem which not only reduces the micropitting risk but also the friction between contact surfaces. These surface treatment processes can eliminate peaks and valleys of the surface roughness leading to maximising the lubricant film thickness along the tooth flanks.

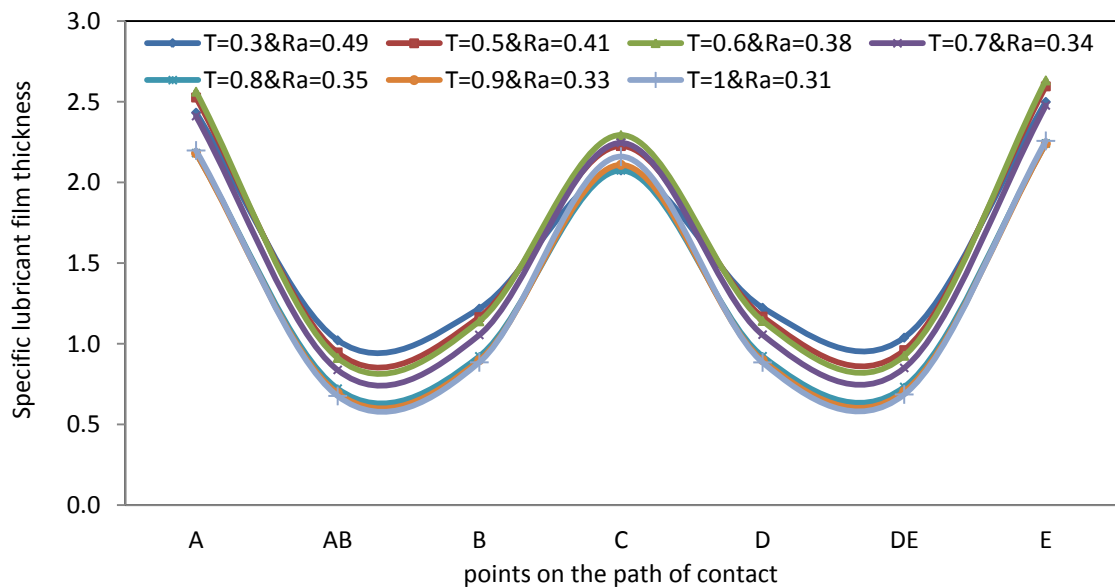


*Figure 6.38: Specific lubricant film thickness at different torque ratios and surface roughness values*

## 6.6 MICROPITTING RISK ASSESSMENT

Figure 6.39 (Linke, 1996 cited in Jelaska 2012) specifies values of the specific lubricant film thickness in relation to surface hardness of gears. The Vickers hardness (HV) of the tested gears used in the experiment is 746. It reveals that the minimum value of specific lubricant film thickness is about 0.7 at the beginning of tip relief, point DE for pinion and point AB for wheel when tested at torque ratio 1.0. Thus, micropitting is most likely

to occur at the addendum and the dedendum of the pinion and the wheel. As can be seen in Figure 6.39, the minimum specific lubricant film thickness values obtained from the analytical calculation fall into the micropitting region, marked by an elliptical line on the Linke curve. The ISO/TR 15144-1 does not recommend any value of safety factor against micropitting, but the Linke curve may be used to evaluate and estimate the micropitting risk, by determining the value of specific film thickness with consideration of surface hardness of the tooth flank. Moreover, according to Dudley (1994), the specific lubricant film thickness should be greater than unity (as detailed in Table 2-1). In addition, Kissling (2012) categorised the micropitting safety factor in a range from low to high risk, as shown in Table 8-2. However, the micropitting safety factor based on the specific film thickness value obtained is less than unity especially when loaded under higher torque ratios. The gear tests have shown that the micropitting has initiated and progressed, then spread out in the addendum and dedendum of the tooth flanks, as shown in Figure 6.8 and illustrated in Table 6-2.

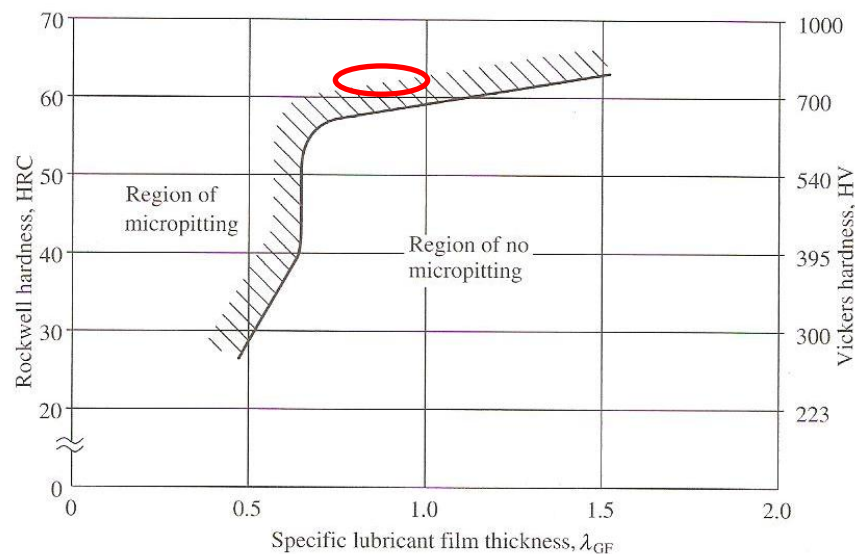


**Figure 6.39: Specific film thickness vs. hardness according to Linke (cited in Jelaska 2012)**

According to the analytical results, the highest load, maximum temperature and minimum specific lubricant film thickness occur at the addendum and dedendum of the pinion, as shown in Figures 6.35, 6.37 and 6.38 respectively, particularly around the tip relief area. Based on the experimental results, the micropitting occurs in these same areas. Thus, the micropitting may be predicted, by applying the analytical procedure based on the ISO/TR method, if detailed measurements of surface roughness and profile modifications are available. AGMA 925-A03 standard defines the specific lubricant

film thickness as a constant value along the line of tooth contact using the EHL central film thickness. The minimum specific lubricant film thickness value using AGMA is about 2.45, which is a very high value indicating that micropitting might not occur. This value is placed in the low risk range and in full film lubrication condition according to Kissling (2012) and Dudley (2004), as discussed later in Chapter 8, Section 8.6. According to AGMA results, the probability of micropitting occurrence is very low as this value is located at regime III and is characterised by a full EHL oil film thickness (AGMA 925-A03, 2003), as explained in Chapter 2, Section 2.5. However, based on experimental results, micropitting occurs progressively at the maximum torque ratio, which contradicts the AGMA results. Therefore, from the experimental testing conducted in this research, the ISO/TR results of local specific lubricant film thickness provide a good correlation with the occurrence of tooth flank micropitting. From this study, it is clear that the excessive load, micro-geometry, surface roughness and their combined effect on the lubricant film thickness are the main influencing factors of micropitting.

## **6.7 DISCUSSION**

### **Effects of lubricant**

The lubricant used in the tests of this study is a mineral oil with certain additives. The additives in the gear oil are very important and contain one or more elements (such as phosphorus, zinc and lead), and can provide protection against wear because of chemical reactions with the tooth flank surfaces (Bartz 1993). The oil type and additives should be selected carefully to fit with the predicted gear temperature during working conditions and by considering the micropitting and wear resistance for long service intervals. Friction is an important factor that can cause micropitting; however by using the chemical additives surface wear rate and/or coefficient of friction can be reduced in order to minimise the risk of the micropitting (Morales-Espejel and Brizmer, 2011). The oil used in this experiment has combined additives for anti-wear and anti-scuffing. The total operation cycle for all load stages in this experiment is 56 million cycles and the same oil is used throughout the experiment without being changed. Therefore, the cumulative debris generated from the tooth surfaces after gears start to pit also contributes to the micropitting progression, and accelerates the process of micropitting. The filtration system in the test rig can only filter about 90% of debris and other

contaminants. An oil condition monitoring procedure can be applied, by taking samples after the filtration process to inspect the cumulative debris for any contaminants after each cycle run.

One of the best solutions to increase the lubricant film thickness is to use lubricant with an acceptable high viscosity. As the viscosity increases, the lubricant film thickness increases too which can provide protection against many types of tooth surface failures. The disadvantages of using very high viscosity lubricant are power loss, high temperature increase of gear contact surfaces and a high temperature of the lubricant, which may lead to different types of gear and bearing failures. The perfect gear lubricant would have its viscosity-temperature balanced with its additives system (Bala et al, 2000). Lubricant with high pressure-viscosity may lead to high friction coefficient (Oila, 2003). It is important to balance the gear working condition and the selection of the correct lubricant oil with additives.

### **Effects of surface roughness**

The tooth flank surfaces have random wave shapes, formed by valleys and peaks at the microscopic level, and the surface roughness depends on the precision of the grinding process used. The surface roughness is very important for the lubrication regime. Since that the two tooth flanks have different values of surface roughness and radii of curvature, big variations in the lubricant film thickness occur during the meshing process. If two high peaks of surface roughness meet in mesh, then there is the possibility of direct contact at a certain point between the tooth flanks. Thus, micropitting failure can initiate at the location where the high peaks exist, as discussed in Section 6.2. It is known that at high peaks the coefficient of friction and contact stress are greater than those at the lower peaks. The high contact stress induced by these peaks (roughness asperities) is established by many researchers (Johnson et al, 1972; Berthe et al, 1980; Jiang et al, 1999; Oila and Bull, 2005; Serest and Akbarzadeh, 2013; Evans et al, 2013). The micropitting initiates at these high peaks due to high contact stress which cause peak to peak contact under the mixed lubricated condition. The direct contact between these peaks cause local plastic deformation and pits in gears, mostly due to plastic deformation at roughness peaks level. The experimental results show that micropitting starts to occur at the load ratio of 0.5 in the dedendum area of pinion. This micropitting is non-progressive along the dedendum area until the final test run. The

peak values of surface roughness deform plastically after each cycle run due to the high coefficient of friction and contact stress, as shown in Figure 6.13. The tooth surface becomes smoother after a certain number of testing cycles, as shown and explained in the surface roughness results (Section 6.2), and thereby increases the specific film thickness where areas of low values of surface roughness exist. The results of lubricant film thickness obtained in this study reveal that the surface roughness variation during tests contributes to a considerable variation in lubricant film thickness along the tooth flank. This variation can be ascribed to changes in surface roughness after gears undergo various running cycles under varying torque levels which may interrupt lubrication and cause micropitting. This can lead to inconsistency in micropitting occurrence area in different tooth flank surfaces, as shown in Table 6-1 and Figure 6.8. Such inconsistency reveals that there is a variation in surface roughness and tooth geometry (Erricho, 2012).

### **Effects of surface temperature**

The tooth surface temperatures vary along the tooth flanks over each meshing cycle with the maximum temperatures occurring when gears mesh at the beginning of the tip relief and the root of the tooth. This is owing to the variations of both load and sliding conditions, which cause various degrees of frictional heating at different contact points. The calculated tooth surface temperatures may be lower than the reality because the oil temperature inside the gearbox may be higher than the inlet oil temperature, however, this is not considered in this study. The gears run nonstop for about 80 hours consisting of seven load levels each running 8 million cycles in this experiment. This accumulates temperature increases inside the gearbox owing to continuous friction heating between the gear teeth. The high temperature can reduce the lubricant viscosity and decrease the lubricant film thickness, particularly at the beginning of the tip relief and the root of the tooth, leading to the micropitting initiation and progression.

### **Effects of effective tip relief**

In this research, the value of effective tip relief at higher torque ratios is greater than the actual tip relief of tested gears, which is 50  $\mu\text{m}$ . The calculated effective tip relief at the highest torque reaches about 82  $\mu\text{m}$ , which means that the actual tip relief used in the test gears is smaller compared with the tip relief determined by the highest load level recommended. A warning message appears in KISSsoft software when the maximum

torque ratio (1.0) is used due to the low tip relief value, as shown in Appendix K. In the tip relief area, which is very small compared to the size of the contact zone, a big impact is expected because of the instantaneous change of loading during meshing-in and meshing-out cycle. These factors may contribute to micropitting at higher torque levels. Therefore, sufficient and adequate tooth profile modification (micro-geometry) should be determined by considering the load levels in operation, to minimise the risk of micropitting.

The most important parameter that is determinate for micropitting is the specific lubricant film thickness. The micropitting occurs or initiates in spots which may not deteriorate as has been observed at the pinion dedendum in this experiment, as the comparison between Figure 6.2 at 0.5 torque ratio and Figure 6.6 at 0.9 torque ratio reveals. These spots may be self rectifying or stop progressing after a certain number of cycles, because of the improvement of tribological conditions, after the peaks of surface roughness are being smoothed out, which could help to increase the specific lubricant film thickness (Errichello and Muller 1994). The micropitting can be reduced by using different surface treatments and a suitable hardening process and selecting a suitable lubricant of viscosity with a good coolant and oil filter system.

## **6.8 SUMMARY**

The gear experimental results show that micropitting initiates at the pinion dedendum but escalates at the addendum, because of the severer progressive micropitting at the mating wheel dedendum. The micropits on the pinion dedendum area are deeper and cause higher profile loss than that in the addendum area, according to the profile deviation results. This indicates that the micropitting on the pinion dedendum causes a greater profile deviation. The micropitting initiates at the beginning of the tip relief area of the pinion and at the root of pinion, with which the beginning of the tip relief area of the wheel first starts to mesh. The tooth profile deviation of wheel gear is worse and more progressive than that of the pinion gear. The wheel profile deviation appears from the root to the tip of the wheel.

The analytical results show that the maximum contact stresses occur at the beginning of the tip relief (addendum) and at the root (dedendum) of the pinion. This indicates that the micropitting can initiate at these areas because of higher contact stresses, greater

sliding causing higher temperatures and lower film thicknesses. The ISO/TR provides a better correlation between the predicted minimum specific lubricant film thickness and the occurrence of micropitting in the experiment, compared to the AGMA standard.

Due to a series of peaks and valleys of tooth surfaces, it can be concluded that micropitting initiates in the form of lines at the peaks in the addendum and the dedendum of the tooth flank. The comparison of the surface roughness measurements before and after the test runs shows that deep valleys exist below the original tooth surface, which indicates that the material is eroded and micropitting exists on the tooth flank. The conducted experimental and analytical studies have found that the excessive loading, micro-geometry, surface roughness and lubricant film thickness are the main factors affecting micropitting. It is also found that the analysis of the specific film thickness is in a reasonably good agreement with the Linke curve for predicting micropitting.

## ***Chapter 7: Analytical Results Using Selected SCADA Data***

---

*This chapter presents the gear micropitting analytical results of HSS pinion gear of a wind turbine gearbox operating under nominal, varying load and speed conditions. As detailed in the experimental results in Chapter 6 micropitting initiates then progresses under various torque levels. In this chapter, results are obtained mainly based on analytical predictions of micropitting risk using recorded SCADA data by applying torque and rotational speed variations within the designed operational conditions of the turbine. Chapter 8 presents results of the probability analysis of gear tooth flank micropitting risk by applying randomly selected samples of the whole SCADA data. The analytical study is carried out to assess the risk of gear micropitting by determining variations of the contact stress, sliding parameter, local contact temperature and lubricant film thickness along the line of action of gear tooth contact.*

*The analysis in this chapter provides some understanding and insight of when and why micropitting damage would occur which is generally difficult to predict or discover during gear pitting experimental tests. Furthermore, the analysis shows that the lubricant film thickness varies considerably at the lowest torque range and under varied rotational speed conditions. The calculation of the lubricant film thickness under variable torque and rotational speed conditions provide a method of predicting the possible risk of gear micropitting for wind turbine applications.*

## 7.1 TORQUE AND SPEED DERIVED FROM SCADA

Various analytical procedures and experimental approaches have been used to determine the extent and characteristics of various gear failure modes, as detailed in Chapter 2. This chapter contains a broad description of the investigation carried out on the effects of variable load and speed conditions on gear tooth micropitting, considering the various factors that cause micropitting failure. Further, it seeks to understand the variation of contact stress, sliding parameter, local contact temperature and lubricant film thickness of gear tooth flank by considering the real-life operation conditions of a WT gearbox by analysing SCADA data of a WT collected in field operation. The analysis procedures are developed through finding solutions at seven different locations of tooth flank along the line of action based on the ISO/TR 15144-1 Technical Report to predict the micropitting risk, as explained in Chapter 4, Section 4.1.5. The HSS pinion gear which locates in the third-stage of wind turbine gearbox is investigated based on recorded SCADA data. Three regions of shaft torque and rotational speed variations are determined according to the relationship between the power curve and generator rotational speed against wind speed. The selection is based on the variation ranges of generator power and rotational speed as recorded by the SCADA data, given in Figure 5.3, Chapter 5. Table 7.1 shows the variations of HSS rotational speed ratios and corresponding torque ratios within the range of 0.25~1.00 for the pinion gear calculated from the SCADA data.

*Table 7-1: Variations of torque and rotational speed ratios of pinion gear shaft*

Rotational Speed Variation (ratio)		Torque Variation (ratio)		
<b>Lowest</b>	0.56	0.25	0.51	0.76
<b>Variable</b>	0.56	0.21	-	-
	0.67	0.31	-	-
	0.78	0.40	-	-
	0.89	0.49	-	-
<b>Highest</b>	1.00	0.59	0.79	1.00

## 7.2 LOCAL CONTACT STRESS

The contact stress can be obtained by varying shaft torque under various shaft rotational speed values using Equation 4-3. The load applied on gear tooth fluctuates in response to the tooth contact cycles and WT operational conditions. To investigate effects of load and speed variations, the HSS pinion gear shaft torque and rotational speed are varied as detailed in Table 7-1. As Figure 4.2 illustrates, the meshing starts at the approach point at point A where the tip of the pinion gear engages with the root of the wheel gear, as explained in Chapters 2, Section 2.5 and Chapter 4, Section 4.1.4. The variations of contact stresses of the HSS pinion gear are shown in Figure 7.1. The contact stresses at the dedendum (point E) of the pinion gear are the highest. This is due to the high loading and the fact that the Hertzian contact stress is inversely proportional to the radius of relative curvature,  $\rho_{t,Y}$ , which is the smallest when the wheel tip and pinion root are in contact.

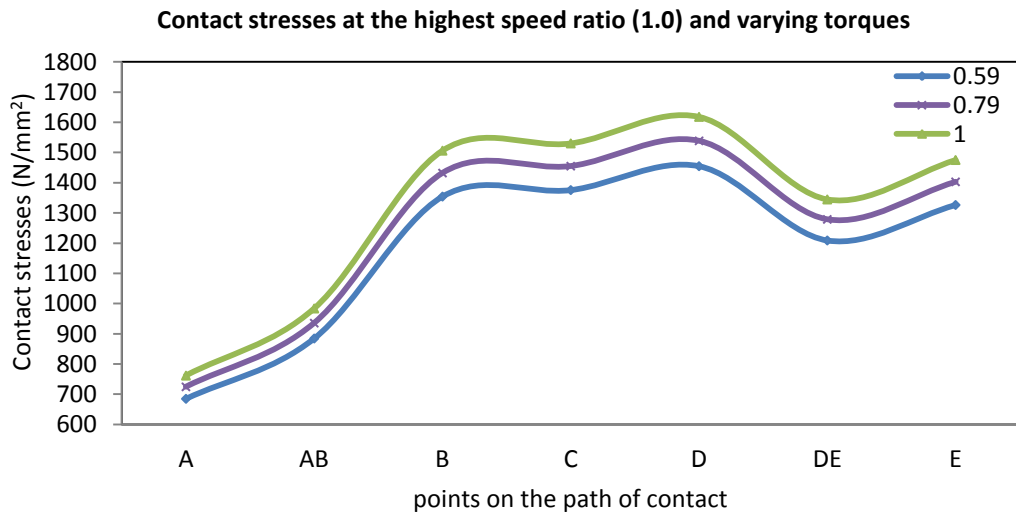


**Figure 7.1: Contact stress variation at the highest speed and varying torque ratios**

As shown in Figure 7.2, the correlation between the contact stress and the torque is a linear relationship for each point along the path of contact. The contact stresses increase as the torque is increased at both high and low rotational speed ratios of 1.00 and 0.56, respectively.

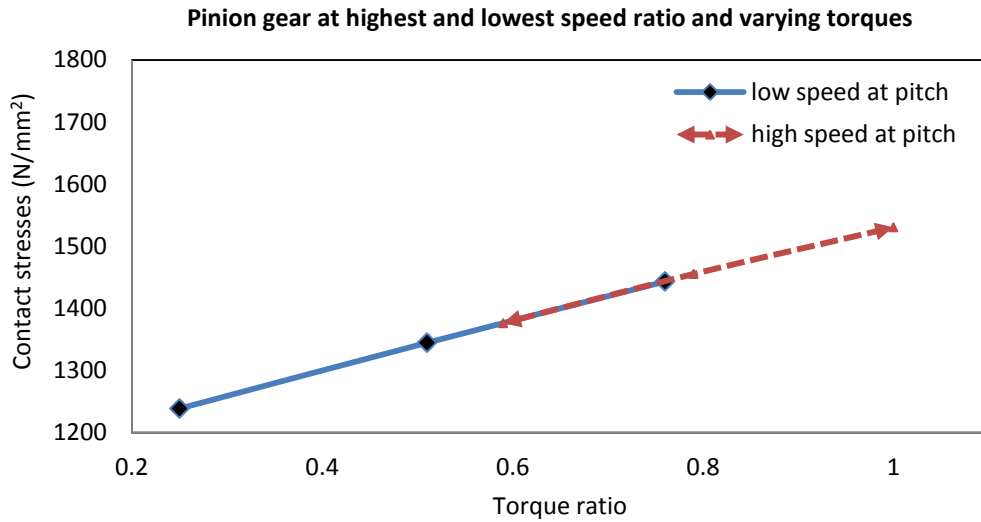


*Figure 7.2: Contact stresses vs. torque at highest and lowest speed ratios*

At the lowest rotational speed, the torque ratio is varied between 0.25 and 0.76 for the pinion gear. The contact stresses increase as the torques are increased and reach a maximum of  $1526 \text{ N/mm}^2$  at the dedendum area near pitch point of the pinion gear, as shown in Figure 7.3.

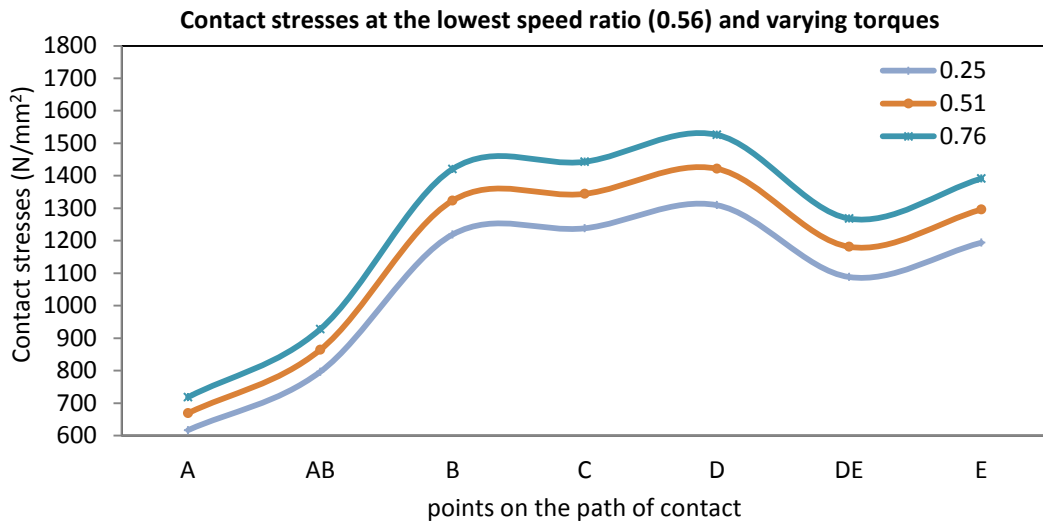


*Figure 7.3: Contact stress variation at the lowest speed and varying torque ratios*

### 7.3 LOCAL SLIDING PARAMETER

Figure 7.4 shows the local sliding parameter along the path of contact points at nominal torque and rotational speed of the WT gearbox. The sliding parameter changes continuously throughout the meshing process with the maximum sliding occurs at the root of the pinion gear when engaging with the tip of the wheel gear (point E) which reaches about 94% of sliding. The pitch point (C) has pure rolling, which means zero

sliding, and the amount of sliding increases as the contact point moves away from the pitch point. The sliding of the tip of the pinion gear when engaging with the root of wheel gear (point A) reaches about 78%. As a result, the dedendum of the HSS pinion gear (point E) has a higher sliding, as shown in Figure 7.4.

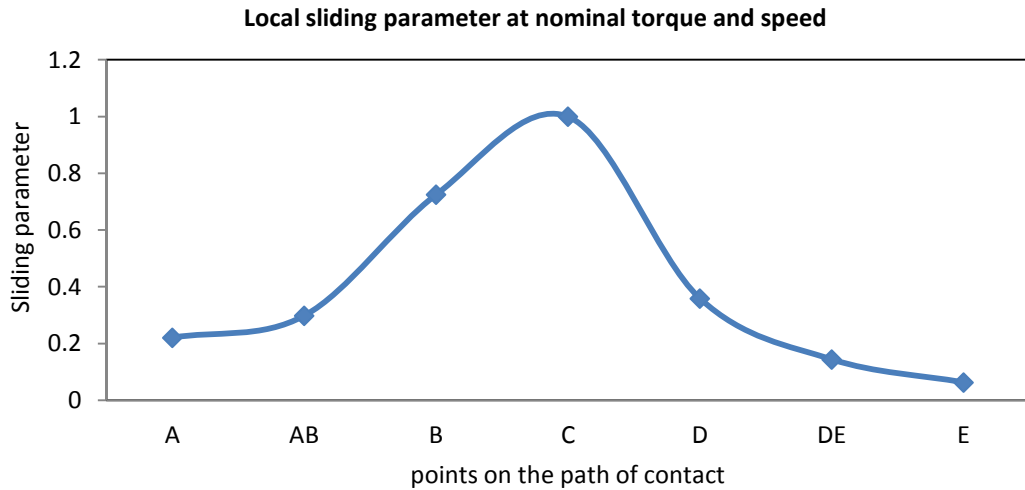


**Figure 7.4: Variation of sliding parameter along the line of action**

The variation of sliding parameter is small between the minimum and maximum torque ratios under varying rotational speed ratios, as shown in Figures 7.5 and 7.6 respectively. As the rotational speed ratio increases from 0.56 to 1.00 at the minimum torque ratio, the sliding variation does not exceed 3.4% at the pinion root and 5.4% at the pinion tip, as shown in Figure 7.5. When the torque is increased from the minimum to the maximum value, the sliding parameter reduces (sliding increases) at tip and root of HSS pinion gear, as the comparison between Figures 7.5 and 7.6 reveals. It is clear that the dedendum of HSS pinion gear has higher sliding than that on the addendum of pinion gear.

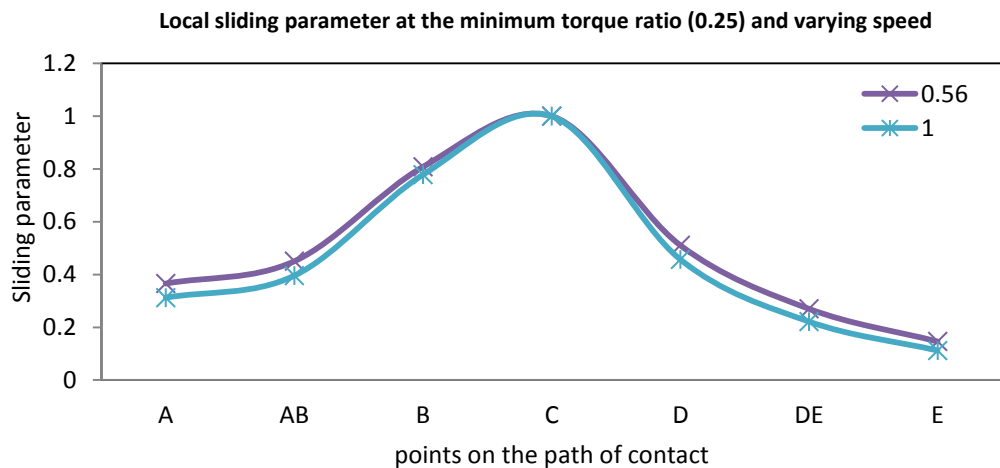


**Figure 7.5: Variation of sliding parameter at the minimum torque and varying speed ratios**

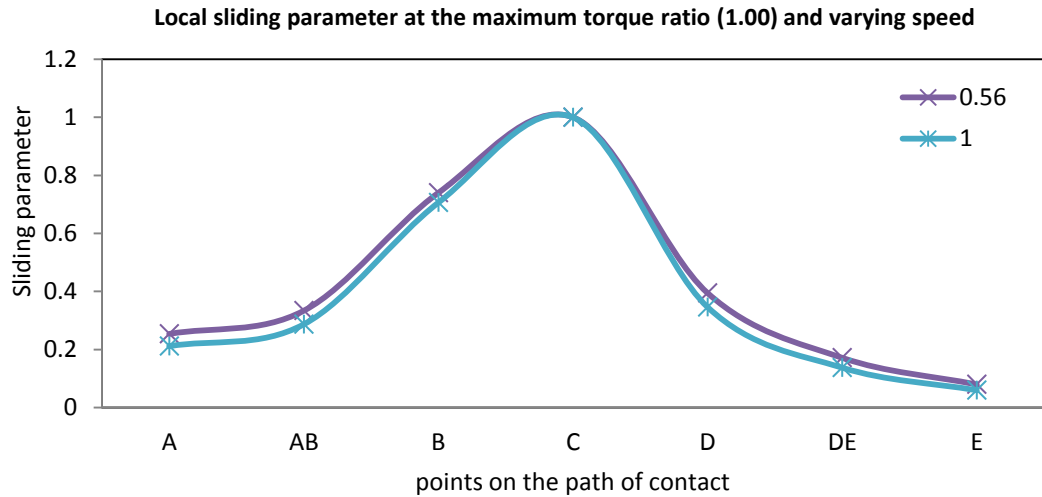


*Figure 7.6: Variation of sliding parameter at the maximum torque ratio and varying speed ratios*

## 7.4 LOCAL CONTACT TEMPERATURE

The tooth surface contact between gear pair meshing and sliding result in heat generation on tooth flank. Higher temperatures due to greater contact stress and sliding can breakdown the lubricant film because the higher temperature reduces dynamic viscosity of the lubricant. Due to higher sliding and surface contact friction, significant temperatures are developed along the tooth flank, as shown in Figure 7.7.

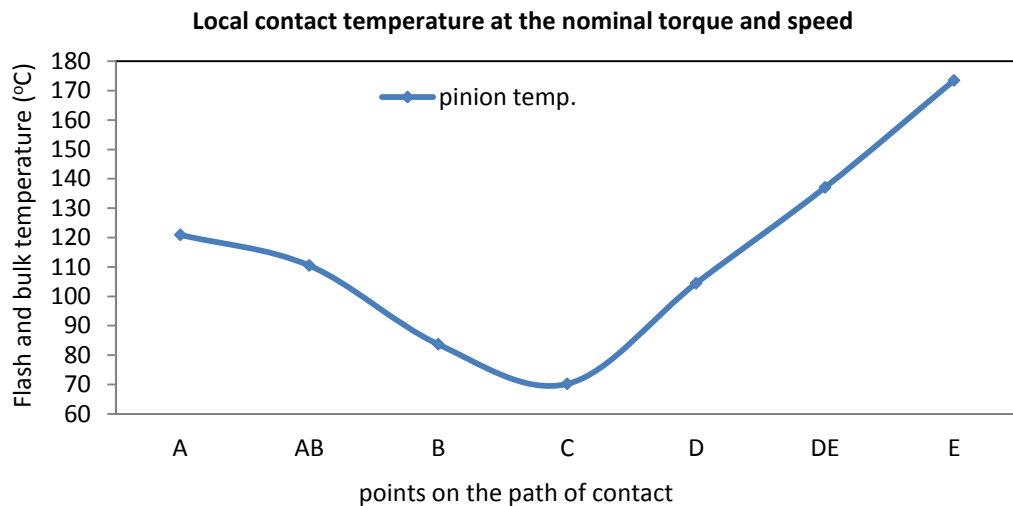


*Figure 7.7: Variation of flash and bulk temperature on the tooth surface*

The surface flash temperature changes are frequent when the gear teeth make contact at every point along the tooth flank. The maximum temperature occurs at the root of the pinion gear, which reaches 174°C, due to the high contact stress and intense sliding in

the area. The temperature at the HSS pinion tip is lower than that at the HSS pinion root because the contact stress and sliding are lower, as shown in Figures 7.1 and 7.4. Higher temperature results in a decrease in the lubricant film thickness, which in turn increases friction between tooth contact surfaces.

The effects of varying torque and rotational speed on local contact temperatures of the pinion gear are investigated. The local contact temperatures increase as the torque is increased, as shown in Figures 7.8 and 7.9. This is due to the direct proportion between the flash temperature and contact stress. At both cases of operating under the lower and higher speeds, the temperature increase is about  $22^{\circ}\text{C}$  between lower and higher torque ratios. It occurs at the dedendum of pinion gear, as shown in Figures 7.8 and 7.9, respectively. The maximum temperature difference between operating at the lowest and highest speed with varying torque values is about  $30^{\circ}\text{C}$  occurring at the root (point E) of the HSS pinion gear when comparing Figures 7.8 and 7.9.

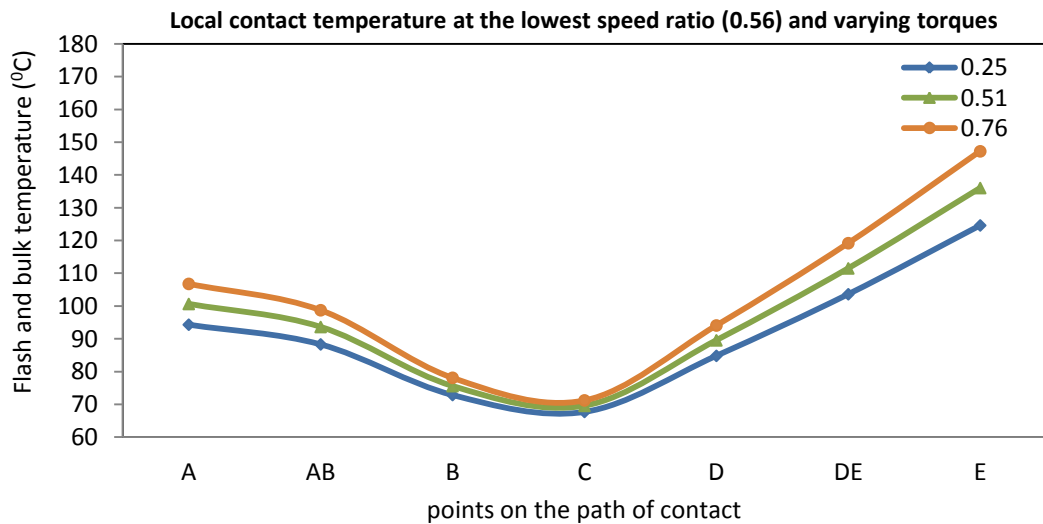


**Figure 7.8: Variation of local contact temperature at the lowest speed and varying torque ratios**

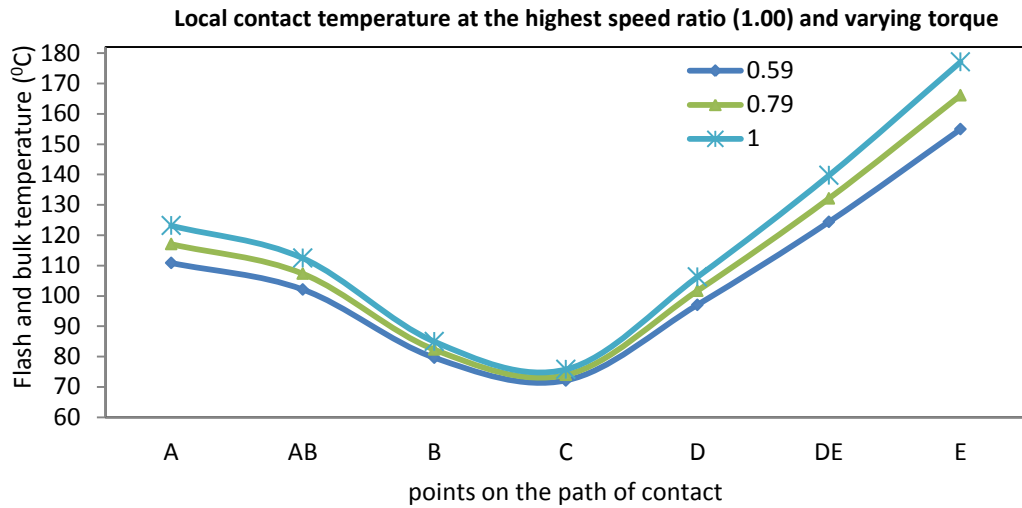


**Figure 7.9: Variation of local temperature at the highest speed and varying torque ratios**

The comparisons of temperature differences indicate that the torque and rotational speed combined together have a greater effect on local contact temperature because of combined effects of contact stress and sliding parameter. Varying torque at the highest speed has a greater effect on the increase of flash temperature. It can be inferred that the torque has a greater effect on the temperature variation than the rotational speed because of a direct proportional relationship between the flash temperature and contact stress. The local contact temperatures are analysed at low and high torque ratios with varied rotational speed ratios. The local contact temperature is not much affected at the lowest torque ratio by varying speed ratios, as shown in Figure 7.10. The highest temperature at the root of the pinion gear is about 134°C at the lowest torque ratio of 0.21, as shown in Figure 7.10. It reaches 155°C at a torque ratio of 0.59, as shown in Figure 7.11 when the rotational speed is at the highest value. As can be observed from Figure 7.10, when the gear pairs are under a low torque ratio, the local contact temperature has a small increase when the rotational speed is higher. The difference is only about 11°C between the highest and lowest rotational speed at the dedendum (point E) of HSS pinion gear.

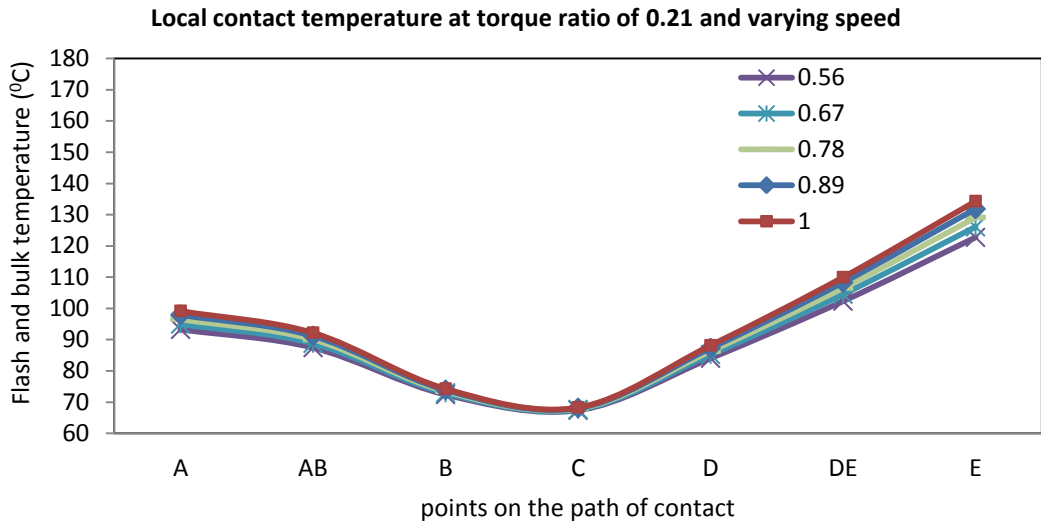


*Figure 7.10: Variation of local temperature at the lowest torque and varying speed ratios*

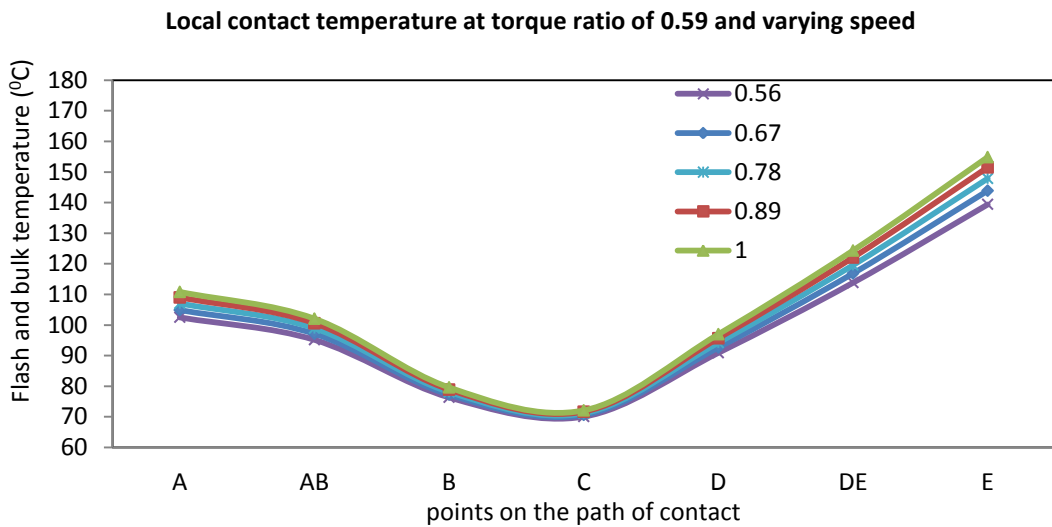


*Figure 7.11: Variation of local temperature at torque ratio of 0.59 and varying speed ratios*

The high torque has a greater impact on the local contact temperatures, as shown in Figure 7.11. However, the temperature differences are also very small when the rotational speed ratio is varied under the torque ratio of 0.59 with a difference of about 16°C between the highest and lowest rotational speed at the dedendum of pinion gear. In comparing Figures 7.10 and 7.11, slightly greater temperature variations can be seen when the rotational speed is varied under the higher torque.

## 7.5 LUBRICANT FILM THICKNESS

The lubricant film thickness varies drastically throughout the contact path of tooth flanks. The maximum lubricant film thickness occurs at pitch point and at the tip of the pinion gear. From Figure 7.12 and earlier explanations regarding the variations of

contact stress, radius of relative curvature and sliding parameter over the tooth flank, it is clear that the lubricant film thickness decreases with the increase of contact stress, sliding parameter and contact temperature. The lubricant film thickness increases only when pure rolling occurs at the pitch line even under high contact stress conditions. In addition, the radius of relative curvature has a great effect on the lubricant film thickness because lower contact stress occurs when the radius of relative curvature is greater. The lubricant film thickness in the addendum of pinion gear is greater than that at the dedendum because of lower contact stress, less sliding and lower contact temperature.

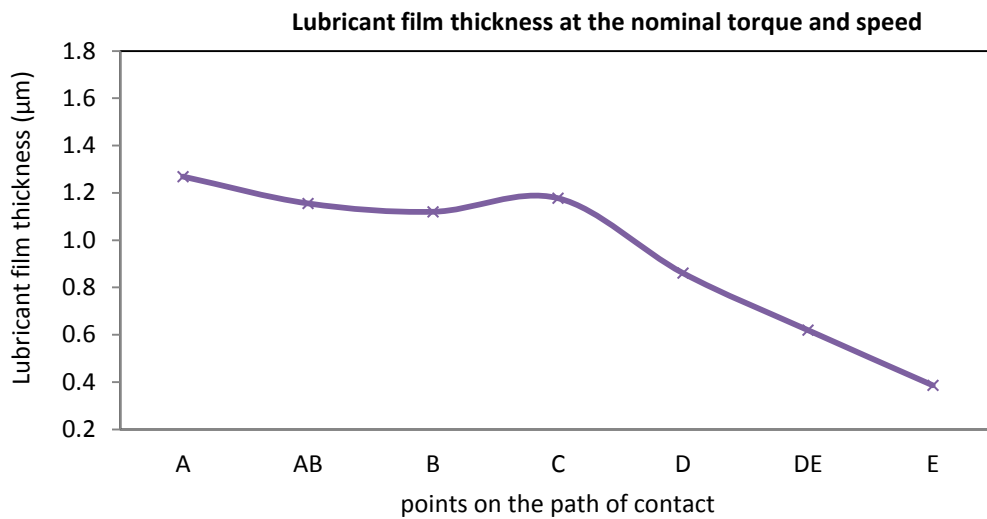


**Figure 7.12: Variation of film thickness at the nominal torque and speed**

As can be observed from Figure 7.12, the lubricant film thickness is at its lowest value at the dedendum of the pinion gear. This can be improved by addendum/dedendum tooth profile modification or tip relief to reduce high sliding occurring in the region. However, this analytical investigation of the HSS pinion gear does not consider any tooth profile modification which can improve the micropitting safety factor. Rather, it investigates the influence of variable load and speed conditions on the risk of micropitting failure.

The effect of the highest and lowest rotational speed ratios with varied torque ratios on the lubricant film thicknesses is investigated. The film thickness decreases when the torque is increased, as shown in Figures 7.13 and 7.14. This is mainly due to the direct proportion of local load parameter,  $W_Y$ , to the local Hertzain contact stress as shown in Equation 4-17. Similarly, the local load parameter is directly proportional to the local lubricant film thickness as shown in Equation 4-25. Under a higher torque ratio, the local sliding increases because of its direct proportion to the dynamic viscosity at local

contact temperature. This dynamic viscosity is related to the local contact temperature which is also affected by the contact stress. The lubricant film thickness is the lowest at the pinion root because of the higher load, greater sliding and higher temperature.

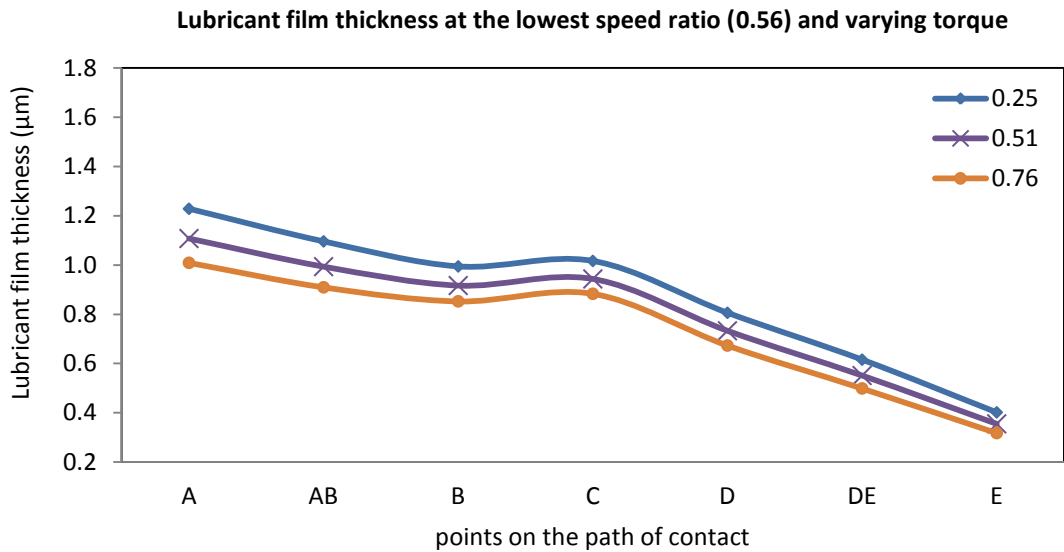


*Figure 7.13: Variation of film thickness at the lowest speed and varying torque ratios*

The high rotational speed helps to increase the film thickness, as shown in Figure 7.14. Comparison of Figures 7.13 and 7.14 shows the considerable effect of the reduction of the rotational speed on the decrease of the film thickness. This is due to the reduction of local velocity parameter which is directly proportional to the lubricant film thickness. The differences in the lubricant film thickness between lower and higher rotational speeds and torques as well as comparisons with the results under the nominal torque and speed values are summarised in Table 7-2.

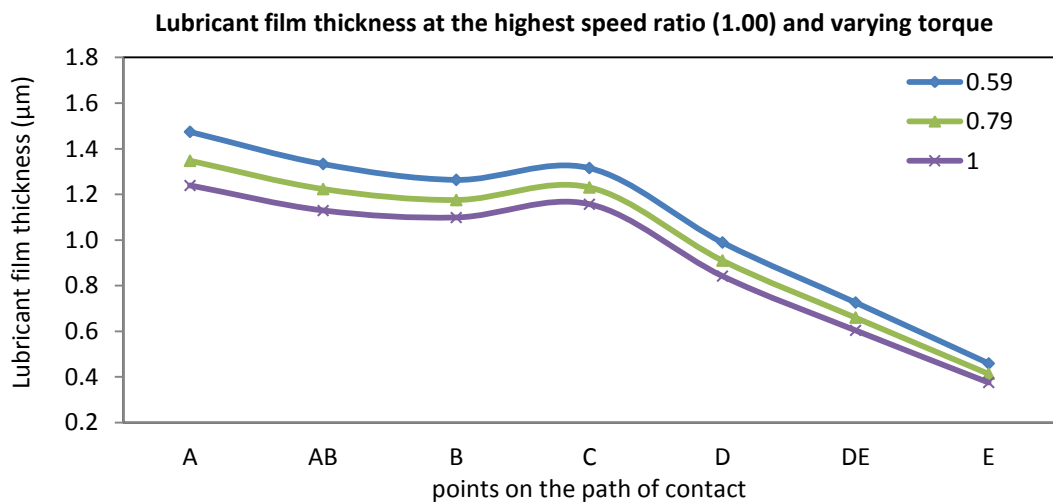


*Figure 7.14: Variation of film thickness at the highest speed ratio and varying torque ratios*

As the rotational speed increases from its minimum value to the maximum value, the film thickness increases slightly when operating under the torque ratio of 0.59, as shown in Figure 7.15. However, there is a considerable increase in the lubricant film thickness at the lowest torque ratio when the rotational speed ratio is varied, as shown in Figure 7.16. It is clear that the combined effect of low torque and high rotational speed ratios can contribute to increase the lubricant film thickness.

The lubricant film thickness varies considerably at the lowest torque and varied rotational speed conditions, as shown in Figure 7.16. This considerable variation in film thickness is obvious when Figures 7.13 to 7.15 are compared with Figure 7.16. The lowest film thickness occurs when the torque ratio is high and the rotational speed ratio is at the lowest, as shown in Figures 7.13 and 7.15. The lubricant film thickness under all investigated conditions, as presented in Table 7-2, has the lowest value of  $0.32 \mu\text{m}$  which indicates the risk of micropitting.

The possibility of micropitting risk occurs at the root of pinion gear where the minimum film thickness presents. Thus, micropitting is most likely to initiate on the dedendum of pinion gear as observed by Skriver's (2010) from inspection on WT gearboxes. The results reveal that micropitting failure is not only affected when the film thickness is insufficient and varies over the tooth flank but also due to temperature variations during each meshing cycle. This occurs due to various degrees of heat generation on gear tooth contact surfaces as a result of different levels of friction and transmitted loads along the gear tooth flank.

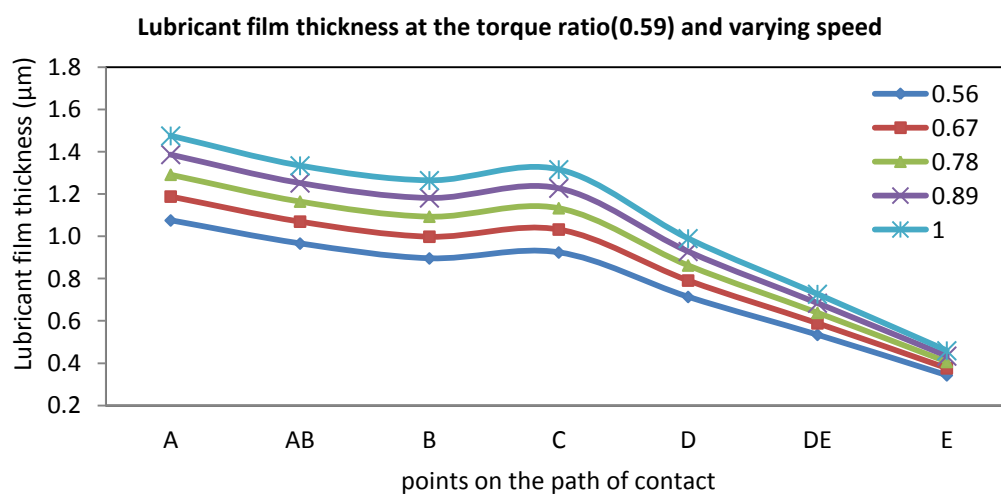


**Figure 7.15: Variation of film thickness at torque ratio of 0.59 and varying speed ratios**

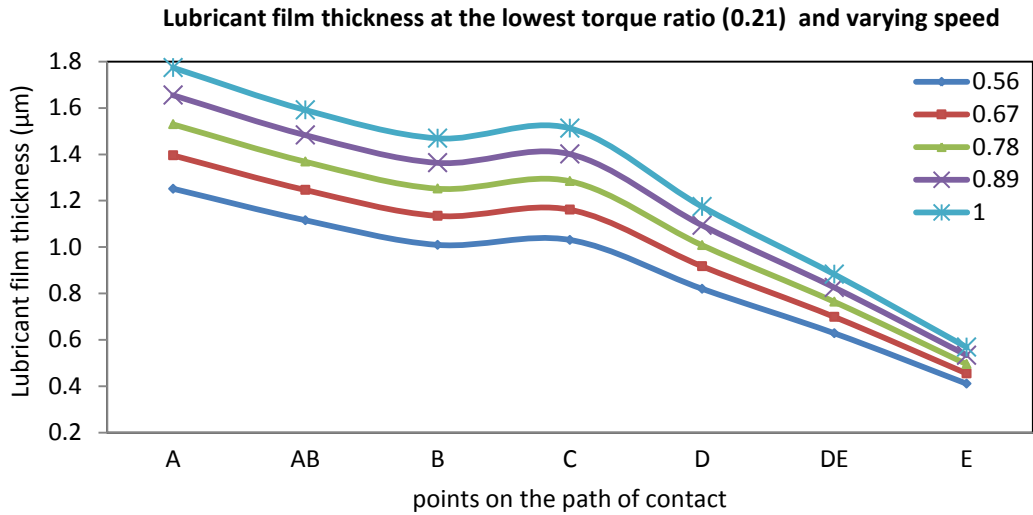


Figure 7.16: Variation of film thickness at the lowest torque and varying speed ratios

Table 7-2: Lubricant film thickness under the considered variable conditions

Rotational speed ratio	Torque ratio	Lubricant film thickness (µm)		
		Pinion root	Pitch point	Pinion tip
Nominal speed ratio	Nominal torque	0.39	1.18	1.27
Highest speed ratio	Lowest torque	0.41	1.32	1.47
	Highest torque	0.38	1.16	1.24
Lowest speed ratio	Lowest torque	0.36	0.94	1.22
	Highest torque	0.32	0.88	1.01
Variable speed and torque ratios	Lowest torque and speed	0.41	1.03	1.25
	High torque and speed	0.46	1.32	1.48

## 7.6 ASSESSMENT OF GEAR MICROPITTING RISK

In ISO/TR 15144-1, the safety factor is defined as the ratio of the minimum specific lubricant film thickness divided by the permissible specific film thickness as shown in Equation 4-28. The risk of micropitting decreases with increasing values of the safety factor; the micropitting safety factor can be improved by macro geometry optimisation and profile modification. There are two different methods in ISO/TR 15144-1 (2010), (methods A and B) for determining the permissible specific film thickness. The permissible specific film thickness can be determined from specific gear testing or

standardised test method. Due to the lack of experimental validation in determining permissible specific film thickness values for WT gearbox applications, this chapter presents results using the lubricant film thickness to illustrate the effects of operational conditions.

Micropitting frequently occurs in areas of high contact stress, high local contact temperature and high sliding. The analysis of HSS gears of the WT gearbox shows that the lubricant film thickness is low at the dedendum of pinion gear, particularly at contact points D, DE and E. This means that the risk of micropitting increases greatly in this area (the risk of micropitting at different contact points is further discussed in Chapter 8). However, the lubricant film thickness at the addendum of the pinion gear is greater than 1.0  $\mu\text{m}$ , as illustrated in Figures 7.12 - 7.16 and Table 7-2. Hence, macro geometry optimisation such as profile shift and pressure angle change can be used to reduce the sliding parameter (Sheng, 2012).

All subsequent calculations are based on the average gear surface roughness of 0.7  $\mu\text{m}$  (maximum value) as recommended by IEC 61400 (2005 and 2012) standards (Appendix L). In this investigation, the minimum value of lubricant film thickness is 0.32  $\mu\text{m}$  under the lowest speed and highest torque condition as shown in Table 7-2. This is equivalent to the value of specific lubricant film thickness of 0.46 ( $=0.32/0.7$ ). The specific lubricant film thickness can increase through the reduction of the surface roughness of gear tooth flanks. It can be ascertained that by assuming an improved surface finishing of average surface roughness up to 0.1  $\mu\text{m}$ , the risk of the micropitting may be reduced considerably. The effects of surface roughness on micropitting is further discussed in Chapter 8, Section 8.6.

This chapter relies mainly on analytical predictions of micropitting risk by considering torque and rotational speed variations based on field SCADA data; its results correlate with evidence from previous relevant research. In Anuradha and Kumar (2012) and Beermann (2010), the variation trends of the film thickness along the line of action are similar to the finding of this study. In a similar study, Larsson (1997) calculated the contact stress, coefficient of friction and film thickness between the spur gear teeth using transient Reynolds equations. Larsson's significant findings pertaining to the lubricant film thickness and contact stress showed similar trends that are presented in this chapter. One of his main findings is that the smallest film thickness occurs at the

dedendum of pinion because of small radius of curvature and rolling velocity which ascertains the findings of this research. In addition, the KISSsoft commercial software is used to validate the results of this study: a report of results obtained at nominal load and speed condition is included in Appendix M. This analytical study may be validated experimentally using contact pattern tests to observe the contact patterns under different torque and rotational speed combinations. Predki et al (2011), as explained in Chapter 2, Section 2.8.2, investigated micropitting of a large spur gear similar to this study. They found that the micropitting occurred mostly in the dedendum area of pinion gear.

## **7.7 DISCUSSION**

### **Effect of variable on gear micropitting**

In this chapter, the torque ratio is varied according to SCADA data and the relationship between the contact stress and torque ratio is linear. The torque ratio has a greater impact on sliding parameter as the torque ratio increases the sliding particularly at tip and root of tooth flank. Consequently, this leads to the increase of local contact temperature and decrease of lubricant film thickness along the contact path of gear flank. The highest contact stress and local contact temperature occur during the greatest shaft torque and rotational speed. The minimum lubricant film thickness occurs at the lowest speed ratio and highest torque ratio. The variation of torque in HSS pinion gear causes great increases of contact stress and local contact temperature. This in turn leads to interrupt the lubrication between the contact gear teeth and may lead to direct surface contact and causes micropitting.

### **Effect of variable rotational speed on micropitting**

At both cases of the lower and higher speed operating conditions, a slight increase in local contact temperature occurs when subjected to a constant torque ratio. A higher rotational speed results in a slight increase in lubricant film thickness because the lubricant film thickness,  $h_y$ , is proportional to the velocity parameter,  $U_y^{0.7}$ , as shown in Equation 4-25. The variation of the rotational speed when subjected to a low torque ratio results in a slight increase in lubricant film thickness than that under a high torque ratio. Compared to the effect of variable torque ratio, varying rotational speed ratio has less impact on the local contact temperature and the lubricant film thickness. The

variation of the torque has a greater impact on the contact stress and flash temperature due to its direct proportional relationship with these variables.

### **Analytical assessment of micropitting**

Gear tooth flanks are subjected to varying loading and relative sliding conditions when the tooth pair engages along the line of action because of different radii of tooth profile curvature at the contact point and changes of single/double tooth contact region. These cause variations of some key variables such as gear tooth contact stress and sliding parameter between two mating teeth during each engagement cycle. The non-uniform distributions of contact stress, sliding parameter, temperature and lubricant film thickness over the tooth flank are obtained due to the variations of torque and rotational speed ratios along the gear shaft. The lubricant film thickness varies along the tooth flank and is at the lowest when the tip of the wheel gear engages with the root of the pinion gear. The lubricant film thickness increases with the increase of rotational speed and decreases as torque and sliding increase. It can be concluded that micropitting is most likely to initiate at the dedendum of pinion gear. The lowest film thickness occurs when the torque ratio is high and the rotational speed ratio is at the lowest which may cause direct tooth surface contact. At the low-torque ratio condition, the varying rotational speed ratio condition may cause a considerable variation of lubricant film thickness thus interrupting the lubrication which may result in micropitting.

## **7.8 SUMMARY**

An analytical study has been undertaken in this chapter to investigate the micropitting risk of the HSS stage gears of a WT gearbox when subjected to variable torque and rotational speed conditions, which result in variations of contact stress, sliding parameter, flash temperature and lubricant film thickness. The highest contact stress and temperature occur at the dedendum of pinion gear. In addition, the higher torque ratio leads to greater sliding on gear tooth flanks particularly at regions when the radius of relative curvature is small. Varying torque ratio at the highest speed ratio has a great effect on the increase of flash temperature. The local contact temperature is not much affected under the low torque ratio when the rotational speed ratio is varied. The lowest film thickness occurs when the torque ratio is high and the rotational speed ratio is at the lowest. The minimum lubricant film thickness  $0.32 \mu\text{m}$  is obtained for the variable

torque and rotational speed conditions considered. The micropitting is most likely to initiate at the dedendum of pinion gear under the condition of the lowest rotational speed ratio and highest torque ratio. At the low-torque ratio condition, the varying rotational speed ratio condition may cause a considerable variation of lubricant film thickness thus interrupting the lubrication which may result in micropitting.

## ***Chapter 8 Analytical Results Using Probabilistic Modelling of SCADA Data***

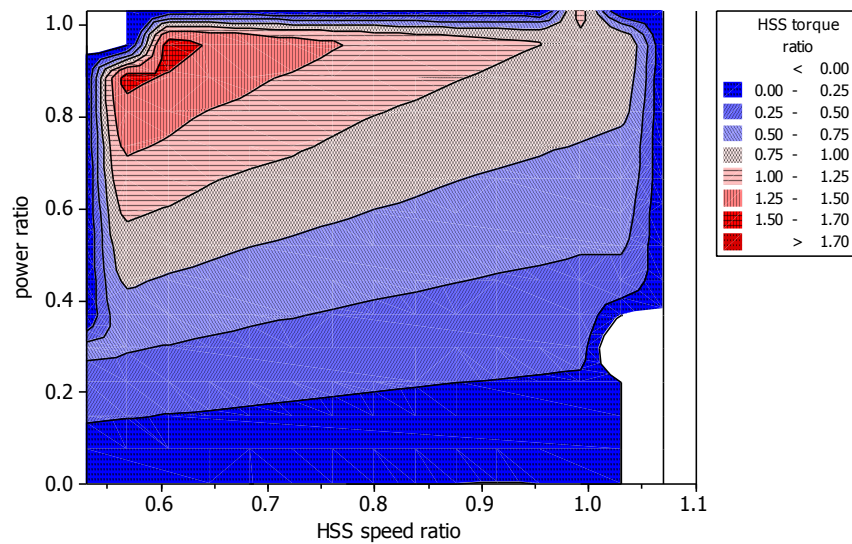
---

*This chapter presents a probability analysis of gear tooth flank micropitting risk by using recorded SCADA data of WTs in field operation. It investigates variations of the HSS pinion gear torque and rotational speed ratios based on selected random samples. Random number datasets of smaller sizes are generated to replace the large amount data in the original SCADA datasets of gear shaft torque and rotational speed, as detailed in Chapter 5. Based on the selected random number datasets the effect of variations of gear shaft torque and rotational speed on the probabilistic characteristics of gear tooth flank micropitting is investigated.*

*The 3000 random number datasets are generated to perform the probability analysis of gear tooth contact stress, sliding parameter, local contact temperature and lubricant film thickness. The results of the rated condition and the random sample dataset are compared. Different values of tooth surface roughness are used to investigate the effect of surface roughness on micropitting.*

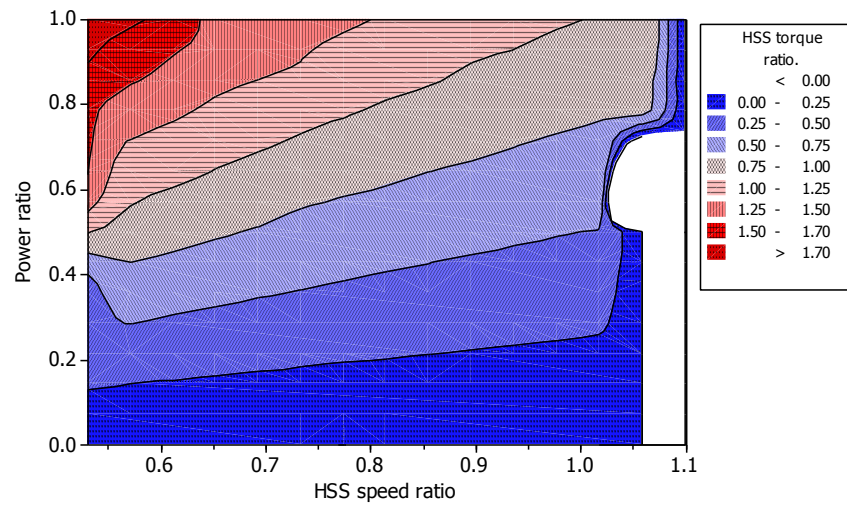
## 8.1 HISTOGRAMS OF SCADA DATA

Figures 8.1 and 8.2 show the contour plot of the calculated HSS torque ratio at the corresponding rotational speed ratio and generator power ratio for two WT gearboxes. It can be seen that the high torque ratio occurs between 0.7 and 1.0 of power ratio for both WTs. WT1 shows a higher number of occurrences operating at the rated torque ratio. However, WT2 reaches 1.9 times higher than the rated torque, as explained in Chapter 5, Section 5.2.2. According to the contour plots shown in Figures 8.1 and 8.2, the high torque occurs when the power ratio is high and the speed ratio is below the rated generator rotational speed.



*WT1 gearbox*

*Figure 8.1: WT1 contour plot of HSS pinion torque ratio vs. power ratio and rotational speed ratio*



*WT2 gearbox*

*Figure 8.2: WT2 contour plot of HSS pinion torque ratio vs. power ratio and rotational speed ratio*

## 8.2 HISTOGRAMS OF RANDOM NUMBERS

The torque ratio histogram obtained from WT1 SCADA data analysis datasets show a similar distribution to that modelled using the IEC recommended load cases, as given in Figure 5.6. Therefore, WT1 SCADA data is used for probabilistic modelling in this chapter. From the WT1 SCADA analysed datasets, 3000 samples are randomly generated for HSS pinion shaft torque ratio and rotational speed ratio using the MT generator. For the purpose of comparison, 1000 random samples of both torque ratio and rotational speed ratio are also generated. Figures 5.4, 5.5, 5.7 and 5.8 in chapter 5 show the histograms derived from the SCADA analysed datasets which can be compared with histograms derived from 3000 random datasets as shown in Figures 8.3 and 8.4. These figures compared to Figures 5.4 and 5.7 of WT1 show that the histograms of HSS pinion shaft torque ratio and rotational speed ratio from the SCADA analysed datasets and the random datasets have similar trends.

The datasets of the HSS pinion shaft torque ratio and rotational speed ratio of WT1 are divided into three regions as shown in Table 8-1. This allows checking the validity of the samples' randomness when compared to the SCADA analysed datasets to avoid the risk of bias. The range of these regions has been chosen based on the data distribution similarities in clustering and dispersion.

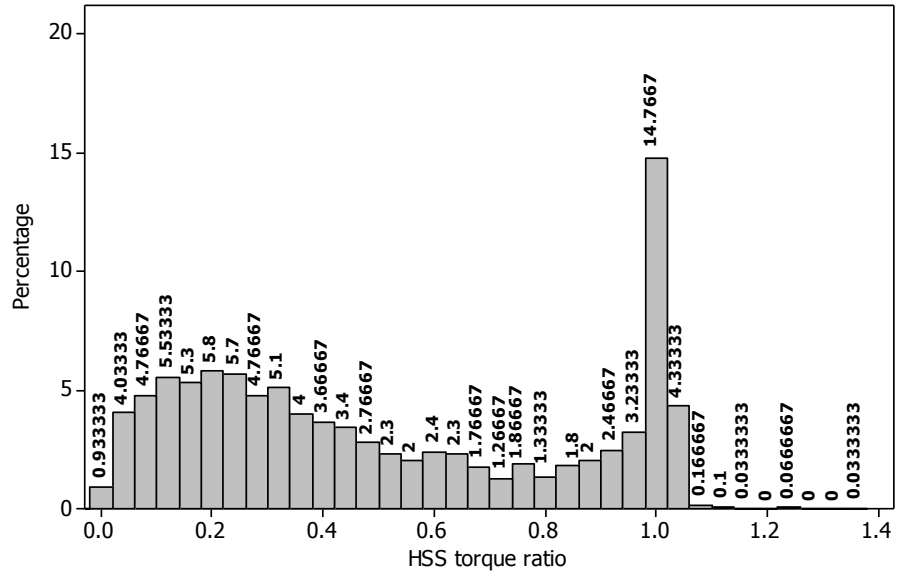


Figure 8.3: Histogram of 3000 random numbers of HSS pinion shaft torque ratio (WT1)

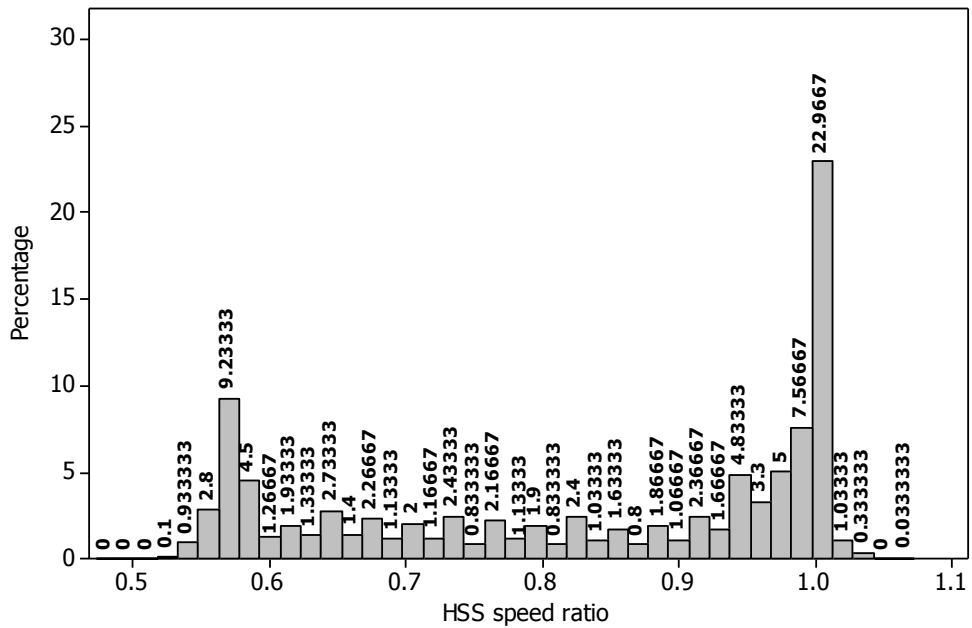


Figure 8.4: Histogram of 3000 random numbers of HSS pinion shaft rotational speed ratio (WT1)

Table 8-1 presents the corresponding percentages of WT1 HSS pinion shaft torque ratio and rotational speed ratio in each range by comparing the SCADA data with random samples datasets. When comparing the torque ratios at lower range of 0~0.54, the difference is around 2% between the SCADA analysed datasets and 3000 random samples. This small difference has negligible effects on the probability failure analysis of gear flank micropitting. Similarly, comparing the rotational speed percentage at

lower range of 0.53~0.63, where the data clustered, there is only a minimal difference between the 3000 random samples and the SCADA analysed datasets, this is also shown in rotational speed ratio histograms Figures 5.7 (Chapter 5) and 8.4. It is clear that the percentage differences are very small between all ratio ranges. The probabilistic comparisons between the three regions of the SCADA analysed and 3000 random samples datasets show that the differences are less than 1% for each range. The quantitative comparisons between the SCADA analysed datasets and random sample sets of 3000 and 1000 show that the 3000 random samplings have a closer approximation of the SCADA analysed datasets, as shown in Table 8-1. Thus, 3000 random samples are used in the probability analysis of gear flank micropitting which will be presented in the following sections. The histograms of 1000 random samples of both torque and speed ratios are shown in Appendix N.

*Table 8-1: Comparisons of different datasets*

Torque Ratio Range	SCADA analysed datasets	3000 random numbers	1000 random numbers
0 ~ 0.54	59%	58%	58.2%
0.541 ~ 0.94	18.1%	19.3%	17.8%
0.941 ~ 1.7	22.9%	22.7%	24%
<b>Speed Ratio Range</b>			
0.53 ~ 0.63	21.6%	20.7%	21.6%
0.631 ~ 0.93	32.9%	32.5%	30.1%
0.931 ~ 1.1	45.5%	46.8%	48.3%

### **8.3 PROBABILITY DISTRIBUTION OF CONTACT STRESS VARIATIONS**

Based on the WT1 datasets, the histogram of contact stress is shown in Figure 8.5, the high contact stresses occur in narrow spikes for all five contact points. In contrast, low contact stresses occur in a broader range. For example, the contact stresses at point D vary from 1187 to 1731 N/mm<sup>2</sup> covering a wide range, but with a high probability of occurrence within a narrow range from 1590 to 1625 N/mm<sup>2</sup>. When comparing the maximum contact stress of the selected random samples using probability analysis (1731 N/mm<sup>2</sup>) with the result of the rated condition (1526 N/mm<sup>2</sup> in Chapter 7, Section

7.2), the difference is  $205 \text{ N/mm}^2$ . The comparison between these two conditions indicates that the HSS gear tooth flank can be subjected to highly variable contact stresses. The histograms of contact stresses and HSS pinion torques have a similar trend and are clustered when the torque ratio being at the rated value. As shown in Figures 5.4 and 8.5, the maximum contact stresses occur at point D (below the tooth pitch line), and the minimum values occur at point A (at the tooth tip).

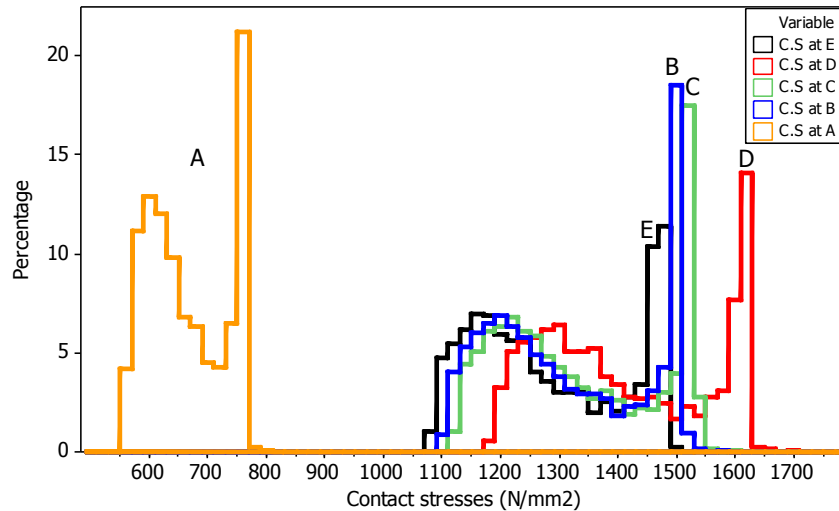


**Figure 8.5: Histogram of contact stresses at 5 contact points on gear tooth flank**

Figure 8.6 shows the histogram of contact stresses at point D on gear flank, extracted from Figure 8.5. It reveals the variation of contact stress and the maximum values in details. The allowable contact stress taken from ISO 6336-5 for material quality grades ME is shown in Figure 8.7. The ME grade is for high quality materials and is used for highly loaded gears. The maximum allowable contact stress for the ME grade is  $1650 \text{ N/mm}^2$ . The probability of failure region marked in the histogram of contact stress at point D shows that some contact stress values have exceeded the allowable contact stress value. About 0.23% of contact stress values are higher than the allowable contact stress for the total of 3000 random samples which are used in the calculation of contact stresses. This small percentage occurs during the different WT operating conditions when the HSS pinion shaft torque ratio exceeds 1.25 and rotational speed ratio ranges 0.55~0.7 as shown in WT1 contour plot in Figure 8.1. It may lead to the development of micropitting on tooth flank particularly at point D (below the pitch line, dedendum) of the pinion gear. This small percentage of high contact stress could reduce the number of operation cycles and accelerates the micropitting progression.

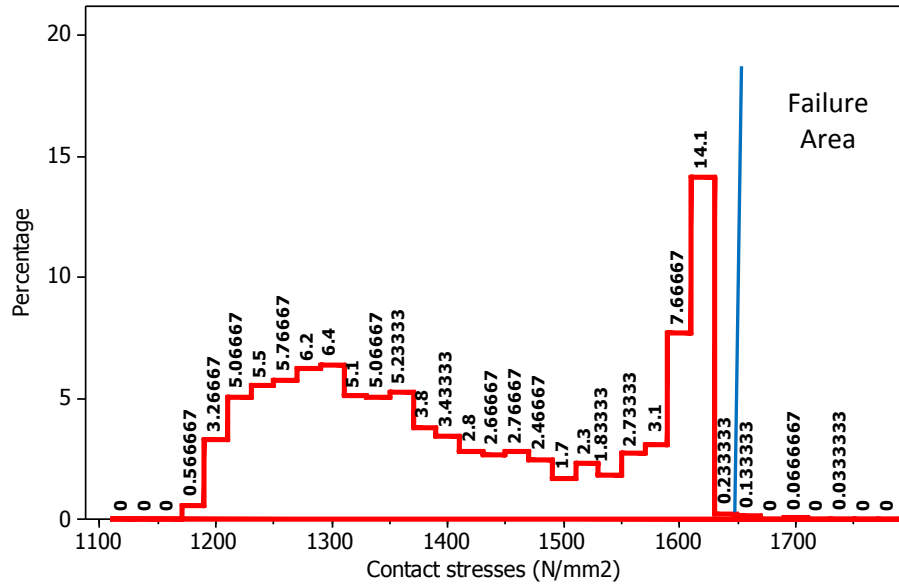


Figure 8.6: Histogram of contact stresses at point D on the path of contact

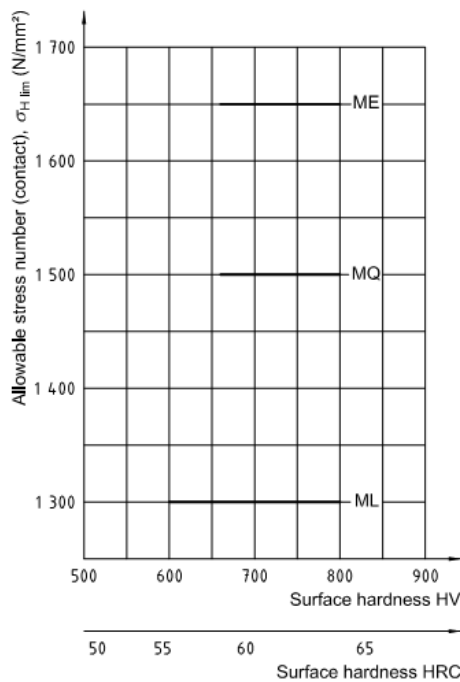
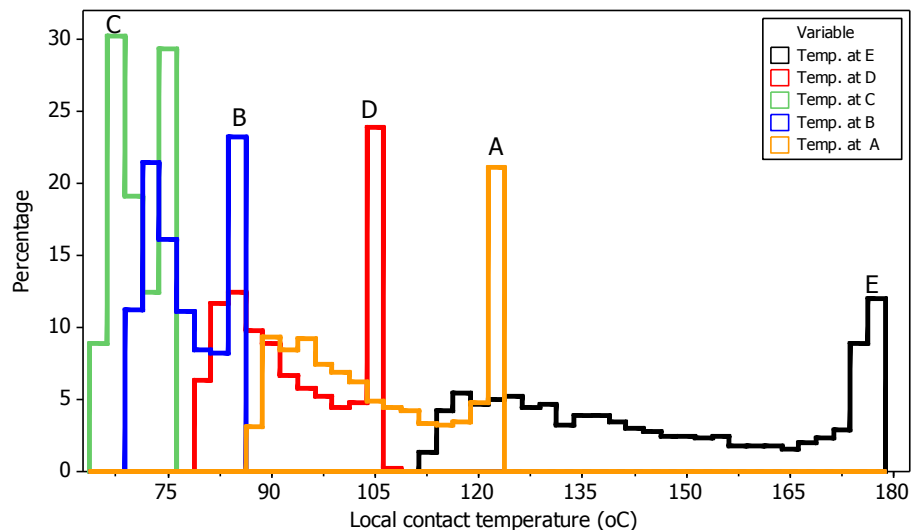


Figure 8.7: Allowable contact stress for case hardened wrought steels material (ISO 6336-5)

## 8.4 PROBABILITY DISTRIBUTION OF LOCAL TEMPERATURE VARIATIONS

Figure 8.8 shows the histogram of local contact temperatures of gear tooth flank. It reveals that the temperatures at point E (at dedendum) change frequently and vary from about 110 °C to 180 °C. The differences between temperature results of rated condition

and random samples condition are very small. This is owing to the fact that the high torque, which occurs at the low rotational speed ratio of about 0.55, as shown in Figures 8.1 and 8.2. The local sliding velocity,  $V_{g,Y}$ , is directly proportional to the flash temperature, as given in Equation 4-20. Thus, the high torque ratio which occurs at the low rotational speed condition has a minor impact on gear tooth flank temperature. As a result, the main cause of micropitting is the overload that leads to high contact stress. The maximum local contact temperatures and frequent temperature changes at point E result from both the higher contact stress and the greater sliding velocity at this region. The contact point C (pitch line) has the minimum temperature values and variations at various torque and rotational speed conditions because of the zero sliding velocity (pure rolling).



*Figure 8.8: Histogram of local contact temperature at 5 contact points on gear tooth flank*

## 8.5 PROBABILITY DISTRIBUTION OF SLIDING PARAMETER VARIATIONS

The histogram of sliding parameter is shown in Figure 8.9. It illustrates that the sliding parameter changes continuously except for point C (pitch point) having pure rolling. The maximum sliding reaches about 95% which occurs at point E at the dedendum of pinion gear where the maximum local contact temperatures occur. Comparing the sliding results of the rated condition and random samples it is clear that the differences are also very small as the bulk and flash temperatures are dependent on the sliding

parameters, as explained in Chapter 7, Section 7.3 and shown in Figure 4.9. Point B has lower sliding than points A, D and E. This is because the radius of relative curvature in this area is bigger than the dedendum area of the pinion gear as explain in Chapter 7, Sections 7.2 and 7.5.

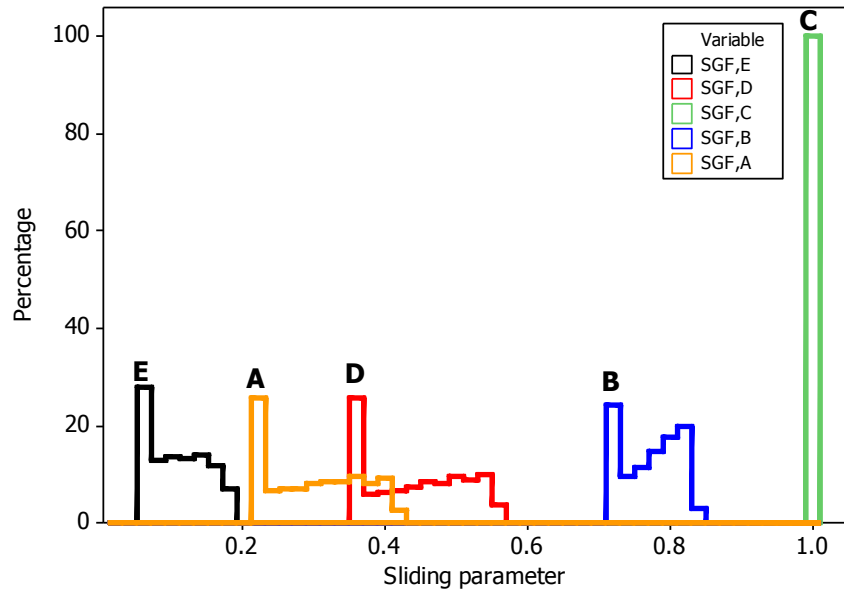


*Figure 8.9: Histogram of sliding parameter at 5 contact points on gear tooth flank*

## 8.6 PROBABILITY DISTRIBUTION OF LUBRICANT FILM THICKNESS VARIATIONS

The probability analysis shows that the worst lubricant film thickness condition occurs at point E, among the five contact points along the gear contact path. The minimum lubricant film thickness reduces to  $0.3 \mu\text{m}$  as shown in Figure 8.10. It is clear that the maximum contact temperature, sliding parameter and the minimum lubricant film thickness all occur at point E, as shown in Figures 8.8, 8.9 and 8.10 respectively. The high temperatures can breakdown the lubricant film because high temperatures reduce the lubricant dynamic viscosity. The minimum lubricant film thicknesses occur due to the high contact stresses, greater sliding parameter and high local contact temperatures. The risk of micropitting increases greatly on the dedendum area because of combinations of high contact stresses, high sliding, high local contact temperatures and low lubricant film thicknesses which occur in this region. The maximum lubricant film thickness occurs at point A (the tooth tip) due to greater relative curvature radii of the

tooth flanks which in turn leads to low contact stress. The radius of relative curvature,  $\rho_{n,Y}$ , is directly proportional to the lubricant film thickness,  $h_Y$ , as Equation 4-25 shows.

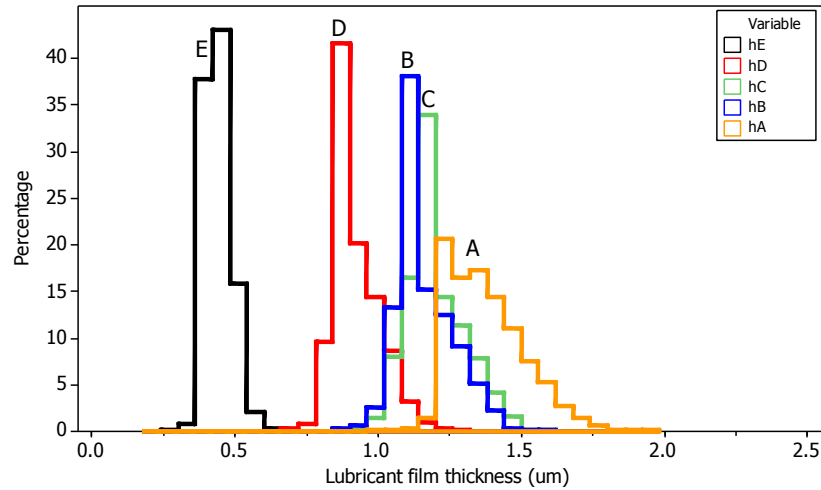


**Figure 8.10: Histogram of lubricant film thickness at 5 contact points on gear tooth flank**

The lubricant film thickness can be increased by reducing the surface roughness of contact gear surfaces. Equation 4-26 can be used to determine the specific lubricant film thickness if the surface roughness of meshing gears is known. WT gears require high accuracy and smooth tooth surface finishing which provide sufficient load capacity to achieve required service cycles. Such a smooth surface is one of the most important factors in micropitting resistance (IEC 61400-1, 2005 and IEC 61400-4 2012). It is recommended in IEC 61400 that the maximum roughness of the WT gear surfaces is equal to or less than  $0.7 \mu\text{m}$ , as explained in Chapter 7, Section 7.6. The safety factor against micropitting is defined as the ratio between the minimum specific lubricant film thicknesses and the permissible specific lubricant film thickness as given by Equation 4-28. Currently there are no recommended values of the required minimum safety factor for wind turbine gearbox applications. However, according to Kissling (2012) the range of micropitting safety factor is defined by rating the risk in three levels: the high risk, limited risk and low risk, as shown in Table 8-2. According to Table 2-1 in Chapter 2, Dudley (1994) found that the specific lubricant film thickness is in full film lubrication condition when it is bigger than unity. The safety factor can be calculated using Equation 4-28 and according to this analysis, the minimum specific lubricant film thickness occurs at point E which is about unity when 0.3 surface roughness is used (Figure 8.14). Based on the above, the specific lubricant film thickness should be equal

to or greater than unity to change the risk from high to limited or low (Table 8-2). Figure 8.11 shows the histogram of specific lubricant film thickness using the contact surface average value of surface roughness of  $0.7 \mu\text{m}$ . It shows that the specific lubricant film thickness at contact point E has the lowest values (less than 1.0) which presents a greater risk of micropitting compared to other contact points according to Table 8-2. Figure 8.12, which is extracted from Figure 8.11, reveals that all values of specific lubricant film thickness at point E is below the limit value  $n \leq 1.0$  indicating it has a high risk of micropitting. In addition, 0.3% of the values of specific lubricant film thickness at point D are equal to or less than 1.0, indicating the presence of a high risk of micropitting. By reducing the maximum surface roughness from  $0.7 \mu\text{m}$  to  $0.3 \mu\text{m}$  a considerable change in the values of specific lubricant film thickness occurs, as shown in Figure 8.13. It indicates that the majority of values of specific lubricant film thickness at point E shift from less than 1.0 to higher values thus reducing the probability of failure from the high risk to the limited risk. Figure 8.14 shows the histogram of specific lubricant film thickness at point E, extracted from Figure 8.13. It shows the occurrence percentages of specific lubricant film thickness at various values and highlights the high risk area. By reducing the surface roughness, the probability of failure, as marked in Figure 8.14, shows a significant reduction of the high risk of micropitting at point E compared to that at the maximum surface roughness of  $0.7 \mu\text{m}$  (Figure 8.12). It only presents about 0.1% of the 3000 random numbers that are used in the calculation of specific lubricant film thickness, as shown in Figure 8.14.

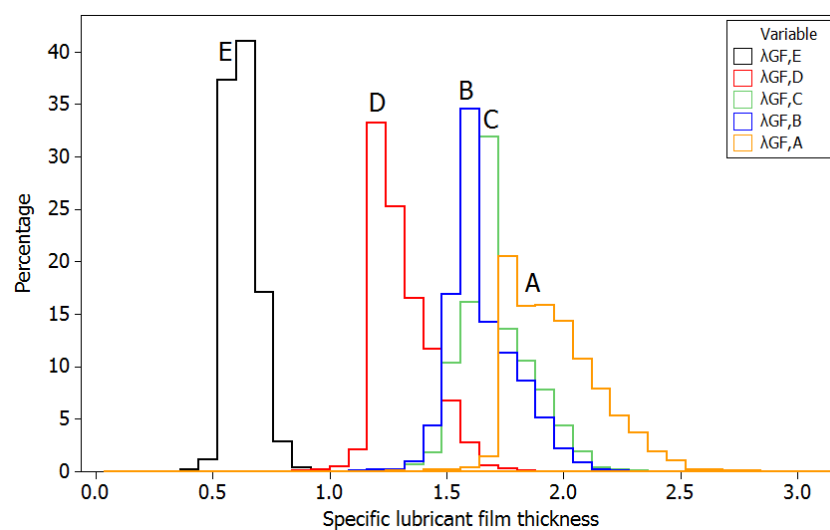


**Figure 8.11: Histogram of specific lubricant film thickness of gear tooth flank ( $0.7 \mu\text{m}$  surface roughness)**

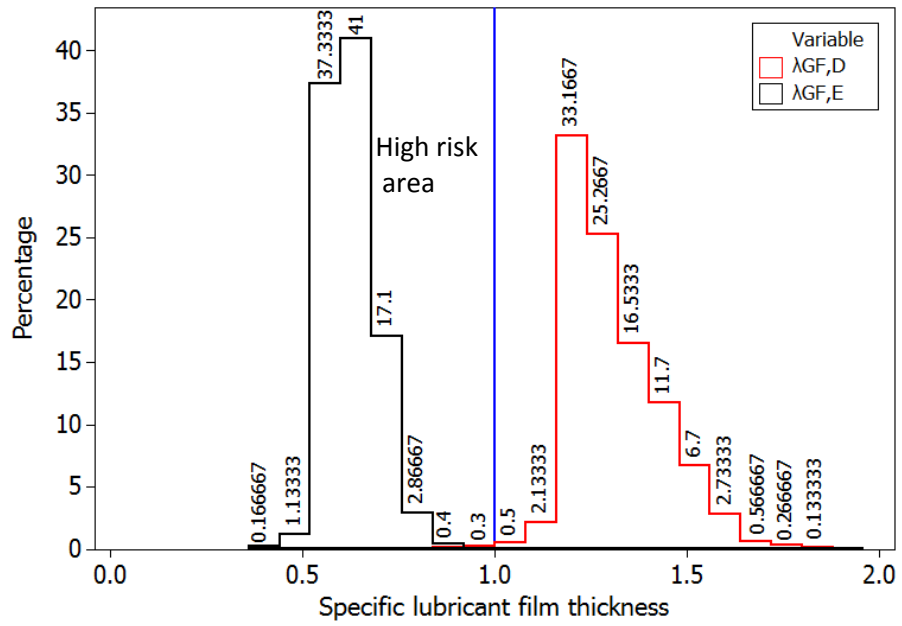


Figure 8.12: Histogram of specific lubricant film thickness at point E and D (0.7 μm surface roughness)

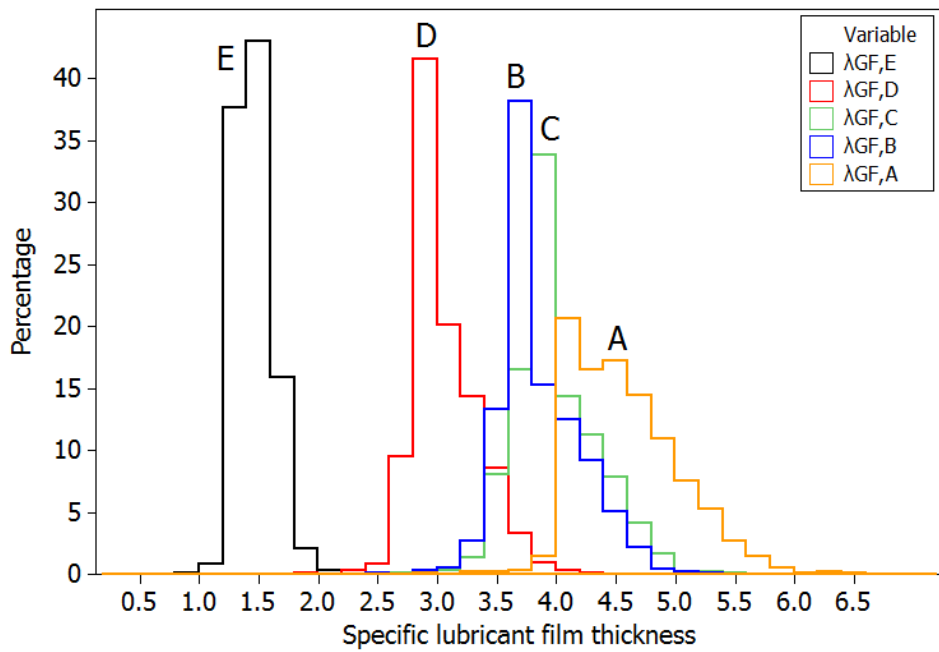


Figure 8.13: Histogram of specific lubricant film thickness of gear tooth flank (0.3 μm surface roughness)

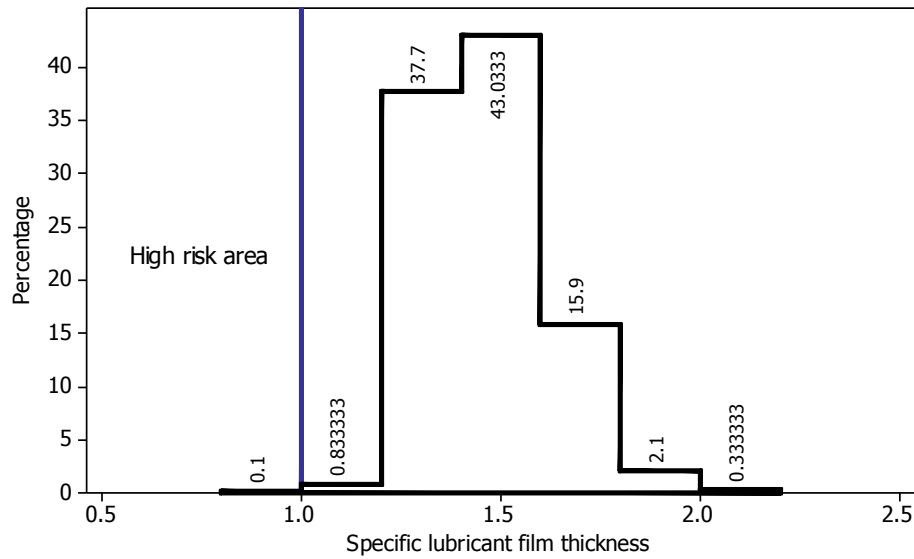


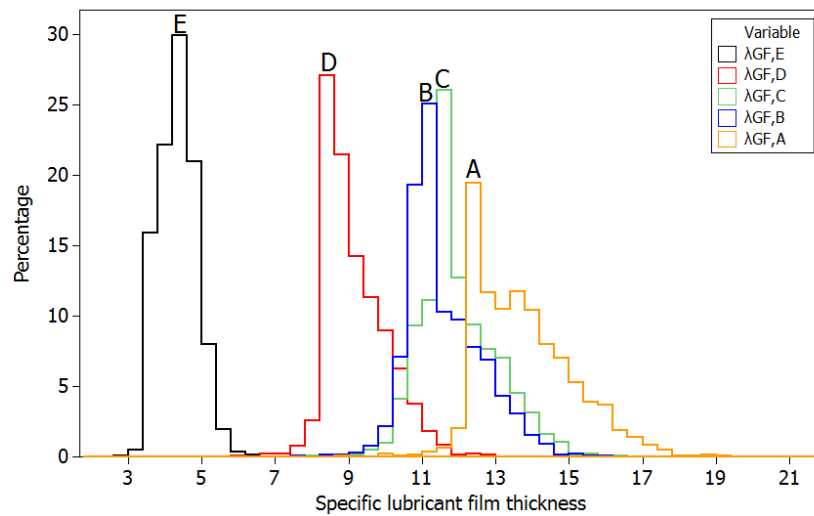
Figure 8.14: Histogram of specific lubricant film thickness at point E (0.3 μm surface roughness)

Table 8-2 Micropitting Safety Factor (Kissling, 2012)

Factor of Safety	Risk Rating
$n < 1$	High risk
$1 \leq n \leq 2$	Limited risk
$n > 2$	Low risk

The minimum specific lubricant film thickness value of about 0.4, which occurs at point E as shown in Figure 8.12, is observed when the maximum average roughness of gear surfaces of 0.7 μm is used as recommended by IEC 61400. However, even with reduced surface roughness of gear contact surfaces up to 0.3 μm, the micropitting safety factor at point E still shows a considerable probability of failure ranging from high risk to limited risk, Figure 8.14. When the maximum surface roughness is 0.3 μm, the probability of micropitting failure consists of 0.1% high risk and 99.6% limited risk, as Table 8-2 and Figure 8.14 show. Winkelmann (2011) found that the superfinished gear tooth flanks to 0.1 μm reduce micropitting and can increase the micropitting safety factor by five. He found that, gear micropitting can be prevented by using up to 0.1 μm surface roughness through applying FZG back to back gear test rig and using low micropitting resistance oil.

Figure 8.15 shows the histogram of specific lubricant film thickness using the value of surface roughness of  $0.1 \mu\text{m}$ , as advised by Winkelmann. It reveals that all values of specific lubricant film thickness at point E are above three, placing them in the low risk of micropitting. It is clear that the risk of micropitting decreases with reducing the surface roughness of the contact surfaces. The high risk of micropitting is caused by the possible torque overloading occurring on the WT gearbox which induces the high contact stresses on tooth flank. The combination of high torques and variation of shaft rotational speed causes great variations of local contact temperature which in turn results in low lubricant film thickness and its considerable variation during each gear meshing cycle. It is also worth mentioning that the probability analysis of the HSS pinion gear has not considered any tooth profile modification such as tip relief and crowning which can help to improve the micropitting safety factor. This analysis has revealed the considerable influence of variable torque and rotational speed conditions on the considerable risk of micropitting failure.



*Figure 8.15: Histogram of specific lubricant film thickness of gear tooth flank ( $0.1 \mu\text{m}$  surface roughness)*

## 8.7 SUMMARY

The probability analysis shows that the highest torque ratio of over 1.6~1.9 can occur in HSS pinion shaft under the condition of the rotational speed ratio of around 0.55 and power ratio of about 0.9 ~ 1.0, i.e. operating at the rated power but at a rotational speed below the rated rotational speed of generator. The overloading condition presents the main cause of HSS pinion gear flank micropitting risk due to high contact stress and

low lubricant film thickness. Furthermore, the highest contact stresses occur below the pitch line in the dedendum region of gear flank and they may exceed the gear material allowable contact stress. In addition, the maximum local contact temperatures occur in the dedendum region where the maximum contact stresses and greater sliding are present.

The calculation of the safety factor of specific lubricant film thickness has shown a considerable risk of micropitting failure when the maximum roughness of gear surfaces of  $0.7 \mu\text{m}$  is used as recommended by IEC 61400. Even with a reduced gear flank surface roughness up to the maximum value of  $0.3 \mu\text{m}$ , the limited risk of micropitting still prevails. The high probability of micropitting failure is at the dedendum area of gear flank. The superfinishing surface treatments may prevent the occurrence of micropitting according to the results of the probability analysis.

## *Chapter 9: Conclusions and Future Work*

---

*This chapter presents the key findings of this study, which demonstrate how the set research aims and objectives have been achieved. Suggestions for future work are described at the end of this chapter.*

## 9.1 CONCLUSIONS

This study investigated the prediction of WT gear micropitting under variable load and speed conditions. The research involved analytical, probabilistic and experimental approaches. These approaches provide different methodologies to predict the risk of gear micropitting and their initiation and progression in WT application. Based on the results obtained and presented in the previous chapters the following conclusions can be drawn.

### 9.1.1 Conclusions Drawn From Experimental Results

- ❖ It is found that the excessive loading, micro-geometry, surface roughness and lubricant film thickness are the main factors affecting micropitting. The micropitting initiates in the form of lines at the peaks in the addendum and the dedendum of the tooth flank (see Figures 6.2 and 6.3). The peaks of surface roughness erode after each cycle run. The comparison of the surface roughness measurements before and after the test runs shows that a deep valley occurs below the original tooth surface, which indicates that the material is eroded and micropitting exists on the tooth flank (see Figure 6.12).
- ❖ Micropitting starts to occur at the load ratio of 0.5 in the dedendum area of pinion (see Figure 6.2). This micropitting is non-progressive along the dedendum area until the final test run. However, the micropitting prevails at the pinion addendum, owing to progressive micropitting at the dedendum of the wheel and the surface roughness variation of gear flanks.
- ❖ The micropitting area at the pinion dedendum is less severe than at the addendum area, but pits are deeper at the dedendum, according to the profile deviation results (see Figure 6.15). This indicates that the micropitting on the pinion dedendum causes greater profile deviation.
- ❖ The tooth profile deviation of wheel gear is worse and more progressive than that of the pinion gear. The wheel profile deviation appears from the root to the tip of the wheel. The beginning edge of the pinion tip relief can contribute to the initiation of micropitting.

The analytical study of the tested gear is conducted to confirm the experimental results. The following conclusions are drawn:

- ❖ The maximum contact stresses occur at the beginning of the tip relief (addendum) and at the root (dedendum) of the pinion. This indicates that the micropitting can initiate at these areas because of higher contact stresses, greater sliding causing higher temperatures and lower film thicknesses (see Figures 6.35 – 6.38).
- ❖ Throughout the experimental testing, the varying surface roughness has a greater effect on the specific lubricant film thickness than the varying torque. The variation of specific lubricant film thickness along the tooth flank at different torque ratios is trivial.
- ❖ The analytical comparisons between the ISO Technical Report ISO/TR 15144-1 and AGMA 925-A03 standard show that the ISO/TR provides a better correlation between the predicted minimum specific lubricant film thickness and the occurrence of micropitting observed in the experiment.
- ❖ The analysis of the specific lubricant film thickness is in a reasonably good agreement with the Linke curve for predicting micropitting (see Figure 6.39).

### **9.1.2 Conclusions Drawn From Analytical Results of Selected SCADA Data**

- ❖ The highest contact stress and temperature occur at the dedendum of pinion gear. The high torque leads to greater sliding on tooth flanks particularly at regions when the radius of relative curvature is small.
- ❖ The combined effect of torque and rotational speed variations has a great effect on the local contact temperature. Varying torque at the highest speed has a significant effect on the increase of flash temperature. In comparison, the torque variation has a greater effect on the flash temperature than that of the rotational speed. The local contact temperature is not much affected under the low torque when the rotational speed varies (see Figures 7.10 and 7.11).

- ❖ The lowest film thickness occurs when the torque is high and the rotational speed is at the lowest. The low torque and high rotational speed can contribute to increase the lubricant film thickness. At the low-torque condition, the varying rotational speed may cause a considerable variation of lubricant film thickness (see Figure 7.16) thus interrupting the lubrication which may result in micropitting.
- ❖ Micropitting is most likely to initiate at the dedendum of the driven pinion gear under the condition of the lowest rotational speed and high torque. The lubricant film thickness increases with the increase of rotational speed and decreases as torque and flash temperature increase.

### **9.1.3 Conclusions Drawn From Analytical Results of Probabilistic Modelling of SCADA Data**

- ❖ Highest torque ratio of over 1.6~1.9 can occur in HSS pinion gear shaft under the condition of the rotational speed ratio of around 0.55 and power ratio of about 0.9 ~ 1.0, i.e. operating at the rated power but at a rotational speed below the rated rotational speed of generator (see Figures 5.4, 5.5 and 8.1).
- ❖ The comparisons of torque and speed ratios between the 3000 random samples using MT random number generator and the whole SCADA analysed datasets show only a minimal difference in statistic characteristics of the datasets (see Table 8-1).
- ❖ Based on SCADA data analysis, the WT gearbox's overloading condition of up to 1.9 torque ratio is the main cause of HSS pinion gear flank micropitting risk due to high contact stress and low lubricant film thickness.
- ❖ The highest contact stresses occur below the pitch line in the dedendum region of gear flank and they may exceed the gear material allowable contact stress. The percentage of contact stresses which exceeds the allowable contact stress is about 0.23% (see Figure 8.6).

- ❖ The differences between temperature results of rated condition and probabilistic modelling are very small. This is owing to the high torque which occurs at the low rotational speed ratio at about 0.55, see Figures (8.1 and 8.2).
- ❖ The calculation of the safety factor of specific lubricant film thickness has shown a considerable risk of micropitting failure when the maximum roughness of gear surfaces of 0.7  $\mu\text{m}$  is used. Even with a reduced gear flank surface roughness up to the value of 0.3  $\mu\text{m}$ , the limited risk of micropitting still prevails. This high probability of micropitting failure is more evident at dedendum area of gear flank.
- ❖ The superfinishing WT gears tooth flanks to 0.1  $\mu\text{m}$  reduces micropitting in WT gearboxes and increases the safety factor. According to the probability analysis, this places the gear tooth flank in the low micropitting risk area.

This research has contributed to new knowledge with regard to micropitting behaviour of gears in the application of wind turbine gearboxes. The combination of experimental and analytical investigation approaches helped to better analyse micropitting under variable load and speed conditions. The toolkit calculation sheet based on ISO Technical Report ISO/TR 15144-1 provides analytical methods to calculate gear contact stress, sliding parameter, local contact temperature and lubricant film thickness which enable the prediction of the onset and development of surface micropitting. Due to the complexity of WT gearbox application and the complex nature of WT control and their working conditions, the prediction of gear micropitting is not limited to the above calculated parameters as a host of other parameters are involved. Other parameters could not be included because of limitations associated with ISO/TR and the limited availability of test data for WT gearboxes. Hence, the development of an empirically- or analytically- based model linking these parameters to appropriate threshold values for the onset of micropitting is the work that has yet to be undertaken by research. This step is essential to produce a complete industrial design tool. Thus, the findings of this research serve as a useful step towards the development of a comprehensive model that integrates various approaches and considers the numerous key parameters involved in micropitting risk prediction.

## 9.2 RECOMMENDATIONS FOR FUTURE WORK

This study investigated micropitting under different operational conditions. Several possible future research areas resulting from this research work are enlisted in this section.

- ❖ Due to the variation of load during each gear meshing cycle, the dynamic factor and gear mesh stiffness variations should be taken into account when calculating gear contact stress for each point of contact instead of using average values.
- ❖ The 3<sup>rd</sup> stage of WT gearbox, HSS pinion gear was analysed in this study. However, the 2<sup>nd</sup> stage can be studied to show the difference in lubrication condition between the 2<sup>nd</sup> stage and 3<sup>rd</sup> stage.
- ❖ In this study, recorded SCADA datasets for two WTs gearboxes are analysed. More WT datasets from different locations using the same methodology can be analysed to investigate the variation in gear tooth flank micropitting risk between different WTs gearboxes.
- ❖ The WT gearbox is speed increaser (pinion is driven) and according to the analysis results the micropitting may initiate at the dedendum area. Whereas in the experiment test the pinion is used as driver and the micropitting at the pinion dedendum is less severe than at the pinion addendum area. More experimental investigations are needed to investigate if using the wheel as driver affects the position of micropitting initiation and progression.
- ❖ Tested gears can be measured using surface roughness instrument to ascertain if high peaks are present in the gear tooth surface. If so then surface finish treatments such as superfinishing or re-grinding can be used to reduce these peaks. By using these treatments if micropitting is still observed, identical tested gears can be remanufactured and retested to observe if the position of micropitting initiation would occur differently.
- ❖ The tested gears are subjected to variable loads and constant speed. Different tests can be performed at the highest load levels (where

micropitting developed progressively and densely in this study) but with different rotational speed at low cycle runs instead of starting at low load to better monitor the micropitting.

- ❖ Using different lubricant oils may be beneficial to reduce the friction between high peaks of surface roughness as micropitting is initiated at these peaks. In addition, different surface coating can be used to minimise the surface roughness and sliding parameter. Furthermore, oil filtration of test rig can be improved to separate particles, such as debris, or any contaminants from recycling within the lubrication system.
- ❖ In all gear tests, the oil inlet temperature was always held constant at (90°C). Different tests can be conducted on the same test rig under different temperatures for further studies. Then a comparison can be made with the current study to explore the behaviour of micropitting progression. It is worth investigating the change of micropitting initiation and progression when the lubricant fluid properties change.
- ❖ Pitting tests can be conducted with a different gear material with different surface treatment and hardness. The micropitting may be related to material microstructure and dislocation motion at the contact surfaces as explained in Chapter 2, Section 2.8.3.
- ❖ Micropitting and other gear failures can occur due to the misalignment or vibration caused by bearings, shaft and joint faults in WT's gearboxes. A comprehensive model can be devised for integrating and considering all these parts in a single analysis model.

---

## REFERENCES

- Abersek, B. and Flasker, J. 2004. *How Gears Break*, Southampton, WIT Press.
- AGMA (American Gear Manufacturers Association), 2003. *ANSI/AGMA/AWEA* (American National Standards Institute and American Wind Energy Association). Standard for Design and Specification of Gearboxes for Wind Turbines. ANSI/AGMA/AWEA 6006-A03. Alexandria; pp. 1-94.
- AGMA 925-A03, 2003. Effect of Lubrication on Gear Surface Distress; *AGMA*, Alexandria.
- Alban, L. E. 1985. Systematic Analysis of Gear Failures. *American Society for Metals*, Metals Park, OH, pp. 94-106.
- Anderson, N., Powertrain, G., Tinkleman, M., Boardman, B., Deere, J., Suren Rao, Brindle, R., Namie, S. and Williams, G. 2004. Gear Industry Vision. A Vision of Gear Industry in 2025. *Technical Report Developed at the Gear Industry Vision Workshop*. Detroit: The report was prepared by Energetics, Inc., and sponsored by U.S. Army, AGMA Foundation, ASME CRTD, Ben Franklin Technology Center, Boeing, Gleason Foundation, GM, and John Deere.
- Anifantis, N. and Dimarogonas, A. D. 1993. Flash and Bulk Temperatures of Gear Teeth Due to Friction. *Mechanism and Machine Theory*, 28, pp. 159-164.
- Antoine, F. and Besson, J. M. 2002. Simplified Modellization of Gear Micropitting. *Proceedings of the Institution of Mechanical Engineers, Part G: Journal of Aerospace*, 216, pp. 291-302.
- Anuradha, P. and Kumar, P. 2012. Effect of Lubricant Selection on EHL Performance of Involute Spur Gears. *Tribology International*, 50, pp. 82-90.
- Arvin, J., Manesh, M. Michaud and Winkelmann, L. 2002. The Effect of Chemically Accelerated Vibratory Finishing on Gear Metrology. *AGMA Technical Paper 02FTMI*, pp. 1-16.
- AWEA (American Wind Energy Association). 2013 [Online]. Available from:- <http://www.awea.org/Issues/Content.aspx?ItemNumber=5083&RDtoken=26861&userID=4379> [Accessed 05 Dec 2013].
- Bala, V., Brandt, G. and Walters, D. K. 2000. Fuel Economy of Multigrade Gear Lubricants. *Industrial Lubrication and Tribology*, 52, pp. 165 - 173.
- Bartz, W. J. 1993. *Lubrication of Gearing: Lubricants and Their Properties, Design of Gears, Practical Gear Lubrication, Failure Analysis*, London, Mechanical Engineering Publication Limited.
- Beermann, S. 2010. Calculating Micropitting for Wind Energy. *KISSsoft*, pp. 54-59.

- Bell, M., Sroka, G. and Benson, R. 2012. *The Effect of the Surface Roughness Profile on Micropitting*, AGMA Technical Paper: 12FTM20. Virginia: American Gear Manufacturers Association.
- Bergseth, E. 2009. *Influence of Gear Surface Roughness, Lubricant Viscosity and Quality Level on ISO 6336 Calculation of Surface Durability*. Stockholm: Department of Machine Design, Royal Institute of Technology.
- Berthe, D., Flamand, L., Foucher, D. and Godet, M. 1980. Micropitting in Hertzian Contacts. *Journal of Lubrication Technology*, 102, pp. 478-489.
- Bhushan, B. 2002. *Introduction to Tribology*, New York, John Wiley & Sons.
- Blok, H. 1937. Theoretical Study of Temperature Rise at Surfaces of Actual Contact Under Oiliness Lubricating Conditions. *Proceedings General Discussion on Lubrication and Lubricants, Institution of Mechanical Engineers*, 2, pp. 222-235.
- Brandão, J. A., Seabra, J. H. O. and Castro, J. 2010. Surface Initiated Tooth Flank Damage. Part II: Prediction of micropitting initiation and mass loss. *Wear*, 268, pp. 13-22.
- Brechot, P., Cardis, A. B., Murphy, W. R. and Theissen, J. 2000. Micropitting Resistant Industrial Gear Oils with Balanced Performance. *Industrial Lubrication Tribology*, 52, pp. 125-136.
- BS ISO 21771, 2007. *Gears - Cylindrical Involute Gears and Gear Pairs — Concepts and Geometry*. U.K: BSI, pp. 1-83.
- BS ISO/TR 13989-2, 2000. *Calculation of Scuffing Load Capacity of Cylindrical, Bevel and Hypoid Gears —Part 2: Integral Temperature Method*. BSI, pp. 1-48.
- Bull, S. J., Evans, J. T., Shaw, B. A. and Hofmann, D. A. 1999. The Effect of the White Layer on Micro-pitting and Surface Contact Fatigue Failure of Nitrided Gears. *Proceedings of the Institution of Mechanical Engineers, Part J: Journal of Engineering Tribology- Part J*, 213, pp. 305-313.
- Carvill, J. 1993. *Mechanical Engineer's Data Handbook*. Oxford, Butterworth-Heinemann.
- Cheng, W., Cheng, H. S., Mura, T. and Keer, L. M. 1994. Micromechanics Modeling of Crack Initiation Under Contact Fatigue. *Journal of Tribology*, pp. 116, 2-8.
- Childs, P. 2004. *Mechanical Design (2nd Edition)*, Oxford: Elsevier Butterworth Heinemann.
- Crook, A. W. 1957. Simulated Gear-Tooth Contact: Some Experiments Upon their Lubrication and Sup-surface Deformation. *Proceedings of the Institution of Mechanical Engineers*, 171.
- Davis C., 2006. A Better Random Number Generator. *Small Talk Newsletter*, Society of Actuaries, 26, pp. 20-21.

- Dawson, P. H. 1962. Effect of Metallic Contact on the Pitting of Lubricated Rolling Surface. *Journal of Mechanical and Engineering Sciences*, 4(1), p. 16.
- Ding, Y. and Rieger, N. F. 2003. Spalling Formation Mechanism for Gears. *Wear*, 254, pp. 1307-1317.
- Djeddou, F. and Zegadi, R. 2007. Practical Statistical Methods for Predicting Life and Reliability of Fine Pitch Gear Pairs. *Journal of Engineering and Applied Sciences*, 2, pp. 494-500.
- Dong, W., Xing, Y., Moan, T. and Gao, Z. 2013. Time Domain-Based Gear Contact Fatigue Analysis of a wind Turbine Drive Train Under Dynamic Conditions. *International Journal of Fatigue*, 48, pp. 133-146.
- Dowling, N. E. 2007. *Mechanical Behavior of Materials: Engineering Methods for Deformation, Fracture, and Fatigue*, New Jersey: Pearson Prentice Hall.
- Dowson, D. 1979. *History of Tribology*. London: Longman Group Ltd.
- Dowson, D. and Higginson, G. R. 1959. A Numerical Solution to the Elastohydrodynamic Problem. *Journal of Mechanical and Engineering Sciences*, 1, pp. 6-15.
- Dowson, D. and Higginson, G. R. 1966. *Elasto-hydrodynamic Lubrication the Fundamentals of Roller and Gear Lubrication*. Oxford: Pergamon Press.
- Dowson, D. and Toyoda, S. 1978. A Central Film Thickness Formula for Elastohydrodynamic Line Contacts. *Proceedings of 5th Leeds- Lyon Symposium*, Paper 11 (VII), pp. 60--65.
- Dudley, D. W. 1994. *Handbook of Practical Gear Design*. N.W.: CRC Press.
- Düzçükoglu, H. and Imrek, H. 2008. A New Method for Preventing Premature Pitting Formation on Spur Gears. *Engineering Fracture Mechanics*, 75, pp. 4431-4438.
- El-Sharkawi, M. A. 2013. *Electric Energy: An Introduction*, USA: Taylor and Francis Group, CRC press.
- Errichello, R. and Muller, J. 1994. Application Requirements for Wind Turbine Gearboxes. *Geartech*; In: Musial, W. (ed.) *National Renewable Energy Laboratory, US, NREL/TP- 442-7076*, pp. 1-56.
- Errichello, R. L. 2012. Morphology of Micropitting. *The Journal of Gear Technology*, 6, pp. 74-81.
- Ertel, A. M. 1939. Hydrodynamic Lubrication Based on New Principles. *Akad. Nauk. SSSR Prikadnaya Matematika I Mekanika*, 3, pp. 41-52.
- Evans, H. P., Snidle, R. W., Sharif, K. J., Shaw, B. A. and Zhang, J. 2013. Analysis of Micro-Elastohydrodynamic Lubrication and Prediction of Surface Fatigue Damage in Micropitting Tests on Helical Gears. *Journal of Tribology*, 135, pp. 1-9.

- Evans, M. H. 2013. *White Structure Flaking Failure in Bearings under Rolling Contact Fatigue*. PhD thesis, University of Southampton.
- EWEA (European Wind Energy Association), 2004. Wind Power Technology: Operation, Commercial Developments, Wind Projects, Grid Distribution. Available from:-  
[http://www.ewea.org/fileadmin/ewea\\_documents/documents/publications/factsheets/fact\\_sheet\\_technology2.pdf](http://www.ewea.org/fileadmin/ewea_documents/documents/publications/factsheets/fact_sheet_technology2.pdf), [Accessed 30 Jun 2014].
- EWEA (European Wind Energy Association), 2013. The European Offshore Wind Industry-key Trends and Statistics 1st Half 2013. Available from:-  
[http://www.ewea.org/fileadmin/files/library/publications/statistics/EWEA\\_OffshoreStats\\_July2013.pdf](http://www.ewea.org/fileadmin/files/library/publications/statistics/EWEA_OffshoreStats_July2013.pdf) [Accessed 03 Dec 2013].
- Fajdiga, G. and Sraml, M. 2009. Fatigue Crack Initiation and Propagation under Cyclic Contact Loading. *Engineering Fracture Mechanics*, 76, pp. 1320-1335.
- Feng, Y., Qiu, Y., Crabtree, C. J., Long, H. and Tavner, P. J. 2012. Monitoring Wind Turbine Gearboxes. *Wind Energy*, (DOI: 10.1002/we.1521).
- Fernandes, P. J. L. and Mcduling, C. 1997. Surface Contact Fatigue Failures in Gears. *Engineering Failure Analysis*, 4, pp. 99-107.
- Flasker, J., Fajdiga, G., Glodez, S. and Hellen, T. K. 2001. Numerical Simulation of Surface Pitting due to Contact Loading. *International Journal of Fatigue*, 23, pp. 599-605.
- Glodež, S. 1995. *The Fracture Mechanics Model of Gear Flank Fatigue*. PhD thesis, University of Maribor (in Slovenian).
- Glodez, S. and Ren, Z. 1998. Modelling of Crack Growth under Cyclic Contact Loading. *Theoretical and Applied Fracture Mechanics*, 30, pp. 159-173.
- Glodez, S., Pehan, S. and Flasker, J. 1998. Experimental Results of the Fatigue Crack Growth in a Gear Tooth Root. *International Journal of Fatigue*, 20, pp. 669-675.
- Goch, G., Knapp, W. and Härtig, F. 2012. Precision Engineering for Wind Energy Systems. *CIRP Annals - Manufacturing Technology*, 61, pp. 611-634.
- Gowans, B. J. M. and Porter, F. E. 1970. Naval Service Experience with Surface-Hardened Gears. *Proceedings of the Institution of Mechanical Engineers*, 184, pp. 53-63.
- Gray, C. S. and Watson, S. J. 2009. Physics of Failure Approach to Wind Turbine Condition Based Maintenance. *Wind Energy*, 13, pp. 395-405.
- Greaves, P., Dominy, R. G., Ingram, G. L., Long, H. and Court, R. 2011. Evaluation of Dual-axis Fatigue Testing of Large Wind Turbine Blades. *Proceedings of the Institution of Mechanical Engineers, Part C: Journal of Mechanical Engineering Science*.
- GWEC (Global Wind Energy Council), 2013. Global Wind Report, Annual Market Update 2012. Available from:-

- [http://www.gwec.net/wpcontent/uploads/2012/06/annual\\_report\\_2012\\_lowres.pdf](http://www.gwec.net/wpcontent/uploads/2012/06/annual_report_2012_lowres.pdf) (ed.) [Accessed 03 Dec 2013].
- Hoehn, B.-R., Stahl, K. and Michaelis, K. 2012. Lubricant Influence on Slow Speed Wear in Gears. *Utjecaj maziva na trošenje zupčanika*, 51, pp. 5-28.
- Hohn, B. R. and Michaelis, K. 2004. Influence of Oil Temperature on Gear Failures *Tribology International*, 37, pp. 103-109.
- Holmes, M. J. A., Evans, H. P. and Snidle, R. W. 2005. Analysis of Mixed Lubrication Effects in Simulated Gear Tooth Contacts. *Journal of Tribology*, 127, pp. 61-69.
- Hutchings, I. M. 1992. *Tribology: Friction and Wear of Engineering Materials*. Elsevier Limited.
- IEA (International Energy Agency), 2010. *Global Gaps in Clean Energy RD & D. Report for the Clean Energy Ministerial*, Update and Recommendations for International Collaboration, OECD/IEA 2010.
- IEC 61400-1, 2005. *Wind Turbines - Part 4: Design Requirements for Wind Turbine Gearboxes*. International Electrotechnical Commission.
- IEC 61400-4, 2012. *Wind Turbines - Part 4: Design Requirements for Wind Turbine Gearboxes*, Geneva, Switzerland: International Organization for Standardization.
- Industries, R. 1978. Failure Analysis Gears-Shafts-Bearings-Seals. In: Rexnord (ed.) *Failure Analysis - Installation and Maintenance*. USA, pp. 1-20.
- ISO 10825, 1995 and BS 7848, 1996. *Gears Wear and Damage to Gear Teeth Terminology*. U.K: BSI, pp. 1-61.
- ISO 1328-1, 1995 and BS 436-4, 1996. *Cylindrical Gears - ISO System of Accuracy - Part 4: Definitions and Allowable Values of Deviations Relevant to Corresponding Flanks of Gear Teeth*. UK: BSI, pp.1-26.
- ISO 6336-1 (2006). *Calculation of Load Capacity of Spur and Helical Gears Part 1: Basic Principles, Introduction and General Influence Factors*. U.K: BSI, pp. 1-109.
- ISO 6336-2, 2006. *Calculation of Load Capacity of Spur and Helical Gears Calculation of Surface Durability (Pitting)*. UK: BSI, pp. 1-33.
- ISO 6336-3, 2003. *Calculation of Load Capacity of Spur and Helical Gears. Part 3: Calculation of Tooth Bending Strength*. UK: BSI, pp. 1-42.
- ISO 6336-5, 2003. *Calculation of Load Capacity of Spur and Helical Gears Part 5: Strength and Quality of Materials*. UK: BSI, pp. 1-43.
- ISO 6336-6 (2006). *Calculation of Load Capacity of Spur and Helical Gears Calculation of Service Life Under Variable Load*. BSI, pp. 1-32.
- ISO/TR 15144-1, 2010. *Calculation of Micro-pitting Load Capacity of Cylindrical Spur and Helical Gears. Introduction and Basic Principles*. BSI Standard Publication.
- Jelaska, D. 2012. *Gears and Gear Drive*. Sussex: Wiley.

- Jiang, X., Ai, X., Lee, S. C., Hua, D. Y. and Cheng, H. S. 1999. A Mixed Elastohydrodynamic Lubrication Model With Asperity Contact. *Journal of Tribology*, 121, pp. 481-491.
- Jindal, K. C. 2010. *Machine Design*. India: Dorling Kindersley.
- Johnson, K. L. 1985. *Contact Mechanics*. Cambridge, UK: Cambridge University press.
- Johnson, K. L., Greenwood, J. A. and Poon, S. Y. 1972. A simple Theory of Asperity Contact in Elastohydro-dynamic Lubrication. *Wear*, 19, pp. 91-108.
- Kelley, B. W. 1953. A New Look at the Scoring Phenomena of Gears. *SAE Transactions*, 61, pp. 175-188.
- Khan, M. A., Cooper, D. and Starr, A. 2009. BS-ISO Helical Gear Fatigue Life Estimation and Wear Quantitative Feature Analysis. *Strain*, 45, pp. 358-363.
- KHK. 2006. *Introduction to Gears*. First edition. Kohara Gear Industry Co., LTD.
- Kim, K., Parthasarathy, G., Uluyol, O., Foslien, W., Shuangwen, S. and Fleming, P. 2011. Use of SCADA Data for Failure Detection in Wind Turbines. *Energy Sustainability Conference and Fuel Cell Conference*, Washington: National Renewable Energy Laboratory.
- Kissling, U. 2012. Application of the First International Calculation Method for Micropitting. *Gear Technology*, pp. 54-60.
- Kleemola, J. and Lehtovaara, A. 2009. Experimental Simulation of Gear Contact along the Line of Action. *Tribology International*, 42, pp. 1453-1459.
- Krishnamurthy, S. and Rao, A. R. 1987. Effect of Sursulf Treatment on the Performance of 0.14% C Steel Gears. *Wear*, 120, pp. 289-303.
- Ku, P. M. 1974. Failure Modes in Gears. In: Guichelaar, P. J., Levy, B. S. and Parikh, N. M. (eds.) *Gear Manufacture and Performance*. USA: American Society for Metals.
- Lainé, E., Olver, A. V. and Beveridge, T. A. 2008. Effect of Lubricants on Micropitting and Wear. *Tribology International*, 41, pp. 1049-1055.
- Larsson, R. 1997. Transient Non-newtonian Elastohydrodynamic lubrication Analysis of An Involute Spur Gears. *Wear*, 207, pp. 67-73.
- Li, S. and Kahraman, A. 2011. A Fatigue Model for Contacts under Mixed Elastohydrodynamic Lubrication Condition. *International Journal of Fatigue*, 33, pp. 427-436.
- Linke, H. 1996. *Stirnradvverzahnung*. Carl Hanser: Munich.
- Lloyd G. , 2003. Guideline for the Certification of Wind Turbines. Hamburg: Germanischer Lloyd Industrial Services.
- Long, H., Lord, A. A., Gethin, D. T. and Roylance, B. J. 2003. Operating Temperatures of Oil-Lubricated Medium-Speed Gears : Numerical Models and Experimental Results.

- Proceedings of the I MECH E part G : Journal of Aerospace engineering*, 217, pp. 87-106.
- Long, H., Wu, J. and Tavner, P. J. 2012. Analysis of Statistical Loading Conditions of Wind Turbine Gearbox Based on SCADA Data. *The EWEA 2012 Conference*, Denmark.
- Lu, H. 2006. *High Order Finite Element Solution of Elastohydrodynamic Lubrication Problems*. PhD thesis, University of Leeds.
- Lubrecht, A. A. 1987. *The Numerical Solution of the Elastohydrodynamically Lubricated Line- and Point Contact Problem, Using Multigrid Techniques*. PhD thesis, Twente University.
- Maitra, G. M. 1994. *Handbook of Gear Design*, New Delhi: Tata McGraw-Hill.
- Martin, H. M. 1916. The Lubrication of Gear Teeth. *Engineering*, 102, pp. 199-204.
- Maru, M. M. and Tanaka, D. K. 2007. Consideration of Stribeck Diagram Parameters in the Investigation on Wear and Friction Behavior in Lubricated Sliding. *Journal of the Brazilian Society of Mechanical Sciences and Engineering*, pp. 55-62.
- Matsumoto, M. and Nishimura, T. Jan. 1998. Mersenne Twister: a 623-Dimensionally Equidistributed Uniform Pseudorandom Number Generator. *ACM Transactions on Modeling and Computer Simulation*, 8(1), pp. 3-30.
- McDuling, C. 1996. *Test Report*. Advanced Engineering and Testing Services. CSIR.
- Mcniff, B. P., Musial, W. D. and Errichello, R. 1991. *Variations in Gear Fatigue Life for Different Wind Turbine Braking Strategies*, Prepared for AWEA Wind Power '90 Washington, D. C. Colorado: Solar Energy Research Institute.
- Moorthy, V. and Shaw, B. A. 2012. Effect of as-Ground Surface and the BALINIT C and Nb-S Coatings on Contact Fatigue Damage in Gears. *Tribology International*, 51, pp. 61-70.
- Morales-espejel, G. E. and Brizmer, V. 2011. Micropitting Modelling in Rolling-Sliding Contacts: Application to Rolling Bearings. *Tribology Transactions*, 54, pp. 625-643.
- Müller, S., Deicke, M. and Doncker, R. W. D. 2002. Doubly Fed Induction Generator Systems for Wind Turbines. *IEEE Industry Applications Magazine*, 8, pp. 26-33.
- Muraro, M. A., Koda, F., JR., U. R. and Silva, C. H. D. 2012. The Influence of Contact Stress Distribution and Specific Film Thickness on the Wear of Spur Gears During Pitting Tests. *Journal of the Brazilian Society of Mechanical Sciences and Engineering*, 34, pp. 135-144.
- Musial, W., Butterfield, S. and McNiff, B. 2007. Improving Wind Turbine Gearbox Reliability, an article by *National Renewable Energy Laboratory*. Presented at the European Wind Energy Conference, Milan, Italy.

- Ognjanovic, M. 2004. Progressive Gear Teeth Wear and Failure Probability Modeling. *Tribology in Industry*, 26, pp. 44-49.
- Oila, A. 2003. *Micropitting and Related Phenomena in Case Carburised Gears*. PhD thesis, University of Newcastle.
- Oila, A. and Bull, S. J. 2005. Assessment of the Factors Influencing Micropitting in Rolling/Sliding Contacts. *Wear*, 258, pp. 1510-1524.
- Olver, A. V. 2002. Gear Lubrication - A Review. *Proceedings of the Institution of Mechanical Engineers, Part J: Journal of Engineering Tribology*, 216, pp. 255-267.
- Otto, F. J. and Herring, D. H. 2002. Gear Heat Treatment: Part I, *Heat Treating Progress*, pp. 55-59.
- Oyague, F. 2009. *Gearbox Modelling and Load Simulation of a Baseline 750-kW Wind Turbine Using State-of-the-Art Simulation Codes*. Technical Report, NREL/TP-500-41160.
- Predki, W., Nazifi, K. and Lutzig, G. 2011. Micropitting of Big Gearboxes: Influence of Flank Modification and Surface Roughness. *Gear Technology*, pp. 42-46.
- Qiu, Y., Feng, Y., Tavner, P., Richardson, P., Erdos, G. and Chen, B. 2011. Wind Turbine SCADA Alarm Analysis for Improving Reliability. *Wind Energy*, 15(8), pp. 951-966.
- Rensselaar, J. V. 2013. Extending Wind Turbine Gearbox Life. *Tribology and Lubrication Technology*. Society of Tribologists and Lubrication Engineers. HighBeam Research. Available from:- <http://www.highbeam.com> [Accessed 05 Jan 2014].
- Reynolds, O. 1886. On the Theory of Lubrication and its Application to Mr Beauchamp Tower's Experiments Including an Experimental Determination of the Viscosity of Olive Oil. *Philosophical Transactions of the Royal Society of London*, 177, pp. 157-234.
- Seireg, A. 2001. Thermal Stress Effects on the Surface Durability of Gear Teeth. *Proceedings of the Institution of Mechanical Engineers*, 215(C), pp. 973-979.
- Serest, A. E. and Akbarzadeh, S. 2013. Mixed-Elastohydrodynamic Analysis of Helical Gears Using Load-Sharing Concept. *Part J: Journal of Engineering Tribology*, pp. 1-12.
- Shell, 2013. Shell Australia Lubricants Product Data Guide, *Industry Gear Oil*. Australia: Industry.
- Sheng, S. (ed). 2010. *Wind Turbine Micropitting Workshop: A Recap*. Report Number: NREL/TP-500-46572. Colorado: NREL , pp. 1-52.
- Sheng, S. 2011. Investigation of Various Wind Turbine Drivetrain Condition Monitoring Techniques. *Wind Turbine Reliability Workshop*, NREL (National Renewable Energy Laboratory), NREL/PR-5000-52352, Albuquerque, NM.

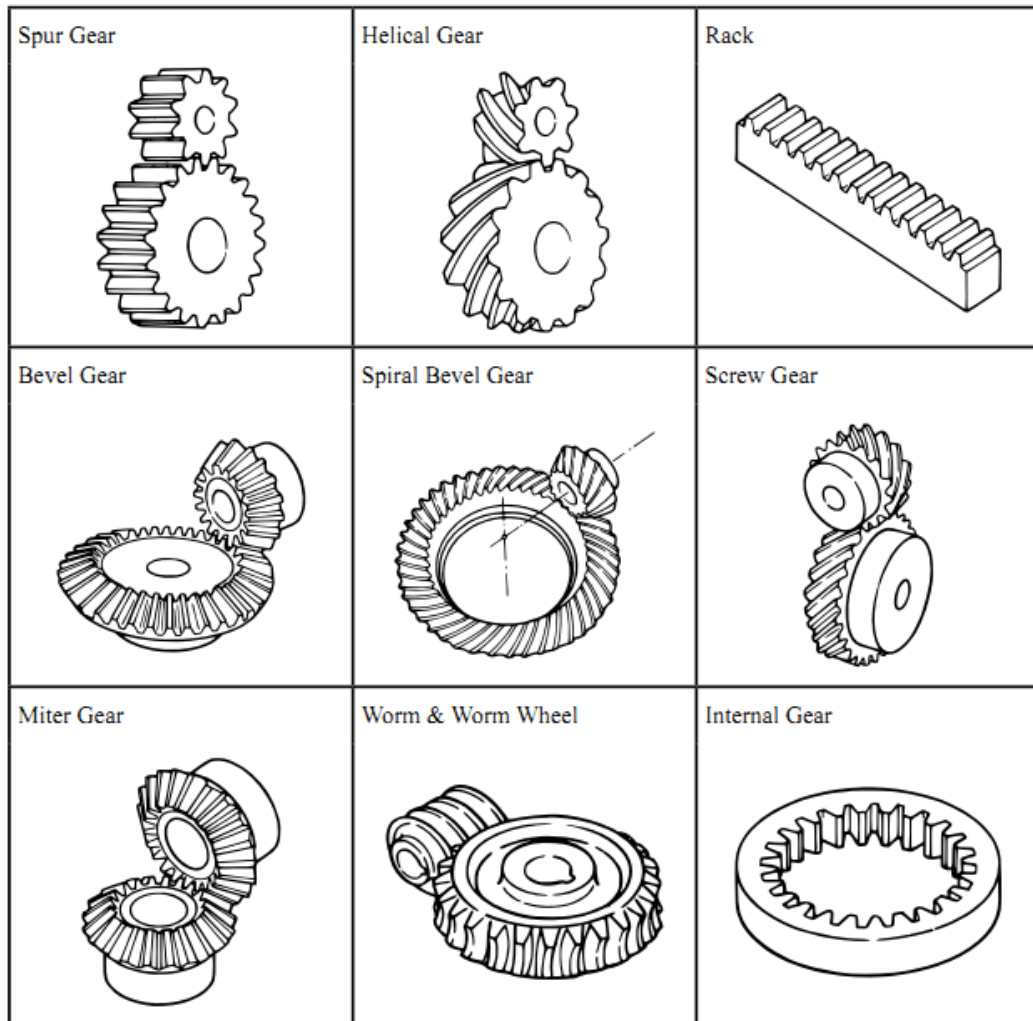
- Shigley, J. E. and Mischke, C. R. 1989. *Mechanical Engineering Design*. Singapore: McGraw-Hill.
- ShIPLEY, E. E. 1974. Failure Modes in Gears. *In: Guichelaar, P. J., Levy, B. S. and Parikh, N. M. (eds.) Gear Manufacture and Performance*. USA: American Society For Metals.
- Skriver, S. 2010. *Determining a Strategy for Managing Gearboxes and Spare Parts*. Glasgow, UK: Wind Farm O&M.
- Smolders, K., Long, H., Feng, Y. and Tavner, P. 2010. Reliability Analysis and Prediction of Wind Turbine Gearboxes. *European Wind Energy Conference 2010 Scientific Track*. Warsaw, Poland:EWEA.
- Snidle, R. W., Evans, H. P., Alanou, M. P. and Holmes, M. J. A. 2004. Understanding Scuffing and Micropitting of Gears. *Paper Presented at NATO Research and Technology Organisation Specialists' Meeting on The Control and Reduction of Wear in Military Platforms , (RTO-MP)*, pp. 1-18.
- Sourkounis, C. and Tourou, P. 2013. Grid Code Requirements for Wind Power Integration in Europe. *In: Al-assaf, Y., Demokritou, P. and Poullikkas, A. (eds.) Conference Papers in Energy*. Cyprus: Hindawi Publishing Corporation.
- Spikes, H. A. and Olver, A. V. 2002. Mixed Lubrication—Experiment and Theory. *In: D. Dowson D., Priest M., Dalmaz G. and Lubrecht A. A. (eds.) Tribology Series*. Elsevier.
- Spinato, F. 2008. *The Reliability of Wind Turbines*. PhD thesis, Durham University.
- Spinato, F., Tavner, P. J., VAN Bussel, G. J. W. and Koutoulakos, E. 2009. Reliability of Wind Turbine Subassemblies. *Renewable Power Generation, IET*, 3, pp. 387-401.
- Swift, K. G. and Booker, J. D. 2003. *Process Selection From Design to Manufacturing*, Oxford: Butterworth-Heinemann.
- Tavner, P. J., Xiang, J. and Spinato, F. 2006. Reliability Analysis for Wind Turbines. *Wind Energy*, 10, pp. 1-18.
- Terauchi, Y. and Mori, H. 1974. Comparison of Theories and Experimental Results for Surface Temperature of Spur Gear Teeth. *Journal of Engineering for Industry-Transactions of the Asme*, 96, pp. 41-50.
- Terry, P. 2013. High-Temperature Gear Materials. *The Journal of Gear Technology*, 6, p. 94.
- Tharmakulasingam, R. 2009. *Transmission Error in Spur Gears: Static and Dynamic Finite-Element Modeling and Design Optimization*. PhD thesis, Brunel University.
- Townsend, D. P. and Akin, L. S. 1981. Analytical and Experimental Spur Gear Tooth Temperature as Affected by Operating Variables. *Journal of Mechanical Design*, 103, pp. 219-226.

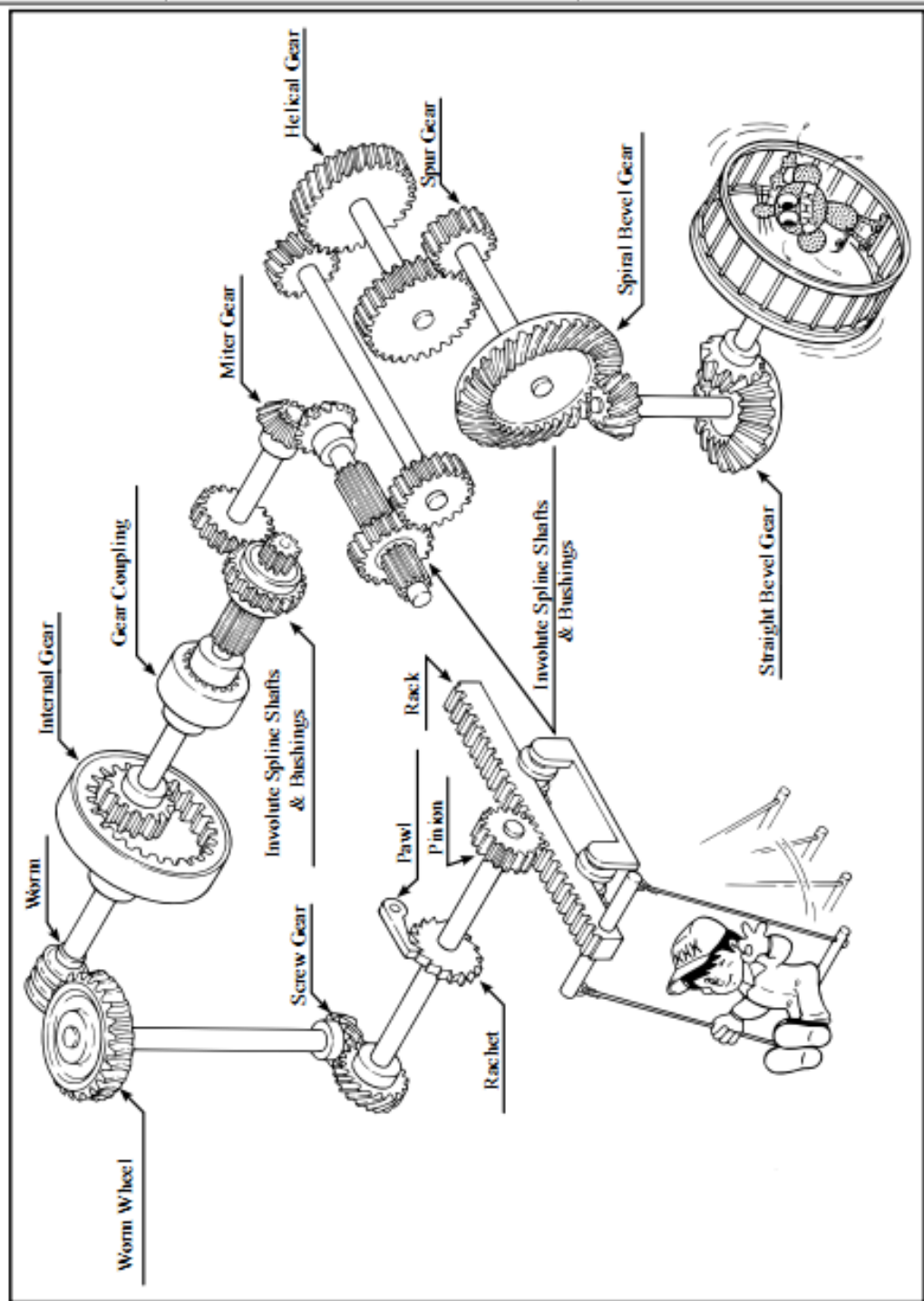
- Townsend, D. P. and Shimski, J. 1995. EHL Film Thickness, Additives and Gear Surface Fatigue. *Gear Technology- The journal of Gear Manufacturing*, pp. 26-31.
- Townsend, D. P. and Zaretsky, E. V. 1986. Effect of Shot Peening on Surface Fatigue Life of Carburized and Hardened AISI 9310 Spur Gears. *Gear Technology- The journal of Gear Manufacturing*, pp. 29-36.
- Veldkamp, D. 2008. A Probabilistic Evaluation of Wind Turbine Fatigue Design Rules. *Wind Energy*, 11, pp. 655-672.
- Wang, K. L. and Cheng, H. S. 1981. A Numerical Solution to the Dynamic Load, Film Thickness and Surface Temperatures in Spur Gears, Part II: Results. *Journal of Mechanical Design*, 103, pp. 188-194.
- Webster, M. N. and Norbart, C. J. J. 1995. An Experimental Investigation of Micropitting Using a Roller Disk Machine. *Tribology Transactions*, 38, pp. 883-893.
- Wilkinson, M., Darnell, B., Delft, T. V. and Harman, K. 2013. Comparison of Methods for Wind Turbine Condition Monitoring with SCADA Data. *EWEA Wind Energy Conference*, Vienna
- Wink, C. H. 2012. Predicted scuffing Risk to spur and Helical Gears in Commercial Vehicle Transmissions. *Gear Technology- The journal of Gear Manufacturing*, 6, pp. 82-86.
- Winkelmann, L. 2011. Surface Roughness and Micropitting. A paper presented by the National Renewable Energy Laboratory at the *Wind Turbine Tribology Seminar*, November 15-17, 2011.
- Winter, H. and Weiss, T. 1980. Some Factors Influencing the Pitting, Micropitting (Frosted Areas) and Slow Speed Wear of Surface Hardened Gears. *ASME*, 80, pp. 1-7.
- Yi, J. and Quinonez, P. D. 2005. Gear Surface Temperature Monitoring. *Proceedings of the Institution of Mechanical Engineers Part J: Journal of Engineering Tribology*, 219, pp. 99-105.
- Zaher, A., McArthur, S. D. J., Infield, D. G. and Patel, Y. 2009. Online Wind Turbine Fault Detection Through Automated SCADA Data Analysis. *Wind Energy*, 12, pp. 574-593.
- Zhang, J. 2005. *Influence of Shot Peening and Surface Finish on the Fatigue of Gears*. PhD thesis, University of Newcastle upon Tyne.
- Zhang, J. and Shaw, B. A. 2011. The Effect of Superfinishing on the Contact Fatigue of Case Carburised Gears. *Applied Mechanics and Materials*, 86, pp. 348-351.
- Zhang, J., Shaw, B. and Aylott, C. 2009. Surface Engineering to Improve Micropitting Performance of Gears. *BGA Gears 09: Technical Awareness Seminar*. Agusta Westland, Yeovil: Newcastle University, Design Unit.

- Zhang, Q., Zhang, J., Wu, C., Xu, Z. and Lyu, S. 2014. The Evaluation of Contact Fatigue Strength for 20MnCr5 Carburized Gear. *International Journal of Precision Engineering and Manufacturing*, 15, pp. 117-121.
- Zhang, Y. M., Liu, Q. and Wen, B. 2003. Practical Reliability-Based Design of Gear Pairs. *Mechanism and Machine Theory*, 38, pp. 1363-1370.
- Zhou, R. S., Cheng, H. S. and Mura, T. 1989. Micropitting in Rolling and Sliding Contact under Mixed Lubrication. *Journal of Tribology*, 111, pp. 605-613.
- Zhu, D. and Wang, Q. J. 2013. Effect of Roughness Orientation on the Elastohydrodynamic Lubrication Film Thickness. *Journal of Tribology*, 135, pp. 1-9.
- Zhu, D., Wang, Q. J. and Ren, N. 2008. Pitting Life Prediction Based on a 3-D Line Contact Mixed EHL Analysis and Subsurface von Mises Stress Calculation. *Technical Sessions - CIST2008 & ITS-IFTtoMM2008*, Beijing, China.

# APPENDICES

## APPENDIX-A: Common Gears Types. (Chapter 2, Section 2.1.1)





Source: KHK (2006, P. 4-5)

APPEDIX-B: Surface Roughness Instrument Calibration. (Chapter 3, Section 3.4.1)

**RANK TAYLOR HOBSON**  
Form Talysurf Series

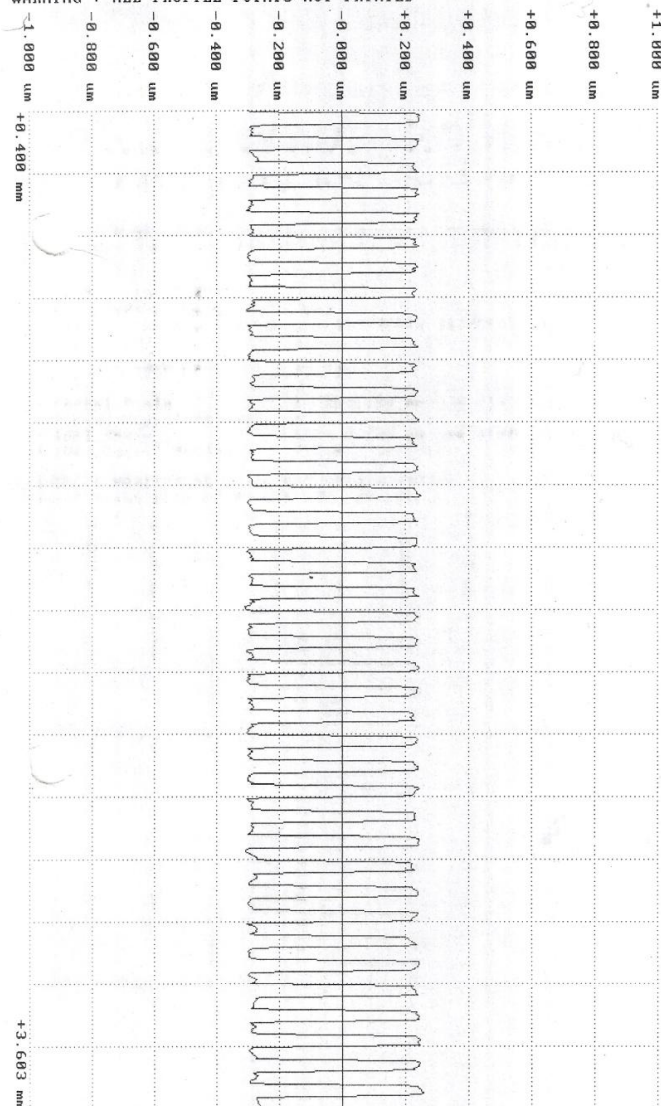
NEWCASTLE UNIVERSITY DESIGN UNIT

19/01/13 13:16:47  
Rough/Gauss/4\*0.8mm,100:1/Convex  
Calibrated: 19:36, 9/01/113, 112/2564, 112/2012, sjw

COMPLETE MODIFIED PROFILE

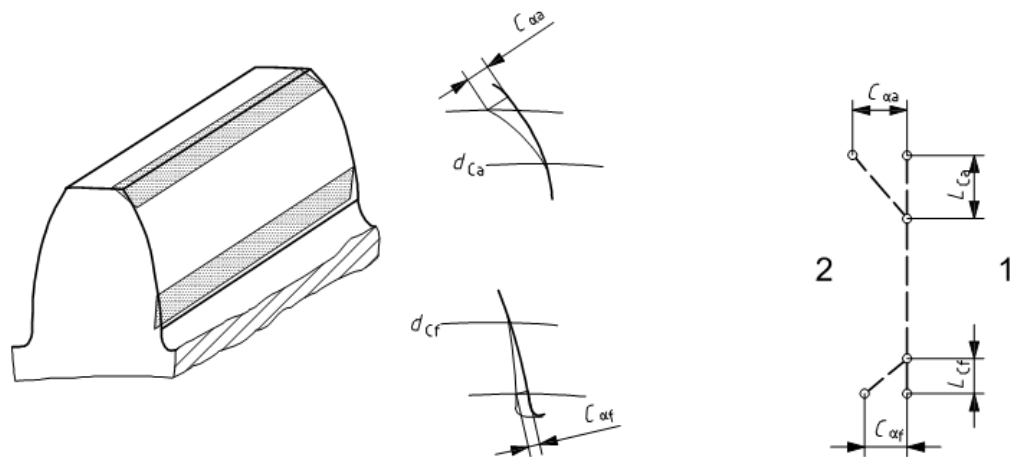
Horizontal Scale : 200.000 um per division  
Horizontal Magnification : x 47.4  
Vertical Scale : 0.200 um per division  
Vertical Magnification : x 47400.0

WARNING : HORIZONTAL SCALE HAS BEEN ADJUSTED  
WARNING : ALL PROFILE POINTS NOT PRINTED



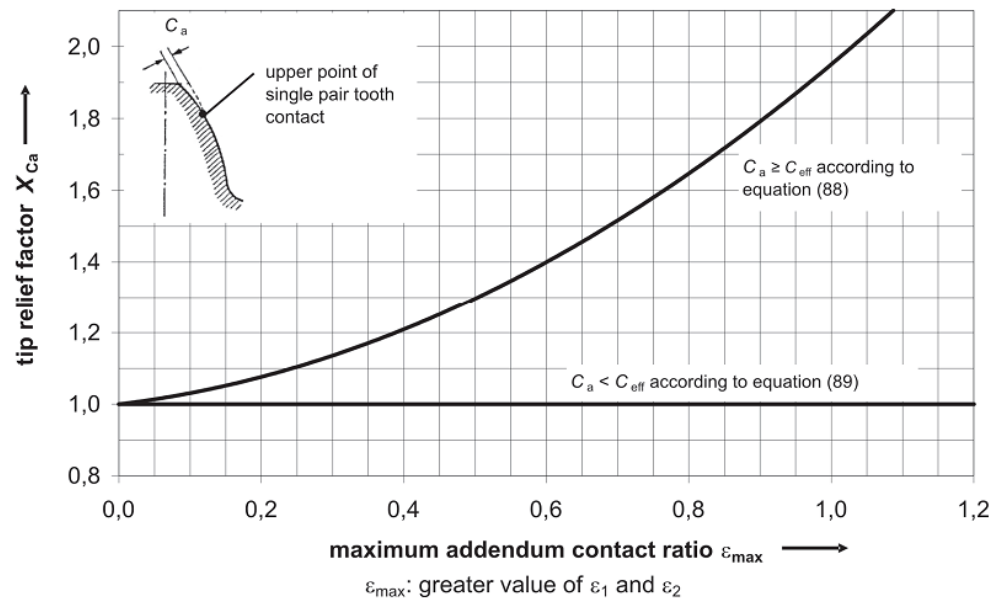
LS Rad 238.743mm

Ra	0.25 um	Rq	0.25 um	Rp	0.26 um
Rv	0.31 um	Rt	0.57 um	Rsk	-0.41
RzISO	0.55 um	RzDIN	0.56 um		

**Appendix-C: Tip and Root Relief. (Chapter 4, Section 4.1.5)**

**Key**

- $d_{Ca}$  tip relief datum diameter
- $L_{Ca}$  tip relief roll length
- $C_{\alpha a}$  amount of tip relief
- $d_{Cf}$  root relief datum diameter
- $L_{Cf}$  root relief roll length
- $C_{\alpha f}$  amount of root relief
- 1 space
- 2 tooth

Source: BS ISO 21771(2007, P. 46)

**Appendix -D: Tip Relief Factor ( $X_{Ca}$ ). (Chapter 4, Section 4.1.6)**

Source: ISO/TR 15144-1 (2010, P. 29)

**APPENDIX-E: Wind Turbine Gearbox Main Characteristics. (Chapter 5, Section 5.1)**

## Stage 1 planetary

parameters	Sun	Planet	Ring	Units
Number of teeth	20	41	103	-
Module	12	12	12	mm
Face width	370	360	360	mm
Pitch diameter	240	492	1236	mm
Tip diameter	264	516	1260	mm
Normal pressure angle	20			degree

## Stage 2 intermediate shaft

parameters	Pinion	Wheel	Units
Number of teeth	26	107	-
Module	9	9	mm
Face width	256	245	mm
Pitch diameter	234	963	mm
Tip diameter	256	981	mm
Normal pressure angle	20		degree

**APPENDIX-F: Excel Macro Programme. (Chapter 5, Section 5.2.4)**

```
Sub Macro2()  
' Macro2 Macro  
Sheets("torque table").Select  
Range("A2").Select  
Do While ActiveCell.Value <> ""  
torque = ActiveCell.Value  
Speed = ActiveCell.Offset(0, 1).Value  
Range("D2").Value = torque  
Range("c2").Value = speed  
Range("e2").Value = speed  
Calculate  
Range("C2:ch2").Copy  
Sheets("results").Select  
Selection.PasteSpecial Paste:=xlPasteValues, Operation:=xlNone, SkipBlanks _  
:=False, Transpose:=False  
ActiveCell.Offset(1, 0).Select  
Sheets("torque table").Select  
ActiveCell.Offset(1, 0).Select  
Loop  
End Sub
```

APPENDIX-G: Surface Roughness at 0.8 Torque Ratio. (Chapter 6, Section 6.2)

**RANK TAYLOR HOBSON**  
Form Talysurf Series

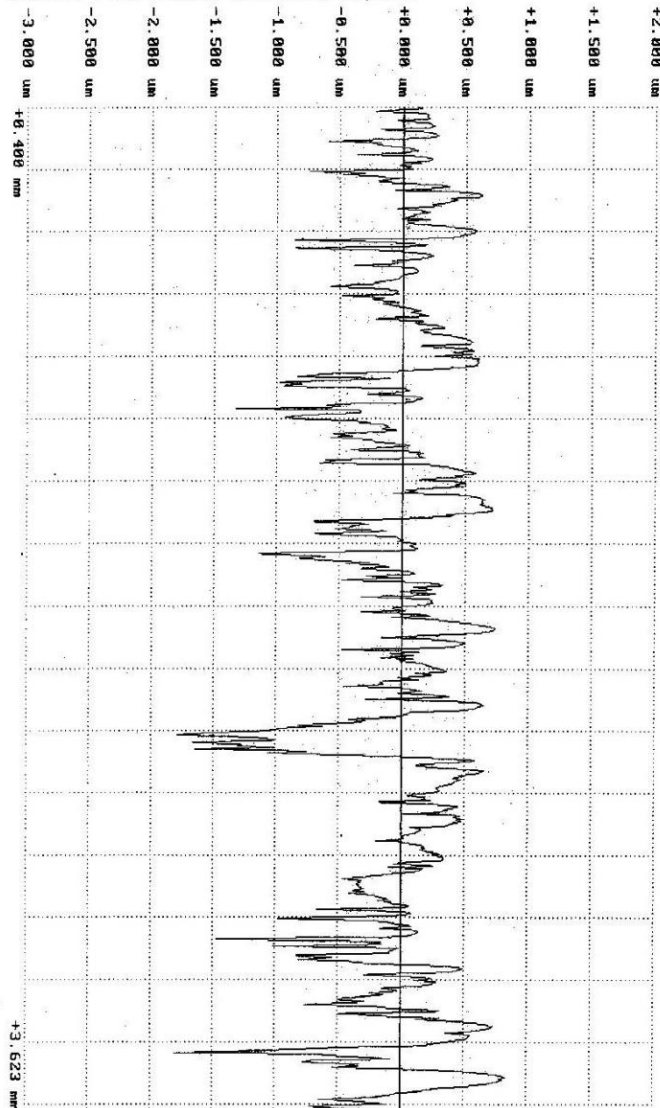
**NEWCASTLE UNIVERSITY DESIGN UNIT**

18/12/12 15:29:45  
Rough/Gauss/4\*0.8mm,100:1/Convex  
Calibrated: 09:45, 31/10/112, 112/2564, 112/2012, sjw

COMPLETE MODIFIED PROFILE

Horizontal Scale : 200.000 um per division  
Horizontal Magnification : x 47.4  
Vertical Scale : 0.500 um per division  
Vertical Magnification : x 10960.0

WARNING : HORIZONTAL SCALE HAS BEEN ADJUSTED  
WARNING : ALL PROFILE POINTS NOT PRINTED



LS Rad 32.8530mm

Ra	0.33 um	Rq	0.44 um	Rp	0.84 um
Rv	1.81 um	Rt	2.65 um	Rsk	-0.97
RzISO	1.41 um	RzDIM	2.28 um		

## Surface Roughness at 0.9 Torque Ratio

# RANK TAYLOR HOBSON

## Form Talysurf Series

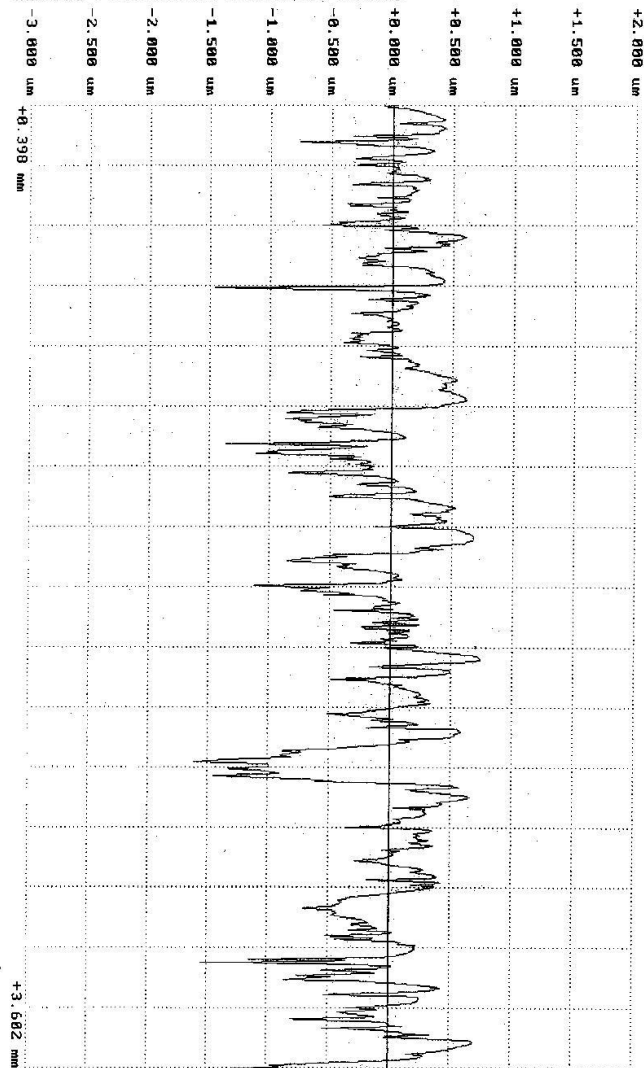
### NEWCASTLE UNIVERSITY DESIGN UNIT

11/01/13 14:58:26  
 Rough/Gauss/4\*0.8mm,100:1/Convex  
 Calibrated: 19:36, 9/01/113, 112/2564, 112/2012, sjw

#### COMPLETE MODIFIED PROFILE

Horizontal Scale : 200.000 um per division  
 Horizontal Magnification x 47.4  
 Vertical Scale : 0.500 um per division  
 Vertical Magnification x 18960.0

WARNING : HORIZONTAL SCALE HAS BEEN ADJUSTED  
 WARNING : ALL PROFILE POINTS NOT PRINTED



LS Rad 32.4911mm

Ra	0.31 um	Rq	0.41 um	Rp	0.75 um
Rc	1.68 um	Rt	2.35 um	Rsk	-0.98
RzISO	1.29 um	RzDIM	2.17 um		

**APPENDIX-H:** Comparison of Gear Geometry and Parameters Using Different Software. (Chapter 6, Section 6.4)

Gear geometry	Toolkit	Dontyne	eAssistant
Tip diameter of pinion (mm)	168.7577024	168.76	168.7573
Tip diameter of wheel (mm)	175.2470111	175.24	175.2398
Centre distance (mm)	160	160	160
helix angle factor	1.06472	1.065	1.0647
Transverse module (mm)	6.80174273	6.802	6.8017
Gear ratio	1.043	1.043	1.043
Transverse pressure angle (°)	22.421304	22.421	22.4213
Base diameter of the pinion (mm)	144.613882	144.61	144.6139
Base diameter of the wheel (mm)	150.901442	150.90	150.9014
Working pressure angle at the pitch cylinder (°)	22.5589	22.559	22.5589
Pitch diameter of pinion (mm)	156.595701	156.44	156.5957
Pitch diameter of wheel (mm)	163.404209	163.24	163.4043
Helix angle base diameter (°)	26.2702976	26.270	26.2703
Addendum contact ratio of the pinion	0.66878477	0.669	-
Addendum contact ratio of the wheel	0.68109841	0.681	-
Transverse contact ratio	1.34988318	1.350	1.3495
Overlap ratio	1.09947008	1.099	1.0995
Total contact ratio	2.44935326	2.45	2.449
Length of path of contact $g\alpha$ (mm)	26.6641784	26.665	26.6566

## Comparison of Materials and Other Factors Using Different Software

Gear geometry	Toolkit	Dontyne	eAssistant
Calculation of materials			
Reduced modulus of elasticity (N/mm <sup>2</sup> )	227473.527	227472.531	-
Elasticity factor ((N/mm <sup>2</sup> ) <sup>0.5</sup> )	190.272	190.272	189.812
Thermal contact coefficient of pinion ((N/mm <sup>2</sup> ) <sup>0.5</sup> )	12427.389	12427.389	13000
Thermal contact coefficient of wheel ((N/mm <sup>2</sup> ) <sup>0.5</sup> )	12427.389	12427.389	13000
Calculation of operating conditions at 0.3 torque ratio			
Transmitted power (kW)	451.60	451.60	451.60
Transverse tangential load at reference cylinder per mesh (N)	18377.64	18377.60	18377.64
Nominal transverse load in plane of action (base tangent plane) (N)	19880.5257	19880.523	19880.523
Pitch line speed (m/s)	24.57	24.60	24.57
Calculation of influence factors at 0.3 torque ratio			
Application factor	1	1	1
Dynamic factor	1.062	1.052	1.079
Transverse load factor	1.023	1.000	1.000
Face load factor	1.000	1.000	1.000
Contact stress (N/mm <sup>2</sup> )	1076	996	950

Dontyne Output Sheet

Calculation Sheet of the Parameters, Geometry, Materials and Other Factors of the Helical Tested Gear Pair

```

***** pinion material Eh
*          DONTYNE SYSTEMS          * wheel material Eh
*          www.dontynesystems.com    * hardness HV          746      746
*****                               * material quality      MQ          MQ
* (University of Newcastle Upon Tyne * roughns flnk/μm Rz    2.7      2.7
* Design Unit Report Style Format) * roughns root/μm Rz   18.0     18.0
*****                               * viscosity @ 40C nu   323
* Dontyne Systems ISO 6336 Rating * pitting permitted?  yes      yes
* V 4.70 Bld24 19/11/2013 14:47:31 * reversing duty?     yes      yes
* P6p3_actual hob_integer centre distance *
*****                               *
number of Teeth z          23      24      applicatn factr KA          1.000
normal module mn          6.000      required life/h          44
transvrs module mt        6.802      load cycles NL          8.0e+06 7.7e+06
gear ratio u              1.043      mesh power/kw P          451.60
centres a                 160.00      torque/Nm T             1437.5 1500.0
facewidth b              44.00      tr tang force/N Ft       18377.6
reference diam d          156.44      speed/RPM n             3000.0 2875.0
base diameter db         144.61      pitch line speed/m/s     24.6
tip diameter da           168.76      tip relief/μm Ca         50.0
root diameter df         139.70      helix modifictn crowning for fma+fsh
tooth depth h            14.533      fav contact pattn posn verifctn? no
internal diameter        83.82      wheel web thickness      44.00 44.00
norm pres angle alphan    20.000      pinion offset s          0.000
transv pres ang alphas    22.421
wkng tr pr ang alphawt    22.559
ref helix angle beta      28.100
base helix ang betab     26.270
prof shift coef x        0.027      0.000      hx dev elast/μm fsh       0.0
sum of "" coefs Sigx      0.027      quality grade g          5          5
bsc rack dedend hFP/mn    1.422      1.400      hx dev manuf/μm fma       7.5
bsc rk root rd roFP/mn    0.400      0.400      init'l misal/μm Fbetax    0.0
residual protub Spr/mn    0.020      0.013      run-in misal/μm Fbetay    0.0
root chord lgth sFn/mn    2.101      2.111      stiff(N/mm/μm) cgamma    13.4
bending mom arm hFa/mn    1.126      1.116
root radius roF/mn        0.603      0.601
tr contct ratio epsalpha  1.350      overlap ratio epsbeta    1.099
-----FACTORS-----
resonance ratio N          0.392      dynamic fct KvB          1.052
-----TOOTH FLANK-----
face load factr KHbeta    1.000
transv load fct KHalp     1.000
zone factor ZH            2.248
elasticity fctr ZE        190.272
single pair fct ZB/ZD     1.000 1.000
cont ratio fctr zepsilon   0.861
helix ang factr Zbeta     1.065
life factor ZN            1.322 1.326
lub inf fct ZLVZR         1.097 1.097
work-hardng fct ZW        1.000
size factor ZX            1.000
-----CONTACT STRESS (N/mm²)-----
allw stress num sGhm      1500.0 1500.0
permiss stress sigHP      2058.9 2064.1
"" (reference) "" ref     1646.1 1646.1
contact stress sigH       996.5 996.5
safety factor SH          2.24 2.25
min safety fctr SHmin     1.00
-----TOOTH ROOT-----
face load factr KFbeta    1.000 1.000
transv load fct KFalpha   1.000
form factor YF            1.540 1.512
stress conc fct YS        1.810 1.823
notch parameter qs        1.741 1.755
cont ratio fctr yepsilon   0.697
helix ang factr Ybeta     0.766
life factor YN            0.981 0.981
notch sensy fct YdreIT    0.992 0.992
surface factor YRrelT     0.964 0.964
size factor YX            0.990 0.990
-----BENDING STRESS (N/mm²)-----
allw stress num sigFE     1014.2 1014.2
permiss stress sigFP      659.2 659.8
"" (reference) "" ref     960.4 960.5
root stress sigF          156.3 154.6
safety factor SF          4.22 4.27
min safety fctr SFmin     1.00
Addendum cont. ratio pin  epsilon1  0.669
Addendum cont. ratio wheel epsilon2  0.681
Addendum cont. ratio max  epsilonmax 0.681
Normal rel. curv rad. (mm) rhonC  17.105
Sum of tangential vel. (m/s) SIGMA_VC  19.694
Nominal base load (N) Fbt  19880.523
Red. modulus of elasticity Er  227472.531
Therm. cont. coef (N/(ms0.5K) BM1  12427.389
Therm. cont. coef (N/(ms0.5K) BM2  12427.389

```

Angles are in ° and distances in mm unless otherwise stated.

## eAssistant Output Calculation of the Parameters, Geometry, Materials and Other Factors of Helical Tested Gear Pair

Report of cylindrical gear calculation according to DIN 3960 , ISO 6336

GWJ Technology - www.eAssistant.de

Issa AL Tubi  
Sheffield University

14. April 2013 - 11:54

**eAssistant**  
the engineering assistant

Version 3.11  
Project: N-design  
Filename: standard.sgp

### Contents

<u>Input values</u>
<u>Geometry</u>
<u>Allowances and quality</u>
<u>Tool</u>
<u>Load capacity</u>
<u>Options</u>
<u>Modifications</u>
<u>Results of calculation</u>
<u>Geometry</u>
<u>Test dimensions</u>
<u>Tolerances</u>
<u>Load capacity (general influence factors)</u>
<u>Load capacity (flank)</u>
<u>Load capacity (root)</u>
<u>Load capacity (Scuffing) (ISO/TR 13989)</u>
<u>Efficiency of gearing</u>
<u>References</u>

### Input values

#### Geometry

##### Cylindrical gear pair

Normal module ( $m_n$ ):	6.0000 mm
Pressure angle ( $\alpha_n$ ):	20.0000 °
Helix angle ( $\beta$ ):	28.1000 °

	<b>Gear 1</b>	<b>Gear 2</b>
	driving	driven
No. of teeth (z):	23	24
Helix direction :	left	right
Profile shift coefficient ( $x^*$ ):	0.0266	0.0000
Face width (b):	44.0000 mm	44.0000 mm
Addendum chamfer ( $h_k$ ):	0.0000 mm	0.0000 mm
Chamfer:	1.0000 mm	1.0000 mm
Inner / Outer diameter:	81.5100 mm	0.0000 mm

Rim width (Pre-setting) ( $b_S$ ):	44.0000 mm	0.0000 mm
------------------------------------	------------	-----------

**Allowances and quality****Cylindrical gear pair**

Tolerance field:	js 5 (ISO 286)	
Centre distance allowance max. value ( $A_{ae}$ ):	9.0000 $\mu\text{m}$	
Centre distance allowance min. value ( $A_{ai}$ ):	-9.0000 $\mu\text{m}$	

	<b>Gear 1</b>	<b>Gear 2</b>
Quality:	5	5
Backlash allowance sequence:	cd	cd
Tolerance sequence:	25	25
Upper tooth thickness allowance ( $A_{sne}$ ):	-95.0000 $\mu\text{m}$	-95.0000 $\mu\text{m}$
Lower tooth thickness allowance ( $A_{sni}$ ):	-145.0000 $\mu\text{m}$	-145.0000 $\mu\text{m}$

**Tool**

	<b>Gear 1</b>	<b>Gear 2</b>
Tool:	Hob	Hob
Basic rack profile:	ISO 53 Profile A	ISO 53 Profile A
Tool tip radius ( $p^*_{ao}$ ):	0.3800	0.3800
Addendum coefficient ( $h^*_{ap}$ ):	1.2500	1.2500
Dedendum coefficient ( $h^*_{dp}$ ):	1.0000	1.0000
Height of the buckling root flank ( $h^*_{ko}$ ):	0.0000	0.0000
Angle of the buckling root flank ( $\alpha_{rk}$ ):	0.0000 °	0.0000 °
Protuberance ( $p^*_{rpo}$ ):	0.0000	0.0000
Allowance (q):	0.0000 mm	0.0000 mm
Angle of protuberance ( $\alpha_p$ ):	0.0000 °	0.0000 °

**Load capacity****Min. safety for load capacity calculation**

Min. safety flank:	1.1000
Min. safety tooth root:	1.3000
Min. safety scuffing (integral):	2.0000
Min. safety scuffing (flash):	3.0000

**Cylindrical gear pair**

Calculation method:	ISO 6336 Method B
Endurance:	20000.0000 h

**Power**

	<b>Gear 1</b>	<b>Gear 2</b>
	Driver	Driven
Comment:		
Power (P):		
Torque (T):		
Rotational speed (n):	3000.0000 1/min	2875.0000 1/min

**Factors for load capacity calculation**

Application factor ( $K_A$ ):	1.0000
Face coefficient ( $K_{H\beta}$ ):	1.0000
	Pitting permitted
Load stage in the FZG test:	12
Relative structure factor ( $X_{W,rel T}$ ):	1.5000
Type of lubricant:	Mineral oil
	Gears are well run-in

**Lubricant**

Kind of lubrication:	Oil injection lubrication
Description of lubricant:	User defined
Comment:	Standard oil ISO viscosity class VG
	320
Viscosity at 40°C:	320.0000 mm <sup>2</sup> /s
Viscosity at 100°C:	26.0000 mm <sup>2</sup> /s
Density:	0.9030 g/cm <sup>3</sup>
Temperature of lubricant:	90.0000 °C
Load stage in the FZG test:	12

**Material**

Source of data Gear 1	DIN 743, DIN EN 10084, Datenbank FORMAT, DIN 3990 Edition 12/87 Part 5
Material quality Gear 1	MQ (according to DIN 3990 Part 5, edition 12/87)
Source of data Gear 2	DIN 743, DIN EN 10084, Datenbank FORMAT, DIN 3990 Edition 12/87 Part 5
Material quality Gear 2	MQ (according to DIN 3990 Part 5, edition 12/87)

	<b>Gear 1</b>	<b>Gear 2</b>
Material:	user defined input	user defined input
Type of material:	Case hardening steel	Case hardening steel
Kind of treatment:	case hardened	case hardened

Hardness:	647.0000 HV10	746.0000 HV10
Poisson's ratio ( $\nu$ ):	0.3000	0.3000
E-Module:	206000.0000 N/mm <sup>2</sup>	206000.0000 N/mm <sup>2</sup>
Yield point ( $\sigma_B$ ):	400.0000 N/mm <sup>2</sup>	400.0000 N/mm <sup>2</sup>
Density ( $\rho$ ):	7.8500 kg/dm <sup>3</sup>	7.8000 kg/dm <sup>3</sup>
Fatigue strength of surface pressure ( $\sigma_{Hlim}$ ):	1500.0000 N/mm <sup>2</sup>	1500.0000 N/mm <sup>2</sup>
Fatigue strength of nominal bending stress in the tooth root ( $\sigma_{Flim}$ ):	659.0000 N/mm <sup>2</sup>	659.0000 N/mm <sup>2</sup>
Roughness tooth flank ( $R_z$ ):	2.7000 $\mu\text{m}$	2.7000 $\mu\text{m}$
Roughness tooth root ( $R_z$ ):	18.0000 $\mu\text{m}$	18.0000 $\mu\text{m}$
Thermal contact coefficient ( $B_M$ ):	13.0000 N/(mm K s <sup>0.5</sup> )	13.0000 N/(mm K s <sup>0.5</sup> )

**Options**

Factor for minimal gear ring thickness: 2.0000

**Modifications**

Superposition of flank and profile modifications  
Use the theoretical path of contact to calculate the length of profile modification.

**Tip relief**

	<b>Gear 1</b>	<b>Gear 2</b>
Type of relief:	linear	linear
Amount ( $C_a$ ):	0.0500 mm	0.0500 mm
Length of relief:		
Length ( $l_a$ ):	2.6700 mm	2.6700 mm
Start of transition ( $l_{a1}$ ):	0.0000 mm	0.0000 mm
End of transition ( $l_{a2}$ ):	2.6700 mm	2.6700 mm
Diameter ( $d_{la}$ ):	166.0680 mm	172.5862 mm
Start diameter of transition ( $d_{la1}$ ):	168.7573 mm	175.2398 mm
End diameter of transition ( $d_{la2}$ ):	166.0680 mm	172.5862 mm

**Lead crowning**

	<b>Gear 1</b>	<b>Gear 2</b>
Type of lead crowning:	symmetric	---
	0.0125 mm	---

Amount ( $C_0$ ):**Results of calculation****Geometry****Cylindrical gear pair**

Normal circular pitch ( $p_n$ ):	18.8496 mm	
Transverse pitch ( $p_t$ ):	21.3683 mm	
Axial pitch ( $p_x$ ):	40.0193 mm	
Circular pitch ( $p_e$ ):	17.7128 mm	
Transverse circular pitch ( $p_{et}$ ):	19.7530 mm	
Transverse pressure angle ( $\alpha_t$ ):	22.4213 °	
Working transverse pressure angle ( $\alpha_{wt}$ ):	22.5589 °	
Helix angle base diameter ( $\beta_b$ ):	26.2703 °	
Helix angle on the pitch circle diameter ( $\beta_w$ ):	28.1237 °	
Transverse module ( $m_t$ ):	6.8017 mm	
Ratio (i):	-1.0435	
Gear ratio (u):	1.0435	
Working centre distance (a):	160.0000 mm	
Standard centre distance ( $a_d$ ):	159.8410 mm	
Sum of profile shift coefficients ( $x^*$ ):	0.0266	
Transverse contact ratio ( $\epsilon_{\alpha}$ ):	1.3495	
Face contact ratio ( $\epsilon_{\beta}$ ):	1.0995	
Total contact ratio ( $\epsilon_{\gamma}$ ):	2.4490	
Length of path of contact ( $g_a$ ):	26.6566 mm	
Beginning of path of contact ( $g_f$ ):	13.2033 mm	
End of path of contact ( $g_a$ ):	13.4532 mm	
Backlash pitch diameter min. value ( $j_{lt}$ ):	207.9616 $\mu\text{m}$	
Backlash pitch diameter max. value ( $j_{te}$ ):	336.1778 $\mu\text{m}$	
Backlash normal plane min. value ( $j_{nt}$ ):	172.3852 $\mu\text{m}$	
Backlash normal plane max. value ( $j_{ne}$ ):	278.6672 $\mu\text{m}$	
Radial backlash min. value ( $j_{rt}$ ):	250.3033 $\mu\text{m}$	
Radial backlash max. value ( $j_{re}$ ):	404.6247 $\mu\text{m}$	
	<b>Gear 1</b>	<b>Gear 2</b>
Generating shift coefficient min. value ( $x^*_{E \text{ Min}}$ ):	-0.0066	-0.0332
Generating shift coefficient max. value ( $x^*_{E \text{ Max}}$ ):	0.0048	-0.0218
Addendum modification (k):	-0.0010 mm	-0.0010 mm
Reference diameter (d):	156.4401 mm	163.2418 mm
Pitch circle diameter ( $d_w$ ):	156.5957 mm	163.4043 mm

Base diameter ( $d_b$ ):	144.6139 mm	150.9014 mm
Diameter at V-Circle ( $d_v$ ):	156.7593 mm	163.2418 mm
Root diameter ( $d_f$ ):	141.7593 mm	148.2418 mm
generated root diameter min. value ( $d_{f \min}$ ):	141.3609 mm	147.8434 mm
generated root diameter max. value ( $d_{f \max}$ ):	141.4983 mm	147.9808 mm
Form diameter of dedendum ( $d_{Ff}$ ):	147.5217 mm	154.0326 mm
Form diameter of dedendum min. value ( $d_{Ff \min}$ ):	147.3187 mm	153.8263 mm
Form diameter of dedendum max. value ( $d_{Ff \max}$ ):	147.3879 mm	153.8967 mm
Diameter of active flank root ( $d_{Nf}$ ):	148.4815 mm	155.0855 mm
Diameter of active flank root min. value ( $d_{Nf \min}$ ):	148.3476 mm	154.9510 mm
Diameter of active flank root max. value ( $d_{Nf \max}$ ):	148.6183 mm	155.2228 mm
Tip diameter allowance max. value ( $A_{dae}$ ):	300.0000 $\mu\text{m}$	300.0000 $\mu\text{m}$
Tip diameter allowance min. value ( $A_{dai}$ ):	-300.0000 $\mu\text{m}$	-300.0000 $\mu\text{m}$
Tip diameter ( $d_a$ ):	168.7573 mm	175.2398 mm
Tip diameter min. value ( $d_{a \min}$ ):	168.4573 mm	174.9398 mm
Tip diameter max. value ( $d_{a \max}$ ):	169.0573 mm	175.5398 mm
Form diameter of addendum ( $d_{Fa}$ ):	168.7573 mm	175.2398 mm
Diameter of active flank tip ( $d_{Na}$ ):	168.7573 mm	175.2398 mm
Tip clearance (c):	1.5004 mm	1.5004 mm
Tip clearance min. value ( $c_{\min}$ ):	1.4720 mm	1.4720 mm
Tip clearance max. value ( $c_{\max}$ ):	1.8586 mm	1.8586 mm
Sliding factor at tooth root ( $K_{gr}$ ):	-0.3302	-0.3365
Sliding factor at tooth point ( $K_{ga}$ ):	0.3365	0.3302
Specific sliding at tooth root ( $\zeta_f$ ):	-1.5359	-1.5367
Specific sliding at tooth point ( $\zeta_a$ ):	0.6058	0.6057

**Test dimensions**

	<b>Gear 1</b>	<b>Gear 2</b>
No. of the teeth for span measurement (k):	4	4
Measurement diameter (span measurement) ( $d_M$ ):	155.8725 mm	161.7264 mm
Span measurement nominal value ( $W_k$ ):	64.8634 mm	64.8742 mm
Span measurement min. value ( $W_{k \min}$ ):	64.7272 mm	64.7380 mm
Span measurement max. value ( $W_{k \max}$ ):	64.7742 mm	64.7850 mm
Diameter of ball or pin ( $D_M$ ):	10.5000 mm	10.5000 mm
Measurement diameter (measurement over balls) ( $d_M$ ):	157.2465 mm	163.8239 mm
Radial single-ball measurement nominal value ( $M_{rK}$ ):	85.8384 mm	89.1068 mm
Radial single-ball measurement min. value ( $M_{rK \min}$ ):	85.6663 mm	88.9327 mm
Radial single-ball measurement max. value ( $M_{rK \max}$ ):	85.7257 mm	88.9927 mm
Measurement over balls nominal value ( $M_{dK}$ ):	171.3011 mm	178.2136 mm
Measurement over balls min. value ( $M_{dK \min}$ ):	170.9577 mm	177.8654 mm
Measurement over balls max. value ( $M_{dK \max}$ ):	171.0761 mm	177.9854 mm

Measurement over pins nominal value ( $M_{dR}$ ):	171.6768 mm	178.2136 mm
Measurement over pins min. value ( $M_{dR \min}$ ):	171.3327 mm	177.8654 mm
Measurement over pins max. value ( $M_{dR \max}$ ):	171.4513 mm	177.9854 mm
Transverse tooth thickness ( $s_t$ ):	10.8159 mm	10.6842 mm
Transverse tooth thickness min. value ( $s_{t \min}$ ):	10.6515 mm	10.5198 mm
Transverse tooth thickness max. value ( $s_{t \max}$ ):	10.7082 mm	10.5765 mm
Transverse tooth thickness at V-Circle ( $s_{vt}$ ):	10.7052 mm	10.6842 mm
Transverse tooth thickness at V-Circle min. value ( $s_{vt \min}$ ):	10.5405 mm	10.5198 mm
Transverse tooth thickness at V-Circle max. value ( $s_{vt \max}$ ):	10.5973 mm	10.5765 mm
Chordal tooth thickness at V-Circle nominal value ( $s_{vn}$ ):	9.4356 mm	9.4216 mm
Chordal tooth thickness at V-Circle min. value ( $s_{vn \min}$ ):	9.2941 mm	9.2801 mm
Chordal tooth thickness at V-Circle max. value ( $s_{vn \max}$ ):	9.3429 mm	9.3289 mm
Chordal height ( $h_v$ ):	6.1095 mm	6.1049 mm
Circular normal space width at V-Circle ( $e_{vt}$ ):	10.7067 mm	10.6842 mm
Normal chordal tooth thickness at standard pitch diameter nominal value ( $s_n$ ):	9.5374 mm	9.4216 mm
Normal chordal tooth thickness at standard pitch diameter min. value ( $s_{n \min}$ ):	9.3959 mm	9.2801 mm
Normal chordal tooth thickness at standard pitch diameter max. value ( $s_{n \max}$ ):	9.4447 mm	9.3289 mm
Normal chordal tooth thickness at tip diameter nominal value ( $s_{an}$ ):	4.4521 mm	4.5089 mm
Normal chordal tooth thickness at tip diameter min. value ( $s_{an \min}$ ):	4.1472 mm	4.2072 mm
Normal chordal tooth thickness at tip diameter max. value ( $s_{an \max}$ ):	4.5014 mm	4.5560 mm
Chordal height at standard pitch diameter ( $h_a$ ):	6.2718 mm	6.1049 mm
Circular normal space width at reference diameter ( $e_t$ ):	10.5524 mm	10.6842 mm
Tooth depth ( $h$ ):	13.4990 mm	13.4990 mm
<b>Tolerances</b>		
	<b>Gear 1</b>	<b>Gear 2</b>
Profile form deviation ( $f_f$ ):	7 $\mu\text{m}$	7 $\mu\text{m}$
Profile slope deviation ( $f_{H\alpha}$ ):	5 $\mu\text{m}$	5 $\mu\text{m}$
Total profile deviation ( $F_f$ ):	9 $\mu\text{m}$	9 $\mu\text{m}$
Adjacent pitch deviation ( $f_p$ ):	7 $\mu\text{m}$	7 $\mu\text{m}$
Tooth to tooth pitch deviation ( $f_u$ ):	8 $\mu\text{m}$	8 $\mu\text{m}$
Total deviation of circular pitch ( $F_p$ ):	25 $\mu\text{m}$	25 $\mu\text{m}$
Variation of tooth thickness ( $R_s$ ):	10 $\mu\text{m}$	10 $\mu\text{m}$
Runout ( $F_r$ ):	18 $\mu\text{m}$	18 $\mu\text{m}$
Total tooth alignment deviation ( $F_\beta$ ):	9 $\mu\text{m}$	9 $\mu\text{m}$
Tooth alignment slope deviation ( $f_{H\beta}$ ):	7 $\mu\text{m}$	7 $\mu\text{m}$

Tooth alignment form deviation ( $f_{\beta F}$ ):	6 $\mu\text{m}$	6 $\mu\text{m}$
Double flank pitch deviation ( $F''_i$ ):	22 $\mu\text{m}$	22 $\mu\text{m}$
Double flank pitch step ( $f''_i$ ):	9 $\mu\text{m}$	9 $\mu\text{m}$
Single flank pitch deviation ( $F'_i$ ):	28 $\mu\text{m}$	28 $\mu\text{m}$
Single flank pitch step ( $f'_i$ ):	11 $\mu\text{m}$	11 $\mu\text{m}$

**Load capacity (general influence factors)****Cylindrical gear pair**

Carried width (tooth root) ( $b^*$ ):	0.0000
Nominal circumferential force at pitch cylinder ( $F_t$ ):	18377.6430 N
Axial force on the reference diameter ( $F_a$ ):	9812.7475 N
Radial force on the reference diameter ( $F_r$ ):	7582.7132 N
Normal tooth force on the reference diameter ( $F_n$ ):	22170.3703 N
Circumferential force on the pitch circle diameter ( $F_{tw}$ ):	18359.3750 N
Axial force on the pitch circle diameter ( $F_{aw}$ ):	9812.7475 N
Radial force on the pitch circle diameter ( $F_{rw}$ ):	7626.8377 N
Normal tooth force on the pitch circle diameter ( $F_{nw}$ ):	22170.3703 N
Circumferential speed ( $v$ ):	24.5736 m/s
Running-in allowance ( $y_\alpha$ ):	0.5250 $\mu\text{m}$
Running-in allowance ( $y_f$ ):	0.5250 $\mu\text{m}$
Running-in allowance ( $y_p$ ):	0.5250 $\mu\text{m}$
Layout value of the profile correction ( $C_{ay}$ ):	1.9954 $\mu\text{m}$
Correction coefficient ( $C_M$ ):	0.8000
Gear body coefficient ( $C_R$ ):	1.0000
Basic rack profile coefficient ( $C_{BS}$ ):	0.9750
Single spring stiffness ( $c'$ ):	11.5859 N/(mm $\mu\text{m}$ )
Meshing spring stiffness ( $c_{\gamma\alpha}$ ):	14.6228 N/(mm $\mu\text{m}$ )
Meshing spring stiffness ( $c_{\gamma\beta}$ ):	12.4294 N/(mm $\mu\text{m}$ )
Reduced mass ( $m_{red}$ ):	0.0427 kg/mm
Reference speed ( $N$ ):	0.3904
Sub-critical range	
Resonance speed ( $n_{E1}$ ):	7684.4861 1/min
Dynamic coefficient ( $K_v$ ):	1.0791

	<b>Gear 1</b>	<b>Gear 2</b>
Number of load changes ( $N_L$ ):	3600.0000 Mio.	3450.0000 Mio.

**Load capacity (flank)****Cylindrical gear pair**

Zone factor ( $Z_H$ ):	2.2477
Elasticity coefficient ( $Z_E$ ):	$189.8117 \text{ (N/mm}^2\text{)}^{0.5}$
Overlap factor ( $Z_\epsilon$ ):	0.8608
Helix angle factor ( $Z_\beta$ ):	1.0647
Lubrication coefficient ( $Z_L$ ):	1.0474
Speed coefficient ( $Z_v$ ):	1.0266
Roughness factor ( $Z_R$ ):	1.0200
Material match coefficient ( $Z_W$ ):	1.0000
Transverse coefficient ( $K_{H\alpha}$ ):	1.0000
Nominal surface pressure at pitch point ( $\sigma_{H0}$ ):	915.1619 N/mm <sup>2</sup>

	<b>Gear 1</b>	<b>Gear 2</b>
Limited life factor ( $Z_N$ ):	0.9136	0.9163
Endurance factor (static strength) ( $Z_{NT}$ ):	1.6000	1.6000
Long life factor ( $Z_{NT}$ ):	0.8500	0.8500
Size factor ( $Z_X$ ):	1.0000	1.0000
Single contact factor ( $Z_{B,D}$ ):	1.0000	1.0000
Existing surface pressure ( $\sigma_H$ ):	950.6693 N/mm <sup>2</sup>	950.6693 N/mm <sup>2</sup>
Permitted surface pressure (static strength) ( $\sigma_{HP \text{ stat}}$ ):	2400.0000 N/mm <sup>2</sup>	2400.0000 N/mm <sup>2</sup>
Permitted surface pressure (fatigue strength) ( $\sigma_{HP \text{ dauer}}$ ):	1645.1157 N/mm <sup>2</sup>	1645.1157 N/mm <sup>2</sup>
Safety flank (stat. strength):	2.5245	2.5245
Safety flank (dyn. strength):	1.5809	1.5856

**Load capacity (root)****Cylindrical gear pair**

Face coefficient ( $K_{F\beta}$ ):	1.0000	
Transverse coefficient ( $K_{F\alpha}$ ):	1.0000	
Helix factor ( $Y_\beta$ ):	0.7658	
Stress correction coefficient ( $Y_{ST}$ ):	2.0000	
	<b>Gear 1</b>	<b>Gear 2</b>
Effective facewidth ( $b_{tr}$ ):	42.0000 mm	42.0000 mm
Angle of load application ( $\alpha_{Fen}$ ):	19.1886 °	19.0980 °
Root fillet radius at 30° tangent ( $r_F$ ):	3.2761 mm	3.3094 mm
Chord of tooth root thickness ( $s_{Fn}$ ):	12.4916 mm	12.4877 mm
Bending moment arm ( $h_{Fe}$ ):	6.0507 mm	6.1101 mm
Existing stress in the tooth root ( $\sigma_F$ ):	163.8937 N/mm <sup>2</sup>	164.4352 N/mm <sup>2</sup>
Nominal stress in the tooth root ( $\sigma_{F0}$ ):	151.8796 N/mm <sup>2</sup>	152.3813 N/mm <sup>2</sup>
Permitted stress in the tooth root (stat. strength) ( $\sigma_{FP \text{ stat}}$ ):	2656.8051 N/mm <sup>2</sup>	2656.2476 N/mm <sup>2</sup>
	1062.7221 N/mm <sup>2</sup>	1062.4990 N/mm <sup>2</sup>

Permitted stress in the tooth root (fatigue strength) ( $\sigma_{FP\ dauer}$ ):		
Form factor ( $Y_F$ ):	1.4030	1.4184
Stress correction coefficient ( $Y_S$ ):	1.9383	1.9235
Limited life factor ( $Y_N$ ):	0.8676	0.8683
Endurance factor (static strength) ( $Y_{NT}$ ):	2.5000	2.5000
Long life factor ( $Y_{NT}$ ):	0.8500	0.8500
Relative notch sensitivity factor ( $Y_{\delta\ Rel\ T}$ ):	0.9941	0.9939
Relative surface factor ( $Y_{R\ Rel\ T}$ ):	0.9639	0.9639
Size factor ( $Y_X$ ):	0.9900	0.9900
Rim thickness factor ( $Y_B$ ):	1.0000	1.0000
Deep tooth factor ( $Y_{DT}$ ):	1.0000	1.0000
Technology factor <sup>1)</sup> ( $Y_T$ ):	1.0000	1.0000
Mode of operation:	oscillating	oscillating
Number of load direction changes ( $N_{rev}$ ):	1	1
Mode of operation factor <sup>2)</sup> ( $Y_A$ ):	0.8500	0.8500
Safety root (stat. strength):	16.6247	16.4594
Safety root (dyn. strength):	5.6256	5.6106

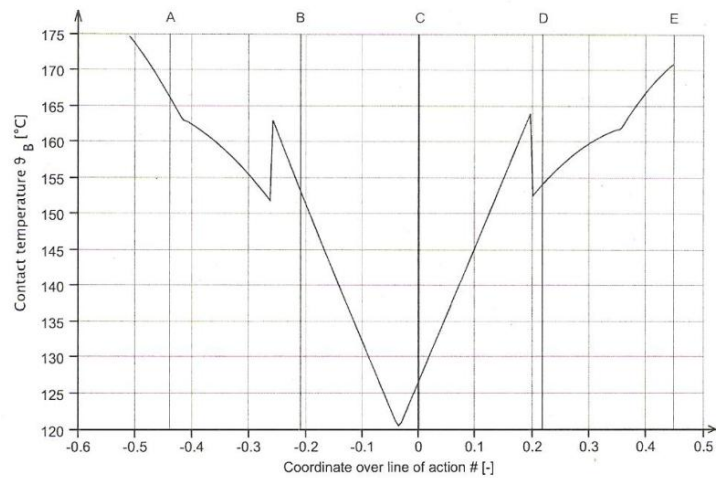
**Load capacity (Scuffing) (ISO/TR 13989)**

Mass temperature at FZG test (approximation) ( $\vartheta_{MT}$ ):	184.6946 °C
Flash temperature at FZG test (approximation) ( $\vartheta_{fla\ max\ T}$ ):	88.0958 °C
Angular factor ( $X_{\alpha\ \beta}$ ):	0.9916
Face coefficient ( $K_{B\ \beta}$ ):	1.0000
Transverse coefficient ( $K_{B\ \alpha}$ ):	1.0000
Decisive circumferential force ( $w_{Bl}$ ):	472.1756 N/mm

**Integral temperature method**

Scuffing integral temperature ( $\vartheta_{int\ s}$ ):	382.9101 °C
Contact ratio factor ( $X_\epsilon$ ):	0.3196
Decisive tip relief ( $C_a$ ):	1.9954 $\mu\text{m}$
Tip relief factor ( $X_{Ca}$ ):	1.0811
Mesh factor ( $X_\alpha$ ):	1.0000
Geometry factor for pinion tooth tip ( $X_{BE}$ ):	0.3388
Flash factor ( $X_M$ ):	53.0595 $\text{K N}^{-0.75} \text{s}^{0.5} \text{m}^{-0.5} \text{mm}$
Lubricant factor ( $X_L$ ):	1.0000
Roughness factor ( $X_R$ ):	0.8860
Run-in factor ( $X_E$ ):	1.0000
Helix factor ( $K_{B\ \gamma}$ ):	1.2140
Average on-site friction coefficient ( $\mu_{mC}$ ):	0.0377

Flash temperature at the tip mesh point E of the pinion ( $\vartheta_{\text{fla}}$ $\epsilon$ ):	101.4824 K
Average flash temperature above mesh ( $\vartheta_{\text{fla int}}$ ):	32.4296 K
Lubrication factor ( $X_S$ ):	1.2000
Mass temperature ( $\vartheta_M$ ):	109.0686 °C
Integral temperature ( $\vartheta_{\text{int}}$ ):	157.7131 °C
Scuffing safety (integral temperature) ( $S_{\text{int S}}$ ):	2.4279
<b>Flash temperature method</b>	
Scuffing contact temperature ( $\vartheta_S$ ):	380.8732 °C
Coordinate of maximum contact temperature ( $\Gamma_{\text{max}}$ ):	-0.4396
Distribution factor ( $X_{\Gamma \text{ max}}$ ):	0.4333
Geometry factor ( $X_{B \text{ max}}$ ):	0.3387
Flash factor ( $X_{M \text{ max}}$ ):	53.0595 K N <sup>-0.75</sup> s <sup>0.5</sup> m <sup>-0.5</sup> mm
Lubricant factor ( $X_L$ ):	0.8429
Roughness factor ( $X_R$ ):	0.8190
Approach factor ( $X_J$ ):	1.0751
Buttressing factor ( $X_{\text{but}}$ ):	1.3000
Average on-site friction coefficient ( $\mu_{\text{my max}}$ ):	0.0375
Mass temperature ( $\vartheta_M$ ):	120.5376 °C
Maximal flash temperature ( $\vartheta_{\text{fla max}}$ ):	54.1446 K
Maximal contact temperature ( $\vartheta_{B \text{ max}}$ ):	174.6822 °C
Scuffing safety (flash temperature) ( $S_B$ ):	3.4349

**Efficiency of gearing**

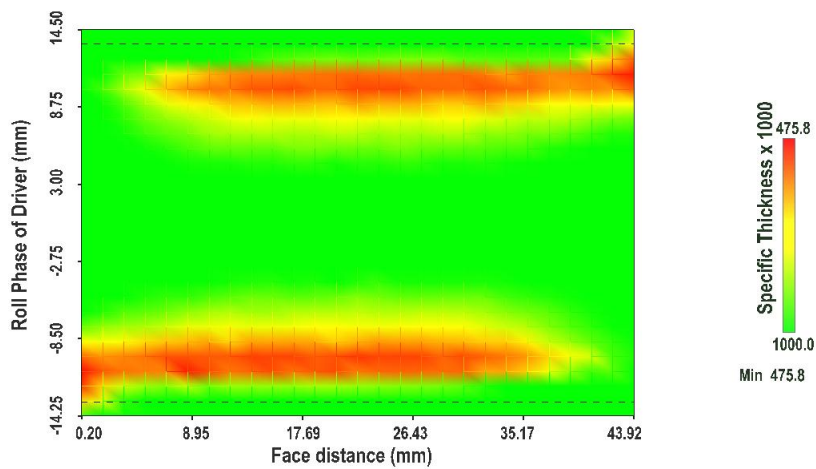
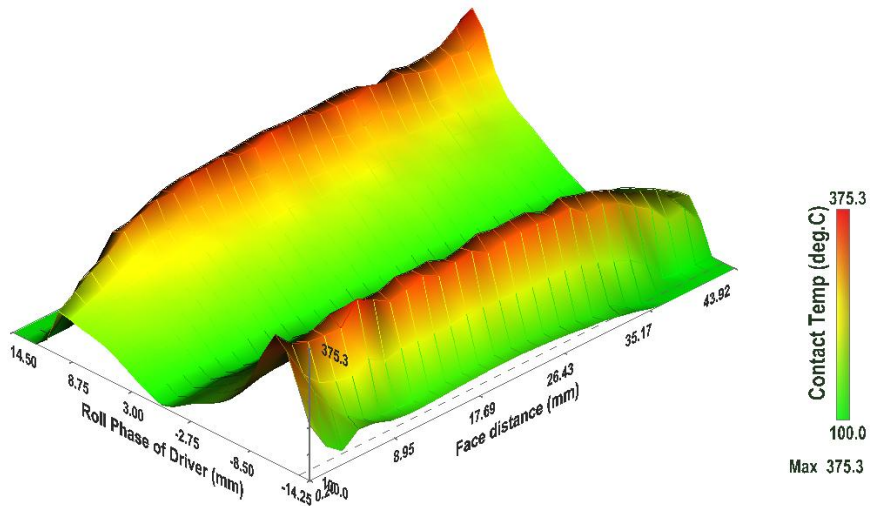
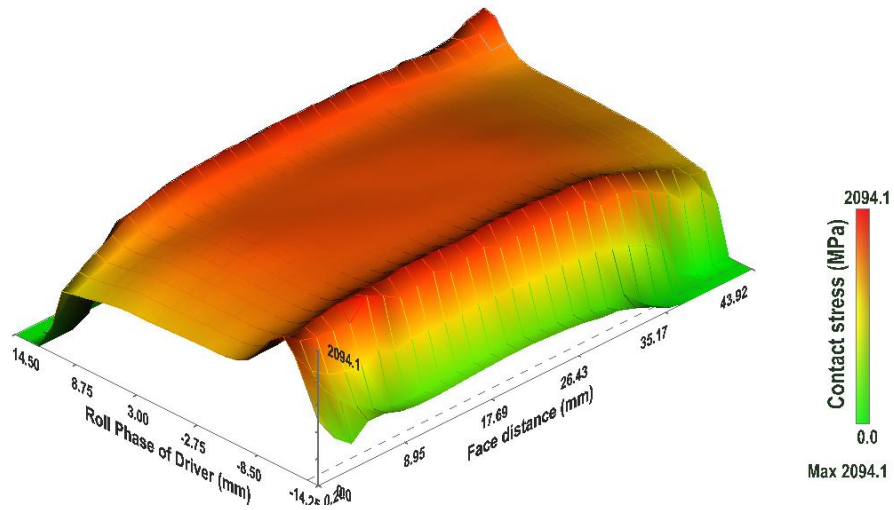
see G.Niemann, H.Winter: Maschinenelemente Vol. II, 2.Auflage 1989, SpringerVerlag, Chap. 21.11

Average coefficient of friction ( $\mu_m$ ):	0.0358
Grade of tooth losses ( $H_v$ ):	0.1674
Tooth friction losses ( $P_{vz}$ ):	2.707931 kW
Efficiency of gearing ( $\eta_z$ ):	99.4 %

**References**

- 1) Influence of the technology factor according to:  
Linke, Heinz: Stirnradverzahnungen  
Carl Hanser publishing company, 1st Edition 1996  
Page 320 (Equation 6.5/36)
- 2) Influence of the mode of operation factor according to:  
Linke, Heinz: Stirnradverzahnungen  
Carl Hanser publishing company, 1st Edition 1996  
Page 320 (Equation 6.5/36) and Page 321 (Table 6.5/7)

**APPENDIX-I:** 3D results by Dontyne Software at 1.0 Torque Ratio of Contact Stress, Local Contact Temperature and Specific Lubricant Film Thickness at 1.0 Torque Ratio Respectively. (Chapter 6, Section 6.4.2)



## APPENDIX-J: KISSsoft Output for Results at 1.0 Torque Ratio. (Chapter 6, Section 6.4.2)



KISSsoft Release 03/2013

## KISSsoft evaluation

File

Name : kisssoft experimental model at 1 torque ratio  
 Description: KISSsoft example  
 Changed by: issa am: 17.03.2014 um: 14:09:50

**Contact analysis**

Mesh gear 1 - gear 2 (Left Tooth Flank)

Accuracy of calculation		low				
Partial load for calculation		100.00	%			
Center distance	[a]	160.0000	mm			
Single pitch deviation	[f <sub>pt</sub> ]	0.0000	μm			
Coefficient of friction	[μ]	0.0350				
Deviation error of axis	[f <sub>Σβ</sub> ]	0.0000	μm			
Inclination error of axis	[f <sub>Σδ</sub> ]	0.0000	μm			
Torque	[T <sub>1</sub> ]					
Torsion		Gear A :-, B :-				
		min	max	Δ	μ	σ
Transmission error	(μm)	-107.8269	-105.6488	2.1781	-106.5766	0.7017
Stiffness curve	(N/mm/μm)	14.8636	15.6681	0.8045	15.3558	0.2386
Line load	(N/mm)	0.0000	1756.9407	1756.9407	1117.8958	315.7719
Torque Gear 1	(Nm)	4786.5622	4795.2828	8.7206	4790.7136	1.7250
Torque Gear 2	(Nm)	4938.7531	4954.0804	15.3273	4946.1743	2.9396
Power loss	(W)	12564.8214	12973.0970	408.2756	12819.6361	112.3643
Flash temperature	(°)	90.0000	343.4828	253.4828	182.3661	62.4700
Lubricating film	(μm)	0.2427	1.7096	1.4669	0.5413	0.2628
Hertzian stress	(N/mm <sup>2</sup> )		2309.6233		1700.5160	
Transverse contact ratio under load	[ε <sub>a</sub> ']	1.600				
Overlap ratio under load	[ε <sub>b</sub> ']	1.060				
Total contact ratio under load	[ε <sub>g</sub> ']	2.660				
Efficiency	[η]	99.15 %				

**K<sub>Hβ</sub> Calculation - Gear 1 - Gear 2**

Left flank

f<sub>Σβ</sub> = 0.000 μm , f<sub>Σδ</sub> = 0.000 μm  
 f<sub>ma</sub> = 0.000 μm , f<sub>Hβ</sub> = 0.000 μm  
 Result after i = 1 iterations of load distribution  
 Gear 1  
 Point in polar co-ordinates:  
 R = 78.298 mm , φ = 0.000 °  
 Displacement calculated in direction 247.441 °

	y	φ1.t	f1.t	f1.b	f1.tot	f1.C	f1.tot+f1.C
1	-21.463 mm	0.0000°	0.0000 μm	0.0000 μm	0.0000 μm	0.0000 μm	0.0000 μm
2	-20.390 mm	0.0000°	0.0000 μm	0.0000 μm	0.0000 μm	-1.3921 μm	-1.3921 μm
3	-19.317 mm	0.0000°	0.0000 μm	0.0000 μm	0.0000 μm	-2.7128 μm	-2.7128 μm
4	-18.244 mm	0.0000°	0.0000 μm	0.0000 μm	0.0000 μm	-3.9622 μm	-3.9622 μm
5	-17.171 mm	0.0000°	0.0000 μm	0.0000 μm	0.0000 μm	-5.1402 μm	-5.1402 μm
6	-16.098 mm	0.0000°	0.0000 μm	0.0000 μm	0.0000 μm	-6.2470 μm	-6.2470 μm
7	-15.024 mm	0.0000°	0.0000 μm	0.0000 μm	0.0000 μm	-7.2823 μm	-7.2823 μm
8	-13.951 mm	0.0000°	0.0000 μm	0.0000 μm	0.0000 μm	-8.2463 μm	-8.2463 μm

1/11



9	-12.878 mm	0.0000°	0.0000 μm	0.0000 μm	0.0000 μm	-9.1390 μm	-9.1390 μm
10	-11.805 mm	0.0000°	0.0000 μm	0.0000 μm	0.0000 μm	-9.9604 μm	-9.9604 μm
11	-10.732 mm	0.0000°	0.0000 μm	0.0000 μm	0.0000 μm	-10.7104 μm	-10.7104 μm
12	-9.659 mm	0.0000°	0.0000 μm	0.0000 μm	0.0000 μm	-11.3890 μm	-11.3890 μm
13	-8.585 mm	0.0000°	0.0000 μm	0.0000 μm	0.0000 μm	-11.9963 μm	-11.9963 μm
14	-7.512 mm	0.0000°	0.0000 μm	0.0000 μm	0.0000 μm	-12.5323 μm	-12.5323 μm
15	-6.439 mm	0.0000°	0.0000 μm	0.0000 μm	0.0000 μm	-12.9970 μm	-12.9970 μm
16	-5.366 mm	0.0000°	0.0000 μm	0.0000 μm	0.0000 μm	-13.3902 μm	-13.3902 μm
17	-4.293 mm	0.0000°	0.0000 μm	0.0000 μm	0.0000 μm	-13.7122 μm	-13.7122 μm
18	-3.220 mm	0.0000°	0.0000 μm	0.0000 μm	0.0000 μm	-13.9628 μm	-13.9628 μm
19	-2.146 mm	0.0000°	0.0000 μm	0.0000 μm	0.0000 μm	-14.1421 μm	-14.1421 μm
20	-1.073 mm	0.0000°	0.0000 μm	0.0000 μm	0.0000 μm	-14.2500 μm	-14.2500 μm
21	0.000 mm	0.0000°	0.0000 μm	0.0000 μm	0.0000 μm	-14.2866 μm	-14.2866 μm
22	1.073 mm	0.0000°	0.0000 μm	0.0000 μm	0.0000 μm	-14.2500 μm	-14.2500 μm
23	2.146 mm	0.0000°	0.0000 μm	0.0000 μm	0.0000 μm	-14.1421 μm	-14.1421 μm
24	3.220 mm	0.0000°	0.0000 μm	0.0000 μm	0.0000 μm	-13.9628 μm	-13.9628 μm
25	4.293 mm	0.0000°	0.0000 μm	0.0000 μm	0.0000 μm	-13.7122 μm	-13.7122 μm
26	5.366 mm	0.0000°	0.0000 μm	0.0000 μm	0.0000 μm	-13.3902 μm	-13.3902 μm
27	6.439 mm	0.0000°	0.0000 μm	0.0000 μm	0.0000 μm	-12.9970 μm	-12.9970 μm
28	7.512 mm	0.0000°	0.0000 μm	0.0000 μm	0.0000 μm	-12.5323 μm	-12.5323 μm
29	8.585 mm	0.0000°	0.0000 μm	0.0000 μm	0.0000 μm	-11.9963 μm	-11.9963 μm
30	9.659 mm	0.0000°	0.0000 μm	0.0000 μm	0.0000 μm	-11.3890 μm	-11.3890 μm
31	10.732 mm	0.0000°	0.0000 μm	0.0000 μm	0.0000 μm	-10.7104 μm	-10.7104 μm
32	11.805 mm	0.0000°	0.0000 μm	0.0000 μm	0.0000 μm	-9.9604 μm	-9.9604 μm
33	12.878 mm	0.0000°	0.0000 μm	0.0000 μm	0.0000 μm	-9.1390 μm	-9.1390 μm
34	13.951 mm	0.0000°	0.0000 μm	0.0000 μm	0.0000 μm	-8.2463 μm	-8.2463 μm
35	15.024 mm	0.0000°	0.0000 μm	0.0000 μm	0.0000 μm	-7.2823 μm	-7.2823 μm
36	16.098 mm	0.0000°	0.0000 μm	0.0000 μm	0.0000 μm	-6.2470 μm	-6.2470 μm
37	17.171 mm	0.0000°	0.0000 μm	0.0000 μm	0.0000 μm	-5.1402 μm	-5.1402 μm
38	18.244 mm	0.0000°	0.0000 μm	0.0000 μm	0.0000 μm	-3.9622 μm	-3.9622 μm
39	19.317 mm	0.0000°	0.0000 μm	0.0000 μm	0.0000 μm	-2.7128 μm	-2.7128 μm
40	20.390 mm	0.0000°	0.0000 μm	0.0000 μm	0.0000 μm	-1.3921 μm	-1.3921 μm
41	21.463 mm	0.0000°	0.0000 μm	0.0000 μm	0.0000 μm	0.0000 μm	0.0000 μm

Gear 2

Point in polar co-ordinates:

R = 81.702 mm , φ = 180.000 °

Displacement calculated in direction 247.441 °

	y	φ2.t	f2.t	f2.b	f2.tot	f2.C	f2.tot+f2.C
1	-21.463 mm	0.0000°	0.0000 μm				
2	-20.390 mm	0.0000°	0.0000 μm				
3	-19.317 mm	0.0000°	0.0000 μm				
4	-18.244 mm	0.0000°	0.0000 μm				
5	-17.171 mm	0.0000°	0.0000 μm				
6	-16.098 mm	0.0000°	0.0000 μm				
7	-15.024 mm	0.0000°	0.0000 μm				
8	-13.951 mm	0.0000°	0.0000 μm				
9	-12.878 mm	0.0000°	0.0000 μm				
10	-11.805 mm	0.0000°	0.0000 μm				
11	-10.732 mm	0.0000°	0.0000 μm				
12	-9.659 mm	0.0000°	0.0000 μm				
13	-8.585 mm	0.0000°	0.0000 μm				
14	-7.512 mm	0.0000°	0.0000 μm				
15	-6.439 mm	0.0000°	0.0000 μm				
16	-5.366 mm	0.0000°	0.0000 μm				
17	-4.293 mm	0.0000°	0.0000 μm				



18	-3.220 mm	0.0000°	0.0000 μm				
19	-2.146 mm	0.0000°	0.0000 μm				
20	-1.073 mm	0.0000°	0.0000 μm				
21	0.000 mm	0.0000°	0.0000 μm				
22	1.073 mm	0.0000°	0.0000 μm				
23	2.146 mm	0.0000°	0.0000 μm				
24	3.220 mm	0.0000°	0.0000 μm				
25	4.293 mm	0.0000°	0.0000 μm				
26	5.366 mm	0.0000°	0.0000 μm				
27	6.439 mm	0.0000°	0.0000 μm				
28	7.512 mm	0.0000°	0.0000 μm				
29	8.585 mm	0.0000°	0.0000 μm				
30	9.659 mm	0.0000°	0.0000 μm				
31	10.732 mm	0.0000°	0.0000 μm				
32	11.805 mm	0.0000°	0.0000 μm				
33	12.878 mm	0.0000°	0.0000 μm				
34	13.951 mm	0.0000°	0.0000 μm				
35	15.024 mm	0.0000°	0.0000 μm				
36	16.098 mm	0.0000°	0.0000 μm				
37	17.171 mm	0.0000°	0.0000 μm				
38	18.244 mm	0.0000°	0.0000 μm				
39	19.317 mm	0.0000°	0.0000 μm				
40	20.390 mm	0.0000°	0.0000 μm				
41	21.463 mm	0.0000°	0.0000 μm				

Explanations:

- y : Width
- φ,t : Static torsion
- f,t : Displacement due to torsion
- f,b : Displacement due to bending
- f,tot : Total displacement (f,b+f,t)
- f,C : Change due to flank line modification

Load distribution

Contact stiffness = 11.179 N/mm/μm

Young's modulus = 207000.0/207000.0 N/mm<sup>2</sup>

	y	δ	g	w
1.	-21.4634 mm	14.2866 μm	133.9699 μm	1497.6708 N/mm
2.	-20.3902 mm	12.8945 μm	135.3619 μm	1513.2330 N/mm
3.	-19.3171 mm	11.5738 μm	136.6827 μm	1527.9977 N/mm
4.	-18.2439 mm	10.3244 μm	137.9321 μm	1541.9649 N/mm
5.	-17.1707 mm	9.1463 μm	139.1101 μm	1555.1345 N/mm
6.	-16.0976 mm	8.0396 μm	140.2168 μm	1567.5065 N/mm
7.	-15.0244 mm	7.0043 μm	141.2522 μm	1579.0810 N/mm
8.	-13.9512 mm	6.0402 μm	142.2162 μm	1589.8580 N/mm
9.	-12.8780 mm	5.1476 μm	143.1089 μm	1599.8375 N/mm
10.	-11.8049 mm	4.3262 μm	143.9302 μm	1609.0194 N/mm
11.	-10.7317 mm	3.5762 μm	144.6802 μm	1617.4037 N/mm
12.	-9.6585 mm	2.8976 μm	145.3589 μm	1624.9906 N/mm
13.	-8.5854 mm	2.2902 μm	145.9662 μm	1631.7799 N/mm
14.	-7.5122 mm	1.7543 μm	146.5022 μm	1637.7716 N/mm
15.	-6.4390 mm	1.2896 μm	146.9668 μm	1642.9658 N/mm
16.	-5.3659 mm	0.8963 μm	147.3601 μm	1647.3625 N/mm
17.	-4.2927 mm	0.5744 μm	147.6821 μm	1650.9617 N/mm
18.	-3.2195 mm	0.3238 μm	147.9327 μm	1653.7633 N/mm
19.	-2.1463 mm	0.1445 μm	148.1119 μm	1655.7673 N/mm
20.	-1.0732 mm	0.0366 μm	148.2199 μm	1656.9739 N/mm



21.	0.0000 mm	0.0000 $\mu\text{m}$	148.2565 $\mu\text{m}$	1657.3829 N/mm
22.	1.0732 mm	0.0366 $\mu\text{m}$	148.2199 $\mu\text{m}$	1656.9739 N/mm
23.	2.1463 mm	0.1445 $\mu\text{m}$	148.1119 $\mu\text{m}$	1655.7673 N/mm
24.	3.2195 mm	0.3238 $\mu\text{m}$	147.9327 $\mu\text{m}$	1653.7633 N/mm
25.	4.2927 mm	0.5744 $\mu\text{m}$	147.6821 $\mu\text{m}$	1650.9617 N/mm
26.	5.3659 mm	0.8963 $\mu\text{m}$	147.3601 $\mu\text{m}$	1647.3625 N/mm
27.	6.4390 mm	1.2896 $\mu\text{m}$	146.9668 $\mu\text{m}$	1642.9658 N/mm
28.	7.5122 mm	1.7543 $\mu\text{m}$	146.5022 $\mu\text{m}$	1637.7716 N/mm
29.	8.5854 mm	2.2902 $\mu\text{m}$	145.9662 $\mu\text{m}$	1631.7799 N/mm
30.	9.6585 mm	2.8976 $\mu\text{m}$	145.3589 $\mu\text{m}$	1624.9906 N/mm
31.	10.7317 mm	3.5762 $\mu\text{m}$	144.6802 $\mu\text{m}$	1617.4037 N/mm
32.	11.8049 mm	4.3262 $\mu\text{m}$	143.9302 $\mu\text{m}$	1609.0194 N/mm
33.	12.8780 mm	5.1476 $\mu\text{m}$	143.1089 $\mu\text{m}$	1599.8375 N/mm
34.	13.9512 mm	6.0402 $\mu\text{m}$	142.2162 $\mu\text{m}$	1589.8580 N/mm
35.	15.0244 mm	7.0043 $\mu\text{m}$	141.2522 $\mu\text{m}$	1579.0810 N/mm
36.	16.0976 mm	8.0396 $\mu\text{m}$	140.2168 $\mu\text{m}$	1567.5065 N/mm
37.	17.1707 mm	9.1463 $\mu\text{m}$	139.1101 $\mu\text{m}$	1555.1345 N/mm
38.	18.2439 mm	10.3244 $\mu\text{m}$	137.9321 $\mu\text{m}$	1541.9649 N/mm
39.	19.3171 mm	11.5738 $\mu\text{m}$	136.6827 $\mu\text{m}$	1527.9977 N/mm
40.	20.3902 mm	12.8945 $\mu\text{m}$	135.3619 $\mu\text{m}$	1513.2330 N/mm
41.	21.4634 mm	14.2866 $\mu\text{m}$	133.9699 $\mu\text{m}$	1497.6708 N/mm

Explanations:

$\delta$  : Gap

g : Flank overlap

w : Line load

Force application point, Y direction: y = 0.000 mm (F = 70463.8 N)

$w_{\text{max}} = 1657.383 \text{ N/mm}$ ,  $w_{\text{m}} = 1601.450 \text{ N/mm}$

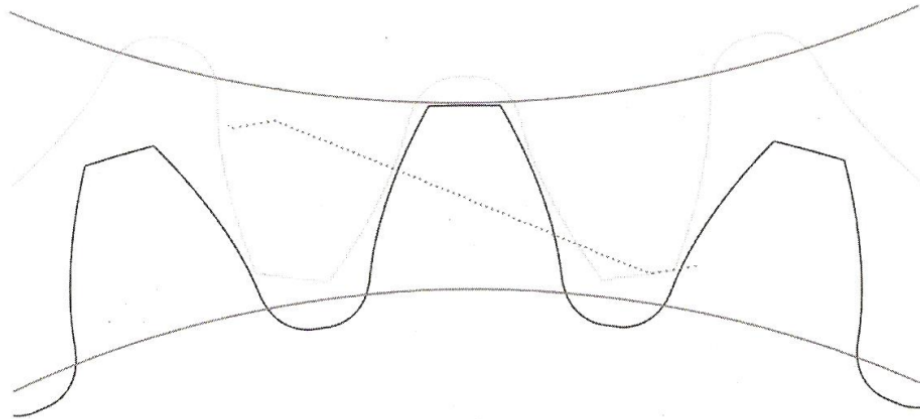
$w_{\text{m}} = K_{\text{V}} * K_{\text{A}} * K_{\text{Y}} * (F_{\text{t}}/b) / \cos(\alpha_{\text{wt}})$

$K_{\text{V}} = 1.062$ ,  $K_{\text{A}} = 1.000$ ,  $K_{\text{Y}} = 1.000$

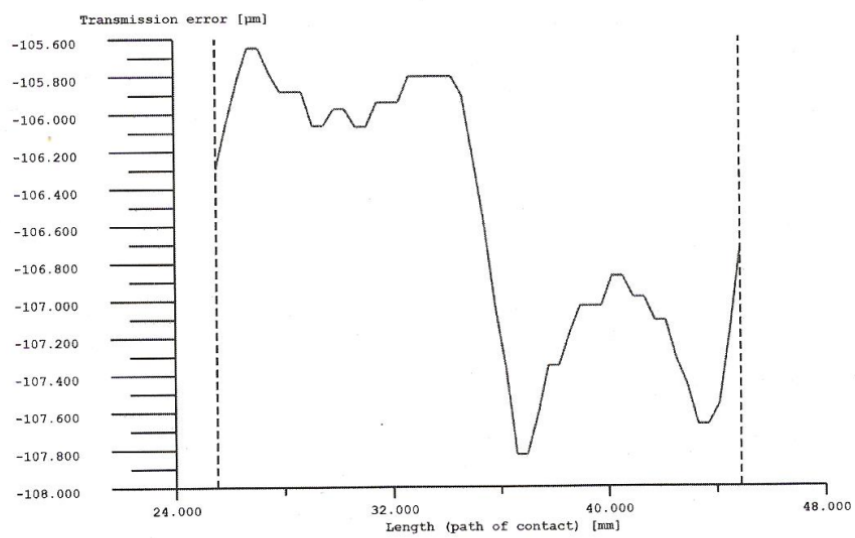
$K_{\text{H}\beta} = w_{\text{max}}/w_{\text{m}} = 1.0349$  (Calculation according to ISO 6336-1, Appendix E)

Notice: The influence of the exceeding facewidth is not taken into account in the calculation of KHbeta.

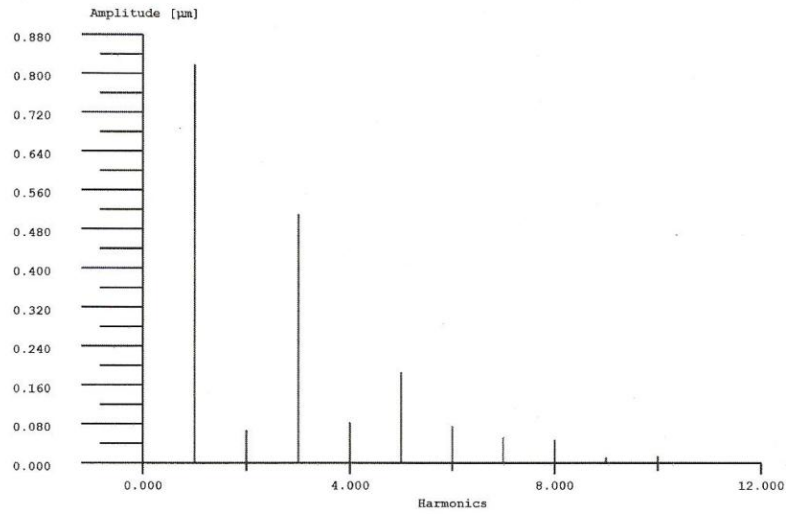
**KISSOFT**  
 Calculation programs for machine design



da1 = 168.7593 mm, df1 = 140.9377 mm, As1 = -0.2990 mm da2 = 175.2416 mm, df2 = 147.4201 mm, As2 = -0.2990 mm  
 Figure: Path of contact



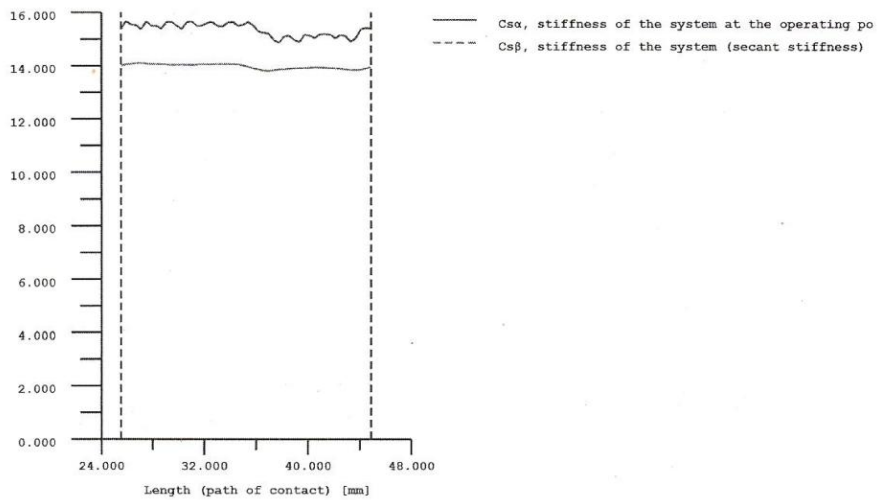
wt = 100 %, a = 160.000 mm, fpt = 0.000 µm, µ = 0.035 Working flank: Left flank  
 Figure: Transmission error



Harmonics      Amplitude [µm]1.    0.8183902.      0.0672213.      0.5104974.      0.0830415.      0.1858696.  
 0.0758187.    0.0520158.      0.0475689.      0.01066510.      0.014476wt = 100 %, a = 160.000 mm, fpt = 0.000 µm, µ =  
 0.035Working flank: Left flank

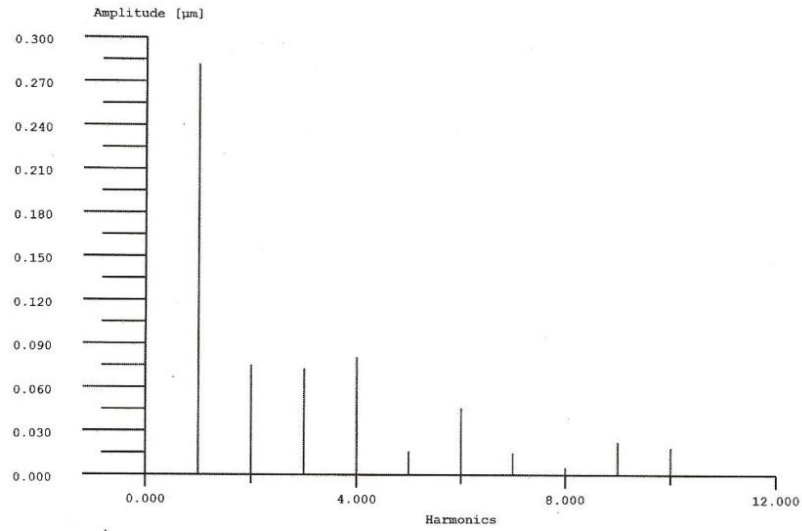
Figure: Amplitude spectrum of transmission error

tooth contact stiffness [N/mm/µm]



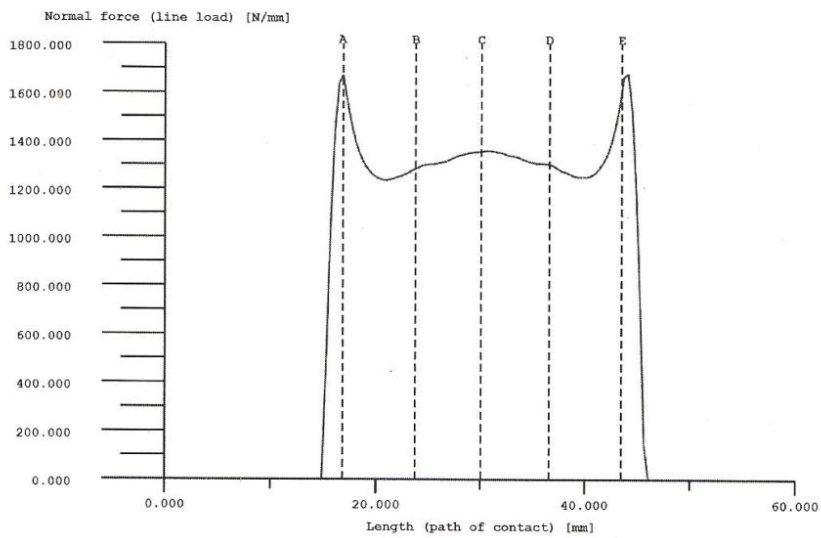
wt = 100 %, a = 160.000 mm, fpt = 0.000 µm, µ = 0.035Working flank: Left flank

Figure: Stiffness curve

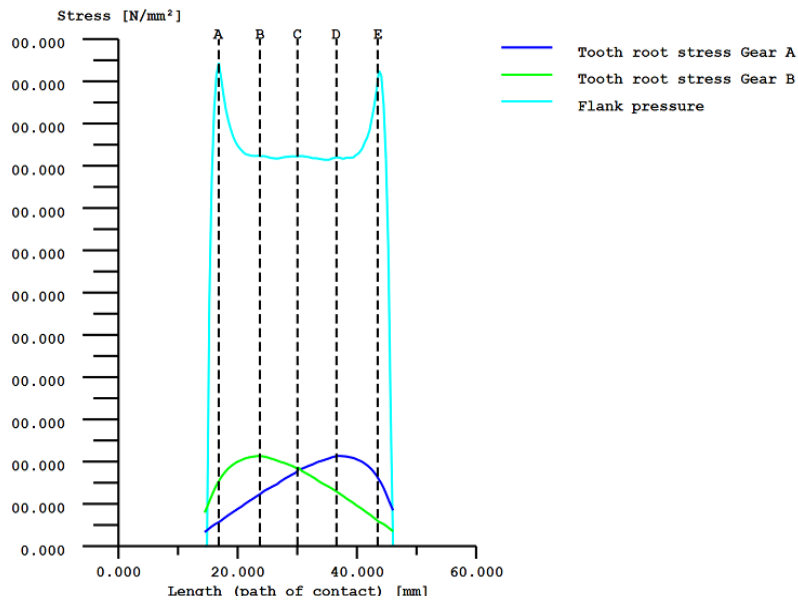


Harmonics      Amplitude [N/mm/μm]1.      0.2818722.      0.0750753.      0.0726984.      0.0805125.  
 0.0161426.      0.0459897.      0.0151158.      0.0050779.      0.02256310.      0.018510wt = 100 %, a = 160.000  
 mm, fpt = 0.000 μm, μ = 0.035 Working flank: Left flank

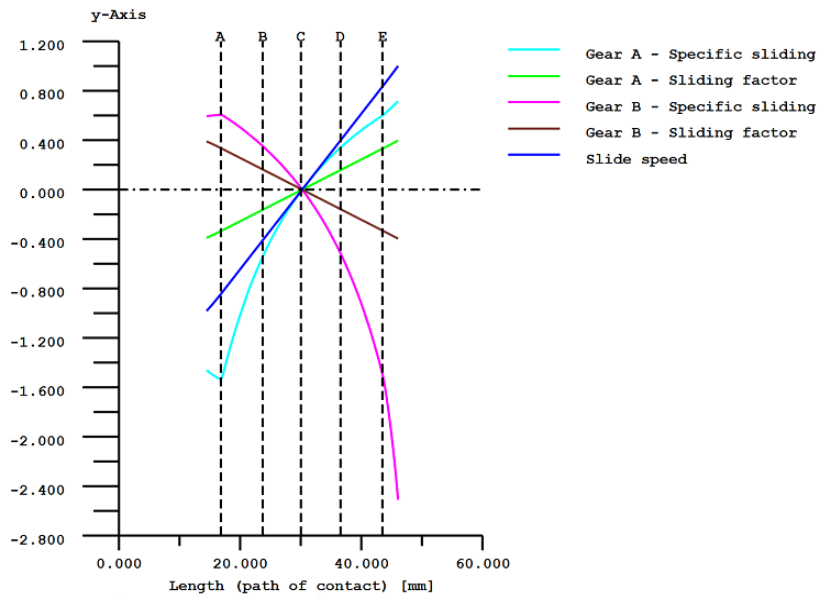
Figure: Amplitude spectrum of contact stiffness



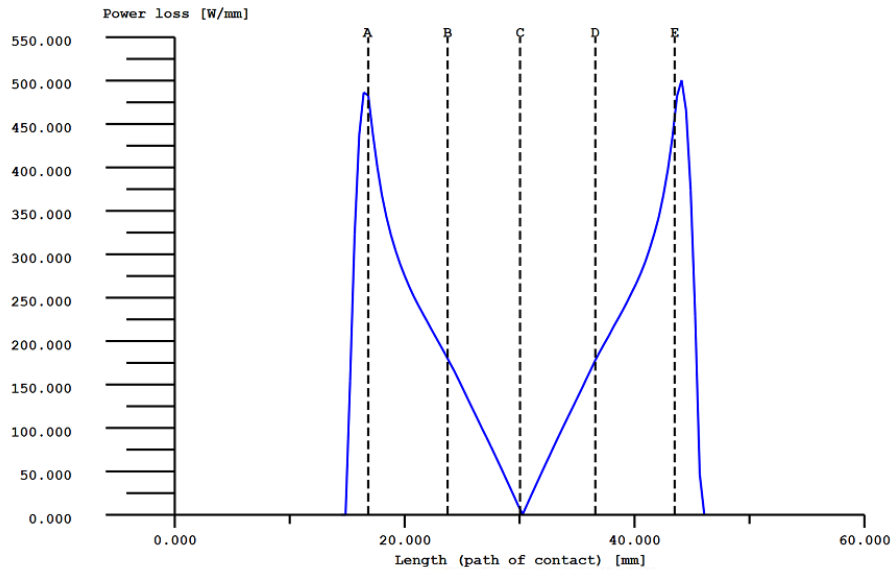
wt = 100 %, a = 160.000 mm, fpt = 0.000 μm, μ = 0.035 Working flank: Left flank  
 Figure: Normal force curve (Line load)



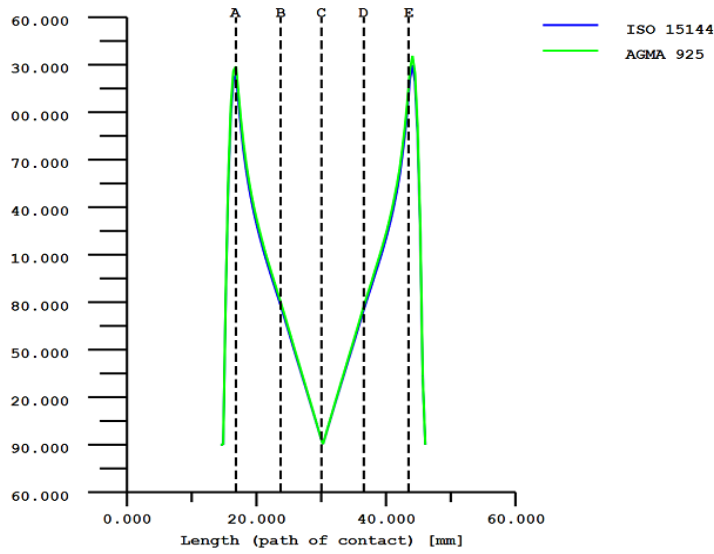
wt = 100 %, a = 160.000 mm, fpt = 0.000  $\mu$ ,  $\mu = 0.035$  Working flank: Left flank  
 Figure: Stress curve



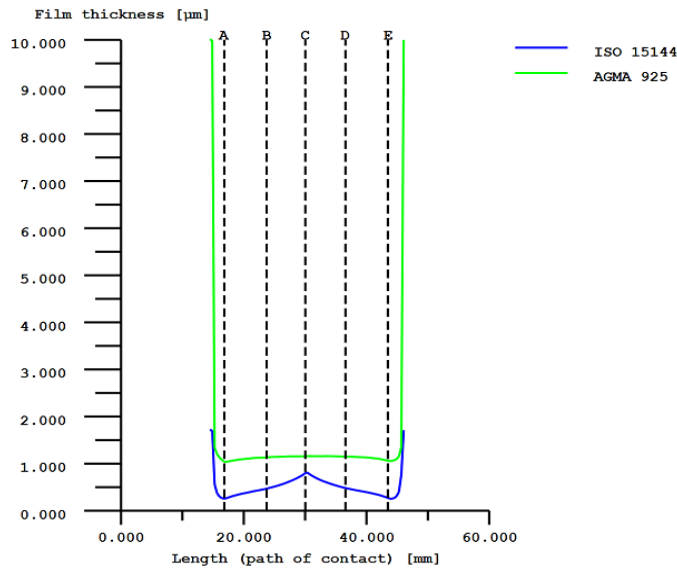
wt = 100 %, a = 160.000 mm, fpt = 0.000  $\mu$ ,  $\mu = 0.035$  Working flank: Left flank Maximum sliding velocity: 9.812 m/s  
 Figure: Kinematics



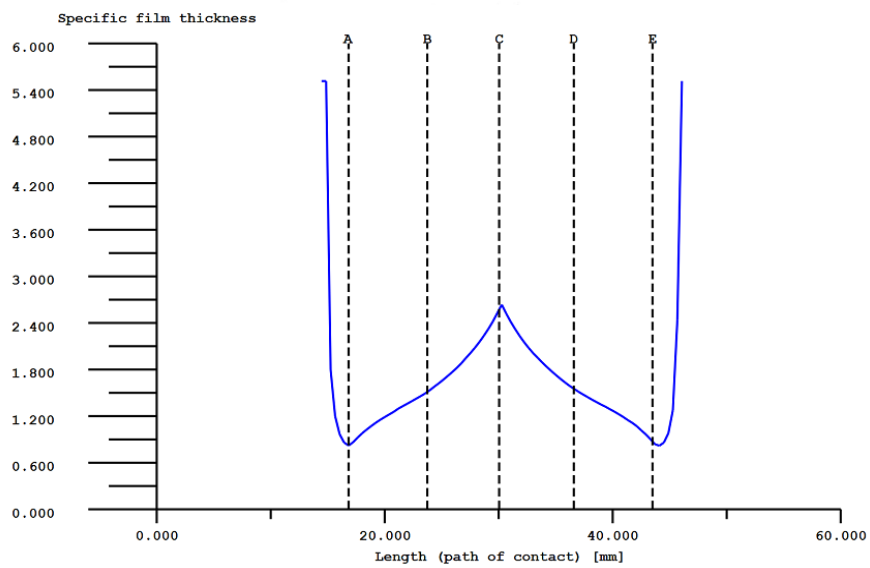
wt = 100 %, a = 160.000 mm, fpt = 0.000  $\mu$ m,  $\mu$  = 0.035  
 Displaying power losses per mm facewidth Working flank: Left flank  
 Contact temperature [ $^{\circ}$ C]



wt = 100 %, a = 160.000 mm, fpt = 0.000  $\mu$ m,  $\mu$  = 0.035  
 the oil = 90.0  $^{\circ}$ C, the M = 90.0  $^{\circ}$ C, etaM = 29.97 mPa\*s  
 Working flank: Left flank  
 Figure: Flash temperature (ISO TR 15144)



wt = 100 %, a = 160.000 mm, fpt = 0.000 µm,  $\mu = 0.035$  the oil = 90.0 °C, the M = 90.0 °C, etaM = 29.97 mPa\*shMini(ISO) = 0.243 µm, Ra = 0.310 µm AGMA: h = hc/1.316 (Wellauer & Holloway criteria) Working flank: Left flank  
 Figure: Lubricating film (ISO TR 15144)



wt = 100 %, a = 160.000 mm, fpt = 0.000 µm,  $\mu = 0.035$  the oil = 90.0 °C, the M = 90.0 °C, etaM = 29.97 mPa\*shMini(ISO) = 0.243 µm, Ra = 0.310 µm, lamGFmin = 0.783 Working flank: Left flank  
 Figure: Specific film thickness (ISO TR 15144)

Remark:

The report contains only the important graphics.

The other graphics can be found in menu 'Graphics' -> 'Contact analysis'.

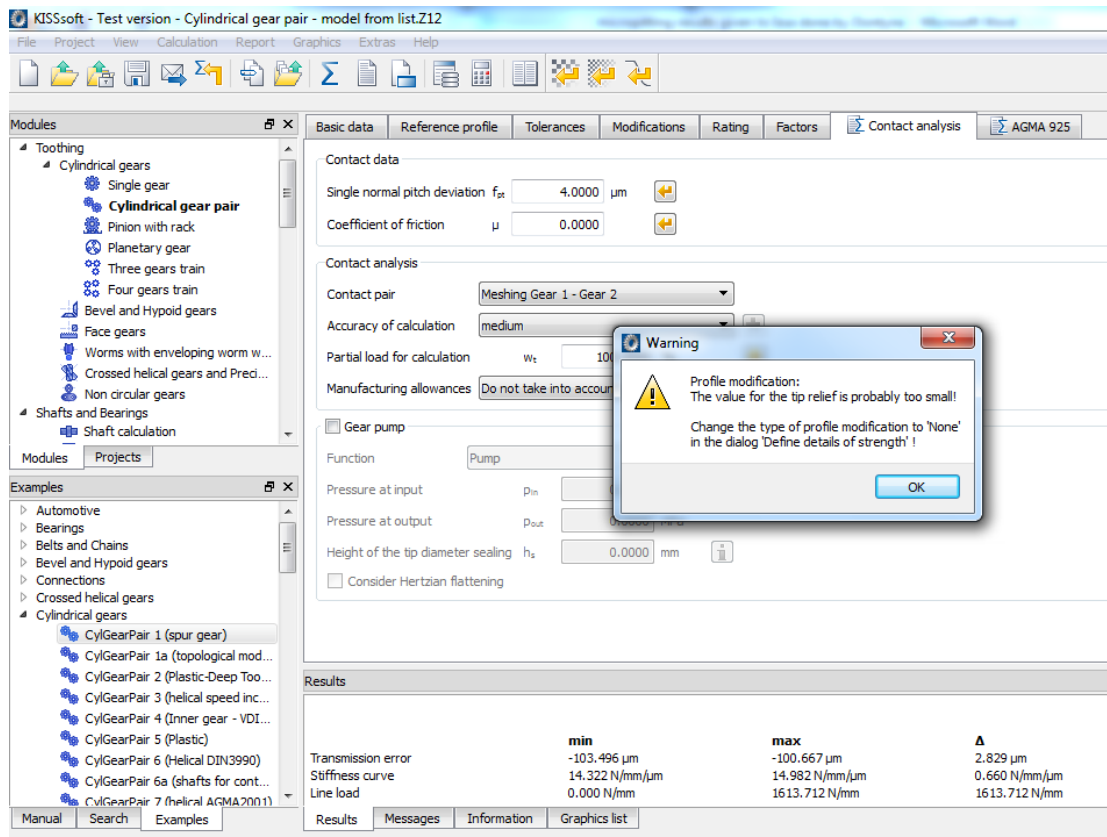


End of Report

lines: 228

---

**APPENDIX-K: KISSsoft warning message at maximum torque ratio. (Chapter 6, Section 6.7)**



The screenshot shows the KISSsoft software interface for a cylindrical gear pair model. The main window displays the 'Contact analysis' tab with various parameters. A warning dialog box is overlaid on the interface, indicating a profile modification issue.

**Warning Dialog Box:**

Profile modification:  
The value for the tip relief is probably too small!  
Change the type of profile modification to 'None' in the dialog 'Define details of strength'!

**Results Table:**

	min	max	$\Delta$
Transmission error	-103.496 $\mu\text{m}$	-100.667 $\mu\text{m}$	2.829 $\mu\text{m}$
Stiffness curve	14.322 N/mm/ $\mu\text{m}$	14.982 N/mm/ $\mu\text{m}$	0.660 N/mm/ $\mu\text{m}$
Line load	0.000 N/mm	1613.712 N/mm	1613.712 N/mm

**APPENDIX-L: Recommended Maximum Values of Gear Tooth Surface Roughness.**  
(Chapter 7, Section 7.6)

<b>Gear</b>	<b><math>R_a</math> <math>\mu\text{m}</math></b>
High speed pinion and gear	$\leq 0,7$
Intermediate pinion and gear	$\leq 0,7$
Low speed pinion and gear	$\leq 0,6$
Low speed sun and planet	$\leq 0,5$

Source: 61400-4 (2012, P. 94)

**APPENDIX-M: KISSsoft Output Results of WT Spur Gear at Rated Condition.**  
(Chapter 7, Section 7.6)



KISSsoft Release 03/2013

---

KISSsoft evaluation

---

File

---

Name : spur gear model by kiss  
 Description: KISSsoft example  
 Changed by: issa am: 10.03.2014 um: 12:38:07

---

**Contact analysis**

Mesh gear 1 - gear 2 (Right Tooth Flank)

Accuracy of calculation		high				
Partial load for calculation		100.00	%			
Center distance	[a]	381.5000	mm			
Single pitch deviation	[f <sub>pt</sub> ]	0.0000	µm			
Coefficient of friction	[µ]	0.0380				
Deviation error of axis	[f <sub>Σβ</sub> ]	0.0000	µm			
Inclination error of axis	[f <sub>Σδ</sub> ]	0.0000	µm			
Torque	[T <sub>1</sub> ]					
Torsion		Gear A :-, B :-				
		min	max	Δ	μ	
Transmission error	(µm)	-54.0796	-31.1250	22.9546	-34.7001	6.1682
Stiffness curve	(N/mm/µm)	13.3413	22.8783	9.5370	21.8111	1.7699
Line load	(N/mm)	3.0724	715.4855	712.4130	360.8575	112.1967
Torque Gear 1	(Nm)	33068.5404	33069.1351	0.5947	33068.8438	0.1000
Torque Gear 2	(Nm)	8747.6790	8845.2082	97.5292	8792.3020	19.7314
Power loss	(W)	10.0409	10992.5900	10982.5491	9105.1906	2865.7424
Flash temperature	(°)	65.0700	165.8356	100.7656	107.7655	25.0521
Lubricating film	(µm)	0.4624	3.8584	3.3960	1.1251	0.3840
Hertzian stress	(N/mm <sup>2</sup> )		1531.1459		793.8083	
Transverse contact ratio under load	[ε <sub>a</sub> ]	1.954				
Overlap ratio under load	[ε <sub>b</sub> ]	0.000				
Total contact ratio under load	[ε <sub>g</sub> ]	1.954				
Efficiency	[η]	99.45	%			

**K<sub>Hβ</sub> Calculation - Gear 1 - Gear 2**

Right flank

f<sub>Σβ</sub> = 0.000 µm , f<sub>Σδ</sub> = 0.000 µm  
 f<sub>ma</sub> = 0.000 µm , f<sub>Hβ</sub> = 0.000 µm  
 Result after i = 1 iterations of load distribution  
 Gear 1  
 Point in polar co-ordinates:  
 R = 301.000 mm , φ = 0.000 °  
 Displacement calculated in direction 110.000 °

	y	φ1.t	f1.t	f1.b	f1.tot	f1.C	f1.tot+f1.C
1	0.000 mm	0.0000°	-0.0000 µm	0.0000 µm	0.0000 µm	0.0000 µm	0.0000 µm

Gear 2

Point in polar co-ordinates:  
 R = 80.500 mm , φ = 180.000 °  
 Displacement calculated in direction 110.000 °

	y	φ2.t	f2.t	f2.b	f2.tot	f2.C	f2.tot+f2.C
--	---	------	------	------	--------	------	-------------



1 0.000 mm 0.0000° 0.0000 μm 0.0000 μm 0.0000 μm 0.0000 μm 0.0000 μm

Explanations:

- y : Width
- φ.t : Static torsion
- f.t : Displacement due to torsion
- f.b : Displacement due to bending
- f.tot : Total displacement (f.b+f.t)
- f.C : Change due to flank line modification

Load distribution

Contact stiffness = 15.496 N/mm/μm

Young's modulus = 206000.0/206000.0 N/mm2

	y	δ	g	w
1.	0.0000 mm	0.0000 μm	68.5911 μm	1062.8559 N/mm

Explanations:

- δ : Gap
- g : Flank overlap
- w : Line load

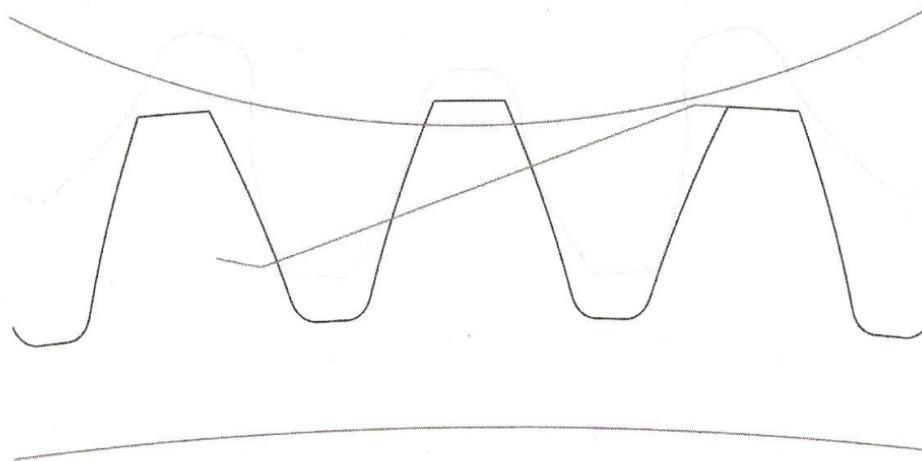
w<sub>max</sub> = 1062.856 N/mm, w<sub>m</sub> = 1062.856 N/mm

w<sub>m</sub> = K<sub>V</sub> \* K<sub>A</sub> \* K<sub>Y</sub> \* (F<sub>t</sub>/b) / cos(α<sub>wt</sub>)

K<sub>V</sub> = 1.200, K<sub>A</sub> = 1.250, K<sub>Y</sub> = 1.000

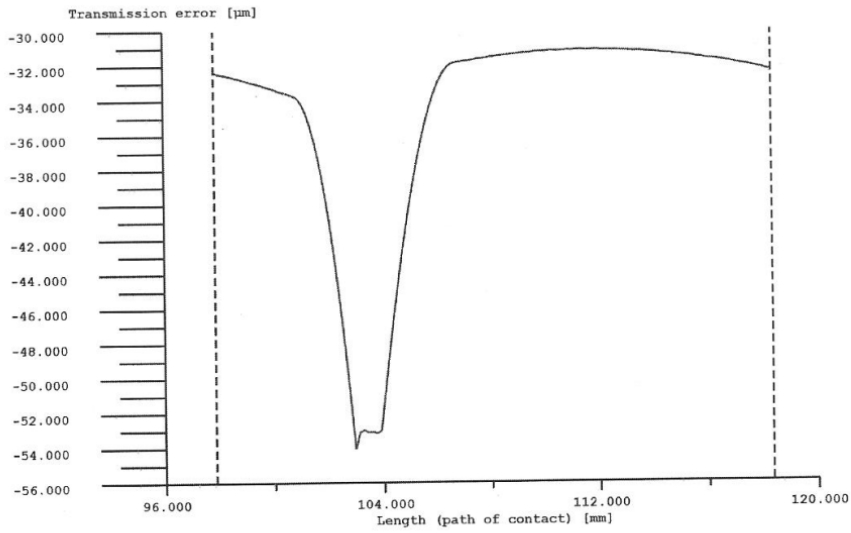
K<sub>Hβ</sub> = w<sub>max</sub>/w<sub>m</sub> = 1.0000 (Calculation according to ISO 6336-1, Appendix E)

Important notice: Since no values are given for shaft deformation or axis inclination, the calculated KHbeta value should not be used in practice.

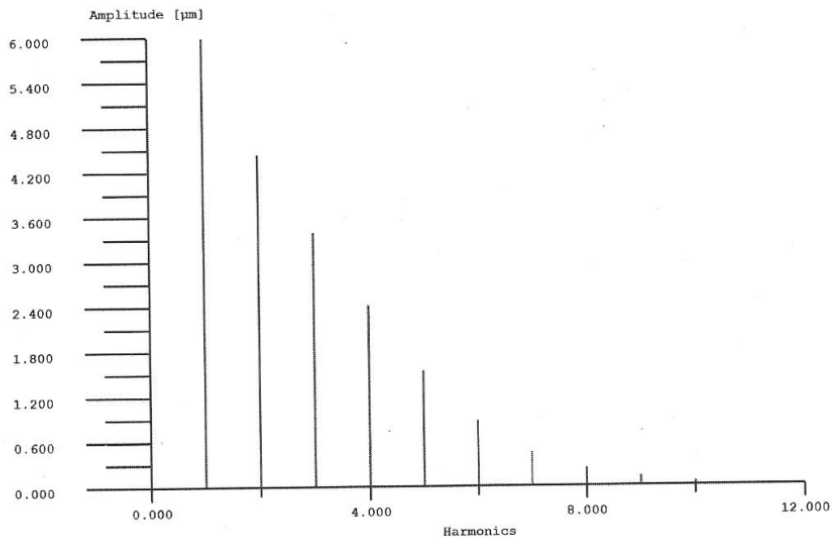


da1 = 615.4974 mm, df1 = 582.4502 mm, As1 = -0.2150 mmda2 = 175.5026 mm, df2 = 142.7165 mm, As2 = -0.1200 mm

Figure: Path of contact

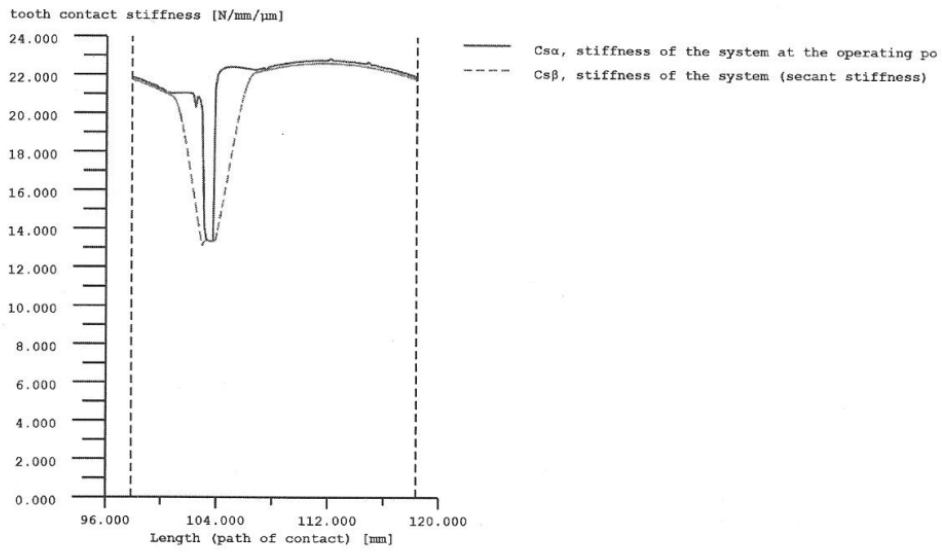


wt = 100 %, a = 381.500 mm, fpt = 0.000 µm, µ = 0.038 Working flank: Right flank  
 Figure: Transmission error

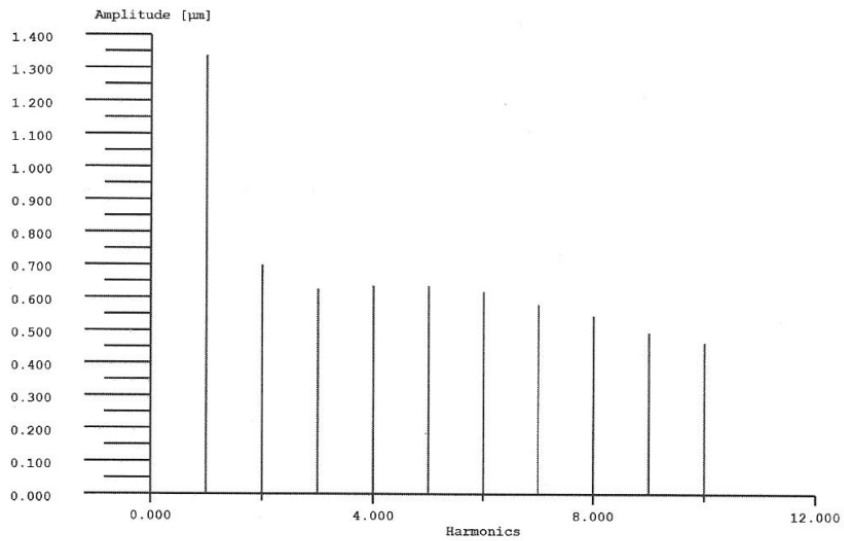


Harmonics	Amplitude [µm]	1.	5.9888712.	4.4363433.	3.3931714.	2.4110565.	1.5411896.
0.8737987.	0.4534948.	0.2378059.	0.12751710.	0.056773	wt = 100 %, a = 381.500 mm, fpt = 0.000 µm, µ = 0.038 Working flank: Right flank		

Figure: Amplitude spectrum of transmission error

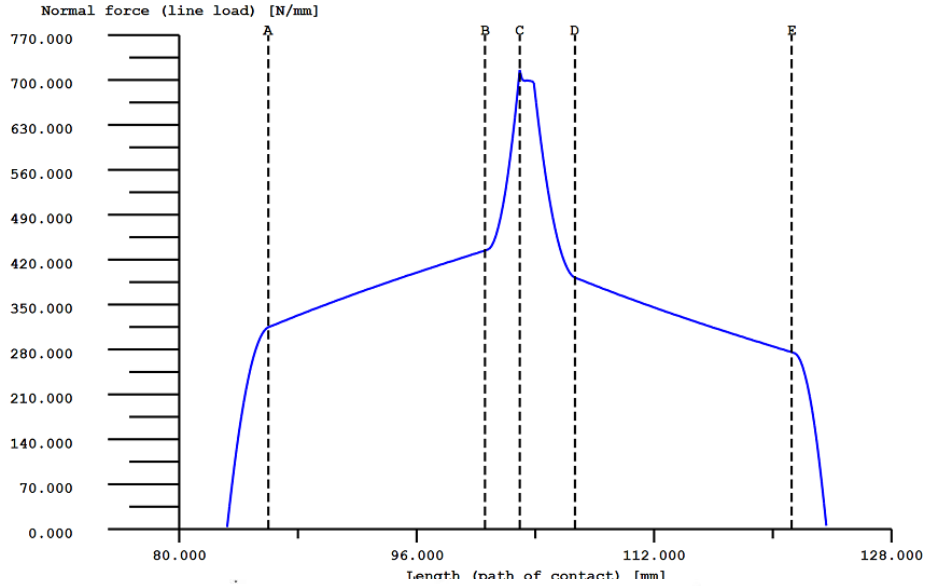


wt = 100 %, a = 381.500 mm, fpt = 0.000 μm, μ = 0.038 Working flank: Right flank  
 Figure: Stiffness curve

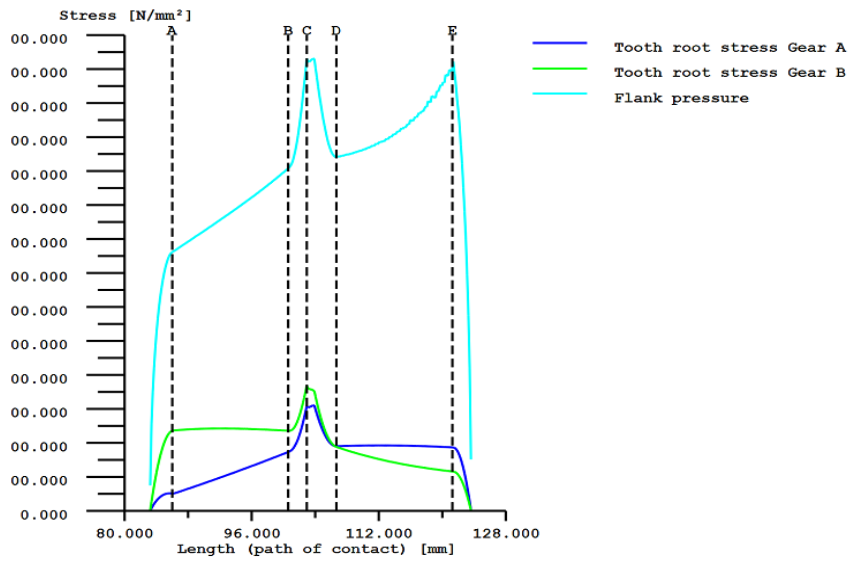


Harmonics	Amplitude [N/mm/μm]	1.	1.3375982.	0.6999513.	0.6267874.	0.6361735.
0.6359536.	0.6185217.	0.5800408.	0.5463809.	0.49509810.	0.463916	wt = 100 %, a = 381.500

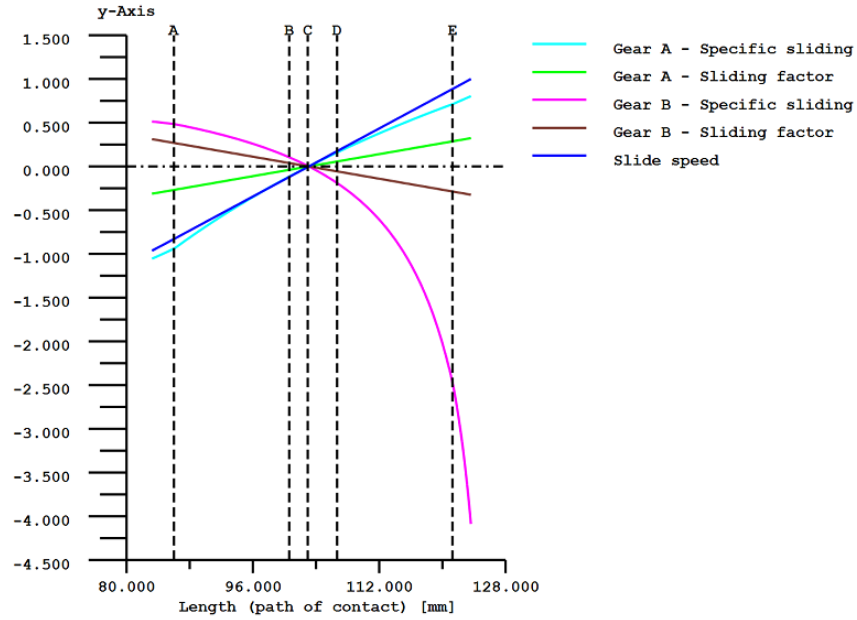
mm, fpt = 0.000 μm, μ = 0.038 Working flank: Right flank  
 Figure: Amplitude spectrum of contact stiffness



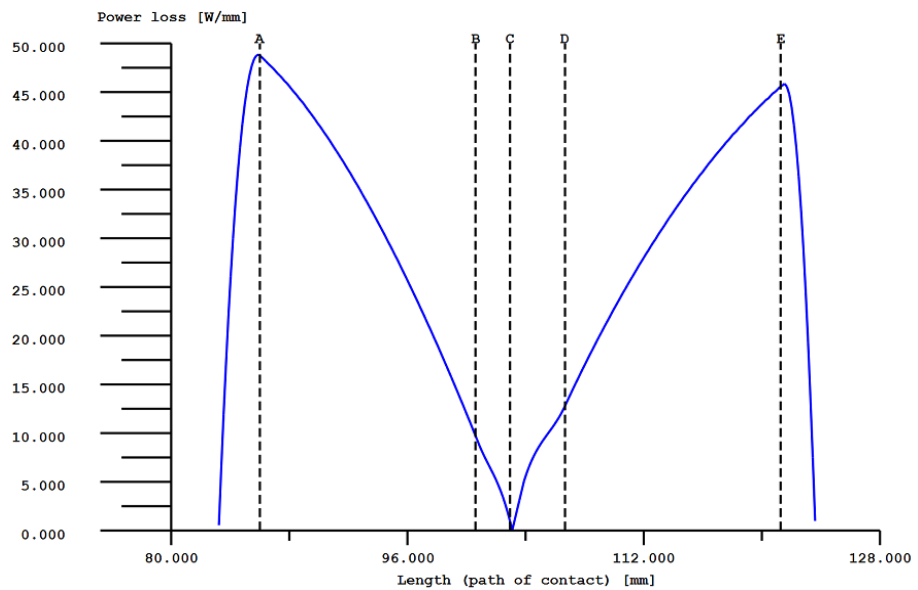
wt = 100 %, a = 381.500 mm, fpt = 0.000  $\mu$ ,  $\mu = 0.038$  Working flank: Right flank  
 Figure: Normal force curve (Line load)



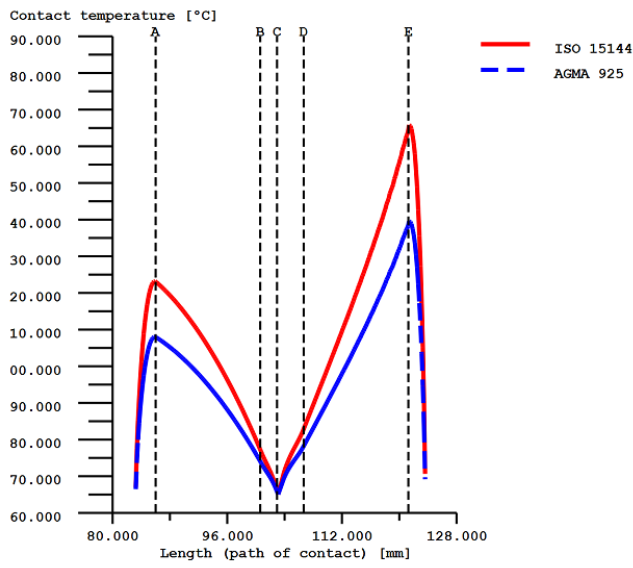
wt = 100 %, a = 381.500 mm, fpt = 0.000  $\mu$ ,  $\mu = 0.038$  Working flank: Right flank  
 Figure: Stress curve



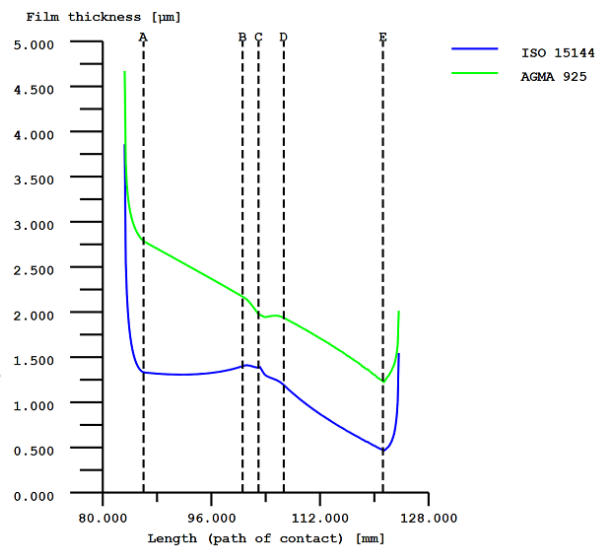
wt = 100 %, a = 381.500 mm, fpt = 0.000  $\mu$ ,  $\mu = 0.038$  Working flank: Right flank Maximum sliding velocity: 4.912 m/s  
Figure: Kinematics



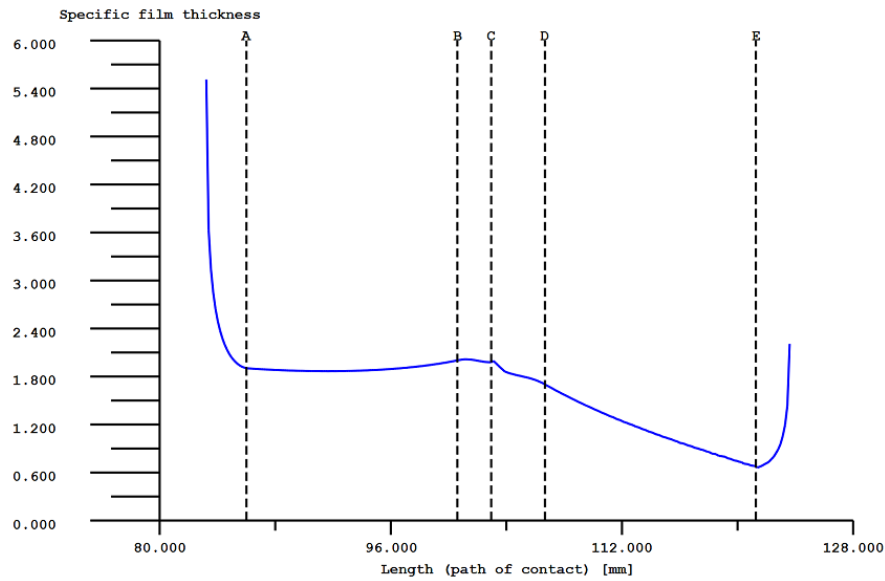
wt = 100 %, a = 381.500 mm, fpt = 0.000  $\mu$ ,  $\mu = 0.038$  Displaying power losses per mm facewidth Working flank: Right flank  
Figure: Specific Power Loss



wt = 100 %, a = 381.500 mm, fpt = 0.000  $\mu\text{m}$ ,  $\mu = 0.038$ ,  $\theta_{oil} = 65.0$  °C,  $\theta_{eM} = 65.0$  °C,  $\eta_{aM} = 85.66$  mPa\*s Working flank: Right flank  
 Figure: Flash temperature (ISO TR 15144)



wt = 100 %, a = 381.500 mm, fpt = 0.000  $\mu\text{m}$ ,  $\mu = 0.038$ ,  $\theta_{oil} = 65.0$  °C,  $\theta_{eM} = 65.0$  °C,  $\eta_{aM} = 85.66$  mPa\*s  $h_{Mini(ISO)} = 0.000$   $\mu\text{m}$ ,  $R_a = 0.700$   $\mu\text{m}$  AGMA:  $h = hc/1.316$  (Wellauer & Holloway criteria) Working flank: Right flank  
 Figure: Lubricating film (ISO TR 15144)



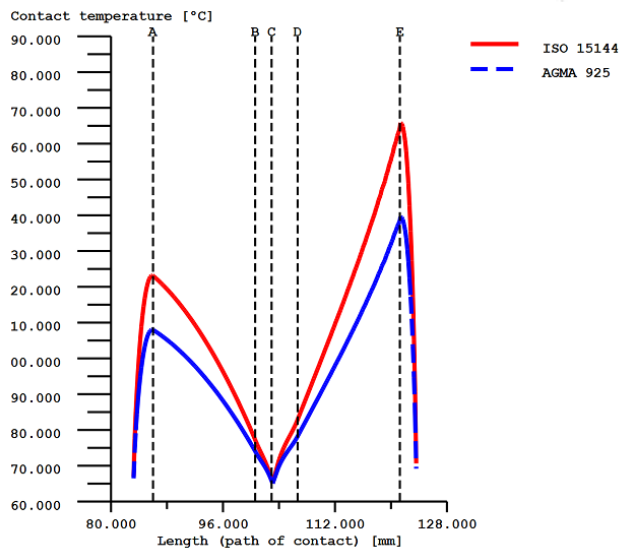
wt = 100 %, a = 381.500 mm, fpt = 0.000  $\mu\text{m}$ ,  $\mu = 0.038$  the oil = 65.0 °C, the M = 65.0 °C, etaM = 85.66 mPa\*s hMini(ISO) = 0.000  $\mu\text{m}$ , Ra = 0.700  $\mu\text{m}$ , lamGFmin = 0.000 Working flank: Right flank

Figure: Specific film thickness (ISO TR 15144)

Remark:

The report contains only the important graphics.

The other graphics can be found in menu 'Graphics' -> 'Contact analysis'.



wt = 100 %, a = 381.500 mm, fpt = 0.000  $\mu\text{m}$ ,  $\mu = 0.038$  the oil = 65.0 °C, the M = 65.0 °C, etaM = 85.66 mPa\*s Working flank: Right flank

Figure: Flash temperature (ISO TR 15144)



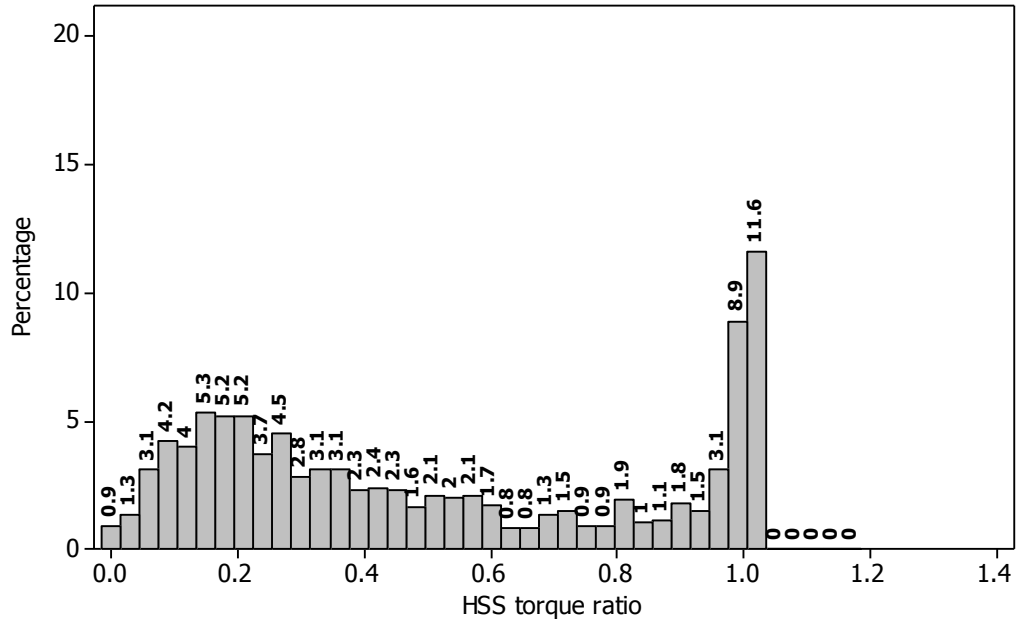
End of Report

lines: 106

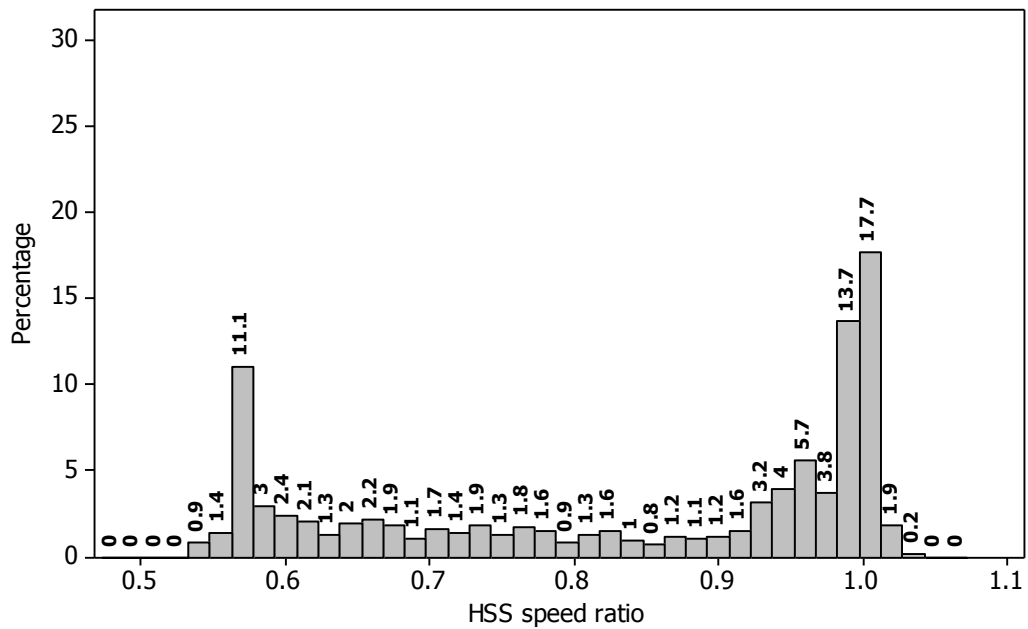
---

**APPENDIX-N: Histograms of 1000 Random Samples of WT1. (Chapter 8, Section 8.2)**

**Histogram of 1000 random numbers of HSS pinion shaft torque ratio (WT1)**



**Histogram of 1000 random numbers of HSS pinion shaft rotational speed ratio (WT1)**



---

## PUBLICATIONS

### Declarations

Some parts of the work presented in this thesis have been published in the following Articles:

Al-Tubi, I. S. and Long, H. 2012. Prediction of Wind Turbine Gear Micropitting under Variable Load and Speed Conditions Using ISO/TR 15144-1: 2010. *Proceedings of the Institution of Mechanical Engineers, Part C: Journal of Mechanical Engineering Science*. 227 (9), 1898-1914.

Long H and Al-Tubi I. 2013. Effects of Operational Conditions on Wind Turbine Gear Micropitting. *The European Wind Energy Association Conference 2013*, Vol. 2013. Vienna, Austria, February 2013.

Al-Tubi, I. S., Long, H., Tavner, P. J., Shaw, B. and Zhang, J. 2014. Probabilistic Analysis of Gear Flank Micropitting Risk in Wind Turbine Gearboxes Using SCADA Data. Submitted to the *IET Renewable Power Generation* (under review).

Al-Tubi, I. S., Long, H., Zhang, J. and Shaw, B. Experimental and Analytical Investigation of Micropitting Initiation and Progression under Varying Load Conditions. Submitted to the *Wear* (under review).

Al-Tubi, I. S. and Long, H. 2013. Effects of Variable Load and Rotational Speed on Gear Pitting in Wind Turbine Gearbox. Poster presented at *10thTribology-UK Conference – Future of Tribology*, March 2013. University of Leeds. UK.

Al-Tubi, I. S. and Long, H. 2013. Effects of Variable Load and Rotational Speed on Gear Pitting in Wind Turbine Gearbox. Poster presented at the *University of Sheffield Engineering Symposium*, May 2013, UK.

Long H., Al-Tubi I. and Martinez M. 2014. Risk Assessment of WT Gear Micropitting under Variable Torque and Speed Conditions. Invited Presentation at *National Renewable Energy Laboratory (NREL) Gearbox Reliability Collaborative (GRC) meeting*, February 2014. US